

# **DOCTORAL THESIS**

Title

**“THREE-DIMENSIONAL SPATIAL DISTRIBUTION OF SCATTERERS  
IN THE CRUST BY INVERSION ANALYSIS OF S-WAVE CODA  
ENVELOPES. A CASE STUDY OF GAURIBIDANUR SEISMIC ARRAY  
SITE (SOUTHERN INDIA) AND GALERAS VOLCANO (SOUTH-  
WESTERN COLOMBIA)”**

Presented by

**EDUARD CARCOLÉ CARRUBÉ**

Centre

**OBSERVATORI DE L'EBRE**

Department

**SEISMOLOGY SECTION**

Directed by

**DRA. ARANTZA UGALDE AGUIRRE**







# TABLE OF CONTENTS

<b>ACKNOWLEDGMENTS</b>	<b>15</b>
<b>1 INTRODUCTION</b>	<b>19</b>
<b>2 CODA CHARACTERISTICS</b>	<b>25</b>
<b>2.1 INTRODUCTION</b>	<b>25</b>
<b>2.2 S-WAVE CODA ATTRIBUTES</b>	<b>28</b>
<b>2.3 CHARACTERIZING S-CODA ENVELOPES</b>	<b>30</b>
<b>2.4 TWO EXTREME MODELS FOR CODA WAVES</b>	<b>33</b>
2.4.1 SINGLE ISOTROPIC SCATTERING MODEL	34
2.4.1.1 Distribution of scatterers. Isotropic scattering assumption	34
2.4.1.2 Single isotropic scattering approximation	35
2.4.1.3 Properties of the solution	37
2.4.2 RATIO OF SINGLE SCATTERED ENERGY VERSUS MULTIPLE SCATTERED ENERGY	38
2.4.3 DIFFUSION THEORY	41
<b>2.5 RADIATIVE TRANSFER THEORY</b>	<b>44</b>
2.5.1 RADIATIVE TRANSFER EQUATION	44
2.5.2 SOLUTIONS OF THE RADIATIVE TRANSFER EQUATION. ISOTROPIC SCATTERING	47
2.5.2.1 Ballistic peak and single scattering	48
2.5.2.2 Multiple scattering	49
2.5.2.3 Analytical approximation of multiple scattering integrals	49
2.5.2.4 Comparing exact solutions and approximate solutions	50
<b>3 SPATIAL DISTRIBUTION OF CODA SCATTERERS</b>	<b>55</b>
<b>3.1 INTRODUCTION</b>	<b>55</b>
<b>3.2 THE OBSERVATIONAL EQUATION</b>	<b>56</b>
<b>3.3 COMPUTATION OF THE ENERGY RESIDUALS</b>	<b>59</b>
<b>4 INVERSION METHODS</b>	<b>63</b>
<b>4.1 INTRODUCTION</b>	<b>63</b>
<b>4.2 ART ALGORITHM</b>	<b>64</b>
4.2.1 CONVERGENCE AND CHARACTERISTICS OF THE SOLUTIONS	67

<b>4.3</b>	<b>SIRT ALGORITHM</b>	<b>68</b>
4.3.1	THE WEIGHT COEFFICIENTS $w_{ij}$	69
<b>4.4</b>	<b>BACKPROJECTION ALGORITHM</b>	<b>70</b>
4.4.1	BACKPROJECTION ALGORITHM IN TWO DIMENSIONS WITH LINEAR ARRAYS OF TRANSDUCERS. GEOMETRY AND DEFINITIONS	70
4.4.2	THE FOURIER SLICE THEOREM	72
4.4.3	RECONSTRUCTION ALGORITHM FOR PARALLEL PROJECTIONS	73
4.4.4	IMPLEMENTING A FILTERED-BACKPROJECTION ALGORITHM FOR PARALLEL DATA	75
4.4.5	EXAMPLES	76
4.4.6	CONNECTION BETWEEN ART AND BACKPROJECTION. A SIMPLE EXAMPLE.	78
4.4.7	BACKPROJECTION ALGORITHM VERSUS ART AND SIRT	80
<b>4.5</b>	<b>BACKPROJECTION ALGORITHM TO FIND 3D DISTRIBUTIONS OF SCATTERING COEFFICIENTS</b>	<b>81</b>
<b>5</b>	<b><i>SPATIAL DISTRIBUTION OF SCATTERERS IN THE CRUST OF GAURIBIDANUR SEISMIC ARRAY REGION (SOUTHERN INDIA)</i></b>	<b>87</b>
<b>5.1</b>	<b>INTRODUCTION</b>	<b>87</b>
<b>5.2</b>	<b>GEOLOGICAL SETTING</b>	<b>88</b>
5.2.1	CLOSEPET GRANITE BATHOLIT	90
5.2.2	GENERAL CHARACTERISTICS OF CRATONS. THE DHAWAR CRATON	93
5.2.3	CHARACTERISTICS OF GAURIBIDANUR ARRAY's SURROUNDING REGION	95
<b>5.3</b>	<b>DATA DESCRIPTION</b>	<b>96</b>
<b>5.4</b>	<b>DATA ANALYSIS</b>	<b>96</b>
<b>5.5</b>	<b>RESULTS</b>	<b>100</b>
<b>5.6</b>	<b>DISCUSSION</b>	<b>106</b>
<b>5.7</b>	<b>CONCLUSIONS</b>	<b>112</b>
<b>6</b>	<b><i>THREE-DIMENSIONAL SPATIAL DISTRIBUTION OF SCATTERERS IN GALERAS VOLCANO, SOUTH-WESTERN COLOMBIA</i></b>	<b>113</b>
<b>6.1</b>	<b>INTRODUCTION</b>	<b>113</b>
<b>6.2</b>	<b>GEOLOGICAL SETTING</b>	<b>115</b>
6.2.1	GEOLOGICAL HISTORY	115
6.2.2	GEOLOGY OF GALERAS VOLCANO	117

6.3	DATA DESCRIPTION	120
6.4	DATA ANALYSIS	123
6.5	RESULTS	125
6.6	DISCUSSION	128
6.7	CONCLUSIONS	131
7	<i>CONCLUSIONS</i>	133
	<i>APPENDIX A. EVENTS AT GBA REGION</i>	137
	<i>APPENDIX B. EVENTS AT GALERAS VOLCANO</i>	139
	<i>APPENDIX C. PROGRAM CODE</i>	155
8	<i>REFERENCES</i>	165



## LIST OF FIGURES

<b>Figure 2-1.</b> Picture of the crystals of granite. _____	25
<b>Figure 2-2.</b> S. Andreas Fault, California. _____	25
<b>Figure 2-3.</b> Non-filtered seismograms corresponding to Galeras volcano events (appendix A). (A) Event 4 station 22, 26/09/1989. (B) Event 75, station 4, 02/06/1992 (C) Event 250 station 19, 16/02/1996, (D) Event 301, station 20, 30/04/1997. Green lines indicate the S-waves arrival time. _____	26
<b>Figure 2-4.</b> Summary of root mean squared coda envelopes for different frequency bands. Data are from many different events. _____	32
<b>Figure 2-5</b> Prolate spheroidal coordinates. $\xi_1 = \sinh \xi$ , $\xi_2 = \cos \eta$ , $\xi_3 = \phi$ . _____	36
<b>Figure 2-6</b> Maximum distance up to which the single scattering approximation may be used ( $v=3.5$ km/s). Blue lines correspond to $n=2$ and red line to $n=3$ . Solid lines correspond to $\xi = 0.2$ and dashed lines to $\xi = 0.43$ . _____	41
<b>Figure 2-7.</b> Lunar earthquakes showing long coda durations. _____	43
<b>Figure 2-8.</b> Propagation through the scattering volume in the $\hat{s}$ direction and emission into the $\hat{s}$ direction from scattering events due to energy from the $\hat{s}'$ direction. _____	45
<b>Figure 2-9.</b> Intensity as a function of time $t$ , at distances $r = 2.0l$ , $2.8l$ and $4.0l$ , from left to right. The blue lines are the exact result, which is very close to the interpolation formulas: green line corresponds to Eq. (2.51) and orange line corresponds to using the approximation in Eq. (2.52). Dashed red lines correspond to the Gaussian diffusive result. _____	53
<b>Figure 3-1.</b> Analysis of event 300 recorded by the station 14 in the Galeras volcano (see appendix A). (A) corresponds to the raw seismogram. (B) corresponds to the filtered seismogram in the 4-8 Hz band. (C) is the power spectrum of the seismogram between $t=3.48$ s and $t=11.48$ s. This lapse time corresponds to the one that will be used to carry out the linear regression in figure (D). First green line indicates $t_s$ in Figs (A-B-D) and second green line indicates $2t_s$ in Figs (B-D). In Fig (C) green lines indicate the frequency band under analysis. (E) corresponds to the logarithm of the coda energy residuals averaged in a time window of 0.5 s. _____	61
<b>Figure 3-2.</b> Analysis of event 128 recorded by the station 14 in the Galeras volcano (see Appendix A). (A) corresponds to the raw seismogram. (B) corresponds to the filtered seismogram in the 8-12 Hz band. (C) is the power spectrum of the seismogram (A) between $t=4.0$ s and $t=13.95$ s. This lapse time corresponds to the one that will be used to carry out the linear regression in figure (D). First green line indicates $t_s$ in Figs (A-B-D) and second green line indicates $2t_s$ in Figs (B-D). In Fig (C) green lines indicate the frequency band under analysis. Dashed line indicates a safe initial time to avoid side effects from saturation of the recorded seismogram. (E) corresponds to the logarithm of the coda energy residuals averaged in a time window of 0.5 s. _____	62
<b>Figure 4-1.</b> The Kaczmarz method of solving algebraic equations is illustrated for the case of two unknowns. One starts with some arbitrary initial guess and then projects onto the line corresponding to the first equation. The resulting point is now projected onto the line representing the second equation. If	

there are only two equations, this process is continued back and forth, as illustrated by the dots in the figure, until convergence is achieved.	65
<b>Figure 4-2.</b> The hyperplane $\vec{w}_1 \cdot \vec{f} = p_1$ (represented by a line in this two-dimensional figure) is perpendicular to the vector $\vec{w}_1$ .	66
<b>Figure 4-3.</b> Illustration of the geometry of a set of parallel projection beams.	71
<b>Figure 4-4</b> Illustration of the Fourier Slice Theorem.	73
<b>Figure 4-5.</b> Shepp-Logan Phantom.	77
<b>Figure 4-6.</b> Sinogram of the Shep-Logan	77
<b>Figure 4-7.</b> Reconstructions for (left to right up to down) N=1, 4, 8, 16, 32, 64 and 128 projections.	77
<b>Figure 4-8.</b> Aliasing effects.	78
<b>Figure 4-9.</b> Object to be measured.	78
<b>Figure 4-10.</b> Projection process.	79
<b>Figure 4-11.</b> Initial Solution.	79
<b>Figure 4-12</b> Result of the first iteration.	79
<b>Figure 4-13</b> Result of the second iteration.	80
<b>Figure 4-14.</b> Prolate spheroid (left) and oblate spheroid (right) .	85
<b>Figure 5-1.</b> Geometry and location of stations of Gauribidanur seismic array.	88
<b>Figure 5-2.</b> General geological sketch map of southern India. DVP, Deccan volcanic province; WDC, western Dharwar craton; EDC, eastern Dharwar craton; SIGT, south Indian granulite terrain; EGGT, eastern Ghat granulite terrain; CPG, closepet granite; CB, Cuddapah basin; PC, Phanerozoic sedimentary cover. Dotted line indicates Fermor's line (boundary between Dharwar craton and south India granulite terrain). (From Tripathi and Ugalde, 2004).	89
<b>Figure 5-3.</b> Detailed geological map corresponding to the eastern and western Dhawar craton and the Closepet granite batholit.	90
<b>Figure 5-4.</b> Sketch drawing of the emplacement mode and strain partitioning in the Closepet granite at contrasted structural levels (Moyen, 2000). Black, thin arrows correspond to melt movement. White, large arrows: kinematics of deformation. Notice three different zones may be defined along the batholit.	93
<b>Figure 5-5.</b> Map of southern India showing the location of the seismic stations and earthquakes used for the analysis.	97
<b>Figure 5-6</b> Illustrating the process to calculate the coda energy residuals for a GBA seismic event	99
<b>Figure 5-7.</b> Hit counts or number of coda residuals contributed by each block. It measures the number of times each block is sampled by the scattering shells of observed coda data. The darker areas are the zones lesser sampled by the spherical shells.	101
<b>Figure 5-8.</b> Spatial distribution of relative scattering coefficients for a synthetic test consisting of a column. It was located northeast from the array centre point, which is shown by a solid triangle. A longitudinal section corresponding to $z=0$ km and the corresponding transversal section are shown.	102
<b>Figure 5-9.</b> Spatial distribution of relative scattering coefficients for different depths and for the two inversion methods used: (a) results for the frequency band 1-2 Hz; (b) 2-4 Hz; and (c) 4-10 Hz. The lightest zones indicate the strongest perturbations from an average scattering coefficient.	103

<b>Figure 5-10.</b> Vertical cross section of relative scattering coefficients at the parallel 13.6°, which corresponds to the latitude of the array cross-point. _____	107
<b>Figure 5-11.</b> Spatial distribution of relative scattering coefficients for a synthetic test consisting of one spheroidal structure with two horizontal semi-axes of 13 km and the vertical semi-axis of 9.3 km. It was located at different distances from the array centre point, which is shown by a solid triangle: (a) to the west; (b) below; and (c) to the east. The pattern recovered at a depth of 0 km is plotted at the top of the figure. The vertical cross section along the plane defined by the latitude of the array centre point is also shown. _____	109
<b>Figure 6-1.</b> Topographic map of Colombia showing the location of the Galeras volcano and the study area. _____	114
<b>Figure 6-2.</b> Galeras volcano from the west flank. Photo by Norm Banks of USGS. _____	115
<b>Figure 6-3.</b> Geological map of the Galeras Region. The map includes the locations of the stations. _____	117
<b>Figure 6-4.</b> Map showing the shape of Galeras volcano and altitude curves . _____	118
<b>Figure 6-5.</b> Sketch of the magmatic plumbing system beneath Galeras. _____	119
<b>Figure 6-6.</b> Three-dimensional of hypocenters (green circles) and stations (blue triangles). _____	121
<b>Figure 6-7.</b> Vertical cross sections of the hit count distribution along the parallel 1.23°N (A) and the meridian 77.36°W (B) which correspond to the coordinates of the summit. The Galeras volcano location is indicated by the solid triangle. _____	126
<b>Figure 6-8.</b> Horizontal sections of the study area showing the distribution of the relative scattering strength ( $\alpha-1$ ) at different depths from 4 km to -4.5 km. The solid triangle indicates the location of the Galeras volcano summit. The topographic contour lines at 4000 m and 3500 m levels are also plotted. _____	127
<b>Figure 6-9.</b> Vertical cross section of the study region along the two planes defined by the summit coordinates, which indicated by the solid triangle (latitude 1.23° and longitude -77.36°). The color scale indicates the perturbation of the scattering coefficient $\alpha-1$ for the 4-8 Hz (A, B) and 8-12 Hz (C, D) frequency bands. _____	129
<b>Figure 6-10.</b> Vertical cross section showing the results of the inversion analysis for a synthetic test consisting of two spherical structures buried at depths of -2 km and -33 km. _____	130



## LIST OF TABLES

<b>Table 2-1</b> Maximum distance where the single scattering approximation may be used ( $v=3.5\text{km/s}$ ). .....	40
<b>Table 5-1.</b> S-wave velocity model for the Gauribidanur region. ....	100
<b>Table 6-1.</b> Number, name and coordinates of each station from which data has been used. ....	123
<b>Table 6-2.</b> S-wave velocity model for the Galeras Volcano region. ....	125



## **ACKNOWLEDGMENTS**

Staff of the Observatori de l'Ebre is thanked for providing the opportunity to develop this thesis.

Thesis advisor Arantza Ugalde is especially thanked for her useful physical insight and thoughtful discussions which provided much-needed guidance throughout this work.

I would like to thank my parents and brothers and sisters for their support and for encouraging me to pursue my doctorate. Most importantly, I would like to thank my wife Maria Cinta for her understanding, emotional support, and never-ending patience over the course of this work.



*“I think however, that there isn’t any solution to this problem of education other than to realize that the best teaching can be done only when there is a direct individual relationship between a student and a good teacher, a situation in which the student discusses the ideas, thinks about the things, and talks about the things. It’s impossible to learn very much by simply sitting in a lecture, or even by simply doing problems that are assigned. But in our modern times we have so many students to teach that we have to try to find some substitute for the ideal. Perhaps my lectures can make some contribution. Perhaps in some small place where there are individual teachers and students, they may get some inspiration or some ideas from the lectures. Perhaps they will have fun thinking them through or going on to develop some ideas further.”*

The Lectures on Physics, Richard Feynmann, June, 1963



# 1 INTRODUCTION

Seismology is the primary tool for the study of the earth's interior. Because few kilometres in depth can be drilled, all the information on deeper depths comes from indirect methods. Seismograms provide the data used for mapping the earth's interior and for studying the distribution of physical properties. The analysis of seismograms is also useful for assessing the societal hazards posed by earthquakes.

Because of the complexity of the processes involved, the approach taken, in general, is to describe them with simplified models that seek to represent key elements of the process under consideration. A hierarchy of different approximations, as appropriate, are used as starting models for more detailed investigations. The most accurate earth model used in Seismology is a laterally heterogeneous sphere. This model is often approximated as being spherically symmetric, with properties varying only with radius. This spherically symmetric model can be further approximated for many purposes as a stratified half-space, in which properties vary only with depth, or as a layered half-space composed of discrete uniform layers (Stein and Wysession, 2003, [1]).

A type of model to represent the earth medium is often chosen, and then seismological and other data is used to estimate the parameters of this model. Thus, a characteristic activity of Seismology is to solve inverse problems. Inverse problems are complicated to solve, because seismograms reflect the combined effect of the source and medium, neither of which is known exactly. Moreover, the inverse problems often have no unique solutions and the model parameters that describe the observations well do not have to reflect the physical reality necessarily. As a consequence, it is necessary to consider issues of precision, accuracy, and uncertainty.

A homogeneous, isotropic, elastic, layered half-space is often used in crust and upper mantle studies, where the distance between source and receiver is less than few hundred kilometres. For larger source-receiver distances, spherical geometry is required. More complex and accurate models consider the anisotropic and anelastic behaviour of the earth, and lateral variations, or heterogeneities.

In addition to reflection and transmission at discrete interfaces, the reasons why seismic waves attenuate or decrease in amplitude as they propagate are: anelasticity (or deviation from elasticity), geometrical spreading, multipathing, and scattering. Anelasticity, also called intrinsic absorption, implies the conversion of seismic energy into heat and it differs from the other processes in that energy is lost, not just moved onto a different path. The geometrical spreading effect is due to the redistribution of energy that occurs as the wave front expands or contracts during seismic waves' propagation. Multipathing implies a focusing and defocusing of seismic waves by lateral variations in velocity.

Scattering is due to the interaction of seismic waves with the heterogeneities of the medium and it occurs depending on the ratio of the heterogeneity size to the wavelength and the distance the wave travels through the heterogeneous region (Aki and Richards, 1980, [2]). When the heterogeneity is large compared to the wavelength, the wave is regarded as following a distinct ray path that is distorted by multipathing. When the heterogeneities are closer in size to the wavelength, scattering occurs. When the heterogeneities are much smaller than the wavelength, they simply change the medium's overall properties.

Scattering is especially important in the continental crust, which has many small layers and reflectors resulting from continental evolution. These structures do not affect waves with wavelengths longer than tens of kilometres, but they act as point scatterers for shorter wavelength waves. Scattering is the cause of the presence, in high frequency (>1Hz) seismograms, of continuous wave trains following the direct S-wave which are known as coda waves. Array observations have shown that they are incoherent waves scattered by randomly distributed heterogeneities having random sizes and contrast of physical properties (Sato and Fehler, 1998) [10].

A number of models have been developed to explain the relationship between coda-waves' envelopes and the spectral structure of the random heterogeneity in the earth. The characterization of the earth as a random medium is complementary to the classical stratified media characterization.

In this thesis, coda waves' recordings from local earthquakes will be analyzed to estimate the three-dimensional spatial distribution of scatterers in the crust. For this

purpose, it is necessary to know how the scattered waves' energy is distributed spatially and as a function of time. Thus, some hypothesis about the media characteristics and how and where the scattering is produced are necessary. The existing models on the scattering process will be reviewed in Chapter 2.

These models for S-coda envelope synthesis are based on the assumption of a homogeneous distribution of isotropic scatterers and they predict results consistent with the observed characteristics of the coda. However, detailed observations show that there may be departures from the observed characteristics of S-coda waves which may be explained by an inhomogeneous distribution of scatterers. This issue will be the subject of Chapter 3.

The problem of estimating deterministically the spatial distribution of scatterers leads to an inversion process of a huge system of equations that can not be solved by traditional methods. They require the use of sophisticated numerical techniques. We are talking about systems of equations with about  $10^5$  unknowns and  $10^5$  equations. These sorts of problems were solved for the first time in medical tomography applications and, since then, the computational methods needed have been applied to other scientific fields. The first approach used to obtain three dimensional reconstructions was an iterative method called ART. Then, other methods based on ART soon appeared. Although these methods are very accurate and the reconstructions are of a high quality, they have an important drawback: they are terribly slow and not appropriate for real time applications. Nowadays, scanners are able to obtain three dimensional images by solving large systems of equations, not by using iterative approaches, but using a remarkably fast non-iterative algorithm: the Filtered Backprojection. The Filtered Backprojection method is based on an important mathematical definition, the Radon Transform, and a theorem that connects the Radon transform and the Fourier Transform of the three-dimensional object to be reconstructed. This theorem is the so-called Fourier Slice Theorem.

In Chapter 4 we will analyze in detail the ART, SIRT and Filtered Backprojection algorithms. ART algorithm has been previously used in other seismological studies (Chen and Long, 2000, [43]). SIRT reconstructions, which are based on ART, are less noisy and better looking than ART reconstructions at the

expense of computation time. We will use this algorithm for the first time in seismological applications. The Filtered Backprojection algorithm had never been used in Seismology because there is no simple way to adapt it to the kind of problem to solve. The Filtered Backprojection algorithm is very sensitive to the geometry defined by the problem to solve. Then, firstly, the Filtered Backprojection algorithm will be derived using a simple approach and, secondly, a generalization by taking into account the special geometry of our problem will be adapted to our case. This is the main mathematical contribution of this thesis.

Chapters 5 and 6 present two applications of the methodology to different geotectonic regions in the earth: a seismically stable region in southern India and an active volcano in south-western Colombia. The three-dimensional spatial distribution of relative scattering coefficients in southern India will be estimated by means of an inversion technique applied to coda wave envelopes recorded by the Gauribidanur Seismic Array (GBA). The inversion analysis will be performed for the first time in this kind of seismological research by means of the Simultaneous Iterative Reconstruction Technique (SIRT) and Filtered Back-Projection method (FBP). Finally, the three-dimensional spatial distribution of relative scattering coefficients will be estimated for the Galeras volcano, Colombia, by means of inversion analysis of coda wave envelopes and using the Filtered Backprojection algorithm. The scientific contribution of these applications is very important, since tomographic results confirm for the first time geological hypothesis on the structure of both regions. On the one hand, the presence of the Closepet granitic batholith to the east of GBA is revealed up to a depth of about 24 km. This granitic intrusion is one of the most important geological features of the region that acts as the major geological boundary in the region. It is believed to be a Precambrian suture zone between the eastern and western Dharwar craton in southern India. On the other hand, the present magmatic plumbing system of Galeras volcano sketched by geological evidences is also confirmed. Two zones of strong scattering are detected: the shallower one is compatible with the presence of a shallow magmatic chamber located at a depth from 4 km to 8 km under the summit. The deeper one is imaged at a depth of ~37 km from the Earth's surface and may be related to a deeper magma reservoir that feeds the system.

Parallel to the theoretical developments in this thesis, an important amount of work

corresponds to programming the numerical algorithms and graphic displays. Numerical algorithms were programmed in C++ using a free version of Borland C++ (BuilderX [3]) and a commercial compiler as Microsoft Visual C++ [4] to assure a high compatibility. The program codes are annexed at the end of the document. Some of the graphic representations were generated with the DISLIN graphic libraries from the Max Planck Institute of Solar Research [5]. Using DISLIN, programs written in C++ were developed to display results. Special look-up tables (pseudocolor) were designed to enhance the significance of the three-dimensional reconstructions. Three-dimensional representations were also developed. The outcome of this effort can be particularly noticed in Chapter 6.



## 2 CODA CHARACTERISTICS

### 2.1 INTRODUCTION

From the geological point of view, it is evident that the earth has heterogeneities on many scales. Rocks have crystals that range in size from fractions of mm to a few cm in scale. An example is in Figure 2-1 where a picture of granite is shown.

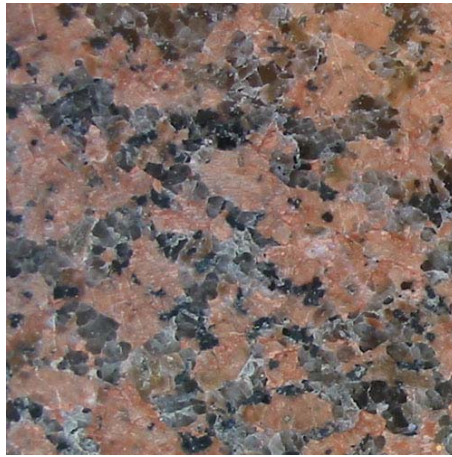


**Figure 2-1.** Picture of the crystals of granite [6].

Also, fractures range in size from submicroscopic to many tens of meters. Faults can be larger than 1000 km as S. Andreas Fault (see Figure 2-2).



**Figure 2-2.** S. Andreas Fault, California [7].

Additionally, the earth's crust contains a wide variation of rock types; its composition can range on scales of a few mm to many km. Tectonic processes also contribute to heterogeneity in the lithosphere by means of faulting and folding.

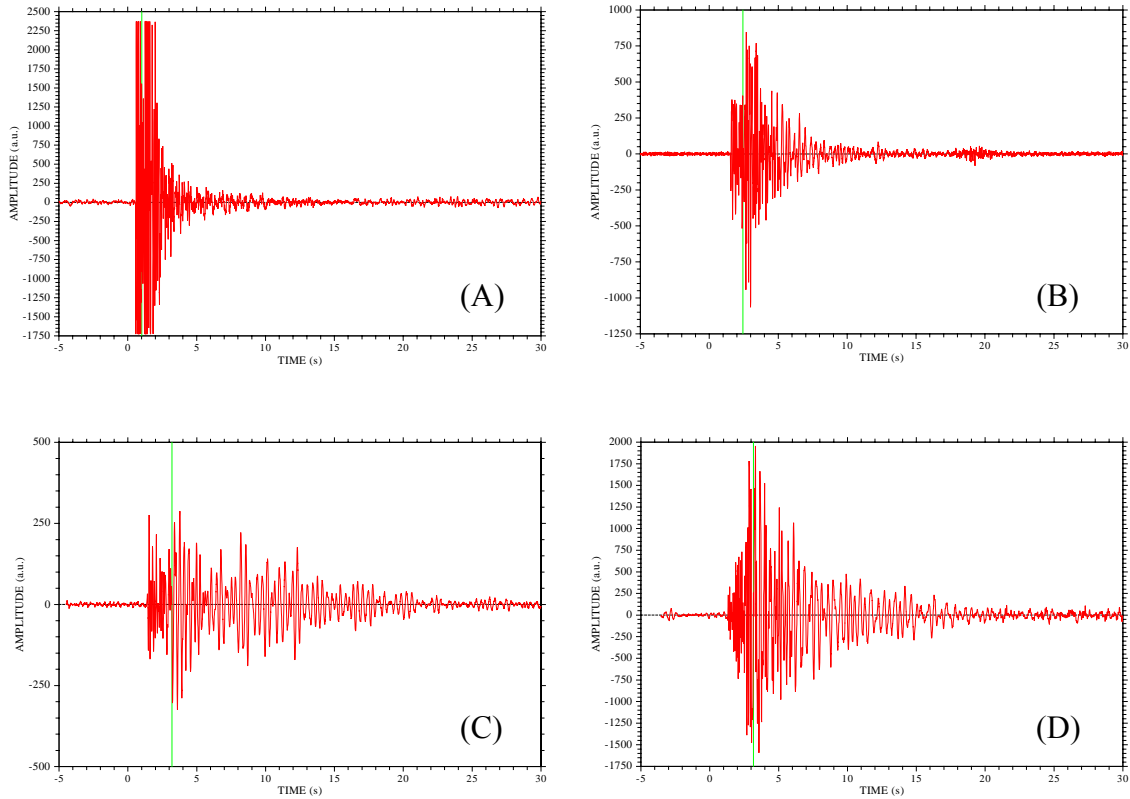


**Figure 2-3.** Non-filtered seismograms corresponding to Galeras volcano events (appendix A). (A) Event 4 station 22, 26/09/1989. (B) Event 75, station 4, 02/06/1992 (C) Event 250 station 19, 16/02/1996, (D) Event 301, station 20, 30/04/1997. Green lines indicate the S-waves arrival time.

Ground motion in the vicinity of earthquakes often dies away slowly leaving a tail following the passage of primary waves. Aki [8] called the observed continuous wave trains “coda waves” and this term has been used since then to describe the tail portion of regional seismograms.

Examples of coda waves following the primary waves corresponding to events in the Galeras volcano (that will be studied in Chapter 6) are shown in Figure 2-3. At present, the word “coda” is used to refer all wave trains except direct waves, thus naming P-coda the waves between the direct P and S waves and S-coda the waves following the direct S-waves. Because the most prominent characteristic of typical high

frequency seismograms of local earthquakes is the coda of S-waves, in this work we will use the word coda for the S-wave coda.

Aki (1969) [8] proposed that the coda was the result of the scattering of seismic waves by random heterogeneities in the earth's lithosphere. Therefore, the later portion of regional seismograms may be considered as a result of some kind of averaging over many samples of heterogeneities, thus suggesting a statistical treatment in which a small number of parameters characterize the average properties of the heterogeneous medium.

Aki and Chouet (1975) [9] developed two simple theoretical models that proved to fit extremely well the observed energy envelopes of coda waves: the single scattering model and the diffusion model. The first one relied on the simple assumption that waves are scattered only once on their way from the source to the station. On the other hand, the second describes the coda by means of a diffusion equation. They also introduced coda  $Q$  ( $Q_c$ ) as a parameter to account for anelastic loss of energy from the wavefield.  $Q_c$ , which describes the rate of decay of seismogram envelopes, has been extensively measured in many regions of the world [10] and it has proved to be an extremely sensitive parameter to the geological environment. Both the single scattering and the diffusion models will be developed in detail in section 2.4.

The physical interpretation of  $Q_c$  in terms of the medium properties still remains unclear. Within the context of the single scattering theory,  $Q_c$  appears to represent an effective total attenuation including both absorption and scattering loss:

$$\frac{1}{Q_c} = \frac{1}{Q_t} = \frac{1}{Q_s} + \frac{1}{Q_i} \quad (2.1)$$

where  $Q_t$ ,  $Q_s$  and  $Q_i$  denote the total, scattering and intrinsic quality factors, respectively. On the other hand, in the diffusion model  $Q_c$  represents the effect of absorption only ( $Q_c = Q_i$ ). In order to give a meaningful interpretation to  $Q_c$ , it is therefore critical to determine the range of validity of the various approximations used to fit the data. The radiative transfer theory is the tool that can address this problem. This theory enables the calculation of energy envelopes of seismic waves taking into account all orders of scattering. Radiative transfer was first introduced in Seismology by Wu [11] and it has, since then, greatly enhanced the understanding of the coda of

earthquakes. Radiative transfer theory shows a different functional dependence for  $Q_s$  and  $Q_i$ . This makes it possible to determine both magnitudes from total attenuation (Frankel and Wennerberg, 1987 [12]; Hoshiya et al., 1991 [13]; Matsunami, 1991 [14]),

The most sophisticated modelling one may hope for is the complete fitting of seismic waveforms, which contain all information on phase and amplitude. The goal of the radiative transfer (and the other models commented above) is more modest as they aim at explaining only the energy envelope of the seismograms. However, at relatively high frequencies, the correlation length of the wavefield is of the order of a few kilometres only (Dainty and Toksöz, 1990 [15]), which makes the waveform fitting procedure almost inapplicable. In disordered media or random media the phase gets randomized by the scattering events. As a consequence, the wavefield at a point can be viewed as a sum of waves whose phase and amplitude are independent random variables. We may then reasonably expect that wave energies rather than amplitudes are additive in random media. But, since on the time scale of seismic observations the Earth is a static disordered medium we do not have access to a true statistical ensemble. In other words, scattering is a deterministic process that happens at cracks, inhomogeneities, faults..., not a stochastic process [16]. Thus, theory and observation can only be connected through some kind of ergodic hypothesis (time average and space average coincide).

## **2.2 S-WAVE CODA ATTRIBUTES**

Let us first enumerate several important observations about the coda waves, which were compiled by Aki and Chouet [9] and that may be satisfactorily explained by a “backscattering model”:

- A. The spectral contents of the early part of a local earthquake seismogram depend strongly on the travel distance and the nature of the wave path to a station. The difference in spectrum among stations, however, diminishes in the later part of the seismograms and disappears in the coda.
- B. The coda length is nearly independent of the epicentral distance or azimuth for a

given region and can be used effectively as a measure of earthquake magnitude.

- C. The power spectra of coda waves from different local earthquakes decay as a function of time in the same manner at all stations and for all events within a given region. The temporal decay shape is independent of earthquake magnitude for events with local magnitudes ( $M_L$ ) less than about 6.
- D. The coda amplitude varies with the local geology at a recording site. It can be 5-8 times larger on the sediment than on granite. Interestingly, the amplitude of ambient ground noise tends to be proportional to the site factor of coda excitation, making the total duration nearly independent of local geology.
- E. The study of coda by a small-aperture array seismographs shows that they are not regular plane waves from the epicenter.

Now let us now follow the waves as they are generated when an earthquake occurs. An important initial consideration is that we expect that the source duration of earthquakes with  $M_L < 6$  is less than a few seconds. This consideration is supported by the fact that the duration of the major event at an earthquake source may be measured roughly by the fault length divided by the rupture velocity, where the fault length for earthquakes with magnitude  $M_L \sim 6$  is about 10 km and the rupture velocity is roughly the shear velocity. Similarly, the duration for an  $M_L \sim 1$  earthquake is probably a few hundredths of a second.

Then, the nature of the primary waves which spread outward from the source and are recorded at a station will depend on the earth's structure along the wave path from source to station. As the primary waves spread out, secondary waves are generated at each of the heterogeneities that they encounter. Suppose for simplicity, that both the primary and the secondary waves are of the same kind of wave with velocity  $v$ . Then we consider a time interval  $(t, t + \Delta t)$  measured from the origin where  $\Delta t$  is longer than the duration of primary waves. During this time interval the secondary waves arrive from the heterogeneities within the zone sandwiched by two ellipsoids, both with the foci at source and station and with the length of the major axis equal to  $vt$  and  $v(t + \Delta t)$ . If we consider seismograms of an event recorded at two different stations, for the given time interval  $(t, t + \Delta t)$  the two ellipsoidal zones will increasingly overlap as  $t$  increases.

Besides, a greater number of heterogeneities will contribute to the later time interval and tend to average out the difference between backscattering energies received at the two stations. Thus the difference in the appearance of seismograms disappears in the coda.

### 2.3 CHARACTERIZING S-CODA ENVELOPES

To characterize S-coda envelopes one often calculates the smoothed trace of the square of the seismogram for a narrow frequency band, which is called the MS seismogram envelope. The amplitude of the MS envelope is linearly proportional to energy density. A very important property of the MS envelopes  $A^2(f, t)$  (which are a function of frequency  $f$  and lapse time  $t$ ) is that they can be described as the product of the spectrum of waves radiated by the source  $S(f)$ , and a function describing the response of the medium to a source  $\phi(f, t)$  (Aki, 1969 [8]):

$$A^2(f, t) = S(f) \cdot \phi(f, t) \quad (2.2)$$

This relation constitutes a cornerstone in coda-wave analysis and has been confirmed for many different areas (Aki and Chouet, 1975[9]; Rautian and Khalturin, 1978 [17]). The assumption that  $\phi(f, t)$  is common to all sources implies that different seismic sources share a common composition of wave types, so that the same scattering effects apply to all. Then, the precise form of  $\phi(f, t)$  depends upon how seismic waves are scattered and attenuated.

Two extreme models of scattering are the single scattering, for which outgoing waves are reflected only once before reaching the receiver, and multiple scattering, to the extent that seismic energy is scattered so much that it diffuses away from the source. For both cases, when the time  $t$  after the event is large compared with the distance to the source,  $r$ , divided by the wave velocities  $v$ , ( $t \gg r/v$ ), theoretically is  $\phi(f, t)$  independent of distance  $r$ , and is of the form:

$$\phi(f, t) = t^{-\nu} \exp\left(-\frac{2\pi ft}{Q_c}\right) \quad (2.3)$$

where  $Q_c$  is a measure of attenuation. The constant  $\nu$  takes into account geometrical

spreading and it is equal to 2 for single scattering of body waves. The diffusion theory gives  $\nu = 3/2$  (Aki and Chouet, 1975 [8]; Rautian and Khalturin, 1978 [17]) Then, if  $A^2(f, t)$  follows Eq. (2.2) and the envelope of the coda is predicted to be and turns out to be independent of the source spectrum  $S(f)$ , in principle the parameters  $\nu$  and  $Q_c$  can be determined. From them, inferences about how scattering takes place can be made and the properties of different regions can be compared.

A remarkable property of the coda is that at any given station, for each frequency band, the dependence of the envelope of the coda on time is nearly identical for all events in a large region surrounding the station. This was noticed by Rautian and Khalturin (1978) [17] when they represented together data from several different events of different magnitudes in a certain region and obtained parallel lines. If the events were combined without regard to their individual levels, they observed a remarkably good overlapping. When they built a summary of coda envelopes for different frequency bands as a function of time they observed that for each band the scatter among the data was remarkably small, in general less than a factor of 2 (see Figure 2-4). Even when these bands were built from events within 50 km of the station, data from events as far as 600 km from intermediate depths also fell on the bands. They concluded that, at a given station, the time dependence of the envelope of the coda in the frequency band 0.1 to 40 Hz is essentially independent of the location of the source, which justifies the separation of the coda spectrum at a given site into a source factor, which is independent of time, and a path factor which shapes the coda with time.

The above authors also experienced that the amount of time that must transpire before the coda envelopes overlap one another depends on epicentral distance. They observed that if  $t_s - t_0$  is the time between the S-wave arrival time  $t_s$  and the origin time  $t_0$ , then often after  $2(t_s - t_0)$  and always after  $3(t_s - t_0)$ , the general form of the coda is established.

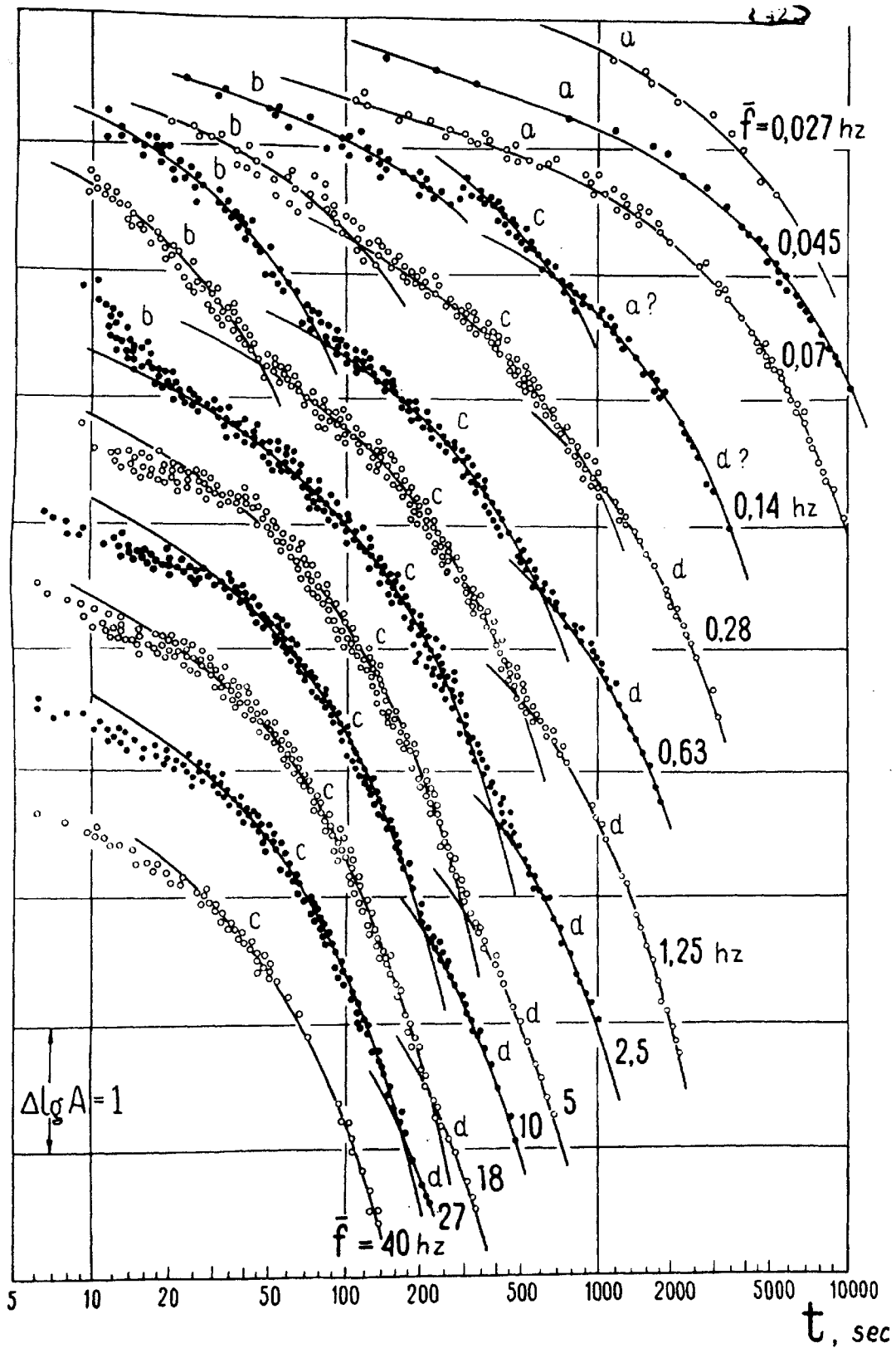


Figure 2-4. Summary of root mean squared coda envelopes for different frequency bands. Data are from many different events [17].

Although the time dependence of the envelope of the coda at a particular station is independent of the position of the earthquake, sometimes the envelopes at different stations from the same earthquake are different in absolute level. This presumably reflects differences in the environments of stations-attenuation and local site effects. The time dependences of the codas for different events differ only by a constant factor for each frequency band. Therefore when a simple correction is applied to the codas at one station, the corrected envelopes overlap the observed envelopes at the other station for all events. This correction is the same for all events independent of the positions of the earthquakes, and therefore epicentral distance. Then, the envelope of the coda over a wide range of frequencies is a very stable function of time and of hypocenter. Rautian and Khalturin (1978) [17] noticed that coda envelopes cannot be described by a single  $Q_c$  value, but it changes with different segments and different frequencies. Single scattering coda models that are based on the assumption of spatial homogeneity of the scattering coefficient and intrinsic attenuation predict that  $Q_c$  is independent of lapse time. Most of the investigators who found a lapse time dependence of the coda decay rate suggested that the later portion of the coda is dominated by energy that has propagated in zones with lower attenuation than energy in the early coda. However, lapse time dependence of coda decay is still an unresolved issue (Sato and Fehler, 1998) [10].

The frequency dependence of  $Q_c$  can be written in the form of a power of frequency  $f$  as  $Q_c \propto f^n$  for  $f > 1$  Hz. The power  $n$  ranges between 0.5 and 1.

## **2.4 TWO EXTREME MODELS FOR CODA WAVES**

Several phenomenological models for coda-wave generation have been proposed. Aki and Chouet (1975) [9] proposed the single backscattering model to explain the time dependence of the scattered energy density at the source location in 3-D space. They considered the case of impulsive spherical radiation of total energy from the source, which location was coincident with the receiver.

Sato (1977)[18] extended the formulation for the case of a single isotropic scattering model for general source and receiver locations. Under the single scattering approximation, the coda is considered as a superposition of backscattering wavelets

from discrete scattering sources. Each wavelet is due to a single scatterer in the absence of the other scatterers. Another extreme model is to consider the seismic energy transfer as a diffusion process (Wesley, 1965 [19]; Aki and Chouet, 1975 [9]; Dainty and Toksöz, 1981 [20]).

## 2.4.1 SINGLE ISOTROPIC SCATTERING MODEL

We are going to consider now how the elastic energy propagates in a three-dimensional infinite elastic medium, in which numerous scatterers are distributed homogeneously and randomly, when the elastic energy is radiated spherically. In other words, we restrict the problem to the body wave isotropic scattering. Then, we will derive a space-time distribution of the mean energy density of the single scattered waves in a similar fashion as the one given by Sato (1977) [18].

### 2.4.1.1 Distribution of scatterers. Isotropic scattering assumption

We suppose that scatterers are distributed randomly and homogeneously with a number density  $n$  in the elastic medium. The scattered waves will be considered as incoherent waves. Scatterers are generally characterized by the effective cross section  $\sigma$ . Here, we notice that  $\sigma$  depends on  $\omega = 2\pi f$ . When scatterers are distributed homogeneously with the number density  $n$ , the length

$$l = \frac{1}{n\sigma} \quad (2.4)$$

is the mean free path and  $l/v$  the mean free time, being  $v$  the wave velocity. The scatterers reduce the mean energy flux density of the incident wave by  $\exp(-x/l)$ , where  $x$  is the distance along the propagation direction. The scattering coefficient (turbidity) corresponds to  $g=1/l$  and can be measured. The turbidity is of the order of  $10^{-5} \sim 10^{-6} m^{-1}$  at frequencies higher than 10 Hz [9].

Here, we will assume isotropic scattering in order to obtain an analytic solution with rather simple calculations. Roughly, isotropic scattering may be assumed when the wavelength  $\lambda \approx a$  where  $a$  is the size of the scatterers (Sato, 1977, [18]). For the sake of simplicity, no conversion between longitudinal waves and transverse waves during

scattering will be considered and the medium will be characterized by a single wave velocity.

### 2.4.1.2 Single isotropic scattering approximation

Let us suppose that the mean free path  $l$  is much longer than the distance  $r$  under consideration ( $r \ll l$ ) or ( $t \ll l/v$ ). Since the scattering is assumed to be a weak process, only single scattering is considered. Let us also suppose that the source emit a unit of energy in the time  $t=0$ . The mean energy density at a certain distance  $r_1$  may then be written as:

$$E_d(r_1, t = r_1/v)dt = \frac{\exp(-n\sigma r_1)}{4\pi r_1^2} \quad (2.5)$$

where  $dt$  is the time it takes to emit the unit energy. Note that  $E_d$  is the energy per unit area and per unit time. The amount of energy scattered at a certain volume ( $dV=dS \cdot dr = dS \cdot v \cdot dt$ ) may then be written as:

$$E_s(r_1, t = r_1/v)vdt dS = \frac{\exp(-n\sigma r_1)}{4\pi r_1^2} \cdot \frac{dr}{l} \cdot dS = \frac{n\sigma \exp(-n\sigma r_1)}{4\pi r_1^2} dV \quad (2.6)$$

where  $E_s$  is the energy scattered per unit volume and per unit time. The mean energy flux re-emitted by a certain scatterer (located inside a certain  $dV$  at the coordinates  $\mathbf{r}_1$ ) at a point  $\mathbf{r}_2$  is then written as:

$$E_s(r, t)vdt dS = \frac{\exp(-n\sigma r_2)}{4\pi r_2^2} \cdot E_s(r_1, t = r_1/v)vdt dS \quad (2.7)$$

where  $\mathbf{r} = \mathbf{r}_1 + \mathbf{r}_2$ . Using Eq.(2.6) we obtain:

$$E_s(r, t)vdt dS = \frac{n\sigma \exp(-n\sigma(r_1 + r_2))}{(4\pi)^2} \cdot \frac{1}{r_1^2 r_2^2} \cdot dV \quad (2.8)$$

In order to get all the energy scattered in a certain time interval  $dt$  we will consider a new set of coordinates (alternate prolate spheroidal coordinates which are adapted to “two-centre” problems [21]):

$$\begin{aligned}
x &= a\sqrt{(\xi_1^2 - 1)(1 - \xi_2^2)} \cos \xi_3 \\
y &= a\sqrt{(\xi_1^2 - 1)(1 - \xi_2^2)} \sin \xi_3 \\
z &= a\xi_1\xi_2
\end{aligned}
\tag{2.9}$$

$$dV = v dt dS = a^3 (\xi_1^2 - \xi_2^2) d\xi_1 d\xi_2 d\xi_3$$

The set of coordinates  $(\xi_1, \xi_2, \xi_3)$  are defined on certain intervals that we write as:  $\xi_1 \in [1, \infty)$ ,  $\xi_2 \in [-1, 1]$ ,  $\xi_3 \in [0, 2\pi]$ .

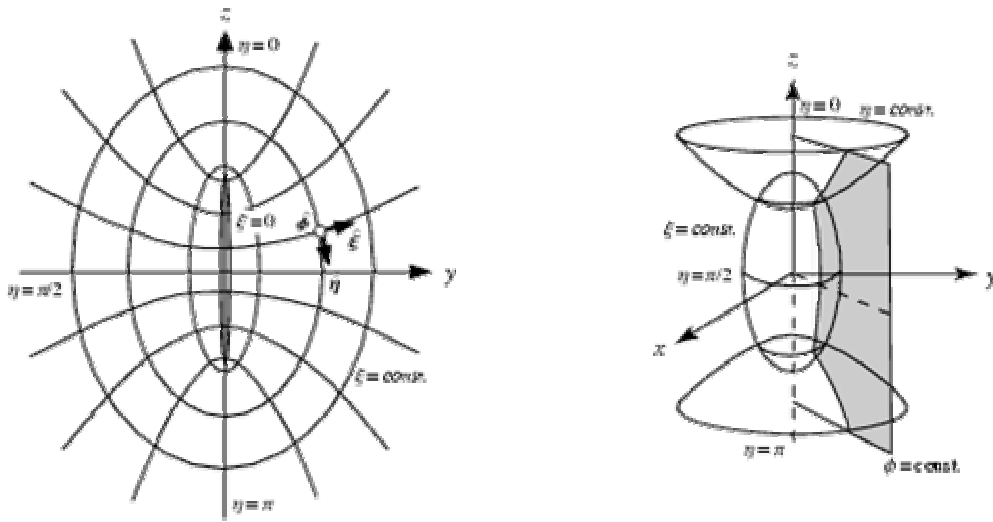


**Figure 2-5** Prolate spheroidal coordinates.  $\xi_1 = \sinh \xi$ ,  $\xi_2 = \cos \eta$ ,  $\xi_3 = \phi$  [21].

Then we write the coordinates of the source as  $(0,0,-a)$ , and the ones of the receiver as  $(0,0,a)$ . Then  $\mathbf{r} = (0,0,2a)$ ,  $\mathbf{r}_1 = (x, y, z + a)$ ,  $\mathbf{r}_2 = (x, y, z - a)$ . Notice the following equalities:

$$\begin{aligned}
r_1 &= a(\xi_1 + \xi_2) & r_2 &= a(\xi_1 - \xi_2) & 2a &= \|\mathbf{r}_1 + \mathbf{r}_2\| = r \\
\xi_1 &= \frac{r_1 + r_2}{2a} = \frac{vt}{r} & \xi_2 &= \frac{r_1 - r_2}{2a}
\end{aligned}
\tag{2.10}$$

where  $r$  is the distance from the source to the observer. Notice that:

$$d\xi_1 = \frac{v}{r} dt \tag{2.11}$$

Then  $dV$  may be written as:

$$dV = vdt dS = vdt \cdot \frac{1}{r} a^3 (\xi_1^2 - \xi_2^2) d\xi_2 d\xi_3 \quad (2.12)$$

and using Eqs. (2.9) , (2.10) and (2.12) in Eq. (2.8) we obtain:

$$E_s(r,t)vdt dS = vdt \frac{n\sigma \exp(-n\sigma)}{(4\pi)^2 r} \frac{1}{a (\xi_1^2 - \xi_2^2)} d\xi_2 d\xi_3 \quad (2.13)$$

Now, integrating the third coordinate:

$$E_s(r,t)vdt dS = vdt \frac{n\sigma \exp(-n\sigma)}{4\pi r^2} \frac{1}{(\xi_1^2 - \xi_2^2)} d\xi_2 \quad (2.14)$$

and then the second we obtain:

$$E_s(r,t)vdt dS = vdt \frac{n\sigma \exp(-n\sigma)}{4\pi r^2} \frac{1}{\xi_1} \ln \left( \frac{\xi_1 + 1}{\xi_1 - 1} \right) \quad (2.15)$$

Using Eq. (2.10) we may finally write:

$$E_s(r,t) = \frac{n\sigma \exp(-n\sigma vt)}{4\pi r} \cdot \frac{1}{vt} \cdot \ln \left( \frac{vt + r}{vt - r} \right) \quad (2.16)$$

### 2.4.1.3 Properties of the solution

It is important to consider how this distribution behaves for  $t \gg r/v$  . Considering a first order Taylor expansion of the logarithmic expression we obtain:

$$\frac{r}{vt} \ln \left( \frac{1 + r/vt}{1 - r/vt} \right) \approx 2 \left( \frac{r}{vt} \right)^2 \quad (2.17)$$

Then, for  $t \gg r/v$  we may write:

$$E_s(r, t) \approx \frac{n\sigma \exp(-n\sigma vt)}{2\pi(vt)^2} \quad (2.18)$$

We observe a  $t^{-2}$  dependence under such condition, as derived for the single backscattering model of Aki and Chouet (1975) [9].

We notice now that Eq. (2.16) makes sense only for  $vt \geq r$ . Then we may write:

$$E_s(r, t) = \frac{n\sigma \exp(-n\sigma vt)}{4\pi r} \cdot \frac{1}{vt} \cdot \ln\left(\frac{vt+r}{vt-r}\right) \theta(vt-r) \quad (2.19)$$

This distribution diverges for  $vt \rightarrow r$ . The total energy scattered up to a certain time  $t$  may be written as:

$$U(t) = \int_0^\infty E_s(r, t) 4\pi r^2 dr = \frac{n\sigma \exp(-n\sigma vt)}{vt} \cdot \int_0^{vt} r \cdot \ln\left(\frac{vt+r}{vt-r}\right) dr \quad (2.20)$$

and solving the integral it yields:

$$U(t) = n\sigma vt \exp(-n\sigma vt) \quad (2.21)$$

Notice that this expression does not tend to one for  $t \rightarrow \infty$ ; it tends to zero. The expressions previously developed are only valid for  $t \ll l/v$ . This means that as time increases, the energy coming from double scattering becomes smaller.

#### 2.4.2 RATIO OF SINGLE SCATTERED ENERGY VERSUS MULTIPLE SCATTERED ENERGY

Equation (2.19) gives us the distribution of energy that arrives at the distance  $r$  at the time  $t$  after a single scattering process. Equation (2.21) gives us the total amount of energy scattered by a single scattering process up to the time  $t$ . This energy is distributed inside a sphere with a radius  $r_U = vt$ . The total amount of energy scattered up to the time  $t$  and also distributed inside a sphere with a radius  $r_U = vt$  may be easily written as:

$$U_{total}(t) = 1 - \exp\left(-\frac{\omega t}{Q}\right) \quad (2.22)$$

Then, we may write the ratio of the single scattered energy to the total scattered energy up to a time  $t$  as:

$$R(t) = \frac{n\sigma vt \exp(-n\sigma vt)}{1 - \exp\left(-\frac{\omega t}{Q}\right)} \quad (2.23)$$

and taking into account the following equalities:

$$l = \frac{1}{n\sigma} = \frac{vQ_c}{\omega} \quad (2.24)$$

we may rewrite the ratio as:

$$R(t) = \frac{\frac{\omega t}{Q} \cdot \exp(-n\sigma vt)}{1 - \exp\left(-\frac{\omega t}{Q}\right)} \quad (2.25)$$

In order to study this expression let us define the following parameter:

$$\xi = \frac{\omega t}{Q} \quad (2.26)$$

Then we rewrite the ratio as:

$$R(\xi) = \frac{\xi \exp(-\xi)}{1 - \exp(-\xi)} \quad (2.27)$$

The ratio takes the following values;  $R(0)=1.0$ ;  $R(0.20)=0.90$ ;  $R(0.43)=0.80$ ;  $R(0.67)=0.70$ . Let us take as a unit of time the arrival time  $t_a = d/v$  ( $d$  is the hypocentral distance); then we shall rewrite the time as  $n \cdot t_a$ . Let us also compute  $\xi$  for  $f=1$  Hz and  $v=3.5$  Km/s for several possible values of  $Q$  and  $n$ . Then, we rewrite  $\xi$  as a function of  $d, n, v$  and  $Q$ :

$$\xi = n \cdot d \cdot \frac{2\pi}{v \cdot Q} \quad (2.28)$$

It might be useful to have  $d$  as function of the other parameters: Then using Eq. (2.28):

$$d = \xi \frac{v \cdot Q}{2\pi n} \quad (2.29)$$

Let us calculate now for what distance  $d$  is  $R(\xi)=0.9$  or  $R(\xi)=0.8$  for  $n=2$  and  $n=3$  for several values of  $Q$ . From Eq. (2.27)  $R(\xi)=0.9$  is verified when  $\xi = 0.2$ , and  $R(\xi)=0.8$  is verified when  $\xi = 0.43$ . We take.  $v=3.5 \text{ km}\cdot\text{s}^{-1}$ .

Results are plotted in table Table 2-1 and represented in Figure 2-6. The table and the figure show the distances (in km) up to which the single scattered energy constitutes the 90% and the 80% of the total radiated energy for several values of the quality factor of the medium. These values indicate that care should be taken when using the single scattering approximation in regions where  $Q$  might be a small number.

$Q$	$d (n=2) \text{ (km)}$		$d (n=3) \text{ (km)}$	
	$\xi = 0.2$	$\xi = 0.43$	$\xi = 0.2$	$\xi = 0.43$
50	2.7	6.0	1.8	4.0
100	5.6	12.0	3.7	8.0
200	11.1	23.9	7.4	16.0
400	22.3	47.9	14.8	31.9
800	44.6	95.8	29.7	63.9

**Table 2-1** Maximum distance up to which the single scattering approximation may be used ( $v=3.5\text{km/s}$ ).

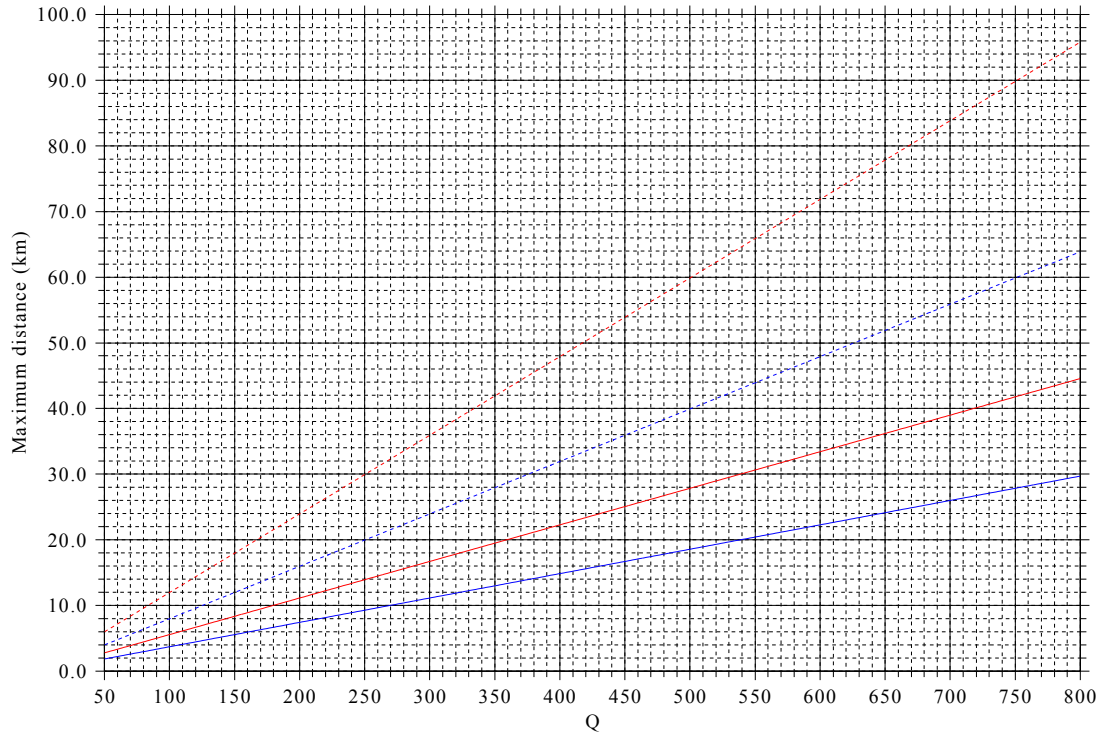


**Figure 2-6** Maximum distance up to which the single scattering approximation may be used ( $v=3.5$  km/s). Blue lines correspond to  $n=2$  and red line to  $n=3$ . Solid lines correspond to  $\xi = 0.2$  and dashed lines to  $\xi = 0.43$ .

### 2.4.3 DIFFUSION THEORY

As lapse time increases it is expected that multiple scattering will dominate compared to single scattering. For large lapse times, it is reasonable to assume that direct energy is small and that multiple scattering produces a smooth spatial distribution of energy density. We shall now describe another model in which a strong multiple scattering process can be formulated by means of the diffusion equation (Sato and Fehler, 1998) [10].

Let  $E(\mathbf{r}, t, \omega)$  be the seismic energy per unit volume within a unit frequency band around  $\omega$ . Taking into account linear dissipation in the medium, the diffusion equation may be written as:

$$\frac{\partial E}{\partial t} = D \cdot \nabla^2 E - \frac{\omega}{Q} \cdot E \quad (2.30)$$

where  $D$  is the diffusivity and the last term represents the loss by anelasticity which

turns the seismic energy into heat. Clearly, here  $Q$  is the intrinsic quality factor and does not include the loss by scattering.

The diffusivity  $D$  may be related to the wave-scattering process. In analogy with the scattering of particles moving with a certain mean free-path, Dainty et al. [20] obtained the relation between  $D$  and the mean free path  $l$  as:

$$D = \frac{v \cdot l}{3} \quad (2.31)$$

where  $v$  is the velocity of the wave propagation and  $l$  is defined as the distance travelled by the primary wave, over which its energy is reduced to  $e^{-1}$  by scattering.

The solution of Eq. (2.30) for a point source in time and space is given by:

$$E(\mathbf{r}, t, \omega) = \frac{U(\omega)}{(4\pi Dt)^{3/2}} \exp\left(-\frac{r^2}{4Dt}\right) \exp\left(-\frac{\omega t}{Q}\right) \quad (2.32)$$

where  $U(\omega)$  is the total seismic energy generated by one earthquake within the unit frequency band around  $\omega$ . For large  $t$ , ( $t \geq 10 \cdot r^2/4D$ ) and small distance  $r$  at which coda waves are observed, Eq. (2.32) becomes a function of only time and is independent of distance:

$$E(\mathbf{r}, t, \omega) = \frac{U(\omega)}{(4\pi Dt)^{3/2}} \exp\left(-\frac{\omega t}{Q}\right) \quad (2.33)$$

The diffusion model solution Eq. (2.33) was used for the analysis of coda recorded near the hypocenter of earthquakes (Wesley, 1965 [19]; Aki and Chouet, 1975 [9]) and the coda of lunar earthquakes (see Figure 2-7) (Nakamura, 1977 [22]; Dainty and Toksöz, 1981 [23]). The energy on the moon is intensely scattered due to the fractured regolith and intrinsic absorption is weak due to the lack of intergranular water.

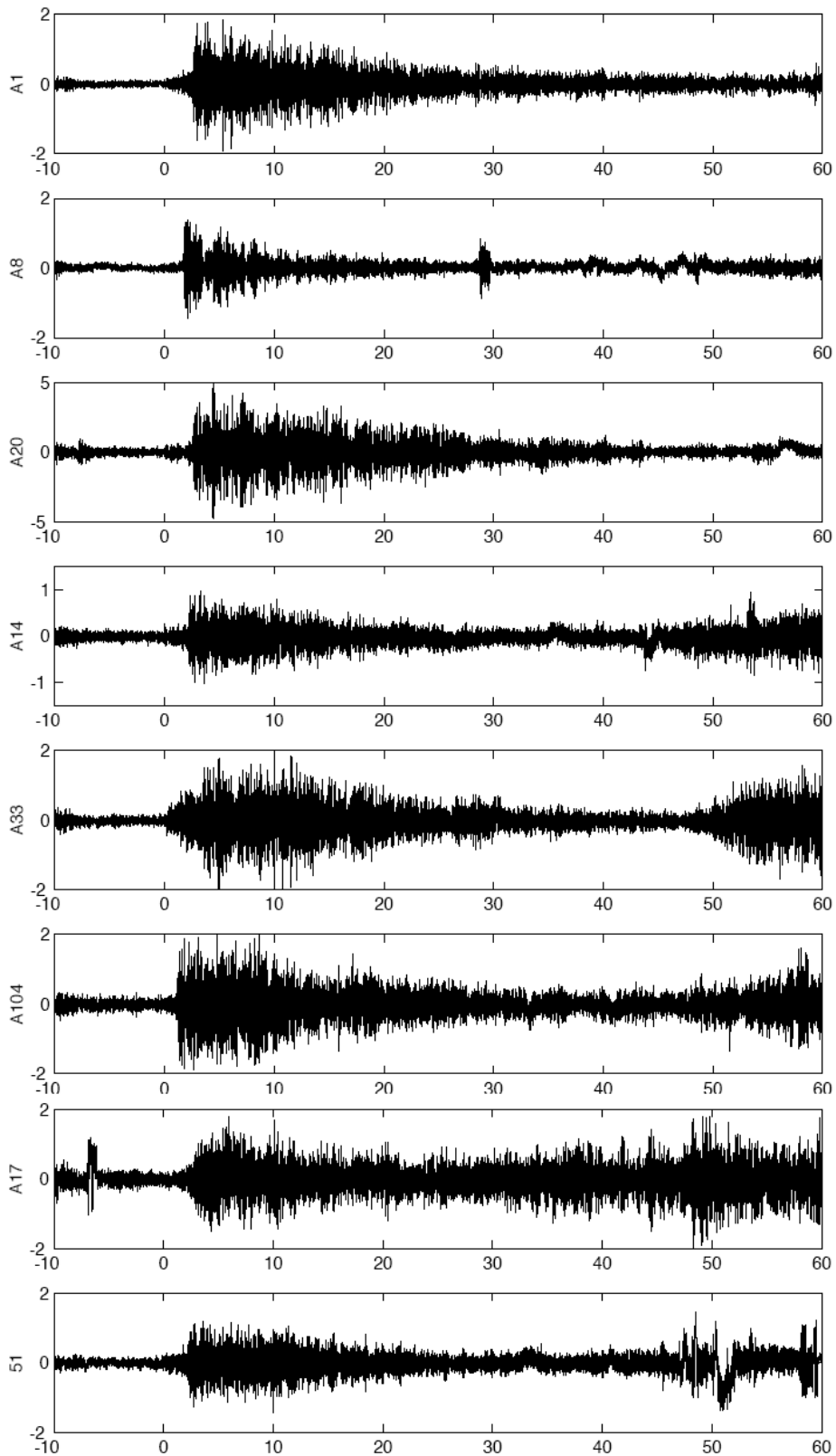


Figure 2-7. Lunar earthquakes [24] showing long coda durations.

## 2.5 RADIATIVE TRANSFER THEORY

The squared sum of incoherent S-waves that are singly scattered by distributed random heterogeneities can provide an adequate first-order model of the MS envelope of S-wave seismograms. However, as lapse time increases, a greater contribution of higher-order multiple scattering is expected. A systematic approach for modelling the multiple scattering process is to use the radiative transfer theory for the energy density. The equation of radiative transfer is a basic analytical tool in nuclear reactor theory, in the kinetic theory of gases or in electron transport through conducting materials. The theory of radiative transfer discards the phase information contained in individual contributions; actually, this theory focus on the transport of energy, very much like a nuclear physicist is interested in the flux of neutron obtained by summing over individual particles. It is assumed that the addition of power holds rather than the addition of wavefields.

We will define now the fundamental quantities which the subject of Radiative Transfer deals with and derive the basic equation (the equation of radiative transfer) [25]. The solution of this equation will provide us an expression describing the characteristics of the envelope of seismograms and will be useful to evaluate the magnitude of certain important parameters.

### 2.5.1 RADIATIVE TRANSFER EQUATION

Consider the elemental volume shown in Fig. 1.1 with cross-section  $da$  and length  $ds$  containing  $nda$  scatterers with  $n$  the number density of scatterers. Let the spatially incoherent intensity be defined as the energy per area, per time, and per solid angle  $d\Omega$  so that the energy emergent from this volume in the  $\hat{s}$  direction is  $I(s,t)da dt d\Omega$ . The energy a distance  $ds$  away, moving at speed  $c$  also in the  $\hat{s}$  direction at a time later will be  $I(s+ds,t+dt)da dt d\Omega$ .

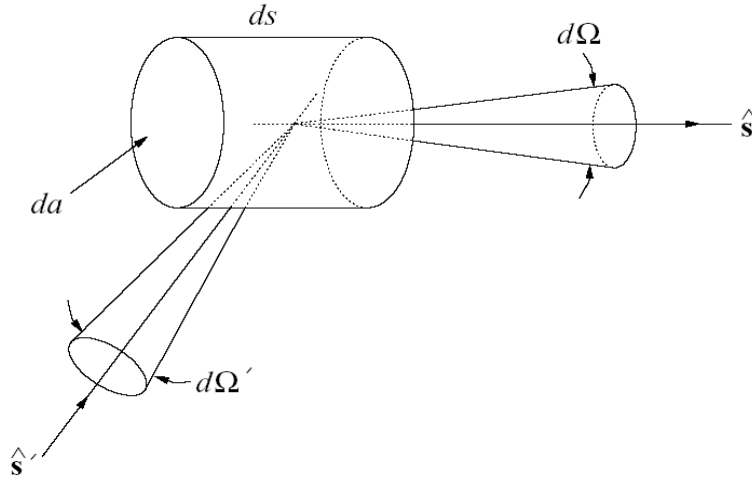


**Figure 2-8.** Propagation through the scattering volume in the  $\hat{s}$  direction and emission into the  $\hat{s}$  direction from scattering events due to energy from the  $\hat{s}'$  direction [26].

The difference in energy can be attributed to a loss caused by absorption and scattering, and an increase caused by emissions into the direction of propagation from other scattering events or from sources within the medium. This energy balance is written as:

$$I(s+ds, t+dt) da dt d\Omega - I(s, t) da dt d\Omega = -\eta I(s, t) da ds dt d\Omega + n\varepsilon(s, t) da ds dt d\Omega \quad (2.34)$$

where  $\eta = n(\sigma_s + \sigma_a)$  is the total intensity attenuation,  $\sigma_a$  is the absorption cross section per scatterer,  $\sigma_s$  is the scattering cross section per scatterer, and  $\varepsilon(s, t)$  is the emission coefficient per scatterer.

The absorption cross section may include absorption within the scatterer as well as dissipation within the medium (which is zero for most applications with electromagnetic waves). The emission coefficient may include emissions from scattering events and primary sources. Equation (2.34) implies that

$$\frac{\partial I(s, t)}{\partial s} ds + \frac{\partial I(s, t)}{\partial t} dt = -\eta I(s, t) ds + n\varepsilon(s, t) ds \quad (2.35)$$

Since  $ds = c dt$ , Eq. (2.35) becomes:

$$\frac{\partial I(s,t)}{\partial s} + \frac{1}{c} \frac{\partial I(s,t)}{\partial t} = -\eta I(s,t) + n\varepsilon(s,t) \quad (2.36)$$

Note that in the absence of emissions,  $I(s,t)$  displaces and attenuates with time in the following manner:

$$I(s,t) = f(s-ct) \exp(-\eta ct) \quad (2.37)$$

In three dimensions the radiative transfer equation becomes

$$\nabla I(s,t) \cdot \hat{\mathbf{s}} + \frac{1}{c} \frac{\partial I(\mathbf{r}, \hat{\mathbf{s}}, t)}{\partial t} = -\eta I(\mathbf{r}, \hat{\mathbf{s}}, t) + n\varepsilon(\mathbf{r}, \hat{\mathbf{s}}, t) \quad (2.38)$$

where  $\hat{\mathbf{s}}$  is the direction of propagation,  $\mathbf{r}$  is the space vector and the total attenuation has been assumed isotropic (*i.e.* independent of  $\hat{\mathbf{s}}$ ).

To find the emission coefficient, consider the same volume of scatterers with radiation incident from the  $\hat{\mathbf{s}}'$  direction within the solid angle  $d\Omega'$  scattering into the  $\hat{\mathbf{s}}$  direction in solid angle  $d\Omega$  also shown in Figure 2-8. Let the angular distribution of the scattered portion of the radiation, scattered from the direction into the direction, be defined by

$$q(\hat{\mathbf{s}}, \hat{\mathbf{s}}') \frac{d\Omega}{4\pi} \quad (2.39)$$

where  $q(\hat{\mathbf{s}}, \hat{\mathbf{s}}')$  is the phase function (Chandrasekhar, 1960)[25] and is  $4\pi$  times the differential scattering cross-section (Ishimaru, 1978, [27]). The phase function is normalized so that

$$\int_{4\pi} q(\hat{\mathbf{s}}, \hat{\mathbf{s}}') \frac{d\Omega}{4\pi} = \sigma_s \quad (2.40)$$

which means that for isotropic scattering  $q(\hat{\mathbf{s}}, \hat{\mathbf{s}}') = \sigma_s$ . This angular distribution multiplied by the intensity and integrated over all incoming directions is the emitted radiation per scatterer. Thus in the absence of primary sources the emission coefficient is:

$$\varepsilon(\mathbf{r}, t, \hat{\mathbf{s}}) = \int_{4\pi} q(\hat{\mathbf{s}}, \hat{\mathbf{s}}') I(\mathbf{r}, t, \hat{\mathbf{s}}) \frac{d\Omega}{4\pi} \quad (2.41)$$

The full scalar radiative transfer equation is then written as:

$$\nabla I(\mathbf{r}, t) \cdot \hat{\mathbf{s}} + \frac{1}{c} \frac{\partial I(\mathbf{r}, \mathbf{s}, t)}{\partial t} = -\eta I(\mathbf{r}, \hat{\mathbf{s}}, t) + \int_{4\pi} p(\hat{\mathbf{s}}, \hat{\mathbf{s}}') I(\mathbf{r}, t, \hat{\mathbf{s}}) \frac{d\Omega}{4\pi} \quad (2.42)$$

where  $p(\hat{\mathbf{s}}, \hat{\mathbf{s}}') = nq(\hat{\mathbf{s}}, \hat{\mathbf{s}}')$  is the phase function for an assemblage of independent scatterers. The radiative transfer equation is a first order integro-partial differential equation in space, time, and propagation direction. Its solutions are in general nontrivial.

### 2.5.2 SOLUTIONS OF THE RADIATIVE TRANSFER EQUATION. ISOTROPIC SCATTERING

Initial seismological models using the radiative transfer theory are those of Wu (1985)[28] and Wu and Aki (1988) [11]. They applied the stationary state solution for media having isotropic scattering. Shang and Gao (1988) [29] first formulated the multiple isotropic scattering process in 2-D space as an integral equation for the nonstationary state for the case of impulsive radiation. Zeng et al. (1991) [30] extended the nonstationary case to 3-D space. Sato et al. (1997) [31] used the radiative transfer theory to investigate the multiple isotropic scattering process for nonspherical source radiation whereas Sato (1994 [32], 1995 [33]) investigated the multiple nonisotropic scattering process in the framework of the radiative transfer theory.

The radiative transfer equation can be solved exactly in the Fourier space [30] in the case of isotropic scattering for one, two, three and four dimensions. It is possible to write an explicit expression in one, two and four dimensions. In three dimensions an accurate interpolation formula can be derived [34].

We will focus in the solutions on the real three-dimensional space. If we consider isotropic scattering, we may rewrite Eq. (2.42) in the following way:

$$\nabla I(s, t) \cdot \hat{\mathbf{s}} + \frac{1}{c} \frac{\partial I(\mathbf{r}, \mathbf{s}, t)}{\partial t} = -(l^{-1} + l_a^{-1}) I(\mathbf{r}, \hat{\mathbf{s}}, t) + l^{-1} I(\mathbf{r}, t) + c^{-1} S(\mathbf{r}, t, \hat{\mathbf{s}}) \quad (2.43)$$

$$I(\mathbf{r}, t) = \int_{4\pi} I(\mathbf{r}, t, \hat{\mathbf{s}}) \frac{d\Omega}{4\pi}$$

where  $l^{-1} = n\sigma_s$  and  $l_a^{-1} = n\sigma_a$  and  $S$  is a source function.

We notice here that the dependence of the intensity on the absorption is through a  $\mathbf{r}$  and  $\hat{\mathbf{s}}$  independent factor

$$I(\mathbf{r}, t)_{\text{with absorption}} = I(\mathbf{r}, t)_{\text{without absorption}} \exp(-ct/l_a) \quad (2.44)$$

Without loss of generality we can, therefore, leave the absorption of our considerations in the following, taking effectively  $l_a \rightarrow \infty$

The solution will be written as a summation of three terms. The first one corresponds to the ballistic peak. The second one corresponds to the contribution due to single scattering. The last term accounts for multiple scattering.

### 2.5.2.1 Ballistic peak and single scattering

The ballistic peak consists of a delta function due to unscattered waves:

$$I_0(r, t) = \frac{1}{4\pi r^2} \delta(r - ct) \exp\left(\frac{-ct}{l}\right) \quad (2.45)$$

This peak will be followed by a tail due to waves which have undergone a single forward scattering event. The shape of the tail is given by  $P_1$ , which can be computed analytically for any dimension.  $P_1$  has an integrable singularity at  $r=ct$ , which adds a tail to the ballistic peak. The singularity is logarithmic:

$$I_1(r, t) = \frac{1}{4\pi l c t r} \exp\left(\frac{-ct}{l}\right) \ln\left(\frac{ct+r}{ct-r}\right) \quad (2.46)$$

### 2.5.2.2 Multiple scattering

The contribution coming from multiple scattering is usually written as the summation of two terms. In this way the corresponding integrals may be evaluated by means of numerical integration techniques. The first term corresponds to double scattering:

$$I_2(r, t) = \frac{1}{16\pi l^2} \exp\left(-\frac{ct}{l}\right) \left[ \frac{\pi^2}{ct} - \frac{3}{r} \int_0^{r/ct} \left( \ln\left(\frac{1+\alpha}{1-\alpha}\right) \right)^2 d\alpha \right] \quad (2.47)$$

and the other terms correspond to multiple scattering (excluding double scattering):

$$\sum_{N \geq 3} P_n(r, t) = \frac{1}{4\pi^3 r l^3} \int_{-\infty}^{+\infty} \frac{\exp(i\Omega ct)}{2} d\Omega \int_0^{\infty} \frac{1}{k^2} \frac{\left[ \arctan\left(\frac{k}{1/l + i\Omega}\right) \right]^4}{\left[ k - \frac{1}{l} \arctan\left(\frac{k}{1/l + i\Omega}\right) \right]} dk \quad (2.48)$$

This is the expression that Passchenns [34] obtained. The expression derived by Zeng [30] including absorption may be written as:

$$\sum_{N \geq 3} P_n(r, t) = \frac{1}{4\pi^3 r l^3} \int_{-\infty}^{+\infty} \frac{\exp(i\Omega ct)}{2} d\Omega \int_0^{\infty} \frac{1}{k^2} \frac{\left[ \arctan\left(\frac{k}{1/l + 1/l_a + i\Omega}\right) \right]^4}{\left[ k - \frac{1}{l} \arctan\left(\frac{k}{1/l + 1/l_a + i\Omega}\right) \right]} dk \quad (2.49)$$

This expression also verifies Eq. (2.44). Actually, it is possible to define a new variable  $\Omega'$  such that:

$$\begin{aligned} i\Omega &= i\Omega' - 1/l_a \\ \Omega &= \Omega' + i/l_a \end{aligned} \quad (2.50)$$

It is then easily demonstrated that both solutions are identical.

### 2.5.2.3 Analytical approximation of multiple scattering integrals

It is possible to derive accurate analytical expressions to compute the integrals corresponding to Eq. (2.47) and Eq. (2.48). The solution may then be written (with accuracy within 2% out of the ballistic peak):

$$\begin{aligned}
I(r,t) &\approx \frac{1}{4\pi r^2} \delta(r-ct) \exp\left(\frac{-ct}{l}\right) \\
&\quad + \frac{(1-r^2/c^2t^2)^{\frac{1}{8}}}{(4\pi l ct/3)} \exp\left(\frac{-ct}{l}\right) G\left(\frac{ct}{l} \left[1 - \frac{r^2}{c^2t^2}\right]^{\frac{3}{4}}\right) \\
G(x) &= 8(3x)^{-3/2} \sum_{N=1}^{\infty} \frac{\Gamma\left(\frac{3}{4}N + \frac{3}{2}\right)}{\Gamma\left(\frac{3}{4}N\right)} \frac{x^N}{N!}
\end{aligned} \tag{2.51}$$

Where it is possible to approximate  $G(x)$  as follows

$$G(x) \approx \exp(x) \sqrt{1 + 2.026/x} \tag{2.52}$$

All these expressions are useful in the calculation of  $l^{-1}$  and  $l_a^{-1}$  [13].

#### 2.5.2.4 Comparing exact solutions and approximate solutions

The only way to compare the analytical approximate solution an the exact solution is to carry out a numerical integration of the double integral in Eq. (2.48). This integral is a difficult one because of the following reasons:

- i. The integrand is highly oscillatory
- ii. The integrand logarithmically diverges in the limits of integrations.

It is possible to use the Fast Fourier Transform (FFT) [35-36] algorithm to evaluate the integral. FFT algorithm may not be an accurate algorithm when the integrand is highly oscillatory. In such a case aliasing effects may arise and the accuracy of the calculation may be low.

To avoid this problem, Paasschens [34] develops real integrals in order to facilitate the numerical inversion of the Fourier Transform in Eq. (2.48). We could not obtain the exact result from that development. We used several cubature algorithms (included the ones described in the next paragraphs) but all of them gave us a wrong solution. We were not able to tell if the error was originated because of a wrong evaluation of the integral by numerical algorithms or because there is a typographic mistake in the Paasschens development. Certainly, the evaluation of two-dimensional integrals is a non-trivial problem, especially if the integrand shows a strong oscillatory behaviour and

also diverges in some regions.

Then we decided to obtain the exact solution directly from Eq.(2.48) using powerful numerical algorithms. We finally used two different algorithms, a two-dimensional adaptative cubature algorithm called Cubpack [37] and a non-adaptive algorithm *r2d2lri* [38]. These algorithms employ very different strategies for automatic integral evaluation. [39]. Then, if both methods give us the same result this will indicate that we are on the right way. A short description of both methods follows.

Cubpack employs a globally adaptative algorithm that uses successive refinements or subdivisions of the integration region (IR) where each subdivision is used to provide a better approximation to the integral. These subdivisions are designed to dynamically concentrate the computational work in the subregions of IR where the integrand is most irregular, and thus to adapt to the behaviour of the integrand. The general structure of the globally adaptive algorithm consists of a sequence of stages. Each stage has the following five main steps:

- i. Select a subregion with largest estimated error from the current set of subregions.
- ii. Divide the selected subregion.
- iii. Apply a local cubature rule to any new subregions.
- iv. Update the subregion set.
- v. Update the global integral and error estimates, and check for termination.

The initial subregion set for the algorithm is the original collection of simplices ( $n$ -dimensional triangles) of IR. The required input for such an algorithm is IR, the integrand, a limit on the number of integrand values allowed, and a requested error tolerance. The algorithm terminates when the estimated global error is less than the one requested or further subdivision would require too many function evaluations.

*r2d2lri* is a non-adaptive algorithm implemented in C++ for performing automatic cubature over a wide variety of finite and non-finite two-dimensional domains. The core integrator of *r2d2lri()* evaluates cubatures over the domain  $[0,1]^2$  using a non-adaptive

sequence of embedded lattice rules, coupled with a sixth-order Sidi transformation (a type of variable transformation for numerical integration). Before any cubature is performed, the provided integral is automatically transformed onto  $[0,1]^2$ . Since different types of non-finite to finite domain transformations suit different forms of integrand behaviour, for non-finite domains, *r2d2lri* performs cubatures using an ordered succession of up to three different transformations onto  $[0,1]^2$  until it is determined that the requested accuracy (or the best achievable result) has been attained.

These methods allow to carry out integrations over real integrands. Notice that the integral in Eq. (2.48) has to be a real number since it corresponds to an addition of multiple scattered energies. Using the following identity:

$$\arctan(z) = \frac{i}{2} \ln \left( \frac{i+z}{i-z} \right) \quad (2.53)$$

it is possible to easily devise an algorithm to compute the real part of the integrand.

To check the accuracy of Eq. (2.51) and Eq. (2.52) we now compare with a numerical evaluation of Eq.(2.46), Eq. (2.47) and Eq.(2.48) in Figure 2-9. Eq. (2.47) may be evaluated with a standard one-dimensional integration algorithm as the Romberg algorithm [46]. Eq.(2.48) will be evaluated using Cubpack++ and *r2d2lri* algorithms. Both algorithms will provide almost identical results. Only the ones obtained with Cubpack++ will then be plotted. Also, the diffusive approximation in Eq.(2.32) is considered in the figure.

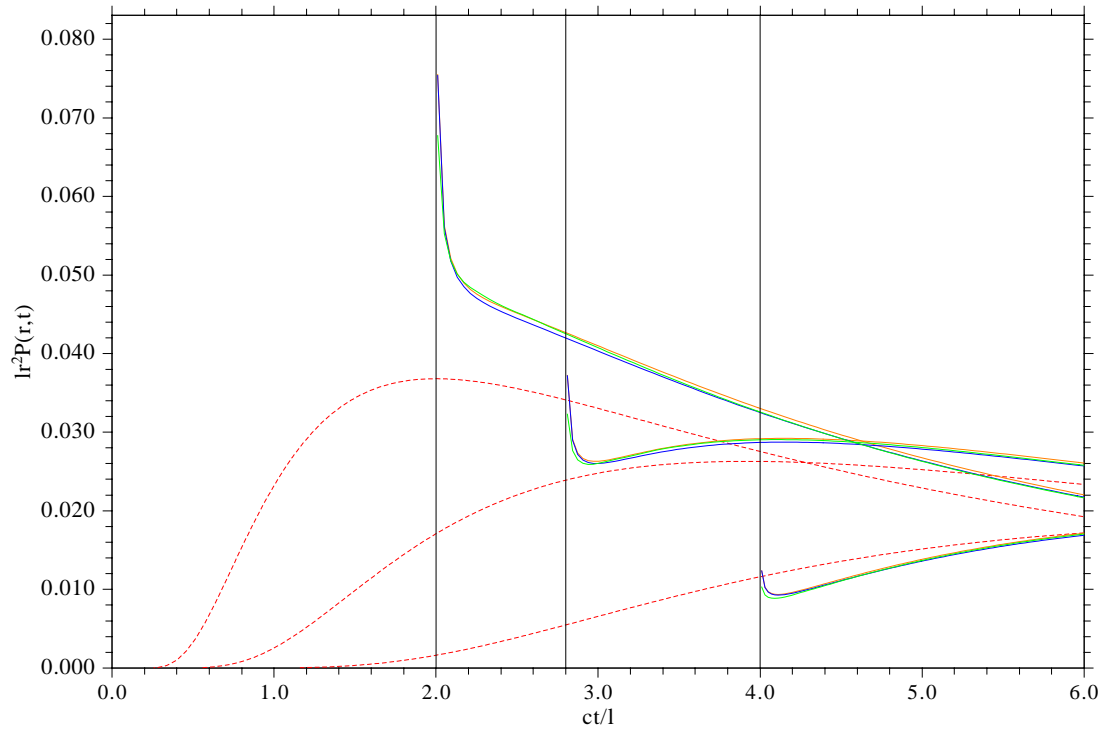


**Figure 2-9.** Intensity as a function of time  $t$ , at distances  $r = 2.0l$ ,  $2.8l$  and  $4.0l$ , from left to right. The blue lines are the exact result, which is very close to the interpolation formulas: green line corresponds to Eq. (2.51) and orange line corresponds to using the approximation in Eq. (2.52). Dashed red lines correspond to the Gaussian diffusive result.



## 3 SPATIAL DISTRIBUTION OF CODA SCATTERERS

### 3.1 INTRODUCTION

The fundamental assumption of all coda models of Chapter 2 is that intrinsic absorption and the distribution of structures causing scattering is random and uniform (e.g. Aki & Chouet, 1975 [9]; Sato, 1977 [18]). As a result of this assumption all these models predict that the envelopes of S coda waves should decay smoothly and that the coda decay rate should be independent of the hypocenter. The observed envelopes of S coda waves differ from those synthesized by models based on the hypothesis of a random and uniform distribution of scatterers in space. Small amplitude fluctuations or ripples overlying on a smoothly decaying coda envelope which is predicted by the scattering theory, are often observed. This observed behaviour can be explained by a non-uniform three-dimensional distribution of scatterers in the crust due to localized inhomogeneities such as active faults, volcanoes, subducting slabs and so on. Then, a deterministic approach on coda waves is necessary in order to elucidate the detailed inhomogeneous structures in the crust and the upper mantle.

Nishigami (1991) [40], identified the structures causing strong scattering by analyzing the observed coda envelope fluctuations from a synthesized model. In this work, he analyzed the seismic data of Hokuriku district of central Japan and detected zones of strong scattering in the surface layer and upper crust; some of these regions of strong scattering were located near major active faults. Applying the coda-envelope-inversion technique to three regions in central part of Japan, Nishigami [41] identified significant heterogeneous structures in the crust around one active fault system and two active volcanoes. In the same way, he established also the three-dimensional distribution of scatterers in the crust in San Andreas Fault system region [42]. There are also other authors applying similar techniques to other regions. Chen and Long (2000) [43], in the Piedmont Province of central Georgia, found a correlation at shallow depths between zones of strong scattering and the location of hypocenters and areas with greater topographic relief, and were able to identify a strong reflecting layer which was consistent with a thrust plain previously reported using other geophysical methods.

More recently, Asano and Hasegawa (2004) [44] suggested the correlation between large scattering zones with the existence of fault-damaged zones in south-western Japan, as well as other scattering properties of the region at different depths.

Following Nishigami's work, in section 3.2, we will develop the method of analysis necessary to establish the distribution of scatterers. This method implies a previous knowledge of the depth dependent velocity model and it assumes a synthetic single isotropic scattering model for the absolute reference scattering coefficients (Sato, 1977, [18]). An important step to establish this distribution is the computation of the energy residuals. This calculation is explained in detail in section 3.3.

### 3.2 THE OBSERVATIONAL EQUATION

In this section, we are going to develop an inversion method of coda waveforms in order to estimate the spatial distribution of coda scatterers deterministically. Therefore we will derive the relationships between the fluctuation of observed coda power envelope and the spatial variation of scattering coefficient.

We start by considering the Single Isotropic Scattering (SIS) model for the shape of the coda of local earthquakes [18] which assumes single isotropic scattering, random and homogeneous distribution of scatterers, and spherical radiation of elastic energy. According to the SIS model, and considering the anelastic attenuation effect, the coda energy density at a frequency  $f$ , hypocentral distance  $r$  and lapse time  $t$  in a three-dimensional space can be expressed as an integral all over the space in the form [18]:

$$E_s(f | r, t) = \int_V \frac{W_0(f)g(f)}{(4\pi)^2 \beta r_1^2 r_2^2} e^{-2Q_c^{-1}\pi f t} \delta \left[ t - \frac{r_1 + r_2}{\beta} \right] dV \quad (3.1)$$

where  $dV = d^3x$ ;  $\mathbf{x}$  is the coordinate vector of the scattering point;  $r_1 = |\mathbf{x}|$  is the distance between the hypocenter and the scatterer;  $r_2 = |\mathbf{x} - \mathbf{r}|$  is the distance between the scatterer and the station;  $r = |\mathbf{r}|$ ;  $t$  is the lapse time measured from the origin time of the earthquake;  $\beta$  is the average S-wave velocity;  $W_0(f)$  represents the total energy radiated from the source within a unit frequency band around  $f$ ; and  $g(f)$  is the total

scattering coefficient for the frequency  $f$ . In a constant velocity medium, the scatterers responsible for the generation of coda waves at a distance  $r$  and time  $t$  are contained in a spheroidal shell whose foci are located at the source and receiver, which is expressed by the term  $(1/\beta)\delta[t-(r_1+r_2)/\beta]$  in Eq. (3.1). The integration of Eq. (3.1) gives [18]

$$E_s(f|r,t) = \frac{W_0(f)g_0(f)}{4\pi r^2} K(a) e^{-2Q_c^{-1}\pi f t} \quad (3.2)$$

for a homogeneous spatial distribution of the scattering coefficient  $g_0(f)$ , being  $K(a) = (1/a)\ln[(a+1)/(a-1)]$  for  $a > 1$ ;  $a = t/t_s$ ; and  $t_s$  the S-wave travel time. For  $a \gg 1$   $K(a) \approx 2/a^2$  and therefore Eq.(3.2) becomes

$$E_s(f|r,t) \approx \frac{W_0(f)g_0(f)}{2\pi\beta^2 t^2} e^{-2Q_c^{-1}\pi f t}, \quad (t > 2t_s) \quad (3.3)$$

which corresponds to the single scattering model of Aki and Chouet (1975) [9].

We divide the area under consideration into a number  $N$  of small blocks of volume  $\delta V$ , as it will be detailed later. Therefore, by multiplying the right side of Eq. (3.1) by the factor 1/2 for including the effect of a half space, then by integrating Eq. (3.1) in the radial direction over the spheroidal shell (which radius is approximated by  $\beta t/2$ ), which corresponds to the lapse time window  $t_j \pm \delta t/2$  (the magnitude of  $\delta t$  will be computed in section 3.3), we obtain:

$$E_{sa}(f|t_j)\delta t \approx \frac{W_0(f)g_0(f)}{4\pi^2\beta t} e^{-2Q_c^{-1}\pi f t_j} \sum_{i=1}^{N_j} \frac{\delta_{ij}}{(r_{1,i}r_{2,i})^2} \delta V \quad (3.4)$$

where the integral has been approximated by a summation of the blocks, where each term corresponds to a certain block  $i$ . The sub index  $a$  in the energy density indicates the consideration of an average scattering coefficient  $g_0$  over the half space.  $\delta_{ij}$  equals 1 when the  $i$ th block lays inside the spheroidal shell which corresponds to the  $j$  time window and equals zero otherwise.  $N_j$  is the total number of scatterers in each spheroidal shell.

The observed coda envelope fluctuations from the theoretical model due to the

non-uniform distribution of scatterers can be expressed mathematically as spatial perturbations of the average scattering coefficient of the medium due to an individual scatterer in the form:  $g=g_0\alpha_i$  ( $\alpha_i \geq 0$ ). Thus, the integration of Eq.(3.1) gives:

$$E_s(f | t_j)\delta t = \frac{W_0(f)g_0(f)}{4\pi^2\beta t} e^{-2Q_c^{-1}\pi f t_j} \sum_{i=1}^{N_j} \frac{\alpha_i \delta_{ij}}{(r_{1,i}r_{2,i})^2} \delta V \quad (3.5)$$

To obtain Eq.(3.4) and Eq. (3.5) we have assumed a constant value of  $Q_c$  in the region, thus neglecting the effect of an spatial variation of  $Q_c$  on the fluctuations of the coda envelope and considering that they are caused mainly by the spatial variations of the scattering coefficient. In order to get a system of equations that will allow us to estimate the spatial perturbations of the scattering coefficient we divide Eq.(3.5) by Eq. (3.4),

$$\frac{E_s(t_j)}{E_{sa}(t_j)} = \frac{1}{\sum_i \frac{\delta_{ij}}{(r_{1,i}r_{2,i})^2}} \sum_i \frac{\alpha_i \delta_{ij}}{(r_{1,i}r_{2,i})^2} \quad (3.6)$$

where the left side of equation Eq. (3.6) is called coda wave energy residual ( $e_j$ ) and it measures the ratio of the observed energy density in this part of the coda to the average energy density of the medium.

If we divide the coda of one seismogram into several small time windows, we will have one equation based on Eq. (3.6) for each time window. Also for each time window, the scatterers contributing to the energy density are contained in a spheroidal shell. Thus, equation Eq.(3.6) can be re-written in the following form:

$$\begin{aligned} w_{11}\alpha_1 + \dots + w_{i1}\alpha_i + \dots + w_{N1}\alpha_N &= e_1 \\ &\vdots \\ w_{1j}\alpha_1 + \dots + w_{ij}\alpha_i + \dots + w_{Nj}\alpha_N &= e_j \\ &\vdots \\ w_{1M}\alpha_1 + \dots + w_{iM}\alpha_i + \dots + w_{NM}\alpha_N &= e_M \end{aligned} \quad (3.7)$$

where M is the total number of equations (number of seismograms multiplied by the number of coda time windows considered), N is the total number of scatterers (number

of small blocks into which the study region is divided) and

$$w_{ij} = \frac{1}{\sum_i \frac{\delta_{ij}}{(r_{1,i}r_{2,i})^2}} \frac{\delta_{ij}}{(r_{1,i}r_{2,i})^2} \quad (3.8)$$

Solving Eq. (3.7) will provide us the scattering coefficient distribution. The methods to solve such a system of equations will be developed in Chapter 4.

### 3.3 COMPUTATION OF THE ENERGY RESIDUALS

We will explain now in detail how to compute the energy residuals from the vertical component of seismograms. The steps to follow are:

- i. Extraction of frequency components from a certain frequency band, i.e, 4-10 Hz. This is done by using a Butterworth or Chebyshev band-pass filter. The filter has to be applied both forward and backward along the time axis to cause no phase delay. We generated the algorithm to apply the filter by means of the software provided by Tony Fisher [45] in his web page. This web page is a tribute to him (he died on February 29<sup>th</sup>, 2000).
- ii. Computation of the rms amplitudes  $A_{\text{obs}}(f|r,t)$  of the filtered traces using a time window for the averaging of about ten times the central period of the filter used [73]. The rms amplitudes for a noise window of 10 s before the P-wave arrival are also computed and only the amplitudes greater than two times the signal to noise ratio are kept.
- iii. The amplitudes are then corrected for geometrical spreading by multiplying by  $t^2$  which is valid for body waves in a uniform medium.
- iv. The average decay curve is estimated for each seismogram by means of a least-squares regression of  $\ln[t^2 A_{\text{obs}}(f|r,t)]$  vs.  $t$  and only the estimates with a correlation coefficient greater than 0.70 are kept. It is convenient to consider starting lapse times from about 1.5-2 times [17] the arrival time of the S wave in

order to increase the resolution near the source region .

- v. The observed coda residuals  $e(t)$  are then calculated by taking the ratio of the corrected observed amplitudes to the estimated exponential decay curve.
- vi. We would like to obtain a limited number of coda residuals. So finally the residuals are averaged in time windows of  $\delta t$  to get  $e_j$  at discrete lapse times  $t_j$ . There is an important reason for this: we will compute the scattering coefficient for each block into which the study region is divided, and every block has a finite volume  $V$ . Then, the residuals should correspond to the energy scattered by a finite volume. If a wave takes a certain time to travel the volume  $\delta\tau \approx 2(\delta V)^{1/3}/v$  (the factor 2 comes from considering the wave going back and forth during the scattering process) then we will consider only a certain number of residuals  $E(t_j)$  coming from the average of  $e(t)$  in a time interval  $\delta(t)$  centered at a discrete lapse time  $t_j$ .  $\delta(t)$  has to be similar but smaller than  $\delta(\tau)$  and we consider  $t_{j+1} - t_j = \delta(t)$ .

All this process is illustrated in Figure 3-1 (for the 4-8 Hz frequency band) and (E)

Figure 3-2 (for the 8-12 Hz) where we show the following: Figures (A) corresponds to a coda waveform of an earthquake at an epicentral distance of 1.91 km and 1.53 km respectively, under Galeras volcano (Colombia). Figures (B) correspond to the band-pass filtered coda waveform of seismograms on figures (A). Figures (C) corresponds to the power spectrum of figures (A). Figures (D) correspond to the logarithm of the running mean-squared amplitudes corrected for geometrical spreading effect. The continuous cyan line is the best linear fitting function to the logarithmic trace. Finally, figure (E) corresponds to the logarithm of the coda energy residuals averaged in a time window of 0.5 s.

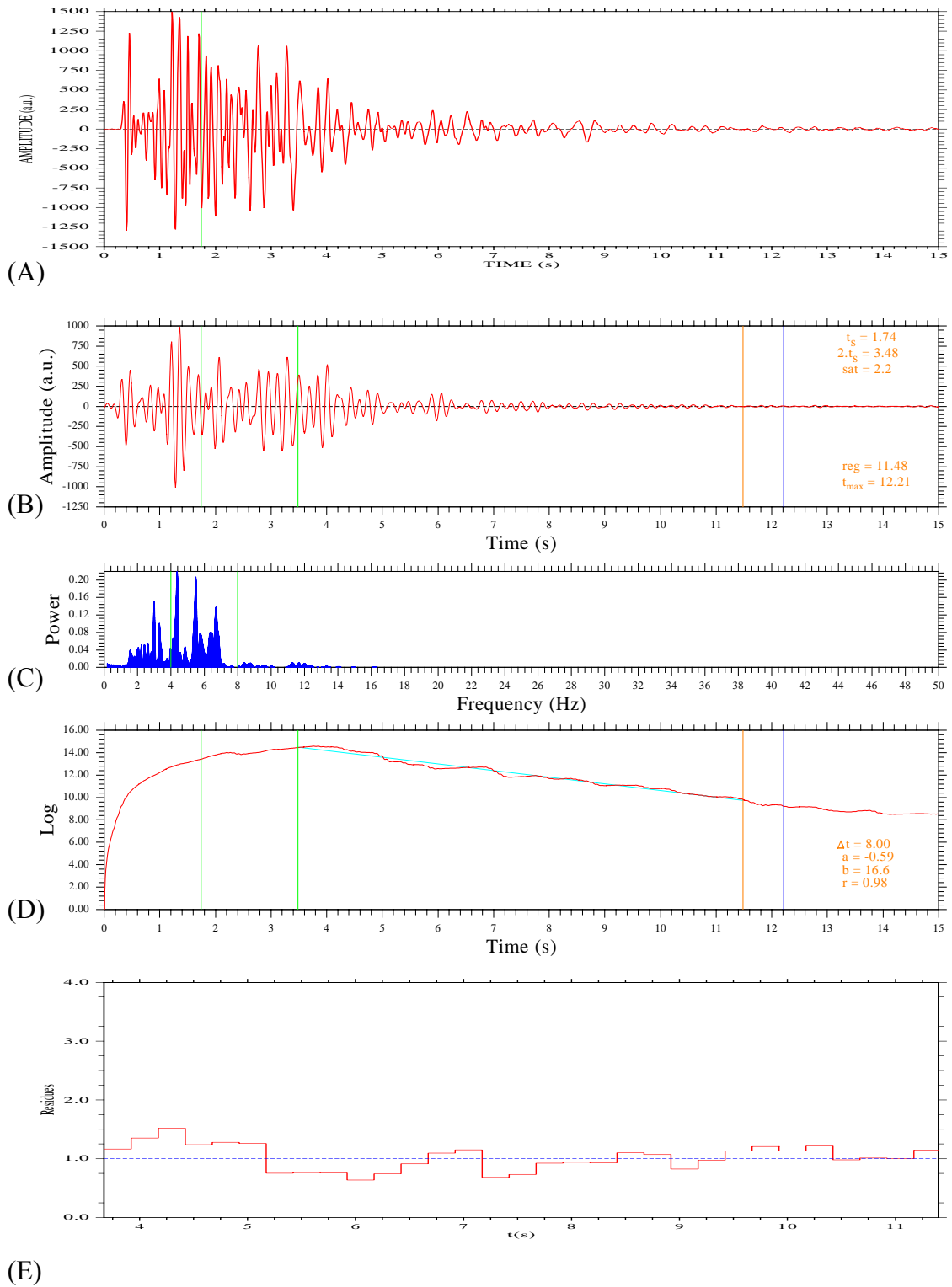


**Figure 3-1.** Analysis of event 300 recorded by the station 14 in the Galeras volcano (see appendix A). (A) corresponds to the raw seismogram. (B) corresponds to the filtered seismogram in the 4-8 Hz band. (C) is the power spectrum of the seismogram between  $t=3.48$  s and  $t=11.48$  s. This lapse time corresponds to the one that will be used to carry out the linear regression in figure (D). First green line indicates  $t_s$  in Figs (A-B-D) and second green line indicates  $2t_s$  in Figs (B-D). In Fig (C) green lines indicate the frequency band under analysis. (E) corresponds to the logarithm of the coda energy residuals averaged in a time window of 0.5 s.

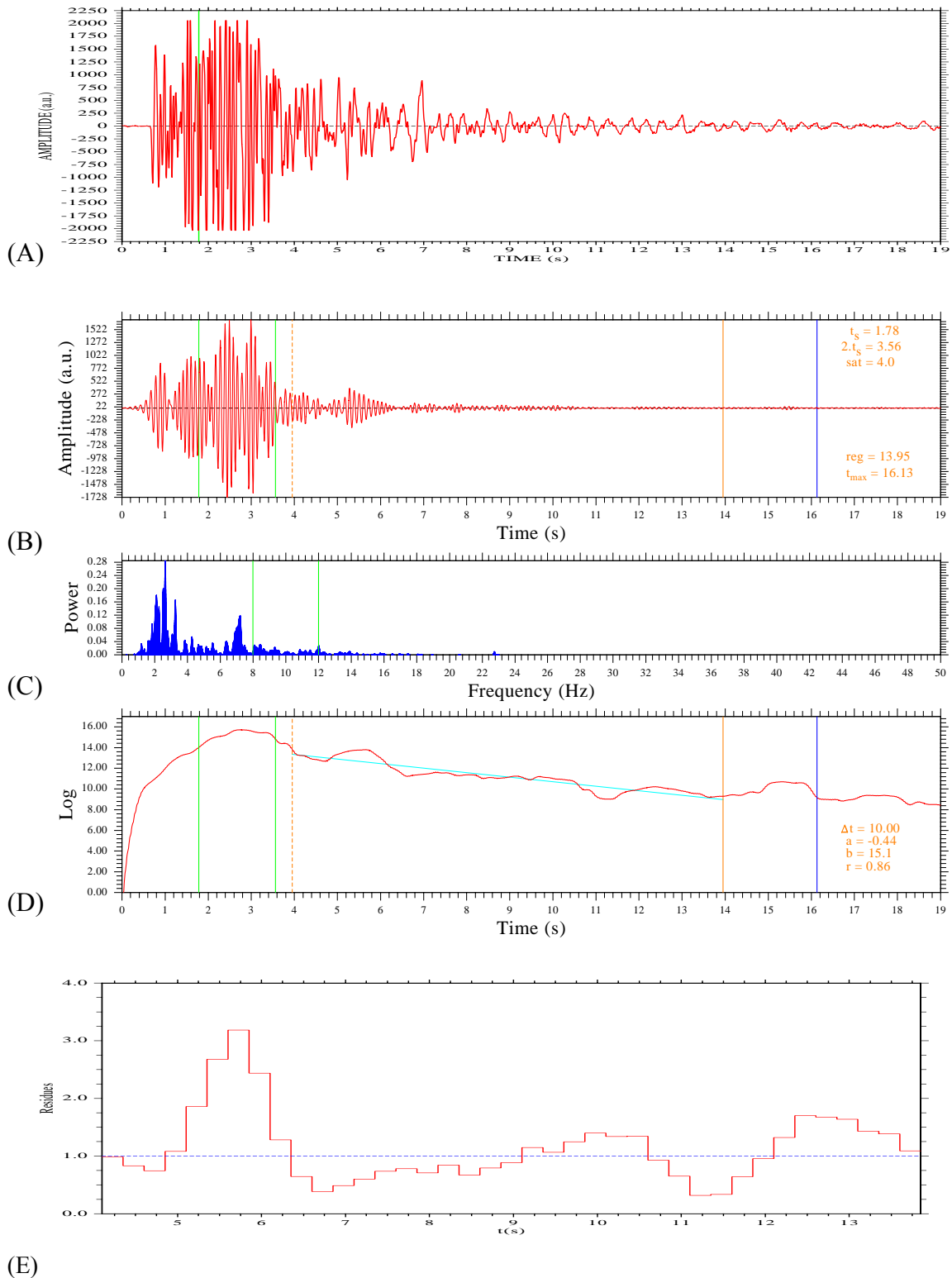


**Figure 3-2.** Analysis of event 128 recorded by the station 14 in the Galeras volcano (see Appendix A). (A) corresponds to the raw seismogram. (B) corresponds to the filtered seismogram in the 8-12 Hz band. (C) is the power spectrum of the seismogram (A) between  $t=4.0$  s and  $t=13.95$  s. This lapse time corresponds to the one that will be used to carry out the linear regression in figure (D). First green line indicates  $t_s$  in Figs (A-B-D) and second green line indicates  $2t_s$  in Figs (B-D). In Fig (C) green lines indicate the frequency band under analysis. Dashed line indicates a safe initial time to avoid side effects from saturation of the recorded seismogram. (E) corresponds to the logarithm of the coda energy residuals averaged in a time window of 0.5 s.

## 4 INVERSION METHODS

### 4.1 INTRODUCTION

As explained in Chapter 3, in order to obtain the magnitude of the scattering coefficient, we have to solve the system of equations:

$$\begin{aligned} w_{11}f_1 + \dots + w_{1j}f_j + \dots + w_{1N}f_N &= p_1 \\ \vdots & \\ w_{i1}f_1 + \dots + w_{ij}f_j + \dots + w_{iN}f_N &= p_i \\ \vdots & \\ w_{M1}f_1 + \dots + w_{1j}f_j + \dots + w_{MN}f_N &= p_M \end{aligned} \tag{4.1}$$

where  $N$  is the number of blocks in which the region has been divided and  $M$  is the number of residuals obtained from the seismograms. In our case  $N \approx 50000$  and  $M \approx 10000$ . To solve such a system of equations it is not possible to use conventional matrix theory methods to invert the system. There are several reasons [46]. The most important reason is that these systems of equations are always close to singular. While not exact linear combinations of each other, some of the equations may be so close to be linearly dependent that round off errors render them linearly dependent at some stage in the solution process. This may make the numerical procedure to fail. If it does not fail, round off errors in the solution process can swamp the true solution. This problem particularly emerges if  $N$  is a large number ( $N > 10$ )!

For large values of  $M$  and  $N$  there are very convenient algebraic iterative methods based on the “method of projections” as first proposed by Kaczmarz [47]. These methods have been successfully used in Computerized Tomographic (CT) imaging for medical applications [48]. The simplest iterative method is the so-called Algebraic Reconstruction Technique (ART) algorithm. Another method based on ART is the Simultaneous Iterative Reconstruction Technique (SIRT). These methods are discussed in sections 4.2 and 4.3.

Algebraic methods are slow although they have some advantages discussed in section 4.4.7. There is a non-iterative algorithm that performs the inversion more

efficiently. This algorithm is the Filtered Backprojection (FBP) algorithm. This algorithm uses a completely different approach to carry out the inversion and the solution is readily obtained as a linear combination of the residuals. The theoretical background necessary to grasp the intuitive ideas behind the method are introduced for 2-dimensional reconstruction problems in section 4.4.1. In section 4.5 the algorithm is generalized in order to carry out inversions in three dimensions.

## 4.2 ART ALGORITHM

In order to solve Eq.(4.1) we may consider the geometrical meaning of a system of equations. We consider a  $N$ -dimensional space. In this space, each equation represents a hyperplane. When a unique solution exists, the intersection of all these hyperplanes is a single point.

The computational procedure to locate the solution consists of first starting with an initial guess, denoted by  $\vec{f}^{(0)} = (f_1^{(0)}, f_2^{(0)}, \dots, f_N^{(0)})$ . In most cases we simply assign a value of zero to all the  $f_i$ 's. This initial guess is projected on the hyperplane represented by the first equation in (4.1) giving  $\vec{f}^{(1)}$ .  $\vec{f}^{(1)}$  is then projected on the hyperplane represented by the second equation in (4.1) to yield  $\vec{f}^{(2)}$  and so on. This is illustrated in Figure 4-1 for a system of two equations with two unknowns.

When  $\vec{f}^{(i-1)}$  is projected on the hyperplane represented by the  $i$ th equation to yield  $\vec{f}^{(i)}$ , the process can be mathematically described by:

$$\vec{f}^{(i)} = \vec{f}^{(i-1)} - \frac{\vec{f}^{(i-1)} \cdot \vec{w}_i - p_i}{\vec{w}_i \cdot \vec{w}_i} \vec{w}_i \quad (4.2)$$

where  $\vec{w}_i = (w_{i1}, w_{i2}, \dots, w_{iN})$ . To see from where Eq.(4.2) comes from we first rewrite the first equation of (4.1) as:

$$\vec{w}_i \cdot \vec{f} = p_i \quad (4.3)$$

The hyperplane represented by this equation is perpendicular to the vector  $\vec{w}_1$  as can be seen in Figure 4-2. The equation (4.3) states that the length of the projection of the vector  $\vec{f}$  on the vector  $\vec{w}_1$  has a constant length (if  $|\vec{w}_1|=1$  then  $p_1$  is the distance of the plane from the origin).

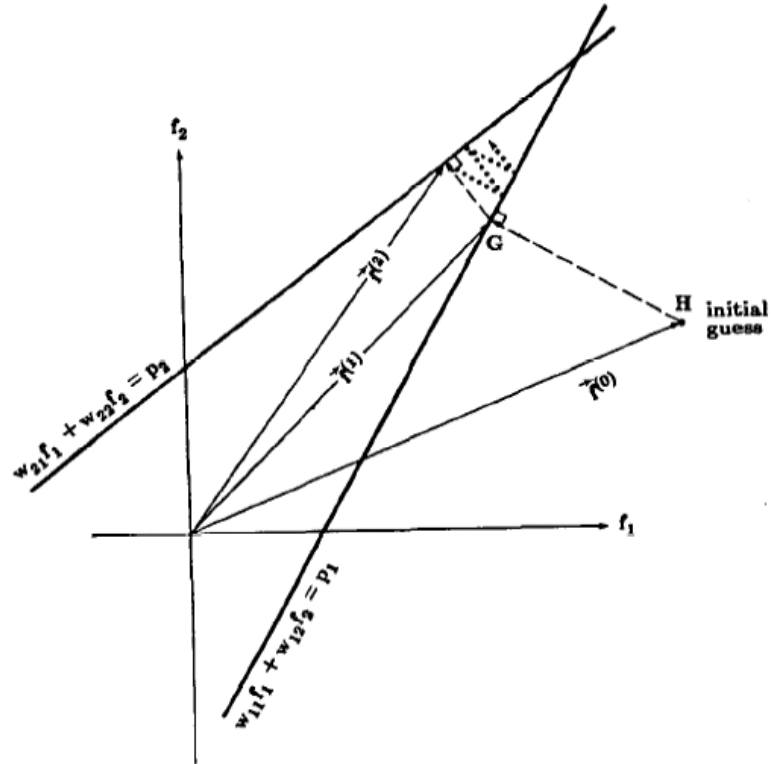


**Figure 4-1.** The Kaczmarz method of solving algebraic equations is illustrated for the case of two unknowns. One starts with some arbitrary initial guess and then projects onto the line corresponding to the first equation. The resulting point is now projected onto the line representing the second equation. If there are only two equations, this process is continued back and forth, as illustrated by the dots in the figure, until convergence is achieved [48].

The unit vector along  $\vec{w}_1$  is given by:

$$\vec{u} = \frac{\vec{w}_1}{\sqrt{\vec{w}_1 \cdot \vec{w}_1}} \tag{4.4}$$



Then, the projection  $\vec{f}^{(1)}$  may be written as:

$$\vec{f}^{(1)} = \vec{f}^{(0)} - \frac{\vec{w}_1 \cdot \vec{f}^{(0)} - p_1}{\sqrt{\vec{w}_1 \cdot \vec{w}_1}} \cdot \vec{w}_1 \quad (4.7)$$

For the computer implantation of this method our initial guess at the solution  $\vec{f}_0$  is a unity value to all the  $f_{0,j}$ . The ART iteration process can be mathematically described by the following equation:

$$\Delta f_j^{(i)} = f_j^{(i)} - f_j^{(i-1)} = \frac{\vec{f}^{(i-1)} \cdot \vec{w}_i - p_i}{\vec{w}_i \cdot \vec{w}_i} \quad (4.8)$$

where  $\vec{w}_i = (w_{i1}, w_{i2}, \dots, w_{iN})$ , and the new solution  $f_j^{(i)}$  is obtained from the last solution  $f_j^{(i-1)}$  by the addition of the change  $\Delta f_j^{(i)}$ . As already stated, every iteration has a geometrical meaning: in each iteration, the solution is projected in the hyperplane represented by each equation. Each projection becomes closer to the solution if it exists.

#### 4.2.1 CONVERGENCE AND CHARACTERISTICS OF THE SOLUTIONS

An important comment about the convergence of the algorithm is in order. If the consecutive hyperplanes have only a very small angle between them, the rate of convergence to the solution might be very slow because only a small increment  $\Delta f_j^{(i)}$  is added from one equation to the next one. If equations are arranged in such way that hyperplanes are as much orthogonal as possible, the rate of convergence becomes much faster. But too much orthogonalization will also tend to enhance the effects of the ever present measurement noise in the final solution. The rate of convergence depends also on the choice of the initial guess  $\vec{f}_0$ .

ART reconstructions usually suffer from “salt and pepper” noise which is caused by the inconsistencies introduced in the set of equations by the approximations commonly used in the calculation of the matrix parameters. It is possible to reduce the effects of this noise by relaxation, in which we update a block by  $\alpha \Delta f_j^{(i)}$  where  $\alpha$  is less than one. In some cases it is convenient to make the relaxation parameter  $\alpha$  a function of the iteration number; that is, it becomes progressively smaller with increase number of

iterations. The resulting improvements in the quality of reconstruction are usually at the expense of convergence. Another method based on the ART may be considered in the next section 4.3 in order to minimize still more this kind of noise.

If  $M > N$  a unique solution of the set of linear system in Eq. (4.1) does not exist, and, in fact, an infinite number of solutions are possible. In this case ART algorithm converges to a solution  $\vec{f}'_s$  such that  $|\vec{f}^{(0)} - \vec{f}'_s|^2$  is minimized. For an over determined problem,  $N > M$ , no unique solution can be found by ART. A not uncommon situation in image reconstruction is that of an over determined system in the presence of measurement noise. That is, we may have  $N > M$  and  $e_j$  corrupted by noise. No unique solution exists in this case: the “solution” doesn’t converge to a unique point, but will oscillate in the neighbourhood of the intersections of the hyperplanes.

One attractive feature of the iterative approach is that it is possible to incorporate into the solution some types of a priori knowledge about the scattering coefficients. For example, if the coefficients are known to be positive, one may set the negative components equal to zero.

### 4.3 SIRT ALGORITHM

The Simultaneous Iterative Reconstructive Technique (SIRT) [49] is another algorithm which eliminates the continual and competing block update as each equation is considered. Then, using the SIRT algorithm smoother and better looking reconstructions are usually obtained at the expense of slower convergence [50]. In each iteration of the SIRT algorithm, the change in each block is computed by the use of the same equations as in the ART algorithm (Eq. (4.8)), but before making any changes, all the equations are considered, and then only at the end of each iteration are the block values changed, the change of each cell being the average value of all the computed changes for that block. It is also known that SIRT algorithms perform better in extreme situations [51] such as uneven distribution of data, incomplete data, etc. It is also possible to easily incorporate constrains as positivity, limited spatial support, etc.

### 4.3.1 THE WEIGHT COEFFICIENTS $w_{ij}$

In applications like ours, requiring a large number of equations the difficulty of using Eq. (4.2) can be in the calculation, storage, and fast retrieval of the weight coefficients  $w_{ij}$ . The number of coefficients is in our case of the order of  $10^9$ . This problem is somewhat eased by making approximations, such as considering  $w_{ij}$  to be only a function of the perpendicular distance of the  $i$ th spheroidal shell and the centre of the  $j$ th cell.

In many ART [52] and SIRT implementations to find the distribution of scattering coefficients the  $w_{ij}$ 's are simply replaced by 1's and 0's depending upon whether the centre of the  $j$ th block is within the  $i$ th spheroidal shell. As consequence extra salt and pepper noise is introduced in the reconstruction. In our calculations the width of the shell is smaller than the width of the blocks. Then it is important to calculate the fraction of volume  $V_{ij}$  of each block lying inside the  $i$ th spheroidal shell. Then, instead of using Eq. (3.8) we will use the following expression for the coefficients  $w_{ij}$ :

$$w_{ij} = \frac{V_{ij}}{\sum_j \frac{V_{ij}}{(r_{1,j}r_{2,j})^2} \cdot (r_{1,j}r_{2,j})^2} \quad (4.9)$$

Also, it is important to use a relaxation parameter ( $\lambda$ , a factor smaller than unity multiplying the increment  $\Delta f_j^{(i)}$ ) which is commonly determined by trial and error. If incorrectly selected, will either cause premature termination and incorrect result or, if number of iterations or  $\lambda$  too small, will result in a reconstruction lacking high-frequency details. By trial and error we chose  $\lambda = 0.01$  for about 120 iterations.

## 4.4 BACKPROJECTION ALGORITHM

We will start the derivation of the Backprojection algorithm [48,53] under the set of conditions as simplest as possible. These conditions will be clearly different from our problem's: two-dimensional distribution, ray emitters and transducers located over arrays around the two-dimensional area. This initial development will be derived in section 4.4.1. Nevertheless, the results that we will obtain with this derivation will be easily extended by intuitive reasoning to the geometry of our case in section 4.5. Then, using this algorithm, scattering coefficients will become a weighted average value of the residues that correspond to a certain block. This will make this algorithm to be much faster than any other iterative method. Computations times will be about 100 times smaller than the ones for ART or SIRT and no relaxation parameter will have to be chosen.

### 4.4.1 BACKPROJECTION ALGORITHM IN TWO DIMENSIONS WITH LINEAR ARRAYS OF TRANSDUCERS. GEOMETRY AND DEFINITIONS

We start by assuming the geometry outlined in Figure 4-3 [51]. Notice that we will use two set of axis: the main set  $(x,y)$  is the original set of coordinates used to describe the object function  $g(x,y)$ . We also have a second frame  $(x',y')$  that takes into account the direction of the beams. We consider then  $g(x,y)$  (from now on it will be noted as object function) to be traversed by a set of parallel beams. There is a set of transducers located on a line recording a "*parallel projection*" of  $g(x,y)$  on a line parallel to the  $x'$  axis at an angle  $\theta$  from main reference frame. The coordinate systems will allow us to describe *line integrals* and *projections* in a simple fashion. Let us define both concepts rigorously.

A *line integral* will represent the integral of the function  $g(x,y)$  along a line. This may correspond to the total attenuation suffered by a ray as it travels in a straight line through the object function. Each line integral may be represented by a set of two parameters  $(\theta, x')$  because the equation of the lines describing the beams in the figure is:

$$\mathbf{x} \cdot \mathbf{n} = x \cos \theta + y \sin \theta = x' \quad (4.10)$$

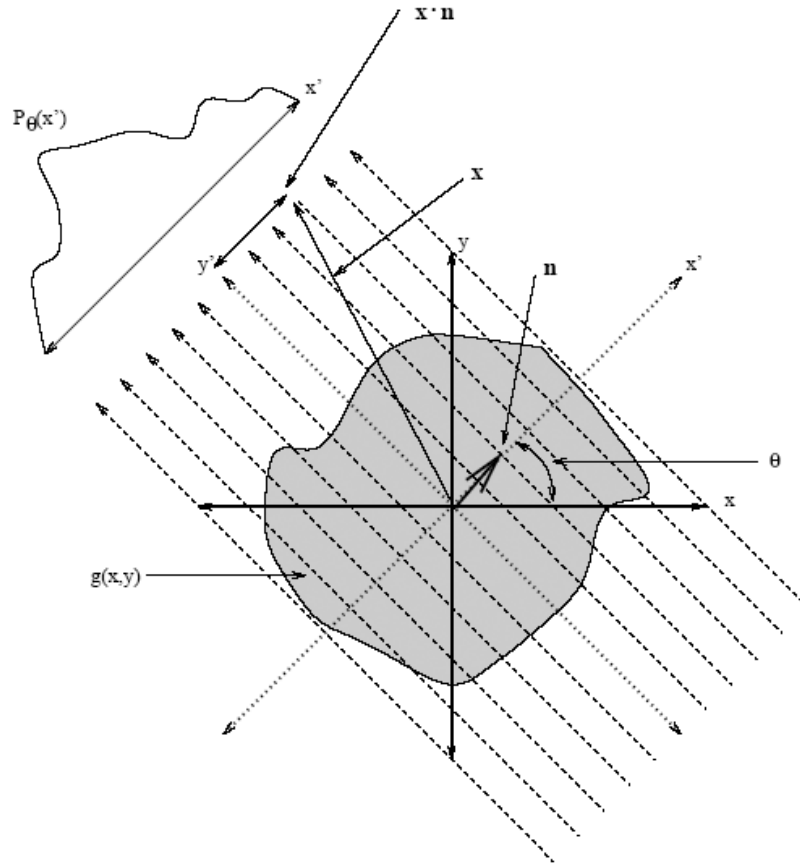


**Figure 4-3.** Illustration of the geometry of a set of parallel projection beams [53].

And we will use this equation to write the line integral  $P_\theta(x')$  as:

$$P_\theta(x') = \int_{-\infty}^{\infty} g(x', y') dy' \quad (4.11)$$

Using a delta function this can be rewritten as :

$$P_\theta(x') = \int_{-\infty}^{\infty} \int_{-\infty}^{\infty} g(x, y) \delta(x \cos \theta + y \sin \theta - x') dx dy \quad (4.12)$$

The function  $P_\theta(x')$  is the so-called Radon Transform of the object function  $g(x,y)$  (the graphic representation of the radon transform is called sinogram). A projection is formed by combining a set of line integrals. The simplest projection is a collection of parallel ray integrals as is given by  $P_\theta(x')$  for a constant  $\theta$ . This is known

as a parallel projection.

We will show now, that if we know  $P_\theta(x')$  for all possible values of  $\theta$  it is possible to estimate  $g(x,y)$  by simply performing a two-dimensional inverse Fourier-Transform. This is done by means of the Fourier-Slice Theorem.

#### 4.4.2 THE FOURIER SLICE THEOREM

The Fourier slice theorem is derived by taking the one-dimensional Fourier Transform of a parallel projection and noting that it is equal to a slice of the two-dimensional Fourier transform of the original function  $g(x,y)$ .

We start by defining the two-dimensional Fourier transform of the object function as:

$$G(u, v) = \int_{-\infty}^{\infty} \int_{-\infty}^{\infty} g(x, y) \exp(-i2\pi \mathbf{x} \cdot \mathbf{u}) dx dy \quad (4.13)$$

where  $\mathbf{u} = (u, v)$ . Likewise we define the Fourier Transform of  $P_\theta(x')$  as:

$$S_\theta(w) = \int_{-\infty}^{\infty} P_\theta(x') \exp(-i2\pi wx') dx' \quad (4.14)$$

Using Eq. (4.11) and Eq.(4.10) in Eq. (4.14) we obtain:

$$S_\theta(w) = \int_{-\infty}^{\infty} \int_{-\infty}^{\infty} g(x', y') \exp(-i2\pi wx') dx' dy' \quad (4.15)$$

This two-dimensional integral may be rewritten in terms of the coordinates  $(x,y)$  as:

$$S_\theta(w) = \int_{-\infty}^{\infty} \int_{-\infty}^{\infty} g(x, y) \exp(-i2\pi w \mathbf{x} \cdot \mathbf{n}) dx dy \quad (4.16)$$

Note that Eq. (4.16) and Eq. (4.13) are very similar. To relate them it is convenient to consider polar coordinates in Eq. (4.13):

$$\begin{aligned} u &= w \cos \theta \\ v &= w \sin \theta \end{aligned} \quad (4.17)$$

Then it is easy to write the following equality:

$$S_{\theta}(w) = G(w, \theta) \quad (4.18)$$

This equality has a fundamental meaning: the Fourier Transform of the projection is identical to the spectrum of the original object function on a slice normal to the direction of the projection beam. This has been illustrated in Figure 4-4:

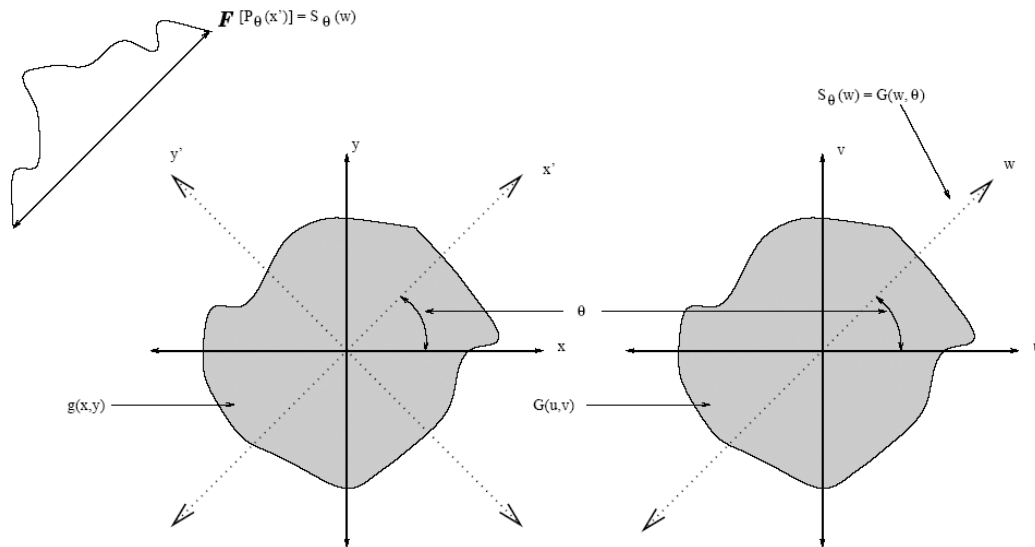


**Figure 4-4** Illustration of the Fourier Slice Theorem [53].

We can see then that it might be possible to recover the object function as a function of the projections.

#### 4.4.3 RECONSTRUCTION ALGORITHM FOR PARALLEL PROJECTIONS

From Eq. (4.18) we wish now to write the object  $g(x,y)$  as a function of  $G(w, \theta)$ . This can be done considering the inverse Fourier transform of  $G(u,v)$  in Eq. (4.13) written in polar coordinates:

$$g(x, y) = \frac{1}{4\pi^2} \int_0^{2\pi} \int_0^{\infty} G(w, \theta) \exp(i2\pi w \{x \cos \theta + y \sin \theta\}) w dw d\theta \quad (4.19)$$

This integral can be split into two by considering:

$$g(x, y) = \frac{1}{4\pi^2} \int_0^\pi \int_0^\infty G(w, \theta) \exp(+i2\pi w \{x \cos \theta + y \sin \theta\}) w \, dw \, d\theta$$

$$+ \frac{1}{4\pi^2} \int_0^\pi \int_0^\infty G(w, \theta + \pi) \exp(+i2\pi w \{x \cos(\theta + \pi) + y \sin(\theta + \pi)\}) w \, dw \, d\theta$$
(4.20)

Using the following property:

$$G(w, \theta + \pi) = G(-w, \theta)$$
(4.21)

and Eq. (4.10) we obtain:

$$g(x, y) = \frac{1}{4\pi^2} \int_0^\pi \int_{-\infty}^\infty G(w, \theta) \exp(+i2\pi wx') |w| \, dw \, d\theta$$
(4.22)

This expression is now ready to include the information from the projections given in Eq. (4.18). Using this equation we rewrite the integral in Eq. (4.22) as:

$$g(x, y) = \frac{1}{4\pi^2} \int_0^\pi \left[ \int_{-\infty}^\infty S_\theta(w) \exp(+i2\pi wx') |w| \, dw \right] d\theta$$
(4.23)

This integral may be expressed as:

$$g(x, y) = \frac{1}{4\pi^2} \int_0^\pi Q_\theta(x \cos \theta + y \sin \theta) \, d\theta$$
(4.24)

where:

$$Q_\theta(x') = \int_{-\infty}^\infty S_\theta(w) \exp(i2\pi wx') |w| \, dw$$
(4.25)

Eqs. (4.24) and (4.25) are the key result of this development. We will now explain the meaning of these expressions.

Eq. (4.25) represents a filtering operation over a certain projection  $P_\theta(x')$ . Notice that the Fourier Transform of  $P_\theta(x')$  is  $S_\theta(w)$  and that we are performing the inverse Fourier transform of  $S_\theta(w)$  times a ramp function  $|w|$ . Thus, Eq. (4.25) represents filtering the projection set  $P_\theta(x')$  with a filter with a frequency response given by  $|w|$ .

Therefore  $Q_\theta(x')$  is called “Filtered Projection”. It is very important now to understand what is  $Q_\theta(x')$  in the real space. Notice that a filtered projection  $Q_\theta(x')$ , for a certain value of  $x'$ , assigns the same contribution to all points  $(x,y)$  lying along the projection (all points on the line  $x \cos \theta + y \sin \theta = x'$ ). Then we say that each function  $Q_\theta(x')$  is *backprojecting* a *filtered projection*. In Eq. (4.24) the resulting projections for different angles  $\theta$  are then *added* to form the estimate of  $g(x,y)$ . We say then that Eq. (4.24) calls for each filtered projection  $Q_\theta(x')$  to be *backprojected*. Now, the name of the algorithm becomes evident.

#### 4.4.4 IMPLEMENTING A FILTERED-BACKPROJECTION ALGORITHM FOR PARALLEL DATA.

Several problems arise when trying to implement Eq. (4.23) in a real case. First, it is only possible to obtain a finite number of projections. If the total number of projections  $N$  is large enough and the projections are distributed over  $180^\circ$  then Eq. (4.23) may be approximated as:

$$g(x, y) \approx \frac{\pi}{N} \sum_{i=1}^N Q_{\theta_i} (x \cos \theta_i + y \sin \theta_i) \quad (4.26)$$

This equation calls for the filtered projections to be backprojected over the  $(x,y)$  plane. Each filtered projection makes an equal contribution to each image point  $(x,y)$ , lying along a parallel projection. However in backprojecting  $Q_{\theta_i}$  to a point  $(x,y)$  we need to know it for  $x' = x \cos \theta_i + y \sin \theta_i$ . However this value of  $x'$  may not correspond to a known value of  $Q_{\theta_i}$  due to the projections being discretely sampled. It is possible to find a value of  $Q_{\theta_i}$  that corresponds to the image point  $(x,y)$  by interpolation. Linear interpolation is often sufficient.

Another problem arises from the filtering of the projection. Notice that the ramp filter in Eq. (4.25) enhances high frequencies making this filtering process extremely sensitive to noise. Therefore, it is necessary to use a different filter to take this into account, usually a band-pass filter. There is a wide variety of choices. Two important examples are the Hamming window:

$$H(w) = w \left( 0.54 + 0.46 \cos \left( \frac{\pi w}{w_c} \right) \right) \quad (4.27)$$

and the Butterworth filter:

$$H(w) = w \sqrt{\frac{1}{1 + \left( \frac{w}{w_c} \right)^{2n}}} \quad (4.28)$$

In the Hamming window  $w_c$  is equal to the maximum frequency the transducers can measure. In the Butterworth filter  $w_c$  is adjusted to filter the noise and allow the information of the object function to be recovered.

Notice then that the filtered backprojection algorithm is sensitive to noise. This sensitivity is due to the fact that the Radon transform is a smoothing transformation, so taking its inverse will have the effect of amplifying noise.

#### 4.4.5 EXAMPLES

A typical example of object function  $g(x,y)$  is the Shepp-Logan Phantom [54]. This phantom appears everywhere through the literature as a standard test for different reconstruction methods. It can be seen in Figure 4-5. The Radon Transform of this Phantom is represented in the corresponding sinogram in Figure 4-6. The horizontal direction corresponds to  $\theta$  and the vertical direction corresponds to  $x'$ . Then in Figure 4-7, we show the reconstruction process as a function of the number of projections used using a ramp filter. We can see that for a low number of projections artefacts appear in the reconstruction image, we say that there is aliasing due to insufficient angular sampling. Those artefacts tend to disappear as the number of projections increases.

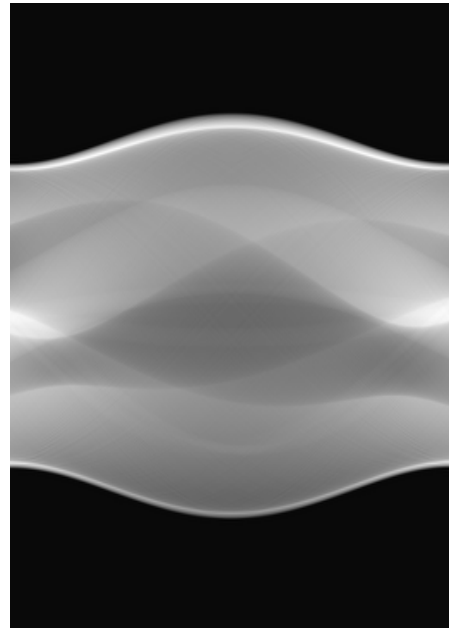


**Figure 4-5.** Shepp-Logan Phantom [55]. **Figure 4-6.** Sinogram of the Shep-Logan Phantom [55].

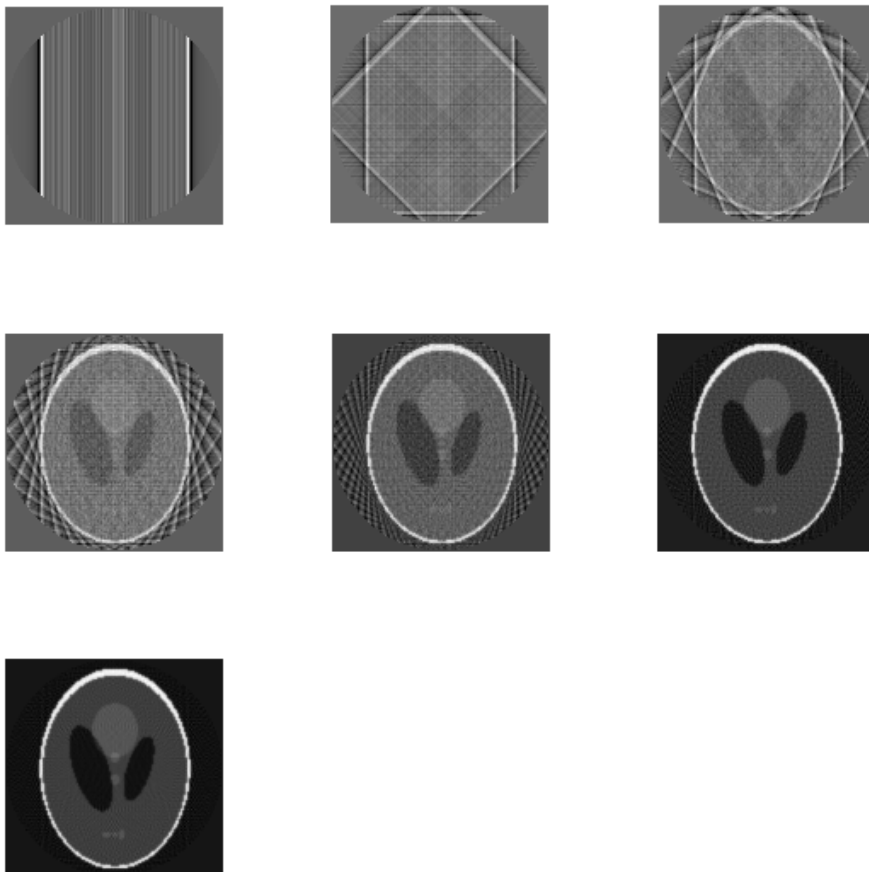


**Figure 4-7.** Reconstructions for (left to right up to down)  $N=1, 4, 8, 16, 32, 64$  and  $128$  projections [55].

If the object function contains a sharp change between two regions one with important values and another with low values the aliasing effects might be even visible for a reconstruction with a large number of projections. This is shown in Figure 4-8 for  $N=256$  projections. The characteristics of the reconstructed phantoms we may be considered to be analogous to reconstructions in the three-dimensional case.

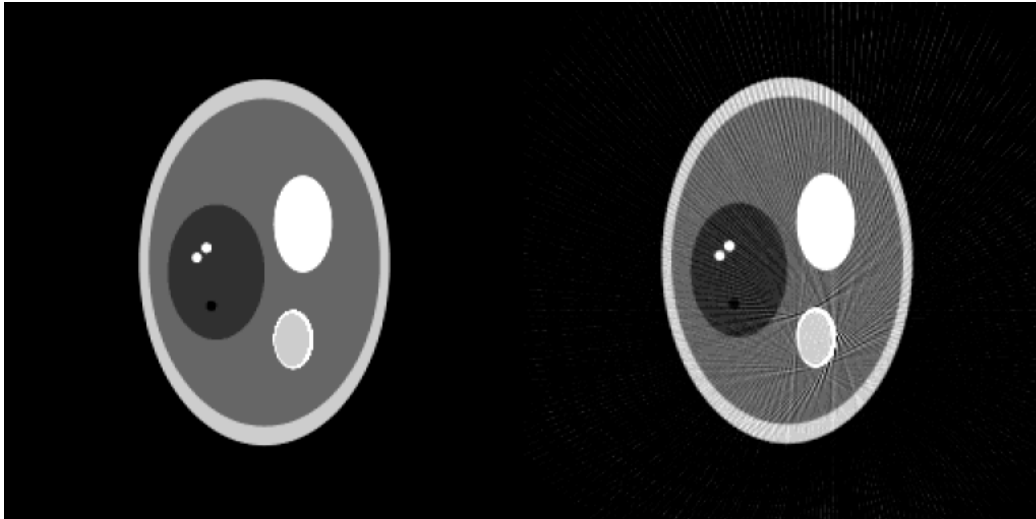


Figure 4-8. Aliasing effects [55].

#### 4.4.6 CONNECTION BETWEEN ART AND BACKPROJECTION. A SIMPLE EXAMPLE.

ART and Filtered Backprojection algorithms seem to be very different and unconnected methods. We will show with a simple example [56] that some similarities exist between both methods. To do this let us consider a very simple example of use of the ART algorithm. Let's assume we use a scanner whose beam scans the sample only along two perpendicular axes. The two-dimensional sample area is divided into a grid of four by four pixels. The embedded object we are interested in absorbs stronger than the matrix and is placed at location [1,1] (numbering the pixels from zero to three). The figure shows the true object. In the real experiment, this is what we would ideally want to measure

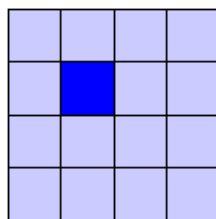
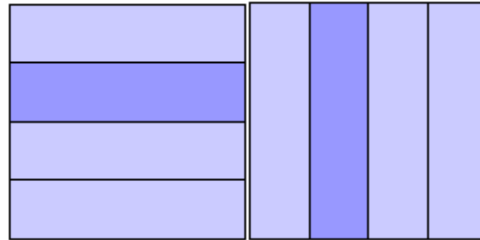


Figure 4-9. Object to be measured [56]

In the experiment, the sample is scanned horizontally and vertically at each row and column of pixels, respectively. The measured value (photon count) is lower in the row(s) and column(s) containing the absorbing object.



**Figure 4-10.** Projection process [56].

To start the reconstruction, each pixel is initialized with the average intensity collected over the whole sample area.

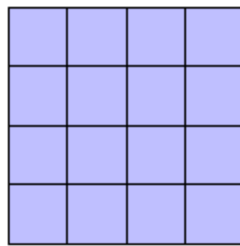


**Figure 4-11.** Initial Solution [56]

The first iteration takes into account the horizontal readings only. Using Eq.(4.7) the absorptivity value of each pixel is corrected by the path-length weighted absorption of its row (this is the meaning of  $\bar{w}$  in this case). Note that the correction is the same one for all the pixels of the row. We may say then that the correction is being “backprojected” to the entire row.

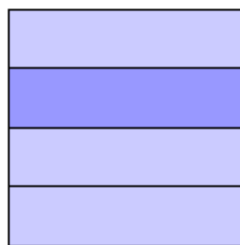


**Figure 4-12** Result of the first iteration [56].

The second iteration improves the image by taking into account the vertical readings. The absorptivity value of each pixel is corrected by the path-length

weighted absorption of its column. Note that, as before, the correction is the same for each pixel along the beam path. Because the absorptivity of the pixels before this iteration *was different*, the corrected absorptivity is also different as can be deduced from Eq. (4.8) that takes into account the previous correction. This is an important difference between ART and FBP. In the Filtered Backprojection Algorithm each projection is considered to be an independent measurement and it is independently backprojected. In ART each backprojected “projection” depends on the others in order to try to solve the system of equations.

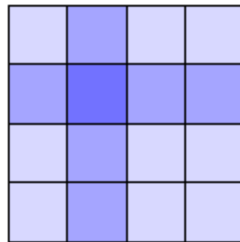


**Figure 4-13** Result of the second iteration [56].

Compare the original sample in Figure 4-9 with the image obtained in Figure 4-13. Obviously, the algorithm underestimates the absorptivity of the object and also of the matrix in general, but those pixels in the matrix which are located in the same row or column as the object are coming out too dark. In effect, the object smears out along the beam paths used. The image doesn't change if more iterations are applied because the two sets of beam paths are orthogonal. What's needed is information on the sample from a variety of angles. Then the image can be updated with the information obtained from each beam. The smearing-out effects, which persist for any single beam, cancel out because the beams are no longer orthogonal. This is true for both ART and FBP.

We are going to generalize now the results we have derived for two dimensional reconstructions to 3 dimensions.

#### **4.4.7 BACKPROJECTION ALGORITHM VERSUS ART AND SIRT**

Backprojection algorithm is a computationally efficient method and it is used in most commercial medical scanners in CT applications and has proved to be extremely accurate and amenable to fast implementation. Backprojection algorithm is then much faster than ART or SIRT and it is able to provide high quality reconstructions. When the

three methods are compared for CT applications, ART and SIRT have a better noise tolerance, and needs fewer projections and perform better when handling for non-uniformly distributed data sets under the condition that angles between projections are not larger than about 20 degrees. Although ART and SIRT may provide sometimes better reconstructions, they are extremely slow and then they are only used for academic purposes or to enhance the quality of a certain reconstruction if an extra amount of time is available.

When the algorithms are compared in other applications, as imaging by transmission measurements using a thermal neutrons to determine water content, cracks and homogeneity in concrete samples the conclusions are different [57]. In this case the Filtered Backprojection produces images of higher contrast, more smoothing and slightly better resolution than those obtained using iterative algebraic methods.

#### **4.5 BACKPROJECTION ALGORITHM TO FIND 3D DISTRIBUTIONS OF SCATTERING COEFFICIENTS**

Let us now write the results from section 4.4.1 in a general way. In Figure 4-3 there is an outline of a measurement process. The measured data set has been called projection. Each projection is a set of numbers. Each number corresponds to an integral of a certain property over a certain region of a certain object function. From the data of all the projections it is possible to reconstruct the original object function. To do this we only have to perform the following process. Firstly, to filter the data corresponding to a certain projection with a ramp filter or some other filter if there is a non-negligible amount of noise in the projection data. Secondly, to backproject the projections one by one. This means to assign each measured number of a certain projection to the region it was coming from. All the data corresponding to a certain pixel or block is then averaged in order to obtain the reconstruction value. From this conclusion, that has been written in a way as general as possible we may derive now an inversion process from the residuals obtained from seismograms.

Let us analyze the meaning of the set of residuals obtained from a certain seismogram. We will show now that a set of residuals from a certain seismogram is analogous to a filtered projection. Each residual corresponds to an average value of the

scattering coefficient in a certain region of the space (a thin volume between two spheroidal shells). The residuals come from seismograms that have been previously filtered by a band-pass Butterworth filter. Then the set of residuals from a certain seismogram are completely analogous to a filtered projection.

To obtain the scattering distribution we will just have to backproject each residual to the corresponding spheroidal region. Finally, the scattering coefficient in a block is obtained by averaging all the residuals corresponding to that block. Block by block the full distribution is obtained. We notice here that the average will become a *weighted* average due to the fact that the geometry of our inversion problem is different. The exact expression to calculate the inversion from the residuals will be now derived.

We start by considering a set of  $k = 1, 2, \dots, K$  events that have happened in a certain region. The region is divided in  $N$  blocks (identified by a subindex  $j$ ) and  $L$  seismometers (identified by the subindex  $l$ ). The correspondence between the coefficients and the residuals are established following several steps:

- i) For each earthquake  $k$ , the travelling time of the signal from the source to the  $j$ th block plus the travelling time from the  $j$ th block to each seismograph  $l$  is computed. This time will be noted as  $T_{jkl}$ . With this data we define the corresponding spheroidal surface that we note as  $S_{jkl}$ . The centre of the  $k$ th block lies on  $S_{jkl}$  and the location of the seismograph and the hypocenter are the corresponding focus of the spheroid. Note that every block defines a different spheroidal surface for the same seismograph and hypocenter.
- ii) The corresponding magnitude of the residuals for each earthquake  $k$  and each seismograph  $l$  at the time  $T_{jkl}$  is computed by simple linear interpolation (we have the magnitudes of the residues only for certain times, as already stated in section 3.3). We note this magnitude as  $R(T_{jkl})$ .
- iii) The contribution of each block is proportional to  $1/(r_{1,j}r_{2,j})^2$ . This geometrical factor indicates whether the contribution of a certain block is more important or less important than the contribution of other blocks on the spheroidal surface  $S_{jkl}$ . Therefore we have to consider a normalized weighted linear combination of residues in order to compute the corresponding

scattering coefficient for each  $j$ th block. Thus the magnitude of the scattering coefficient should be written as:

$$f_j = \frac{\sum_k \sum_l w_{jkl} R(T_{jkl})}{\sum_k \sum_l w_{jkl}} \quad (4.29)$$

The problem now is to find a suitable definition for the weights  $w_{jkl}$ . An important fact that has to be taken into account is that each weight in Eq. (4.29) corresponds to a *different spheroidal surface*. The importance of the contribution depends on the magnitude of  $1/(r_{1,j}r_{2,j})^2$  on each spheroidal surface. In order to normalize the importance of the weights for each spheroidal surface we consider that a good definition for the weights  $w_{jkl}$  in Eq. (4.29) would be:

$$w_{jkl} = \frac{(1/r_{1,j})^2 (1/r_{2,j})^2}{\left\langle (1/r_{1,j})^2 (1/r_{2,j})^2 \right\rangle_{S_{jkl}}} \quad (4.30)$$

where  $\left\langle (1/r_{1,j})^2 (1/r_{2,j})^2 \right\rangle_{S_{jkl}}$  is the average value of  $(1/r_{1,j})^2 (1/r_{2,j})^2$  on the surface  $S_{jkl}$ .

Note that this definition (that may be considered as inspired in Eq. (3.8)) is very convenient since an analytical expression will be written for the average value. Note also that Eq. (4.30) makes the weights only depend on the time  $T_{jkl}$  and the position of the  $j$ th block, the  $l$ th seismograph and the  $k$ th hypocenter. This is a quite important point in order to perform a very fast calculation. We will now derive an explicit analytical expression for Eq. (4.30).

We start by writing the average value as a two-dimensional integral:

$$\left\langle (1/r_{1,j})^2 (1/r_{2,j})^2 \right\rangle_{S_{jkl}} = \frac{1}{A_{jkl}} \int_{S_{jkl}} (1/r_{1,j})^2 (1/r_{2,j})^2 dS \quad (4.31)$$

where  $A_{jkl}$  is the area of  $S_{jkl}$ . This integral is analogous to the one solved in section 2.4.1. Using the same spheroidal coordinates and taking into account that  $r$  is the distance

between the two centres (hypocenter and station) and that we must use  $T_{jkl}$  instead of  $t$  in Eq. (2.10) we may rewrite the integral in Eq. (4.31) as:

$$\left\langle \left( \frac{1}{r_{i,j}} \right)^2 + \left( \frac{1}{r_{i,j}} \right)^2 \right\rangle_{S_{jkl}} = \frac{1}{A_{jkl}} \frac{2}{r^2} \int_0^{2\pi} \int_{-1}^1 \frac{1}{(\xi_1^2 - \xi_2^2)} d\xi_2 d\xi_3 \quad (4.32)$$

Solving it we obtain:

$$\int_{S_{jkl}} \left( \frac{1}{r_{1,j}} \right)^2 \left( \frac{1}{r_{2,j}} \right)^2 dS = \frac{4\pi}{rvT_{jkl}} \cdot \ln \left( \frac{vT_{jkl} + r}{vT_{jkl} - r} \right) \quad (4.33)$$

We need now to write a expression for the area of the spheroidal shell  $S_{jkl}$ . There are two types of spheroidal shells, prolate spheroidal shells and oblate spheroidal shells, as can be seen in Figure 4-14. The corresponding equation for both types of spheroids is the same one:

$$\frac{x^2}{a^2} + \frac{y^2}{b^2} + \frac{z^2}{b^2} = 1 \quad (4.34)$$

where  $a$  and  $b$  are the length of the semi-axis. For the prolate spheroid ( $a > b$ ) and looks like a rugby ball and for the oblate spheroid ( $a < b$ ) and can resemble a disk. Although the equation describing both spheroids is the same one, the expression for the area of the corresponding surface is different and care should be taken choosing the right one. We are interested in the area of the prolate spheroidal shell. It can be written as:

$$A = 2\pi a^2 + \frac{2\pi ab}{\varepsilon} \arcsin \varepsilon \quad (4.35)$$

where  $a$  and  $b$  are the major and minor semiaxes and  $\varepsilon$  is the eccentricity of the spheroidal shell and can be written as:

$$\varepsilon = \frac{\sqrt{b^2 - a^2}}{b} \quad (4.36)$$

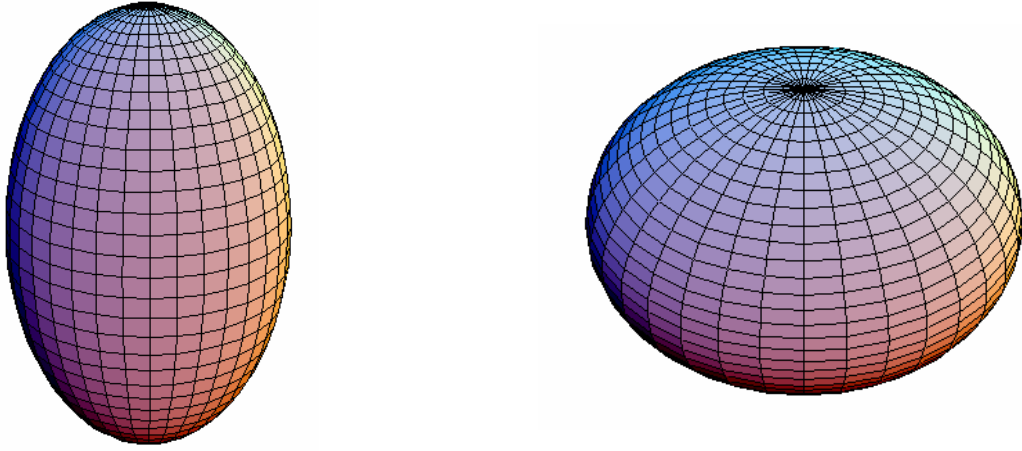


**Figure 4-14.** Prolate spheroid (left) and oblate spheroid (right) [58].

Taking into account the following identities:

$$\begin{aligned}
 a &= \frac{vT_{jkl}}{2} \\
 b &= \left(\frac{vT_{jkl}}{2}\right)^2 - \left(\frac{r}{2}\right)^2
 \end{aligned}
 \tag{4.37}$$

and using them in Eq.(4.36) we obtain:

$$\varepsilon = \frac{r}{vT_{jkl}}
 \tag{4.38}$$

Combining Eqs. (4.37) and (4.38) in Eq. (4.35) we may then write:

$$A_{jkl} = \frac{\pi}{2} \left( v^2 T_{jkl}^2 - r^2 + v^2 T_{jkl}^2 \frac{\sqrt{1 - (r/vT_{jkl})^2}}{r/vT_{jkl}} \arcsin(r/vT_{jkl}) \right)
 \tag{4.39}$$

And by using Eq. (4.39) in Eq.(4.30), we finally obtain the expression we were looking for:

$$w_{jkl} = \frac{rvT_{jkl}}{8(r_{1,j}r_{2,j})^2} \frac{\left( v^2T_{jkl}^2 - r^2 + v^2T_{jkl}^2 \frac{\sqrt{1 - (r/vT_{jkl})^2}}{r/vT_{jkl}} \arcsin(r/vT_{jkl}) \right)}{\ln\left( \frac{vT_{jkl} + r}{vT_{jkl} - r} \right)} \quad (4.40)$$

Note that this expression depends only on  $v$ ,  $T_{jkl}$ ,  $r$  (distance between hypocenter and seismometer) and  $r_{1,j}$  and  $r_{2,j}$ .

## **5 SPATIAL DISTRIBUTION OF SCATTERERS IN THE CRUST OF GAURIBIDANUR SEISMIC ARRAY REGION (SOUTHERN INDIA)**

### **5.1 INTRODUCTION**

The three-dimensional spatial distribution of relative scattering coefficients in southern India is going to be estimated by means of an inversion technique applied to coda wave envelopes. The inversion technique implies mainly two steps. First we will follow the development outlined in Chapter 3. In this chapter we showed that to carry out the inversion it is necessary to solve a system of linear equations where the independent coefficients are the energy residuals computed from the seismograms, the unknowns correspond to the scattering coefficients in a certain small volume of the region under study, and the coefficients of each unknown indicate the importance of each small volume in the computation of a certain residual. This system of equations is huge and the number of unknowns and the number of equations is of the order of  $10^5$ .

There are several methods to invert such a system. Some of them are outlined in Chapter 4. For the first time in this kind of seismological research we will solve the system of equations by means of the Simultaneous Iterative Reconstruction Technique (SIRT) and Filtered Back-Projection method (FBP). Both algorithms are commonly used in biomedical applications but they have not been used previously to find spatial distribution of relative scattering coefficients.

SIRT algorithm has been previously described in section 4.3. SIRT allows to obtain more exact solutions than ART but it is slower. The Filtered Backprojection method was described in section 4.4 and its use to seismology was developed in section 4.5. It was shown to be much faster than any other non-iterative algorithm because each scattering coefficient can be simply computed as a weighted average of certain number of residuals. Filtered Backprojection has proved to provide very accurate reconstructions in biomedical applications and we will show that this is also valid in seismological applications.

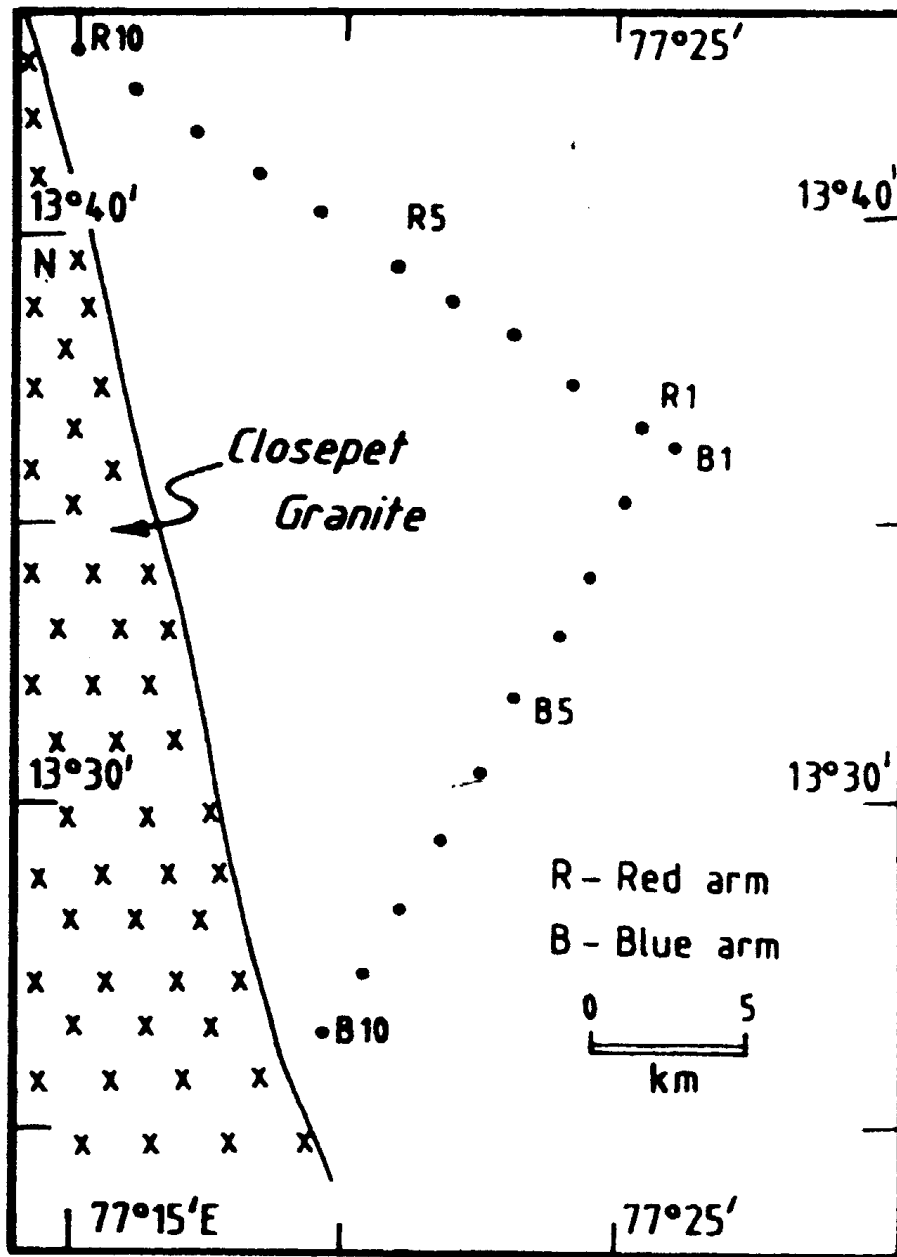
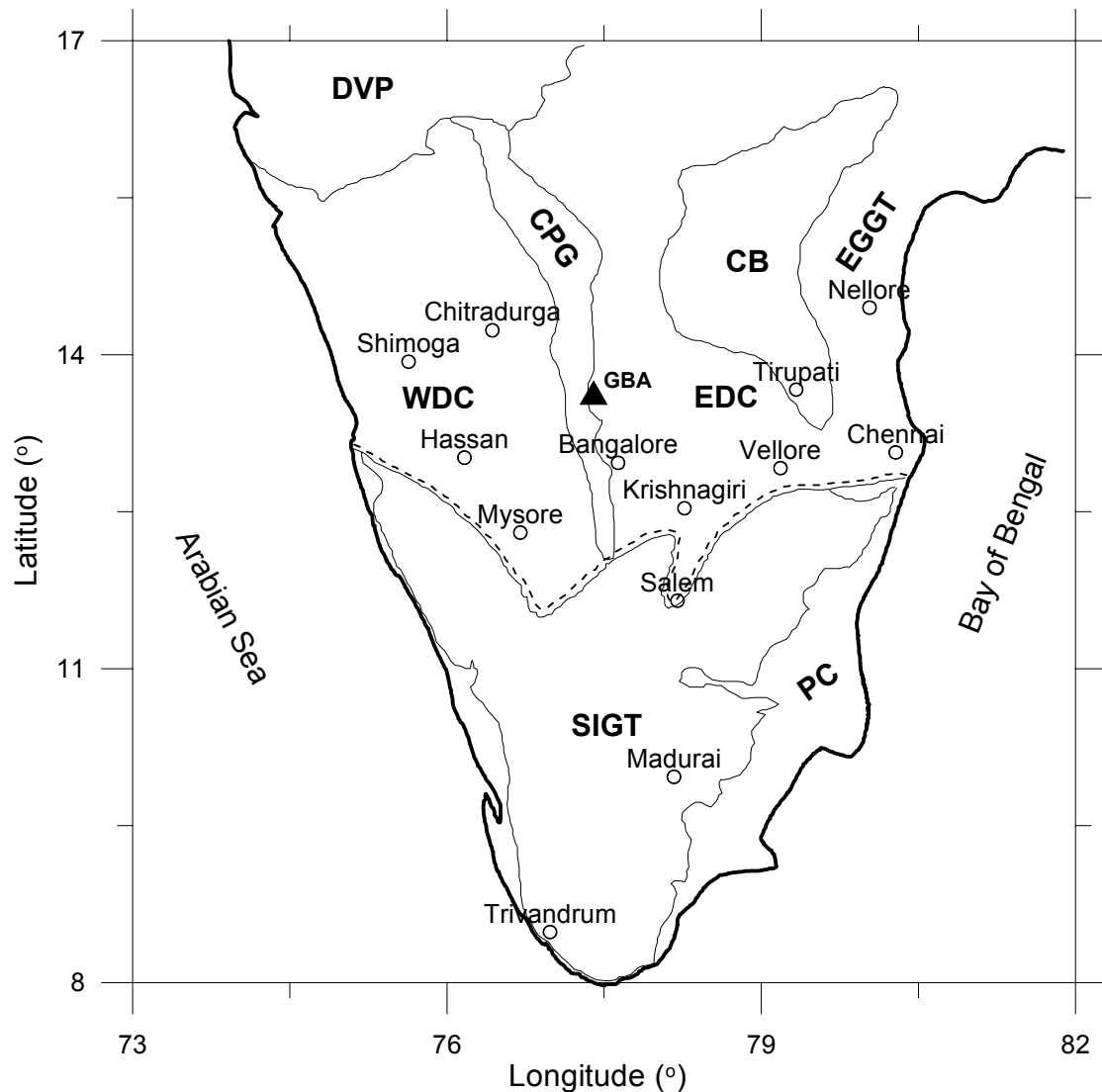


Figure 5-1. Geometry and location of stations of Gauribidanur seismic array [58].

## 5.2 GEOLOGICAL SETTING

The Gauribidanur seismic array is located in the Indian peninsula, about 90 km north of Bangalore, on the western flank of the eastern Dharwar craton which is one of the oldest geological provinces in southern India as sketched in Figure 5-2. The region, as can be

seen in Figure 5-3, is divided into the western (which is composed of old gneisses and greenstones with very few granites) and eastern (which is made of younger rocks with widespread N-S elongate plutons of late Archean granites) parts by the 400 km long and 20-30 km wide, north-south trending granitic intrusion named Closepet batholith (Moyen et al., 2003, [59]). We are going now to describe with a certain detail the main characteristics of the Dhawar Craton and the Closepet Batholith.



**Figure 5-2.** General geological sketch map of southern India. DVP, Deccan volcanic province; WDC, western Dharwar craton; EDC, eastern Dharwar craton; SIGT, south Indian granulite terrain; EGGT, eastern Ghat granulite terrain; CPG, closepet granite; CB, Cuddapah basin; PC, Phanerozoic sedimentary cover. Dotted line indicates Fermor's line (boundary between Dharwar craton and south India granulite terrain). (From Tripathi and Ugalde, 2004, [60]).

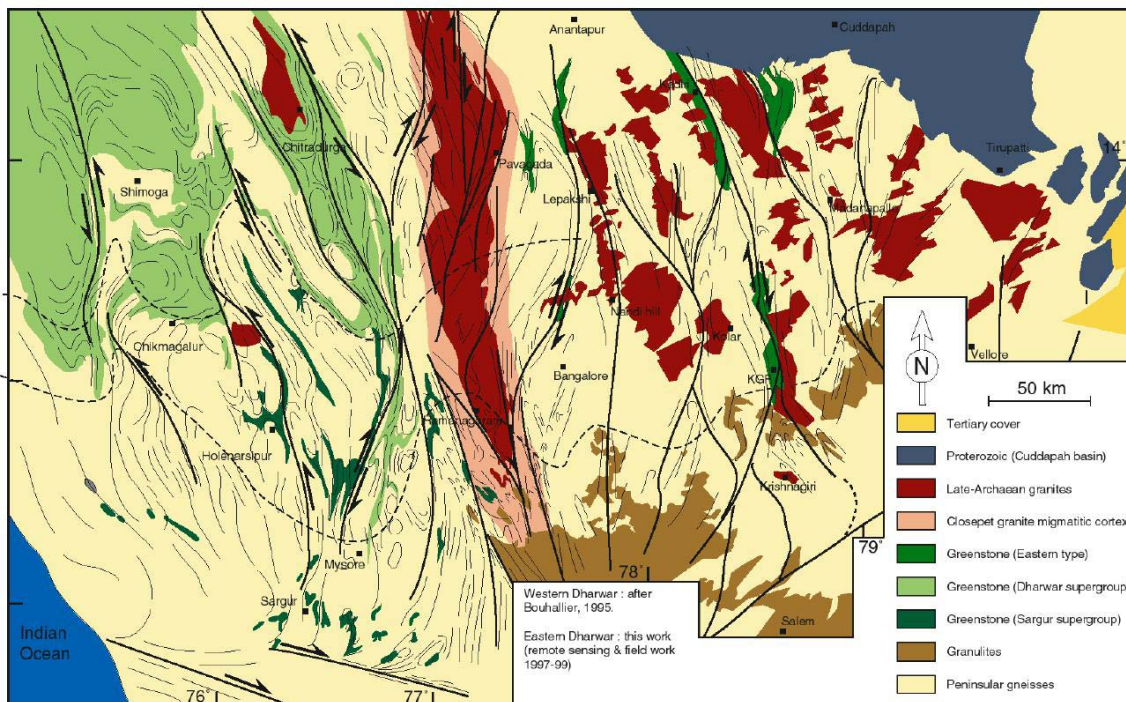


**Figure 5-3.** Detailed geological map corresponding to the eastern and western Dharwar craton and the Closepet granite batholith [61].

### 5.2.1 CLOSEPET GRANITE BATHOLIT

A batholith is a large emplacement of igneous intrusive (also called plutonic) rock that forms from cooled magma deep in the earth's crust. Igneous rocks are formed when magma cools and solidifies, with or without crystallization, either below the surface as intrusive (plutonic) rocks or on the surface as extrusive (volcanic) rocks. This magma can be derived from either the Earth's mantle or pre-existing rocks made molten by extreme temperature and pressure changes. The word "igneous" is derived from the Latin ignis, meaning "fire". Batholiths are almost always made mostly of felsic (silicate minerals or rocks) such as granite.

Although they may appear uniform, batholiths are in fact structures with complex histories and compositions. They are composed of multiple masses, or plutons, of magma that travelled toward the surface from a zone of partial melting at the base of the earth's crust. While moving, these plutons of relatively buoyant magma are called plutonic diapirs. Because the diapirs are liquefied and very hot, they tend to rise through the surrounding country rock, pushing it aside and partially melting it. Most diapirs do

not reach the surface to form volcanoes, but instead slow down, cool and usually solidify 5 to 30 kilometres underground as plutons (hence the use of the word pluton; in reference to the Roman god of the underworld Pluto).

A batholith is formed when many plutons converge together to form a huge expanse of granitic rock. Some batholiths are found paralleling past and present subduction zones and other heat sources for hundreds of kilometres in continental crust. An example of batholith, found predominantly in the mountains of western Canada, extends for 1,800 kilometres and reaches into south-eastern Alaska.

The word batholith is used by geographers to mean an exposed area of mostly continuous plutonic rock that covers an area larger than 100 square kilometres. However, the majority of batholiths visible at the surface (via outcroppings) have areas far greater than 100 square kilometres. These areas are exposed to the surface through the process of erosion accelerated by continental uplift acting over many tens of millions to hundreds of millions of years. This process has removed several tens of kilometres of overlying rock in many areas, exposing the once deeply buried batholiths.

Batholiths exposed at the surface are also subjected to huge pressure differences between their former homes deep in the earth and their new homes at or near the surface. As a result, their crystal structure expands slightly and over time. This manifests itself by a form of mass wasting called exfoliation. This form of erosion causes convex and relatively thin sheets of rock to slough off the exposed surfaces of batholiths (a process accelerated by frost wedging). The result is fairly clean and rounded rock faces.

The Closepet granite in southern India, is a large (400 km long but only 30km wide) elongate Late Archean granitic body. The Closepet granite was emplaced syntectonically within an active strike-slip shear zone. Structural levels from deep crust to upper levels crop out (see Figure 5-4). Despite local petrographic heterogeneities, a physical continuity of the porphyritic monzogranite can be observed all over the closepet structure. Consequently, the Closepet granite appears as a single magmatic body but different zones may be identified. Differential erosion has exposed it from the lower (25 km) to upper crust (5 km).

Four main parts are recognized from bottom to top (see Figure 5-4):

- i. The root zone is located south of 13°N. In the root zone, magmas were formed, collected and rose within active shear zones. The surrounding crust was highly ductile, leading to diffuse deformation. The root zone consists in a network of small dykes, plugs and sheets of granitoids injected in ductile shear zones and along foliation planes into Peninsular Gneisses. A wide range of magma compositions are found there, from monzonites (SiO<sub>2</sub>= 51%) to granites (SiO<sub>2</sub>= 75 %). It has been demonstrated that all magmatic facies result from magma mixing between a mafic, mantle-derived one, and a felsic one, generated by anatexis (partial melting of rocks, especially in the forming of metamorphic rocks) of the surrounding peninsular Gneisses.
- ii. A transfer zone, where the magma was progressively enriched in K-feldspar phenocrysts during its ascent. In this part, the granite rose as a mush moving as a whole within a less ductile crust. Slow cooling was responsible for a long magma residence time under conditions favouring to fabric enhancement and strain partitioning, leading to horizontal and vertical melt migration. There, a single, continuous mass (150 x 30 km) of porphyritic monzogranite (SiO<sub>2</sub>= 65-70 %) intrudes the gneissic basement. The monzogranite results from magma mixing recognized in the root zone. In some narrow areas, corresponding to high strain zones on its margins, the Closepet granite is rich in enclaves of cumulate, mafic magmatic facies similar to those observed in the root zone. All these enclaves were carried upwards from deeper crustal levels. The same areas also commonly show K-feldspar phenocrysts accumulations.
- iii. A "gap" (dyke complex that acted as a filter zone), where the ascent of the mush was stopped, probably due to high phenocryst load and high viscosity contrast with the wall rocks. Only crystal-poor melts could continue their ascent through the dykes. The ascent of the mush is stopped at a level corresponding to the gap. At this level, only crystal-poor liquids are able to rise through a network of dykes, leaving below most crystals, and enclaves of all kinds.

- iv. A zone of shallow intrusions, where the liquids extracted from the mush filled small, elliptical plutons, cooling quickly and developing only very weak fabrics. The Closepet granite appears as a suite of small (commonly 10-30 km long), elliptical plutons crosscutting an gneissic basement. Individual intrusions display mutually cross-cutting relationships. In this area, only homogeneous, enclave-free granites ( $\text{SiO}_2 = 70-75\%$ ) are found, at the exclusion of less differentiated facies. Porphyritic facies are rare, in marked contrast to the lower levels, where these facies are ubiquitous.

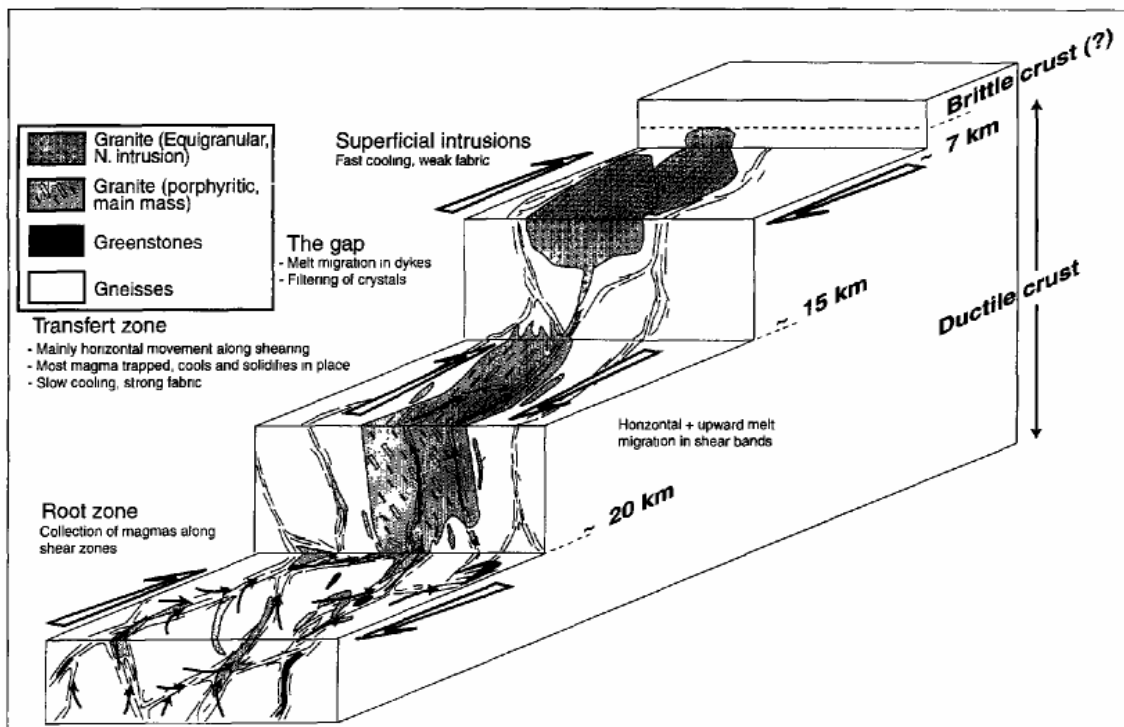


**Figure 5-4.** Sketch drawing of the emplacement mode and strain partitioning in the Closepet granite at contrasted structural levels (Moyen, 2000). Black, thin arrows correspond to melt movement. White, large arrows: kinematics of deformation. Notice three different zones may be defined along the batholith [59].

## 5.2.2 GENERAL CHARACTERISTICS OF CRATONS. THE DHAWAR CRATON

The continental crust is the layer of granitic, sedimentary and metamorphic rocks which form the continents and the areas of shallow seabed close to their shores, known as continental shelves. It is less dense than the material of the Earth's mantle and thus "floats" on top of it. Continental crust is also less dense than oceanic crust, though it

is considerably thicker; 20 to 80 km versus the average oceanic thickness of around 5-10 km. About 40% of the Earth's surface is now underlain by continental crust.

As a consequence of the density difference, when active margins of continental crust meet oceanic crust in subduction zones, the oceanic crust is typically subducted back into the mantle. Because of its relative low density, continental crust is only rarely subducted or re-cycled back into the mantle (for instance, where continental crustal blocks collide and overthicken, causing deep melting). For this reason the oldest rocks on Earth are within the cratons or cores of the continents, rather than in repeatedly recycled oceanic crust; the oldest continental rock is the Acasta Gneiss at 4.01 Ga, while the oldest oceanic crust is of Jurassic age.

A craton is then an old and stable part of the continental crust that has survived the merging and splitting of continents and supercontinents for at least 500 million years. Cratons are generally found in the interiors of continents and are formed of a crust of lightweight felsic igneous rock such as granite attached to a section of the upper mantle. A craton may extend to depth of 200 km.

Cratons are subdivided geographically into geologic provinces, each province being classified as an Archon, a Proton or a Tecton according to its age: Archons: consist of rocks from the Archean era, older than 2.5 billion years (2.5 Ga). Protons: consist of rocks from the early to middle Proterozoic era, older than 1.6 Ga. Tectons: consist of rocks from the late Proterozoic era, with ages between 1.6 Ga and 800 million years (800 Ma). The Dhawar Craton belongs to the Archean era (3.5-2.6 Ga).

As minerals (such as precious metals and diamonds) in the earth's crust tend to become separated with time, the oldest cratons are of the greatest interest to mining companies. This also applies to the Dhawar Craton; actually, mostly, our data comes from chemical explosions in mines).

The Dhawar craton is classically divided into three litological units:

- i. A gneissic basement of peninsular gneisses dated between 3.3 and 2.7 Ga. Gneiss is a common and widely distributed type of rock formed by high grade regional metamorphic processes from pre-existing formations that were originally either igneous or sedimentary rocks. Gneissic rocks are coarsely

foliated (typically by compositional banding due to segregation of mineral phases) and largely recrystallized. Gneisses that are metamorphosed igneous rocks or their equivalent are termed granite gneisses, granodiorite gneisses, etc. The word "gneiss" is from an old Saxon mining term that seems to have meant decayed, rotten, or possibly worthless material.

- ii. Greenstone belts overlying the gneisses, dated between 3.3 and 3.1 Ga for the oldest ones, and between 3.2 and 2.7 Ga for the younger ones. Greenstone is a non layered metamorphic rock derived from basalt or similar rocks containing sodium-rich plagioclase feldspar ( $\text{NaAlSi}_3\text{O}_8$  (Albite)-  $\text{CaAl}_2\text{Si}_2\text{O}_8$  (Anorthite)), chlorite ( $(\text{Mg,Fe})_3(\text{Si,Al})_4\text{O}_{10}(\text{OH})_2 \cdot (\text{Mg,Fe})_3(\text{OH})_6$ ), epidote ( $\text{Ca}_2(\text{Al,Fe})_3(\text{SiO}_4)_3(\text{OH})$ ) and quartz. Chlorite and epidote give the green colour.
- iii. Late Archean K-rich granitoids, consisting of N-S elongate bodies, among which the Closepet granite is the most spectacular. Several of these granites have been dated in the range 2.5 -2.6 Ga. Granite is a common and widely-occurring type of intrusive felsic igneous rock. Granites are usually a white or buff colour (a pale, light, or moderate yellowish pink to yellow) and are medium to coarse grained, occasionally with some individual crystals larger than the groundmass forming a rock known as porphyry. Granites can be pink to dark grey or even black, depending on their chemistry and mineralogy. Outcrops of granite tend to form tors (large hill, usually topped with rocks), rounded massifs, and terrains of rounded boulders (large rounded masses of rock lying on the surface of the ground or embedded in the soil) cropping out of flat, sandy soils.

The Dhawar craton is subdivided into western and eastern parts. The western Dhawar craton is made of 3.0-3.3 Ga old gneisses and greenstones, with very few 2.5 Ga granites; on the other hand, the eastern Dhawar Craton is made of younger (2.7-3.0 Ga) rocks with widespread elongate plutons of Late Archean granites. The Closepet granite represents the boundary between the two parts.

### **5.2.3 CHARACTERISTICS OF GAURIBIDANUR ARRAY'S SURROUNDING REGION**

The area around the array is relatively flat (average elevation about 750 m), with a few hill ranges towards the east and the south. The rocks beneath the array are gneisses

and granites of Archean age. A thin layer of soil varying in thickness from 1.5 m to 4.5 m covers the siting area. Thus, the topographic influence on scattering would be very small. A crustal model consisting of a 16 km thick top granitic layer over a second layer 19 km thick above the mantle (i.e. with the Moho at 35 km depth) was proposed by Arora (1971) [62]. (Table 5-1).

### 5.3 DATA DESCRIPTION

Waveform data used consisted of selected 636 vertical-component, short period recordings of microearthquake codas from shallow earthquakes recorded by the Gauribidanur seismic array (GBA). They were selected from 80 earthquakes with epicentral distances up to 120 km which were recorded by the GBA in the period January 1992 to December, 1995. GBA is a seismic array that was sponsored by the U.K. Atomic Energy Authority (UKAEA) in the early sixties with the cooperation of the Bhabha Atomic Research Centre (BARC), Government of India. The array is L-shaped and each arm contains ten short-period ( $T_0=1$  s) vertical-component Wilmore MkII seismometers spaced at intervals of about 2.5 km. The output of each instrument is carried by a telemetry system to a central laboratory where it is digitized at a sampling interval of 0.05 s and it is recorded in analog form on a 24-channel FM magnetic tape. All the events are shallow (depths less than 10 km) and local magnitudes range between 0.3 and 3.7 (see Figure 5.5).

### 5.4 DATA ANALYSIS

Each seismogram was bandpass-filtered over the frequency bands 1-2 ( $1.5\pm 0.5$ ) Hz, 2-4 ( $3\pm 1$ ) Hz and 4-10 ( $7\pm 3$ ) Hz. Then, the rms amplitudes  $A_{\text{obs}}(f|r,t)$  were calculated by using a 0.25 s spaced moving time window of length  $t\pm 2$  s,  $t\pm 1$  s, and  $t\pm 0.5$  s for the first, second and third frequency band, respectively. The time interval for the analysis started at 1.5 times the S-wave travel times (in order to increase the resolution near the source region) and had a maximum length of 20 s (to minimize the effects of multiple scattering). The rms amplitudes for a noise window of 10 s before the P-wave arrival were also computed and only the amplitudes greater than two times

the signal to noise ratio were kept. The amplitudes were then corrected for geometrical spreading by multiplying by  $t^2$  which is valid for body waves in a uniform medium. Then, the average decay curve was estimated for each seismogram by means of a least-squares regression of  $\ln[t^2 A_{\text{obs}}(f|r,t)]$  vs.  $t$  and only the estimates with a correlation coefficient greater than 0.60 were kept. The observed coda residuals  $e(t)$  were then calculated by taking the ratio of the corrected observed amplitudes to the estimated exponential decay curve. Finally the residuals were averaged in time windows of  $\delta t = 0.5$  s to get  $e_j$  at discrete lapse times  $t_j$ . The decrease of  $\delta t$  increases the spatial resolution, but also the size of the inversion problem.

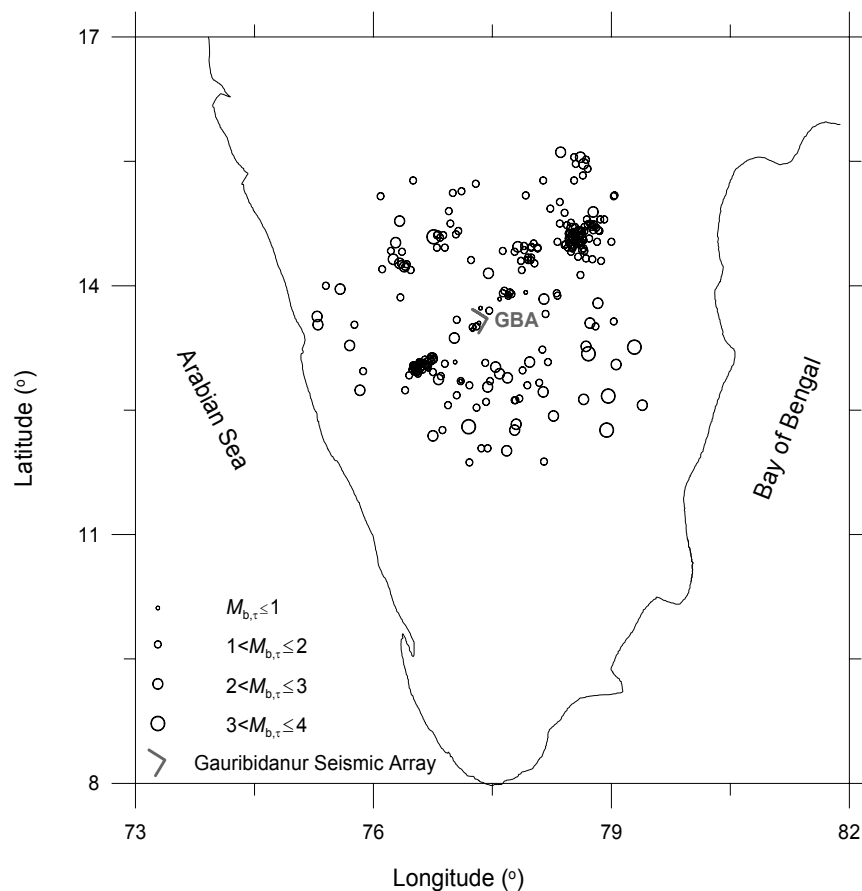


**Figure 5-5.** Map of southern India showing the location of the seismic stations and earthquakes used for the analysis [60].

The time window for the averaging must also satisfy the condition  $\delta t \leq 2(\delta V)^{1/3} / \beta$ , where  $\delta V$  is the volume of one small block into which the study area is divided and  $\beta=3.65 \text{ km}\cdot\text{s}^{-1}$  in this region (Arora, 1971, [62]; Krishna & Ramesh, 2000, [63]). This condition assures that the width of each spheroidal shell is smaller than the size of a block. All this process is illustrated in Figure 5-6 where we show the following: Figure (a) corresponds to a band-pass filtered coda waveform of an earthquake at an epicentral distance of 90.6 km in a region around Gauribidanur array (India). Figure (b) corresponds to the logarithm of the running mean-squared amplitudes corrected for geometrical spreading effect. The discontinuous line is the best linear fitting function to the logarithmic trace. Finally, figure (c) corresponds to the logarithm of the coda energy residuals averaged in a time window of 0.5 s.

The corresponding system of equations to solve is (see Chapter 3):

$$\begin{aligned}
 w_{11}\alpha_1 + \dots + w_{i1}\alpha_i + \dots + w_{N1}\alpha_N &= e_1 \\
 &\vdots \\
 w_{1j}\alpha_1 + \dots + w_{ij}\alpha_i + \dots + w_{Nj}\alpha_N &= e_j \\
 &\vdots \\
 w_{1M}\alpha_1 + \dots + w_{iM}\alpha_i + \dots + w_{NM}\alpha_N &= e_M
 \end{aligned} \tag{5.1}$$

In this case, the system has a number of equations  $M \approx 2700$  for the frequency bands centred at 1.5 Hz and 7 Hz, and  $M \approx 5200$  equations for the 3 Hz centre frequency. To write the system, we considered a 155 km x 155 km in horizontal and 80 km in depth study region attending to the stations and hypocenters distribution and it was divided into  $N=50 \times 50 \times 25$  blocks. This means we have  $N=62500$  unknowns in Eq. (5.1). To write the system, it is important also to know the velocity of S waves. Then, the observational system of equations (Eq. (5.1)) was created by assuming the layered velocity structure by Arora (1971, [62]) (see table Table 5-1) and it was solved using the SIRT and FBP algorithms (see Chapter 4).

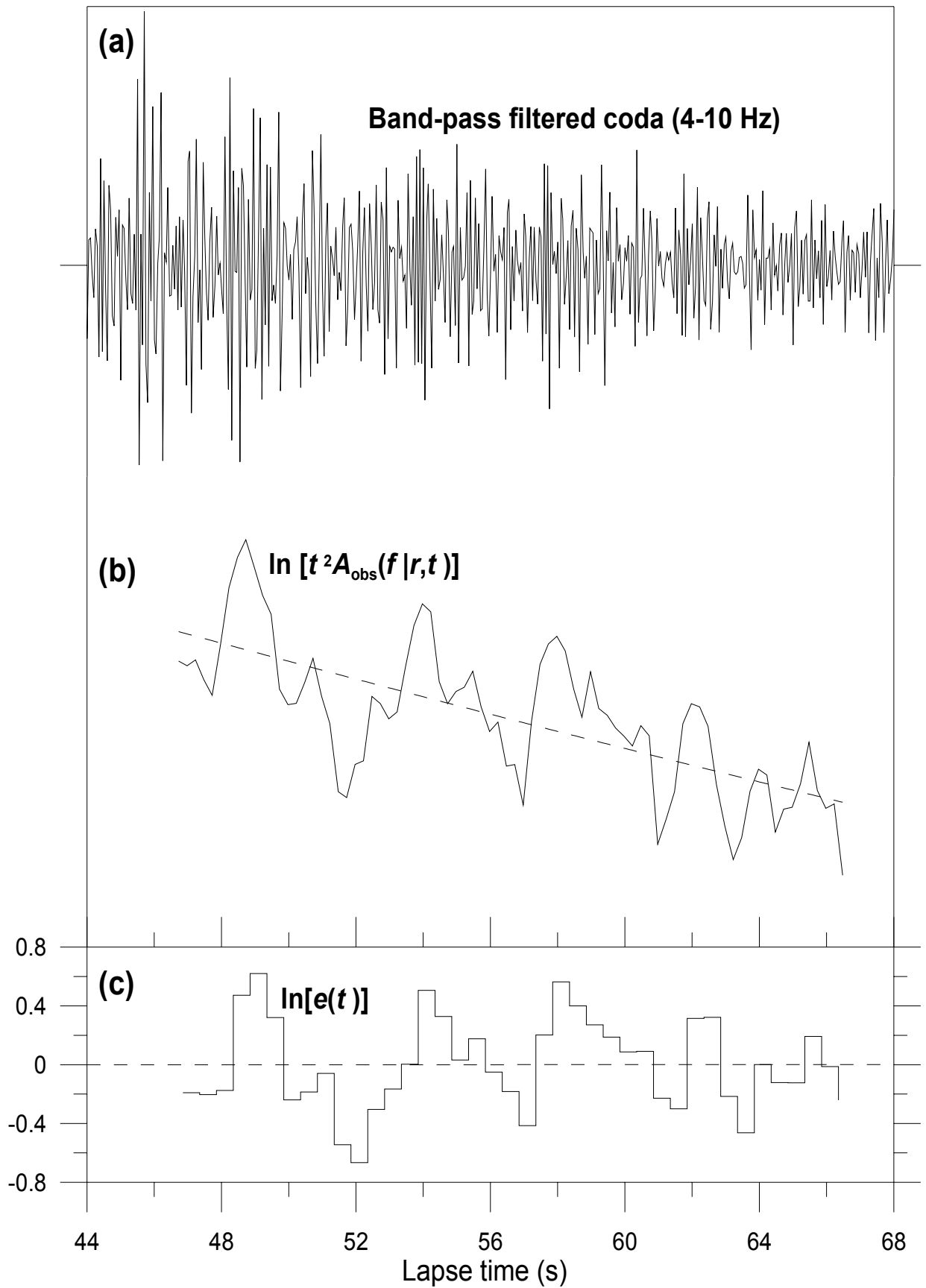


Figure 5-6 Illustrating the process to calculate the coda energy residuals for a GBA seismic event

Depth (km)	S-wave velocity (km/s)
$0 < z < 15.8$	3.46
$15.8 < z < 34.7$	3.96
$z > 34.7$	4.61

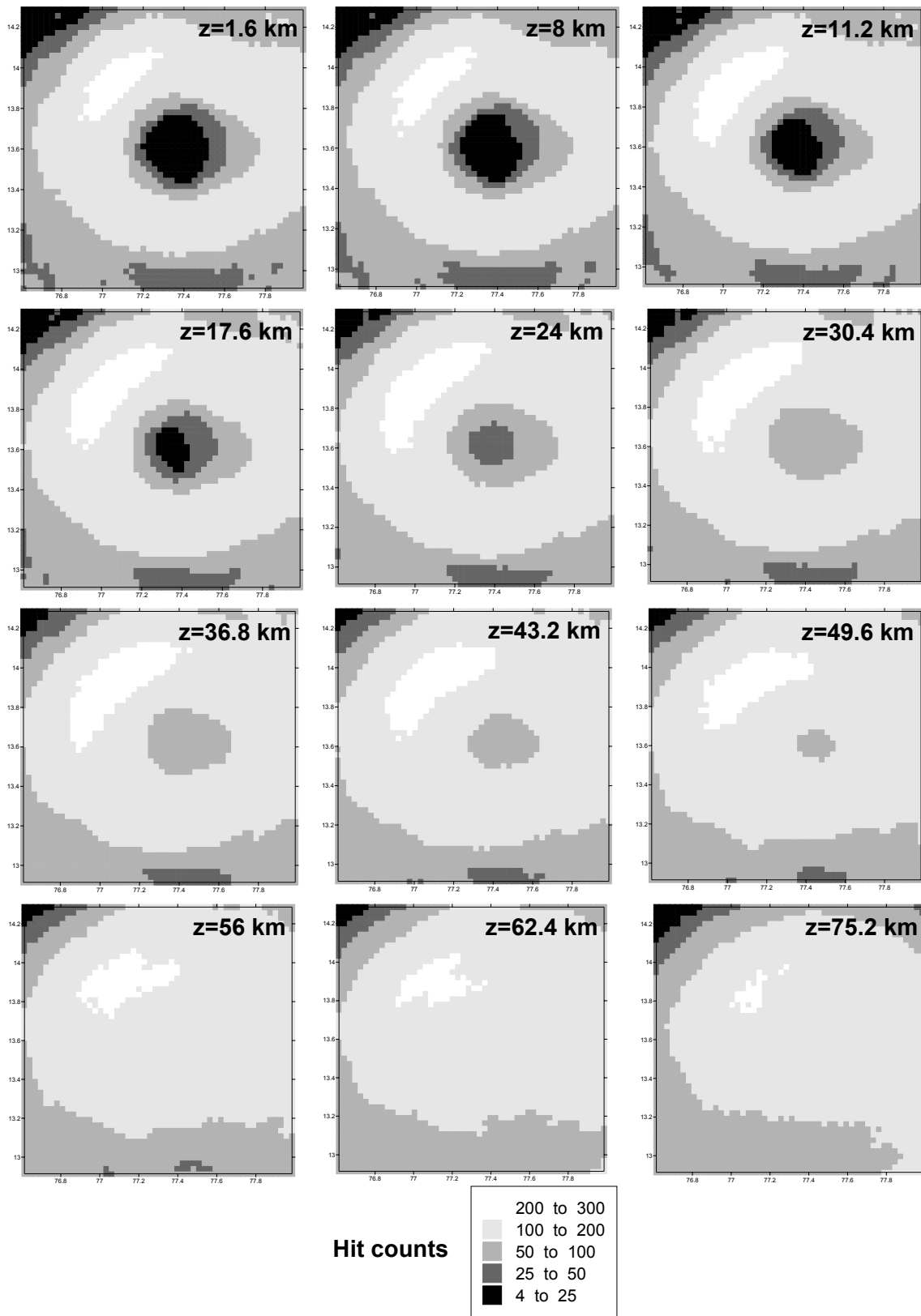
**Table 5-1.** S-wave velocity model for the Gauribidanur region.

## 5.5 RESULTS

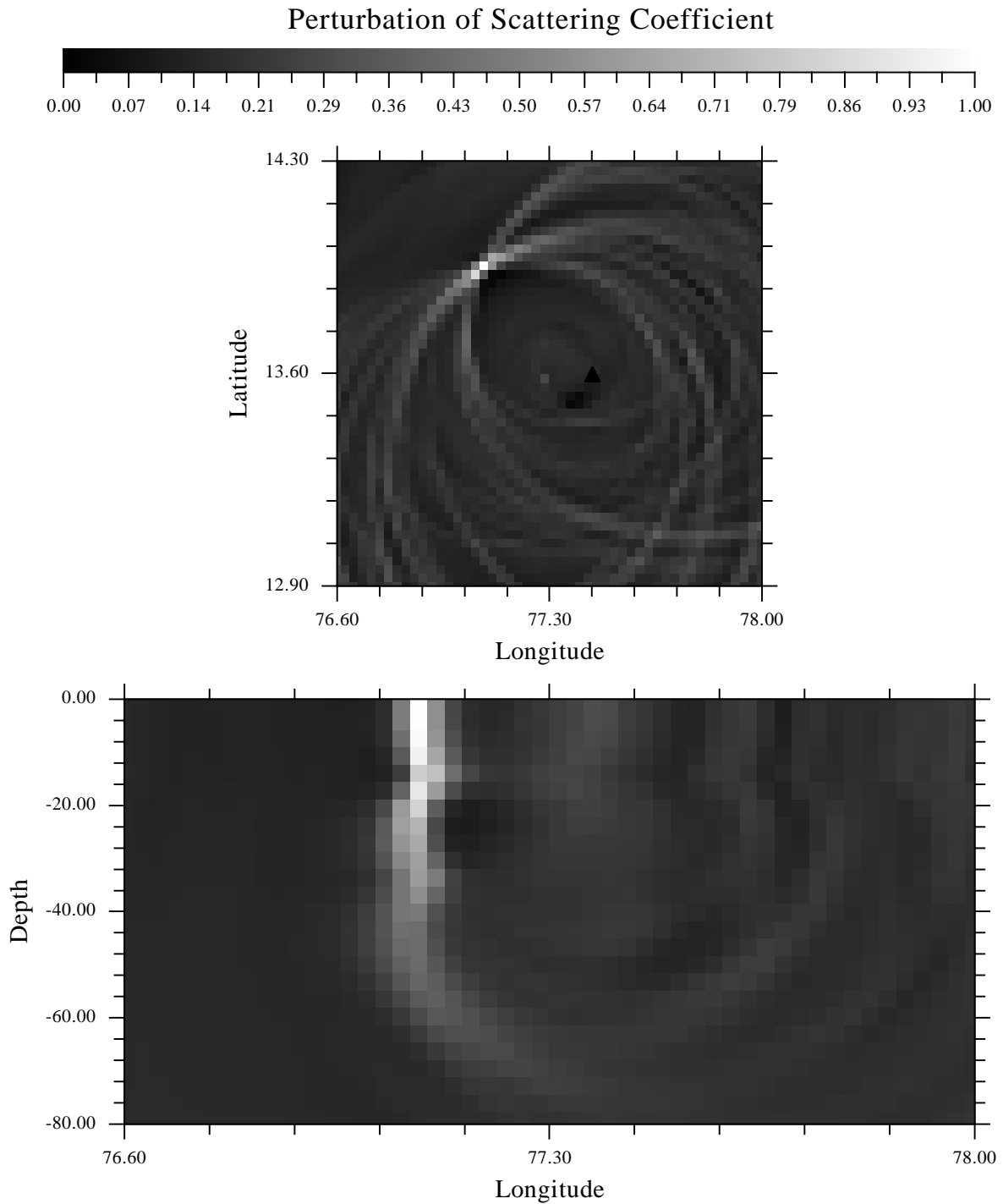
Before discussing the results, we will examine the reliability of the solution. Figure 5-7 plots the hit counts, or number of coda residuals contributed by each block, that shows which grid zones may be affected by sampling insufficiency for the grid defined. It can be observed that the entire region is sampled by the ellipses, however, the hit counts are much less in an area close around the array and they increase both in horizontal and depth directions up to the considered depth of 80 km. This happens because the stations are concentrated in a small area, which makes all the blocks which are close to the array to correspond to short lapse times, and they are few because we omitted the earliest portion of the S-wave coda by adopting  $1.5t_s$  as start time for the analysis.

On the other hand, we tested the resolution of the inversion methods by synthesizing the coda energy residuals from the observational equation using a given test distribution of scattering coefficients and the same distribution of stations and events used in the analysis. We generated vertical structures with positive perturbations of the scattering coefficient with horizontal dimensions equal to one block and depths up to 80 km embedded in a non perturbed medium.

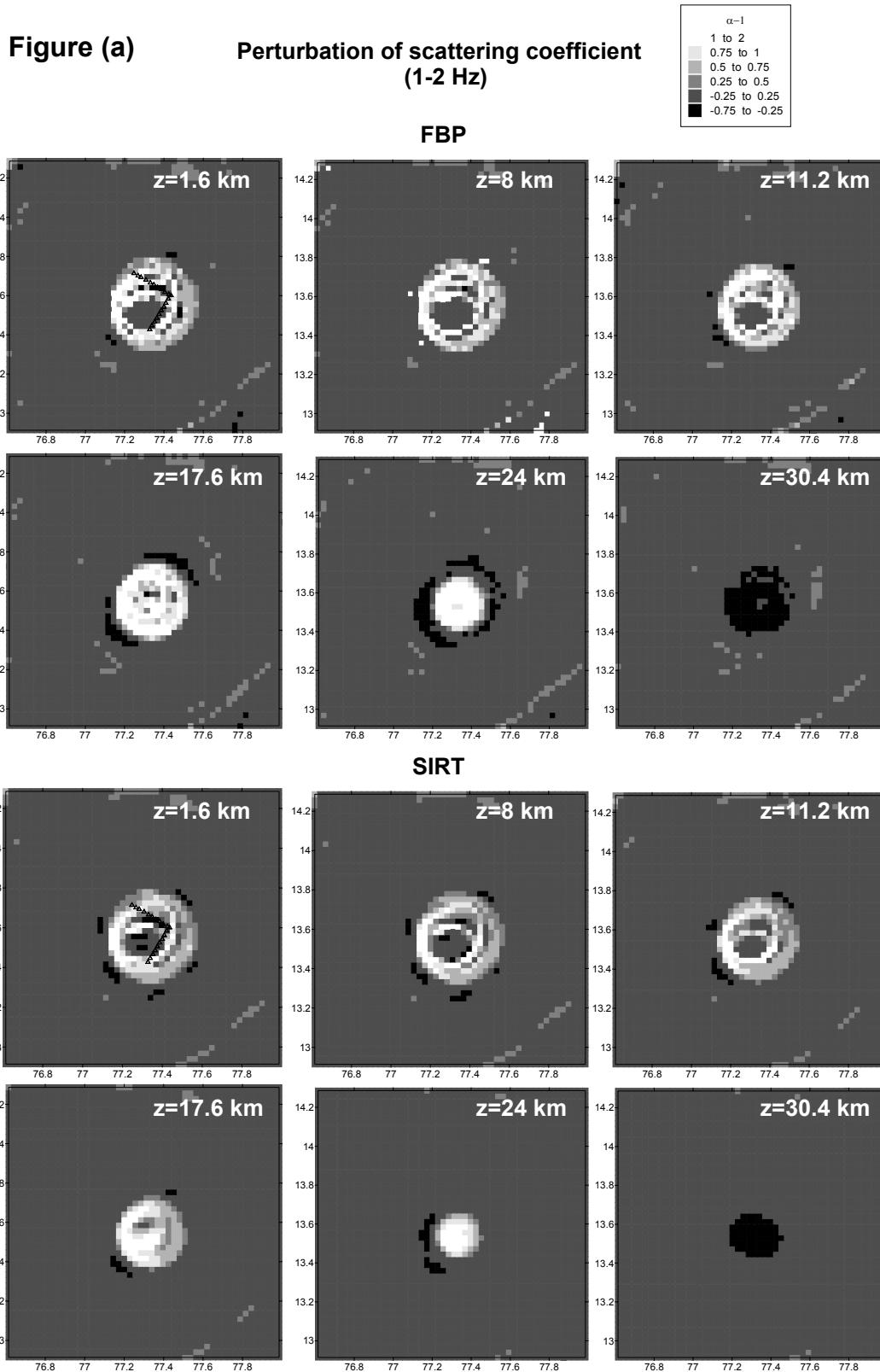
Then the synthesized residuals were inverted. Results show that although the vertical structures are seen almost up to the maximum depth considered of 80 km, they are well reproduced (more than 50% of the perturbation value is returned) only up to the seventh block (22.4 km). The results are shown in Figure 5-8.



**Figure 5-7.** Hit counts or number of coda residuals contributed by each block. It measures the number of times each block is sampled by the scattering shells of observed coda data. The darker areas are the zones lesser sampled by the spherical shells.



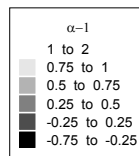
**Figure 5-8.** Spatial distribution of relative scattering coefficients for a synthetic test consisting of a column. It was located northeast from the array centre point, which is shown by a solid triangle. A longitudinal section corresponding to  $z=0$  km and the corresponding transversal section are shown.



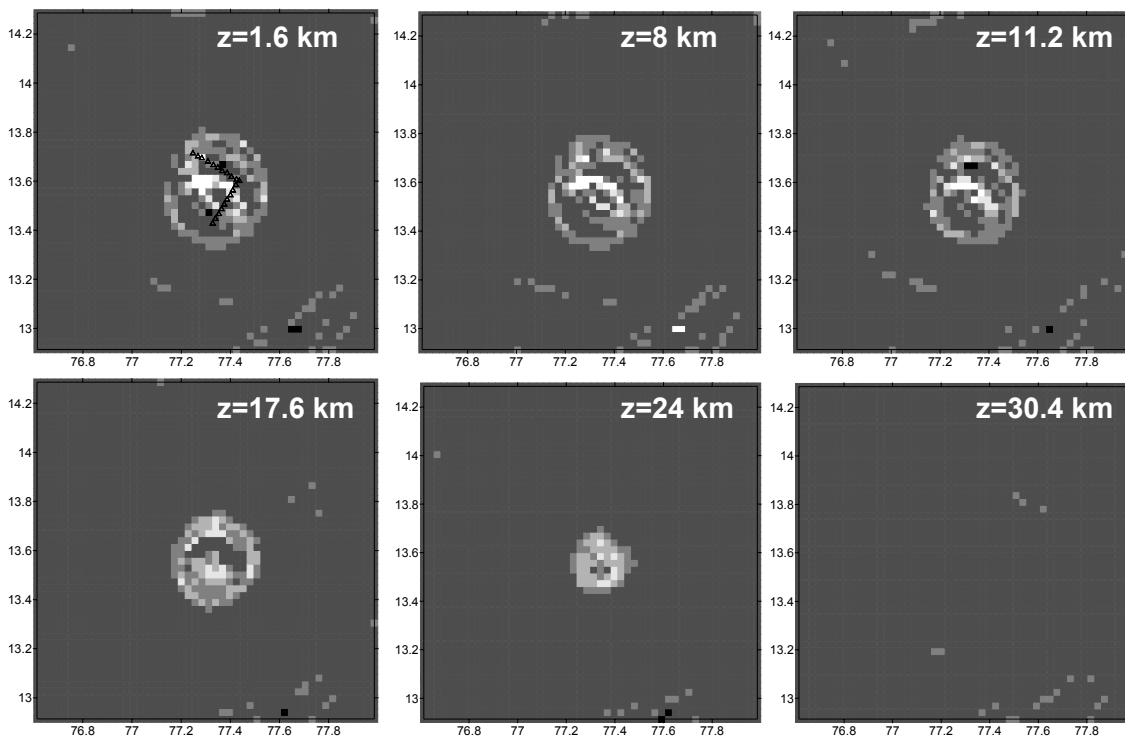
**Figure 5-9.** Spatial distribution of relative scattering coefficients for different depths and for the two inversion methods used: (a) results for the frequency band 1-2 Hz; (b) 2-4 Hz; and (c) 4-10 Hz. The lightest zones indicate the strongest perturbations from an average scattering coefficient.

Figure (b)

Perturbation of scattering coefficient  
(2-4 Hz)



FBP



SIRT

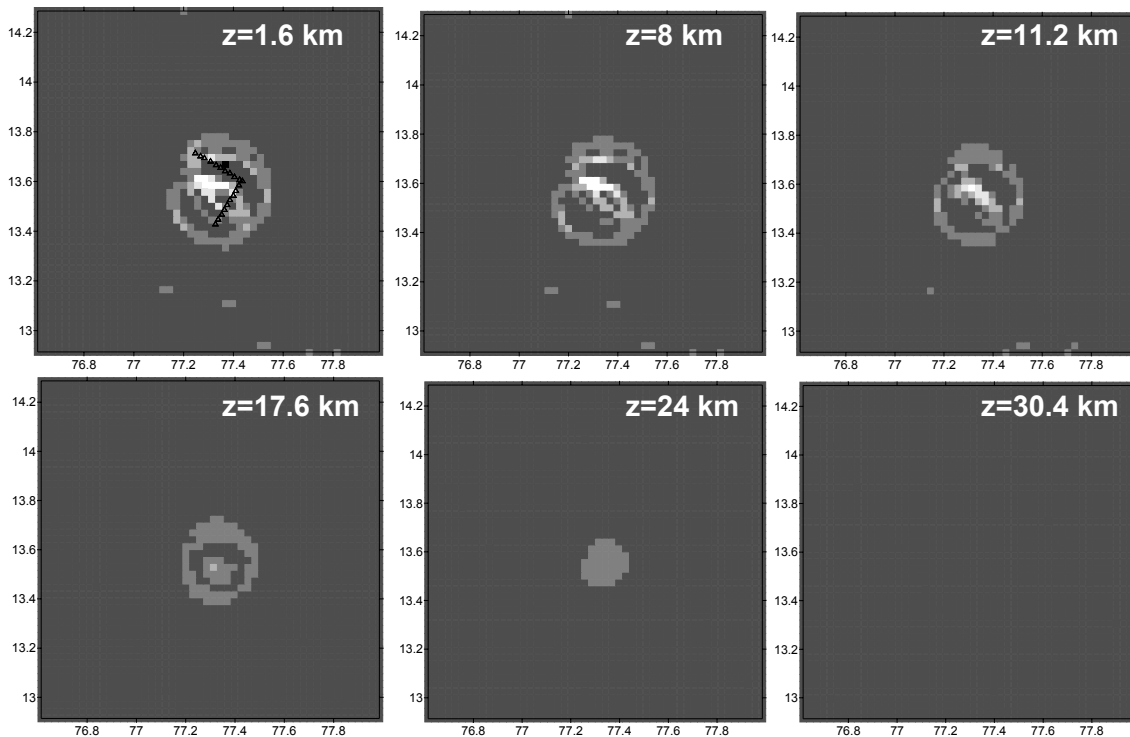
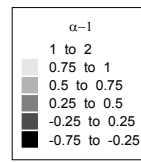


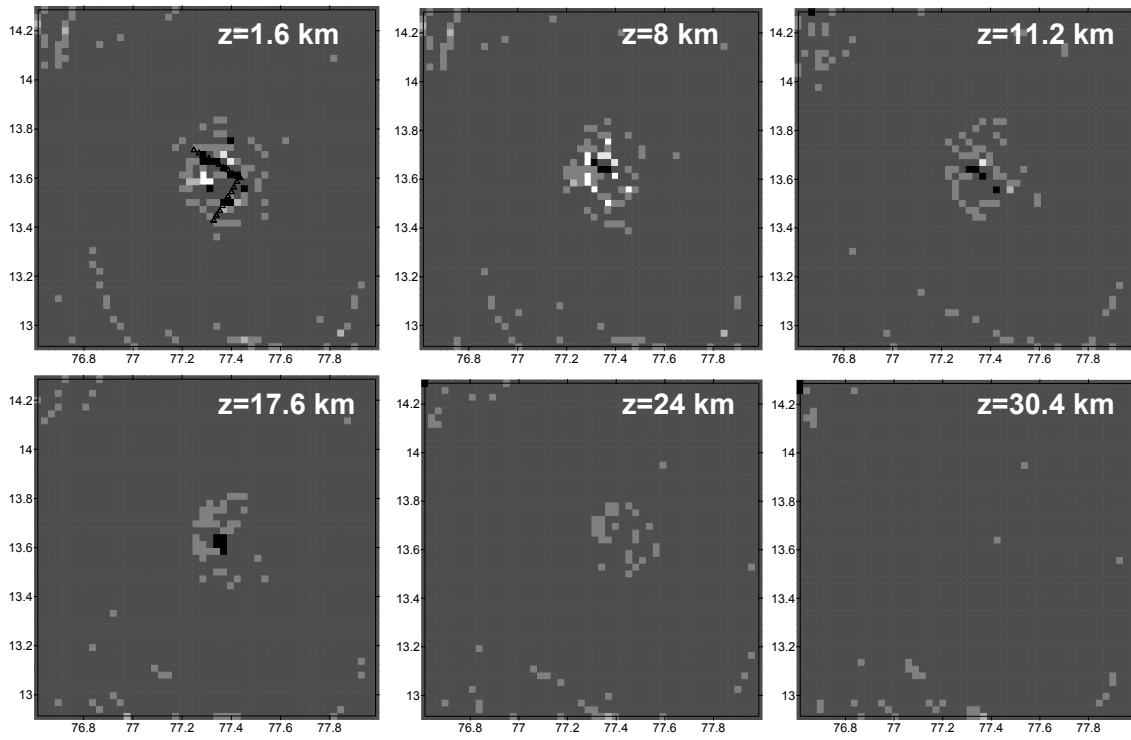
Figure 5-9. (continued)

Figure (c)

Perturbation of scattering coefficient  
(4-10 Hz)



FBP



SIRT

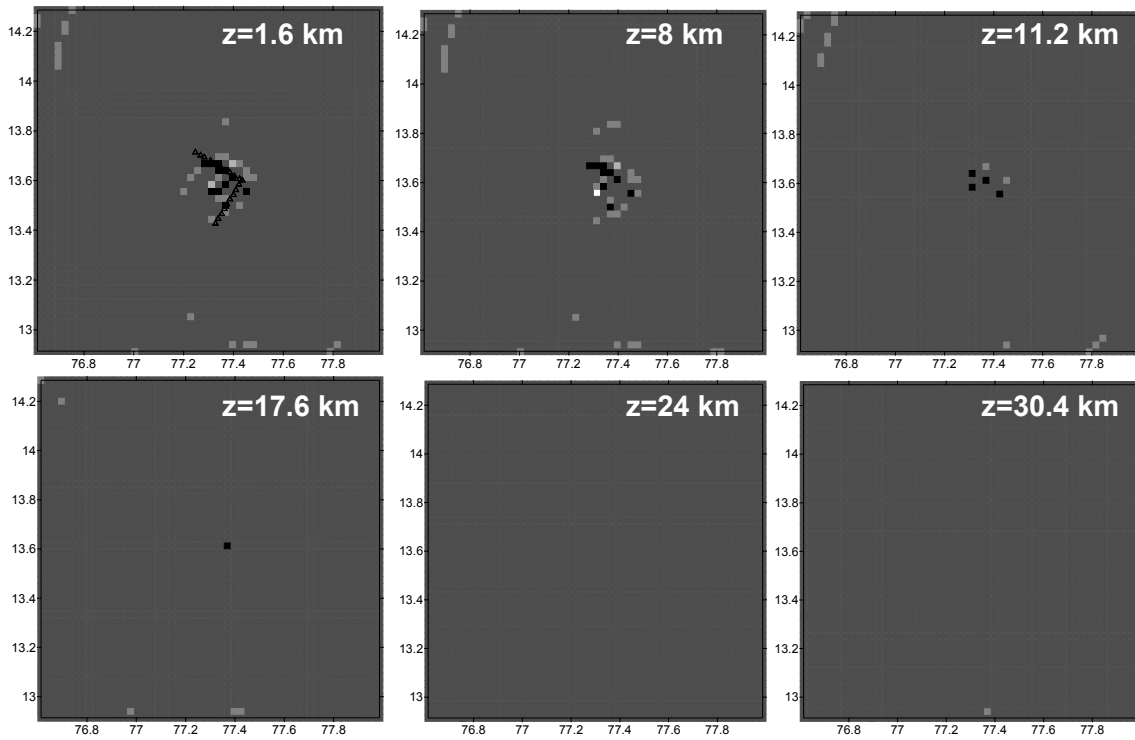


Figure 5-9. (continued)

The resulting distribution of relative scattering coefficients  $\alpha - 1 = \frac{g - g_0}{g_0}$  in the study region for the three analyzed frequency bands and for different depths is plotted in Figure 5-9. The lightest tones indicate scattering coefficients larger than the average in this region.

## 5.6 DISCUSSION

It can be observed that we obtain practically the same distribution of relative scattering coefficients regardless of applying the SIRT or FBP inversion algorithms. Whereas the SIRT algorithm provides slightly lower values of the relative scattering coefficients, the FBP method provides more contrast. Thus, we would recommend the use of the FBP method, which requires much lesser (about 100 times) computation time.

On the other hand, Figure 5-9 shows that more than the 90% of the analyzed region reveals a spatial perturbation of the scattering coefficient between  $\pm 25\%$ . This means that the crust around GBA presents a remarkably uniform distribution of scattering coefficients. For low frequencies, this uniformity is broken by the presence of a strong scattering area which is recognized from the surface up to a depth of 24 km just below the array. This structure is not observed at high frequencies. In fact, each analyzed frequency band is giving us information about inhomogeneous structures with sizes comparable to the seismic wavelengths ( $\sim 1.8$  to  $\sim 3.6$  km for 1-2 Hz,  $\sim 900$  m to  $\sim 1.8$  km for 2-4 Hz, and  $\sim 360$  m to  $\sim 900$  m for 4-10 Hz in this case). Figure 5-10 shows a cross section of relative scattering coefficients shown in Figure 5-9 projected onto the vertical plane defined by the parallel of the array centre point. It can be observed that the strongest scatterers are located on the western part of GBA. However, Figure 5-9 and Figure 5-10 show that the heterogeneity follows an ellipsoidal pattern. This may happen because this area is poorly sampled by the ellipses as previously discussed in Figure 5-7, however, the behaviour is only observed for the lowest frequency band analyzed. In fact, we detected high values of the residuals at low frequencies and short lapse times. In order to establish the validity of the results of this study we tested the inversion method by means of a synthetic test.

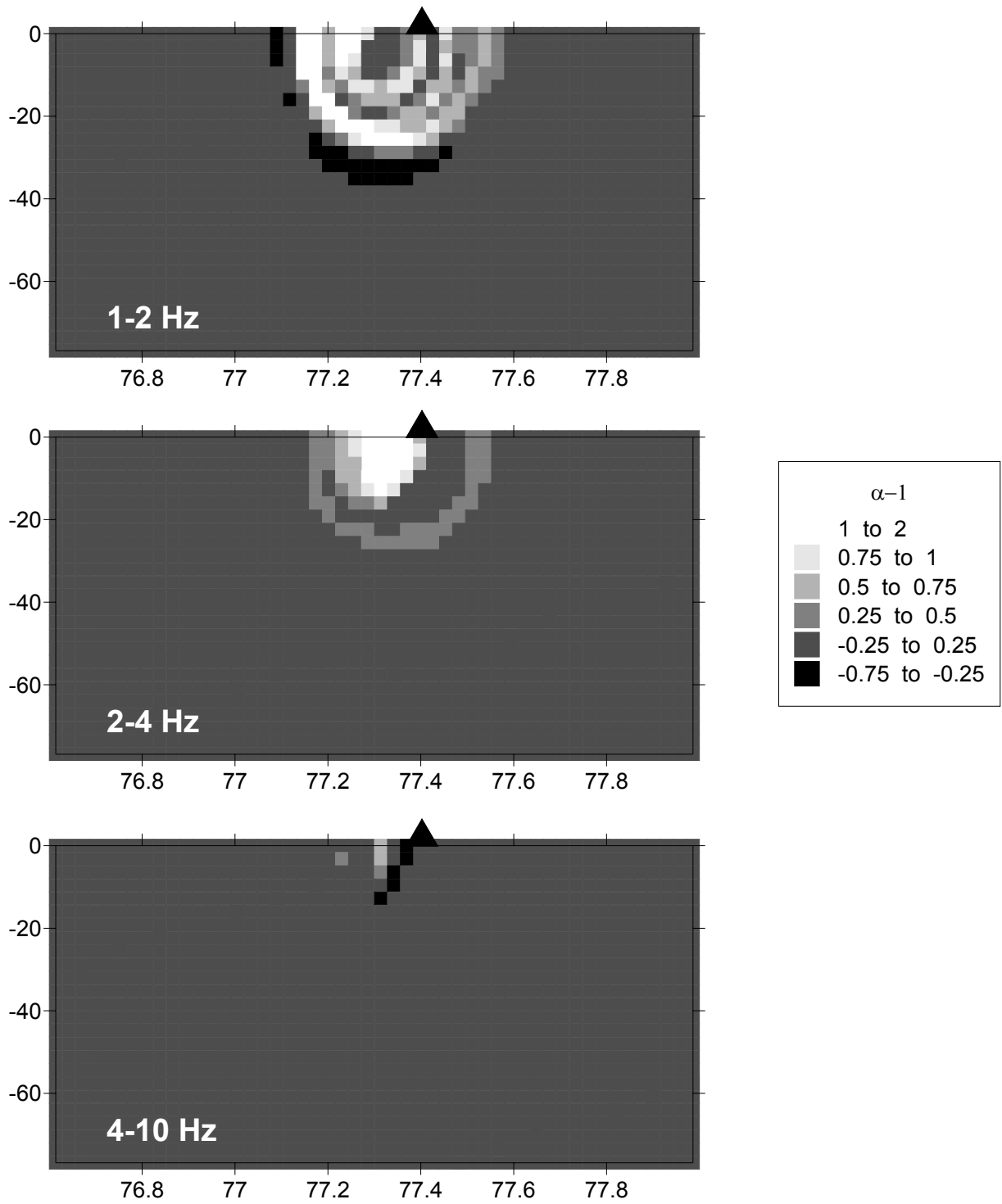


**Figure 5-10.** Vertical cross section of relative scattering coefficients at the parallel 13.6°, which corresponds to the latitude of the array cross-point.

Because the most notable geological feature in the considered region is the 400 km long and 20-30 km wide, north-south trending Closepet granitic intrusion, we simulated the existence of a single spheroidal structure with positive perturbations of the scattering coefficient at different locations in a non-perturbed medium.

Results of the inversion of the synthesized residuals are shown in Figure 5-11. It can be observed that the patterns of the test are well reproduced. We may then conclude that the scattering region observed near the array centre point (Figure 5-9) is neither a ghost image nor a mathematical artefact. Thus we may consider that the inversion method may reproduce up to a certain extent the observed data.

With respect to the uniform distribution of scattering coefficients, our results are in accordance with previous studies performed in the region. In an early work in this region using statistical analysis of observed teleseismic traveltime residuals, Berteussen et al. (1977) [64] remarked that the area on which GBA is sited presents exceptionally homogeneous structures, apart from the general existing velocity perturbations of the order of a few percent. This conclusion was partly supported by Mohan & Rai (1992) [58], who also detected the presence of a prominent scatterer in the deep crustal and uppermost mantle level (30-55 km) in this region from a semblance technique analysis. The scattering region coincided with the Closepet granitic intrusion in the region. Krishna & Ramesh (2000) [63] performed a frequency-wavenumber ( $f-k$ ) spectral analysis of P-coda waveforms to mine tremors and explosions recorded at GBA array. They found a near-on azimuth dominant energy peak with apparent velocity appropriate to the upper crustal depths and they interpreted the result by the presence of a scattering waveguide at upper crustal depths (5-15 km) which might be also related to the granitic batholith. In our case, the zone of strong relative scattering coefficients at low frequency to the west of the GBA array cross-point also coincides with the so-called Closepet batholith, which is a granitic intrusion that acts as the major geological boundary in the region and it is believed to be a Precambrian suture zone between the eastern and western Dharwar craton.

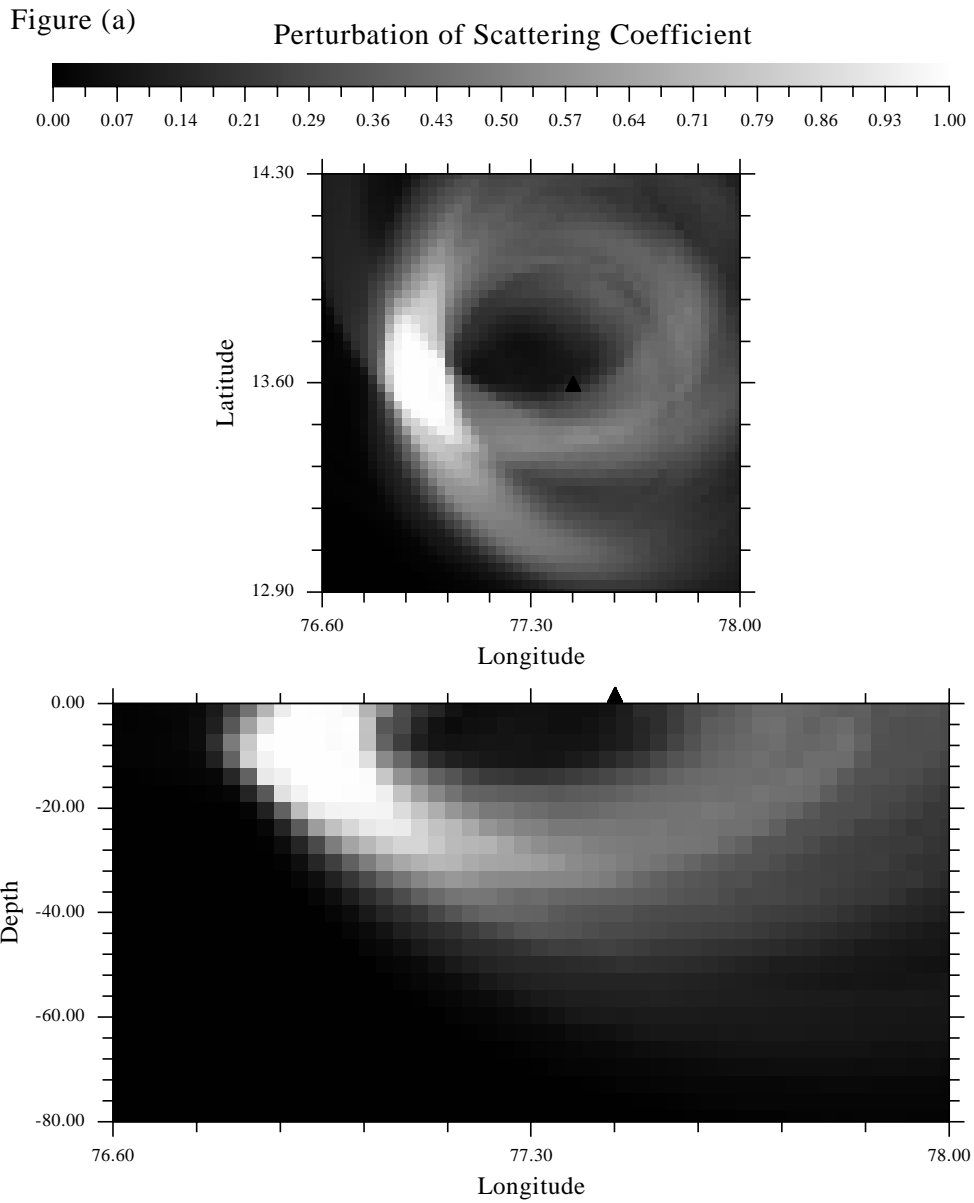


**Figure 5-11.** Spatial distribution of relative scattering coefficients for a synthetic test consisting of one spheroidal structure with two horizontal semi-axes of 13 km and the vertical semi-axis of 9.3 km. It was located at different distances from the array centre point, which is shown by a solid triangle: (a) to the west; (b) below; and (c) to the east. The pattern recovered at a depth of 0 km is plotted at the top of the figure. The vertical cross section along the plane defined by the latitude of the array centre point is also shown.

Figure (b)

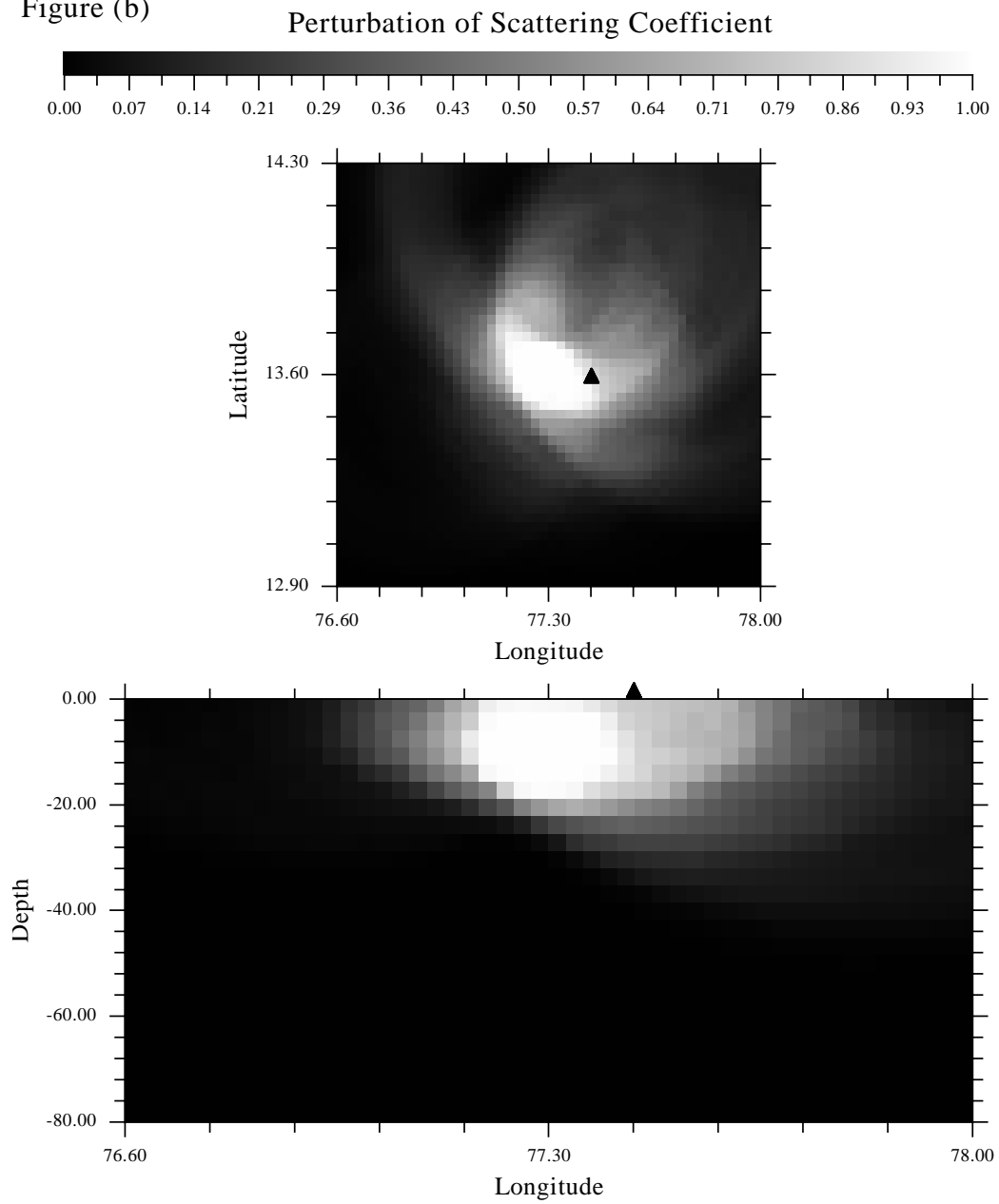


**Figure 5-11. (Continued)**

Figure (c)

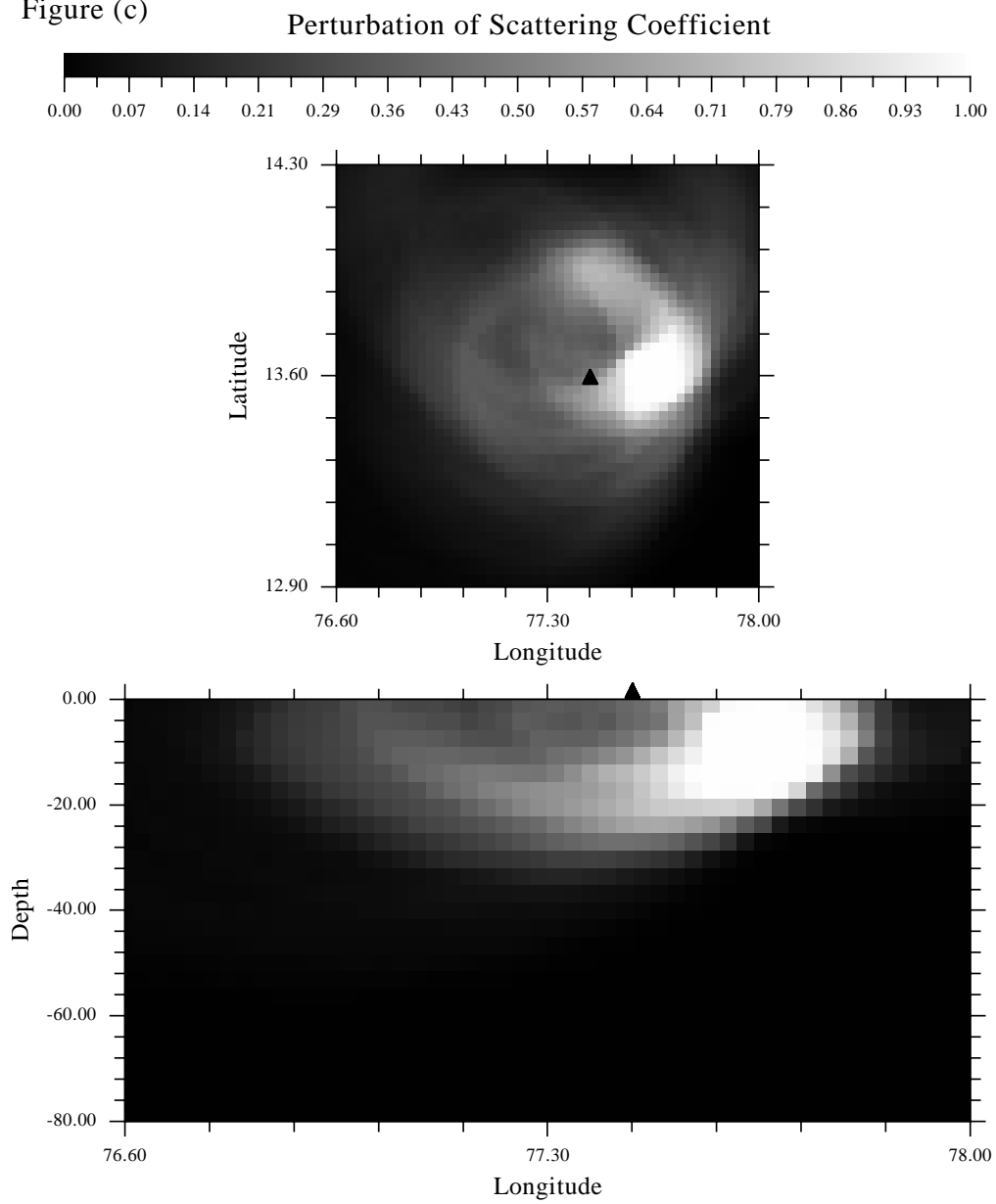


Figure 5-11. (Continued)

## 5.7 CONCLUSIONS

We estimated the three-dimensional distribution of relative scattering coefficients in the crust in southern India by means of an S-wave coda envelope inversion technique applied to local recordings by the Gauribidanur seismic array. Two different inversion algorithms were used for the first time in this type of seismological research: the Simultaneous Iterative Reconstruction Technique (SIRT) and the Filtered Back-Projection (FBP) method. The results allowed to reach the following conclusions:

- 1) The spatial distribution of the relative scattering coefficients obtained was almost independent of the inversion method used.
- 2) The FBP method is very convenient and appropriate for solving these kinds of problems because it requires about 100 times less computation time than the SIRT algorithm to invert the data.
- 3) The crust of the analyzed region around GBA showed a remarkably uniform distribution of scatterers at more than the 90% of the area, which is in accordance with the conclusions of previous studies in the region using statistical analysis of observed teleseismic traveltimes residuals.
- 4) An inhomogeneous structure with size comparable to a wavelength of  $\sim 1.8$  to  $\sim 3.6$  km for 1.5 Hz was detected to the west of GBA from the surface up to a depth of about 24 km just below the array and it coincides with the Closepet granitic intrusion which is the major geological boundary between the eastern and western Dharwar craton.

## **6 THREE-DIMENSIONAL SPATIAL DISTRIBUTION OF SCATTERERS IN GALERAS VOLCANO, SOUTH-WESTERN COLOMBIA**

### **6.1 INTRODUCTION**

In this chapter we will focus on the imaging of small-scale heterogeneities by the estimation of three-dimensional spatial distribution of relative scattering coefficients from shallow earthquakes occurred under the Galeras volcano region. The technique for the inversion of coda-wave envelopes was previously developed in Chapters 3 and 4. In this case, among the possible inversion methods to use for solving the problem, we will use the Filtered Backprojection method, because in Chapter 5 it was demonstrated that the results were almost independent of the inversion method used. Moreover, the FBP method required much less computation time to perform the inversion.

Galeras is a 4276-m high andesitic stratovolcano in south-western Colombia near the border to Ecuador (see Figure 6-1). It is a 4,500 years old active cone of a more than 1 Ma old volcanic complex located in the Central Cordillera of the south-western Colombian Andes. It is historically the most active volcano in Colombia and it has been reactivated frequently in historic times [65]. It awakened again gradually in 1988 after more than 40 years of repose.

Galeras is situated at  $1^{\circ}14'N$  and  $77^{\circ}22'W$ , and its active summit raises 150 m up from the 80 m deep and 320 m wide caldera, which is open to the west (see Figure 6-2). The present active crater lies about 6 km west of Pasto, which has a population of more than 300,000 and with another 100,000 people living around the volcano. Although it has a short-term history of relatively small-to-moderate scale eruptions, the volcanic complex has produced major and hazardous eruptions [Calvache et al. [66], 1997] thus constituting a potential risk to the human settlements in this region.

There are also three smaller craters in the caldera. The diameter on the foot of

the volcano is 20 kilometres. Long term extensive hydrothermal alteration has affected the volcano. This has contributed to large-scale edifice collapse that has occurred on at least three occasions, producing debris avalanches that swept to the west and left a large horseshoe-shaped caldera, inside which the modern cone has been constructed. Major explosive eruptions since the mid Holocene have produced widespread tephra deposits and pyroclastic flows that have swept down all but the southern flanks.

Galeras was designated a Decade Volcano in 1991, which identified it as a target for intensive and interdisciplinary study during the United Nations' International Decade for Natural Disaster Reduction. With the aim of enlarging the knowledge of the internal structure of the volcano as well as to serve for its seismic hazard assessment, the present study is a different complementary contribution to the interdisciplinary research (geological, geophysical and geochemical) being conducted in the region since the re-activation of Galeras volcano.

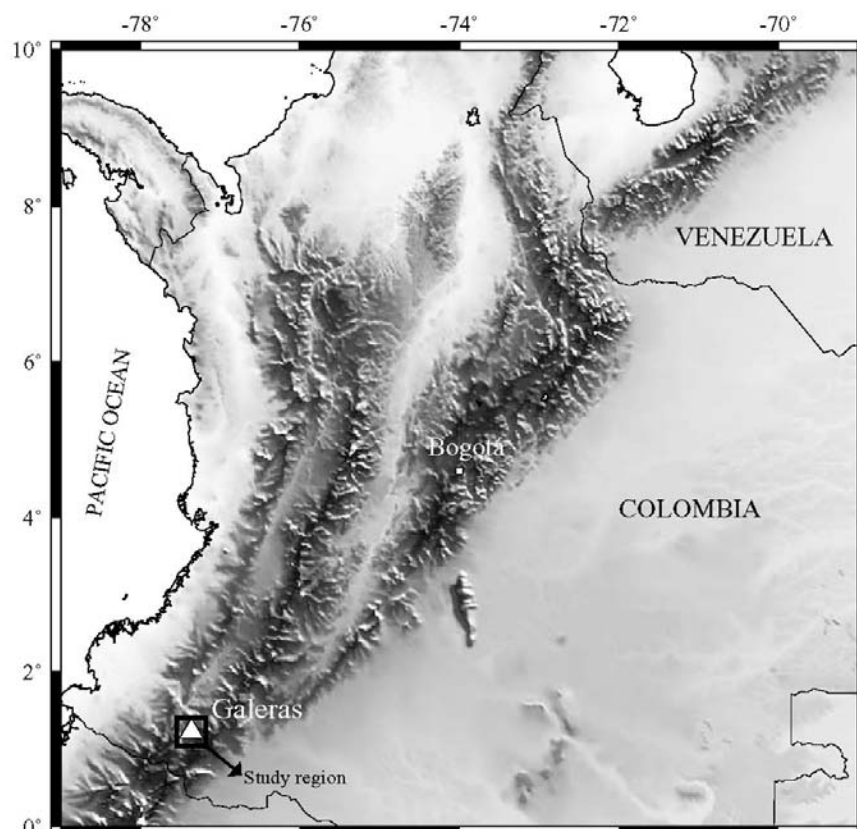


**Figure 6-1.** Topographic map of Colombia showing the location of the Galeras volcano and the study area.

## 6.2 GEOLOGICAL SETTING

### 6.2.1 GEOLOGICAL HISTORY

Galeras has been erupting lavas and pyroclastic flows during the last million years. Two major caldera-forming eruptions have occurred, the first about 560,000 years ago in an eruption which expelled about 15 cubic kilometres of material, and the second some time between 40,000 and 150,000 years ago, in a smaller but still sizable eruption of 2 km<sup>3</sup> of material. Subsequently, part of the caldera wall has collapsed, probably due to instabilities caused by hydrothermal activity, and later eruptions have built up a smaller cone inside the now horseshoe-shaped caldera.



**Figure 6-2.** Galeras volcano from the west flank. Photo by Norm Banks of USGS [67].

At least six large eruptions have occurred in the last 5000 years, most recently in 1886, and there have been at least 20 small to medium sized eruptions since the 1500s.

Galeras is one of the 16 Decade Volcanoes identified by the International Association of Volcanology and Chemistry of the Earth's Interior (IAVCEI) as being worthy of particular study in light of their history of large, destructive eruptions and proximity to populated areas. The Decade Volcanoes project encourages studies and

public-awareness activities at these volcanoes, with the aim of achieving a better understanding of the volcanoes and the dangers they present, and thus being able to reduce the severity of natural disasters. The project was initiated as part of the United Nations-sponsored International Decade for Natural Disaster Reduction.

Galeras had become active in 1988 after 40 years of dormancy. In 1993, the volcano erupted when several volcanologists were inside the crater taking measurements. The scientists had been visiting Pasto for a conference related to the volcano's designation as a Decade Volcano. Six were killed, together with three tourists on the rim of the crater. The eruptive period lasted until 1995. Since then, the volcano has been in a relative calm stage with some ash and gas emission episodes and low-level eruptive activity (a crater located to the east of the main one was re-activated in 2002 after more than 10 years of inactivity) dusting nearby villages and towns with ash. A new eruptive episode began in 2004 (three explosive events have occurred in this period) and it continues active at the time of this writing (the activity reports are available at <http://www.volcano.si.edu/>).

The volcano has continued to be well studied, and the studies concerning predictions of eruptions at the volcano have improved. One phenomenon which seems to be a reliable precursor to eruptive activity is a shallow-source, low frequency seismic events known as a “tornillos” which are related to magmatic activity and that have also been recorded during different stages of volcanic activity at Galeras [Gómez and Torres, 1997 [68]]. These have occurred before about four-fifths of the explosions at Galeras, and the number of “tornillo” events recorded before an eruption is also correlated with the size of the ensuing eruption.

Seismicity in the region since 1988 has been characterized by long period events, volcano-tectonic earthquakes and tremor episodes. The level of seismic activity has presented fluctuations, alternating periods of low-level seismicity with episodes of seismic activity increase in terms of the number and/or magnitude of the events. Some shallow (up to 8 km) volcano-tectonic earthquakes have reached local magnitudes up to 4.7.

## 6.2.2 GEOLOGY OF GALERAS VOLCANO

Galeras is located in a region with a metamorphic rock basement of Precambrian and Paleozoic ages [69]. The basement is overlaid by metamorphic rocks of Cretacic age with low and medium grade associated with amigdular metabasalts. All of this is covered by volcano sedimentary units of Tertiary age that made a plateau, over which the Pleistocenic and Holocenic volcanoes have emerged. The tectonic plate of this region is very complex, as a result of the collision between the Nazca and south American plates. This causes the uplift of the Andes and the volcanism in the region. The structural trend is N40°E and the principal tectonic feature is the Romeral Fault Zone, which has been interpreted as the limit between continental crust to the east and the oceanic crust to the west (Barrero, 1979). This system includes the Silvia-Pijao and Buesaco faults, both of which cross under Galeras, and are associated with many old caldera systems as can be seen in Figure 6-3.

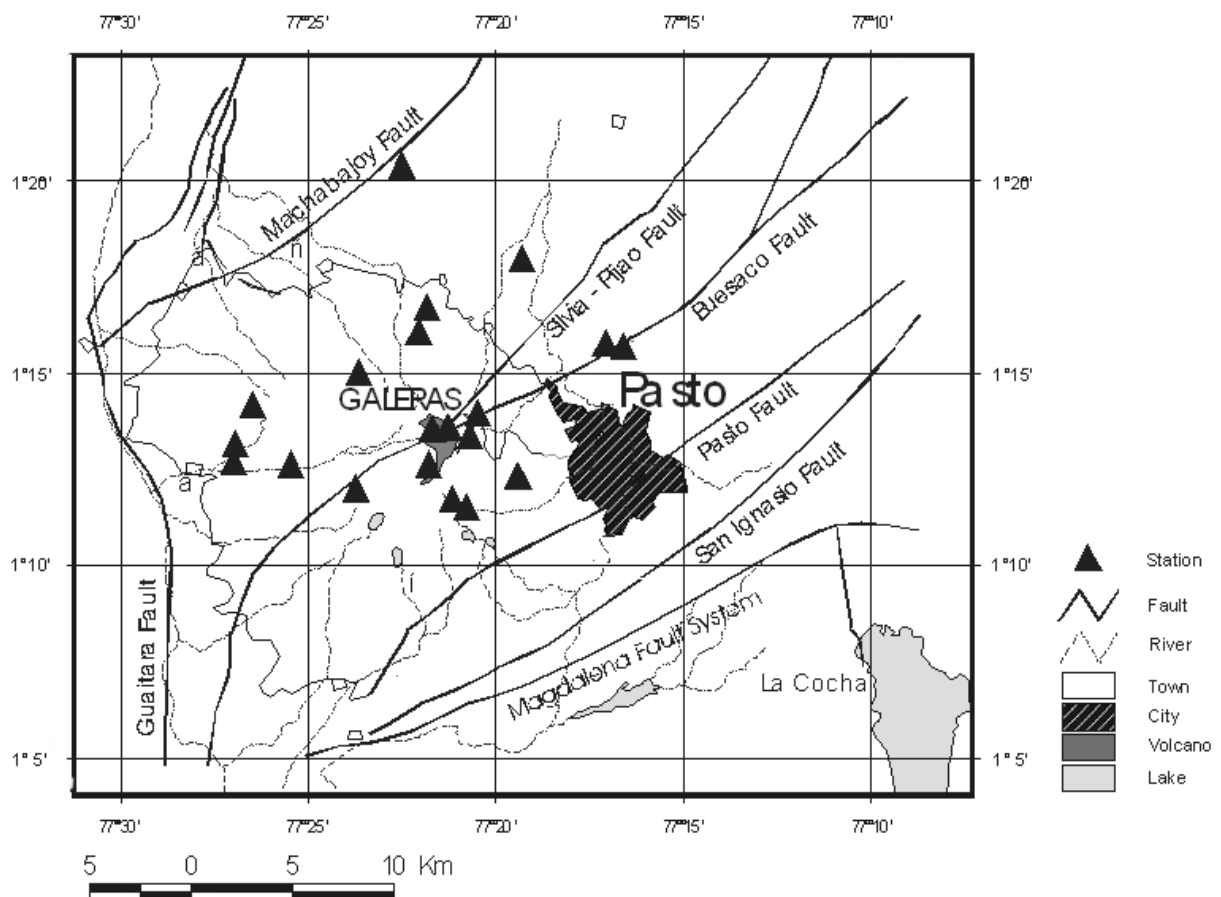


Figure 6-3. Geological map of the Galerías Region. The map includes the locations of the stations.

Galeras is a stratovolcano. Stratovolcanos are usually tall, conical mountains composed of both hardened lava and volcanic ash. The shape is characteristically steep in profile because lava flows that formed them were highly viscous, and so cooled and hardened before spreading very far. Such lava tends to be high in silica (mafic magma). All these characteristics apply to the Galeras volcano. In Figure 6-4 altitude curves are represented and the shape and steepness of this volcano becomes evident. Stratovolcanoes are often created by subduction of tectonic plates as in our case.

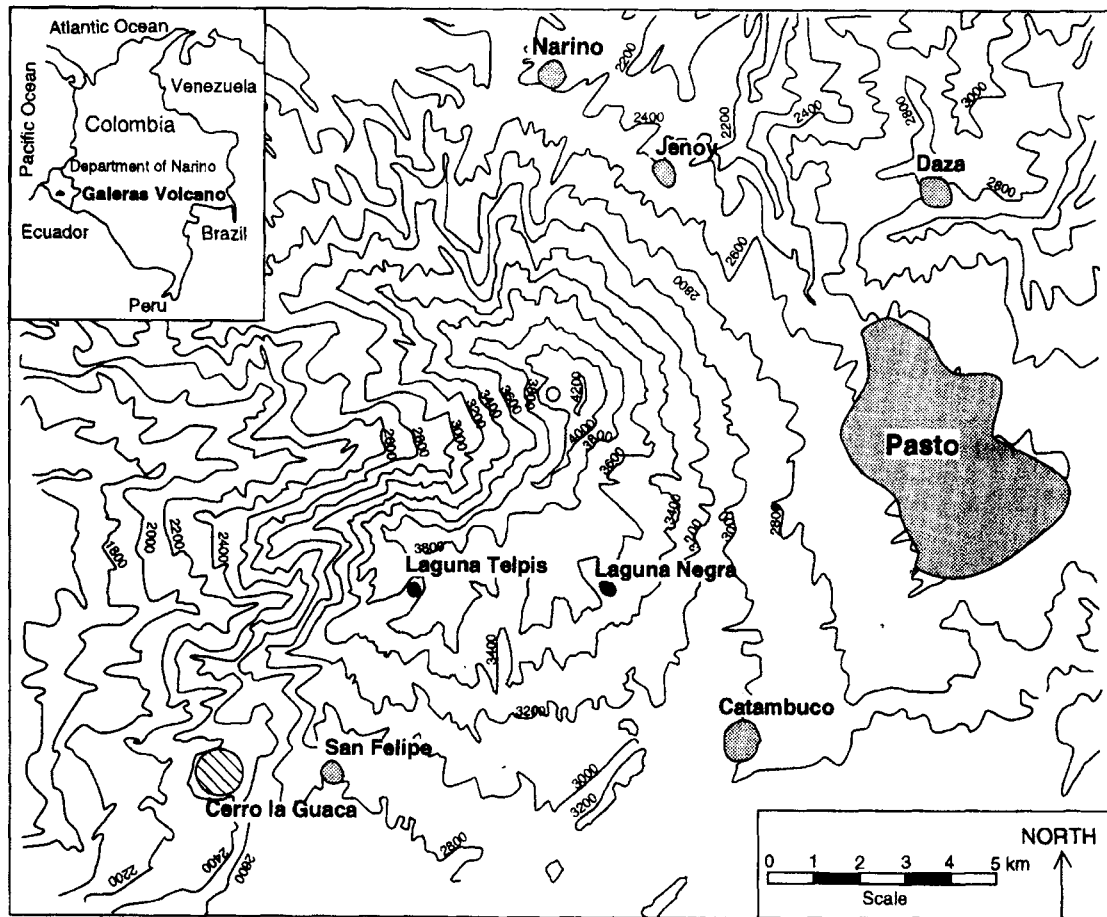


Figure 6-4. Map showing the shape of Galeras volcano and altitude curves [72].

Studying  $SO_2$  emissions it is possible to infer the internal structure of the Galeras volcano. The emissions of  $SO_2$  are not constant. Usually, emissions decrease with time. Then, during eruption periods, emissions become intense. When the eruption has finished, a new period of emission decrease starts over again. The general decrease of the flux with time is interpreted as a progressive degassing of a single batch of magma followed by the obstruction of the conduit by emplacement of the dome. The

large amounts of sulfur degassed from Galeras strongly suggest that a reservoir of sulphur rich magma underlies the shallow magma in the conduit of the active cone.

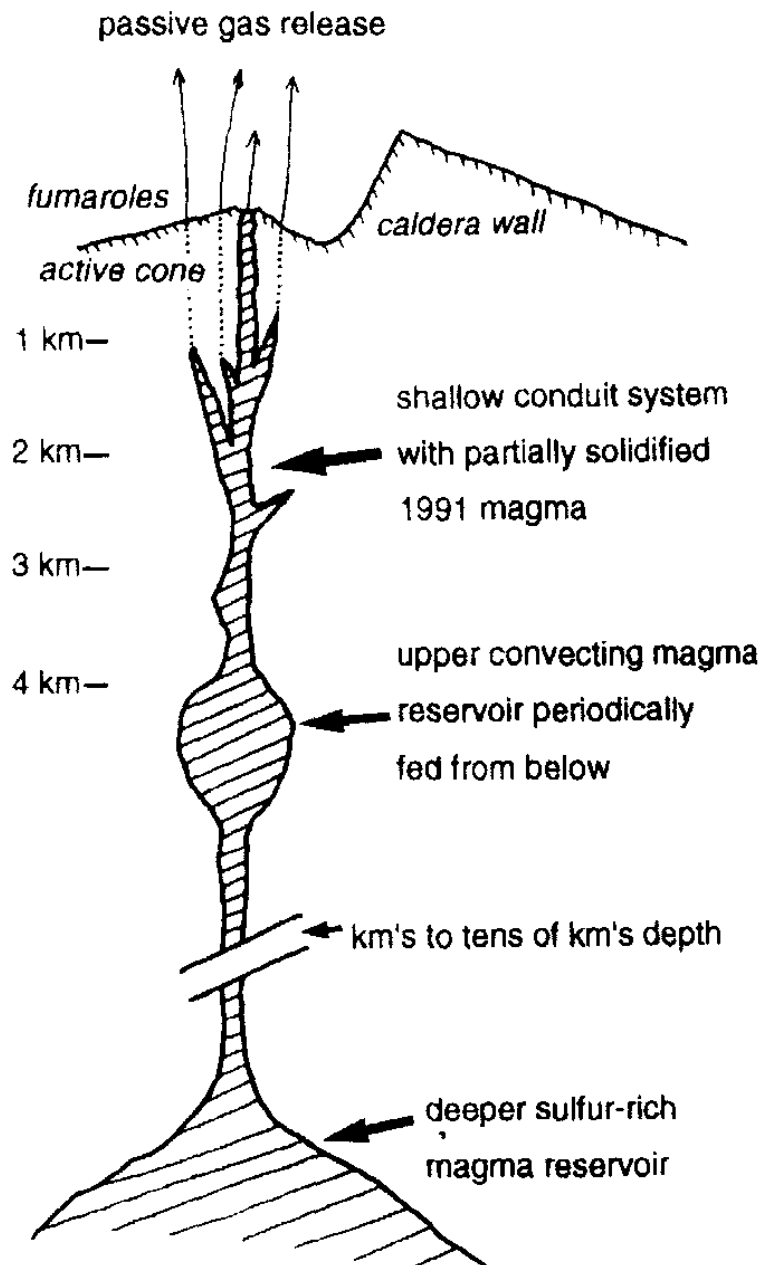


Figure 6-5. Sketch of the magmatic plumbing system beneath Galeras [72].

The presence of this hypothetical reservoir is also supported by petrologic and seismic data [70] which indicate that the reservoir is located at a depth of 4-5 km. The reservoir is able to supply  $SO_2$  and other gasses to the upper, more open and fractured

reaches of the volcano through a complex conduit system. Strong degassing fumaroles are surface expressions of this upper conduit system. As the reservoir cools becomes less convective and the result is a progressive decline in  $SO_2$  fluxes from the volcano. Then, the reservoir becomes isolated: the reservoir is no longer feed with fresh magma from deeper regions. During a reactivation cycle, the reservoir is initially supplied with mafic, sulphur rich magma from a deeper level after a repose period of tens of years. This supply of magma could be the result of tectonic disturbances nearby. Once this occurs, the magma can degas from the upper reservoir through the shallow conduit system and eventually rise to erupt explosively or effusively.

Then, the behaviour suggests that the internal structure of the Galeras volcano is like the one outlined in Figure 6-5, where the magmatic plumbing system beneath Galeras is sketched. The plumbing system comprises the following structures:

- i) A sulphur-rich mafic magma at intermediate to deep levels in the crust
- ii) An upper reservoir fed from deeper levels
- iii) Shallow conduits through which most of the degassing takes place

### **6.3 DATA DESCRIPTION**

Data used in this study is a selection of 1564 high quality coda waves' recordings from shallow earthquakes (depths less than 10 km from the Earth's surface) with local magnitudes less than 2.0 occurred in the region since 1989 to 2002. The 31 short-period ( $T_0=1$  s), vertical component recording stations used were deployed at different stages of the Galeras seismic network operation and they were located at distances less than 10 km from the active crater. The three-dimensional distribution of hypocenter and stations can be seen in Figure 6-6 and the coordinates and designation of each station can be found in Table 6-1.

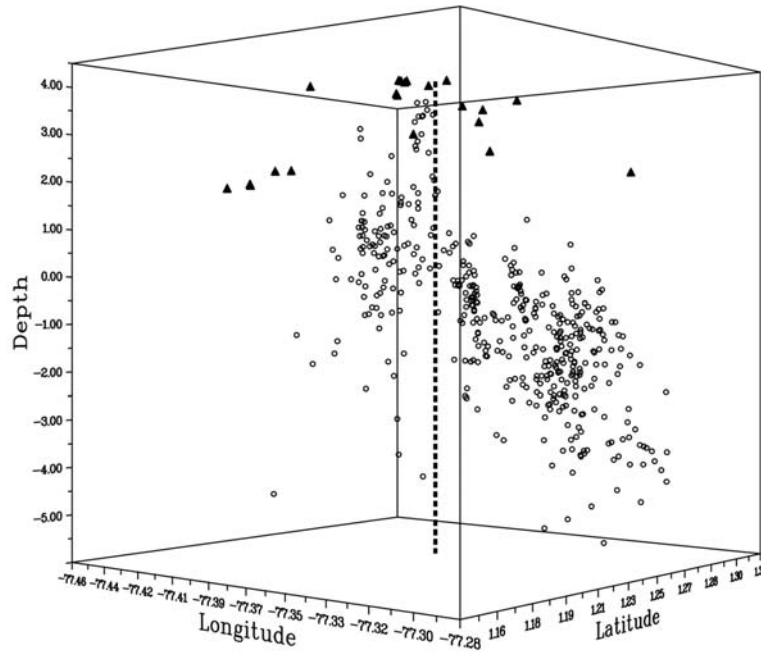


**Figure 6-6.** Three-dimensional of hypocenters (green circles) and stations (blue triangles).

Station number	Name	Latitude (°)	Longitude (°)	Altitude (km)
0	ARLS	1.2500	-77.3913	3250
1	CALA	1.2063	-77.4227	2353
2	CB2R	1.1910	-77.3490	3625
3	CB3D	1.1910	77.3490	3625
4	COB3	1.1910	77.3490	3625
5	CON4	1.2053	-77.4478	2050
6	COND	1.1938	-77.3925	4000
7	CONO	1.2202	-77.3588	4010

Station number	Name	Latitude (°)	Longitude (°)	Altitude (km)
8	CR2D	1.2102	-77.3607	4058
9	CR2G	1.2107	-77.3620	4032
10	CR2R	1.2773	-77.3620	4032
11	LOEW	1.3537	-77.3780	2350
12	LOMV	1.3537	-77.3780	2350
13	LONS	1.3537	-77.3780	2350
14	NAR2	1.2688	77.3687	2870
15	OLGA	1.2223	-77.3523	4100
16	PLAZ	1.2593	-77.2790	3000
17	PUYI	1.2977	-77.3230	2370
18	TEL2	1.257700	-77.2740	3070
19	URCR	1.2188	-77.3423	3494
20	UREW	1.2188	-77.3423	3494
21	URNS	1.2188	-77.3423	3494
22	CBA2	1.1885	-77.3463	3570
23	CO2R	1.2153	-77.4455	2168

Station number	Name	Latitude (°)	Longitude (°)	Altitude (km)
24	CON2	1.2160	-77.4460	2140
25	CON3	1.2337	-77.4410	2530
26	CRA2	1.2078	-77.3612	4040
27	CRA3	1.2065	-77.3612	4040
28	OBEW	1.2033	-77.3227	3010
29	OBNS	1.2033	-77.3227	3010
30	URCO	1.2260	-77.3387	3435

**Table 6-1.** Number, name and coordinates of each seismic station from which data has been used.

## 6.4 DATA ANALYSIS

In order to estimate the inhomogeneous spatial distribution of relative scattering coefficients in the crust we followed the method proposed in Chapter 3. The system of equations relating the spatial distribution of relative scattering strength to the observed coda energy residuals under the assumption of single isotropic scattering and spherical radiation of a seismic source can be written as:

$$\begin{aligned}
 w_{11}\alpha_1 + \dots + w_{i1}\alpha_i + \dots + w_{N1}\alpha_N &= e_1 \\
 &\vdots \\
 w_{1j}\alpha_1 + \dots + w_{ij}\alpha_i + \dots + w_{Nj}\alpha_N &= e_j \\
 &\vdots \\
 w_{1M}\alpha_1 + \dots + w_{iM}\alpha_i + \dots + w_{NM}\alpha_N &= e_M
 \end{aligned} \tag{6.1}$$

We remind that this system of equations is obtained by dividing the coda of each seismogram into several small time windows. Then, in Eq.(6.1) there is an equation for every time window of every seismogram. Also for each time window, the scatterers

contributing to the energy density are contained in a spheroidal shell. Therefore,  $M$  is the total number of equations (number of seismograms multiplied by the number of coda time windows considered), and  $N$  is the total number of scatterers (number of small blocks into which the study region is divided). The right side of equation (6.1) is called coda wave energy residual ( $e_j$ ) which measures the ratio of the observed energy density in this part of the coda to the average energy density of the medium.

We will carry out the inversion of the system by using the Filtered Backprojection Algorithm developed in Section 4.5.

Because each analyzed frequency band is giving us information about inhomogeneous structures with sizes comparable to the seismic wavelengths, and given that the signal energy contents of the available data decays abruptly for frequencies  $f$  above 12 Hz, we decided to calculate the coda wave energy residuals [Nishigami, 1991 [40]; Ugalde et al., 2005 [71]] for the frequency bands 4-8 ( $6\pm 2$ ) Hz and 8-12 ( $10\pm 2$ ) Hz, thus allowing us to image structures of sizes comparable to wavelengths of  $\sim 400$  to  $\sim 800$  m for 4-8 Hz, and  $\sim 300$  m to  $\sim 400$  m for 8-12 Hz. These sizes are derived by considering an average S-wave velocity of  $\beta=3.3$  km/s in the study region. From the bandpass-filtered seismograms, we calculated the rms amplitudes  $A_{\text{obs}}(f|r,t)$  for each hypocentral distance  $r$  by using a 0.25 s spaced moving time window of length  $t\pm 1$  s, and  $t\pm 0.5$  s for the 6 Hz and 10 Hz centre frequencies, respectively.

The time interval for the analysis started at 1.5 times the S-wave travel times (in order to increase the resolution near the source region) and had a maximum length of 20 s (to minimize the effects of multiple scattering). We also computed the rms amplitudes for a noise window of 10 s before the P-wave arrival and only the amplitudes greater than two times the signal to noise ratio were kept. Then, the average decay curve was estimated for each seismogram by means of a least-squares regression of  $\ln[t^2 A_{\text{obs}}(f|r,t)]$  vs.  $t$ , where the term  $t^2$  is a geometrical spreading correction which is valid for body waves in a uniform medium. We only kept the estimates with a correlation coefficient greater than 0.60. The observed coda energy residuals  $e(t)$  were then calculated by taking the ratio of the corrected observed amplitudes to the estimated exponential decay curve. Finally the residuals were averaged in time windows of

$\delta t = 0.25$  s to get  $e_j$  at discrete lapse times  $t_j$ .

A 20 km x 20 km in horizontal and 50 km in depth study region was selected taking into account the stations and hypocenters distribution. It was divided into  $N=50 \times 50$  blocks, the volume of which satisfies the condition  $\delta t \leq 2(\delta V)^{1/3} / \beta$ . Then, the observational system of equations (6.1) was created by assuming the layered velocity structure shown in Table 6-2 and it was solved using the FBP algorithm [Ugalde et al., 2005, [71]].

Depth (km)	S-wave velocity (km/s)
4	2.0
2	2.1
0	2.2
-4	3.4
-22	3.8
-40	4.5

**Table 6-2.** S-wave velocity model for the Galeras Volcano region.

## 6.5 RESULTS

To check for sampling insufficiencies, we plotted in Figure 6-7 a vertical cross section of the hit counts, or number of coda residuals contributed by each block. The figure shows that the entire region is sampled by the ellipses although the number of hit counts is smaller at the deepest levels and also inside a shallow area to the north-east of the volcano summit.

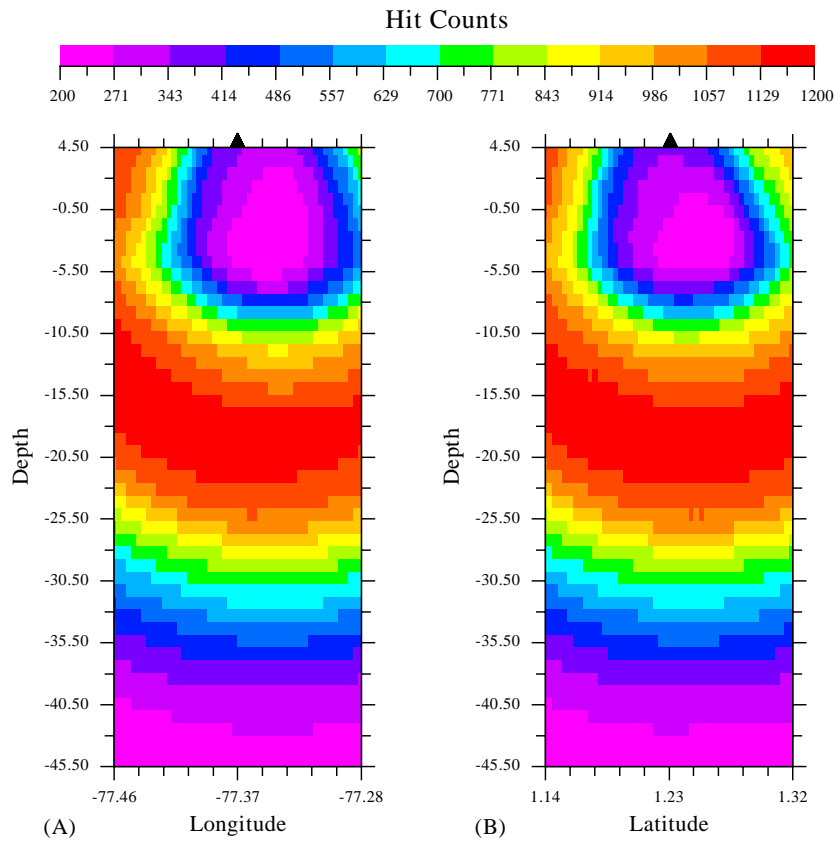


**Figure 6-7.** Vertical cross sections of the hit count distribution along the parallel 1.23°N (A) and the meridian 77.36°W (B) which correspond to the coordinates of the summit. The Galeras volcano location is indicated by the solid triangle.

The resulting distribution of relative scattering coefficients  $\alpha - 1$  in the study region for the analyzed frequency bands and for different depths up to 10 km from the summit is plotted in Figure 6-8. The colour scale indicates the perturbation of scattering coefficients from the average in this region, being the largest values  $\sim 3.0$  and the minimum  $\sim 0.5$ .

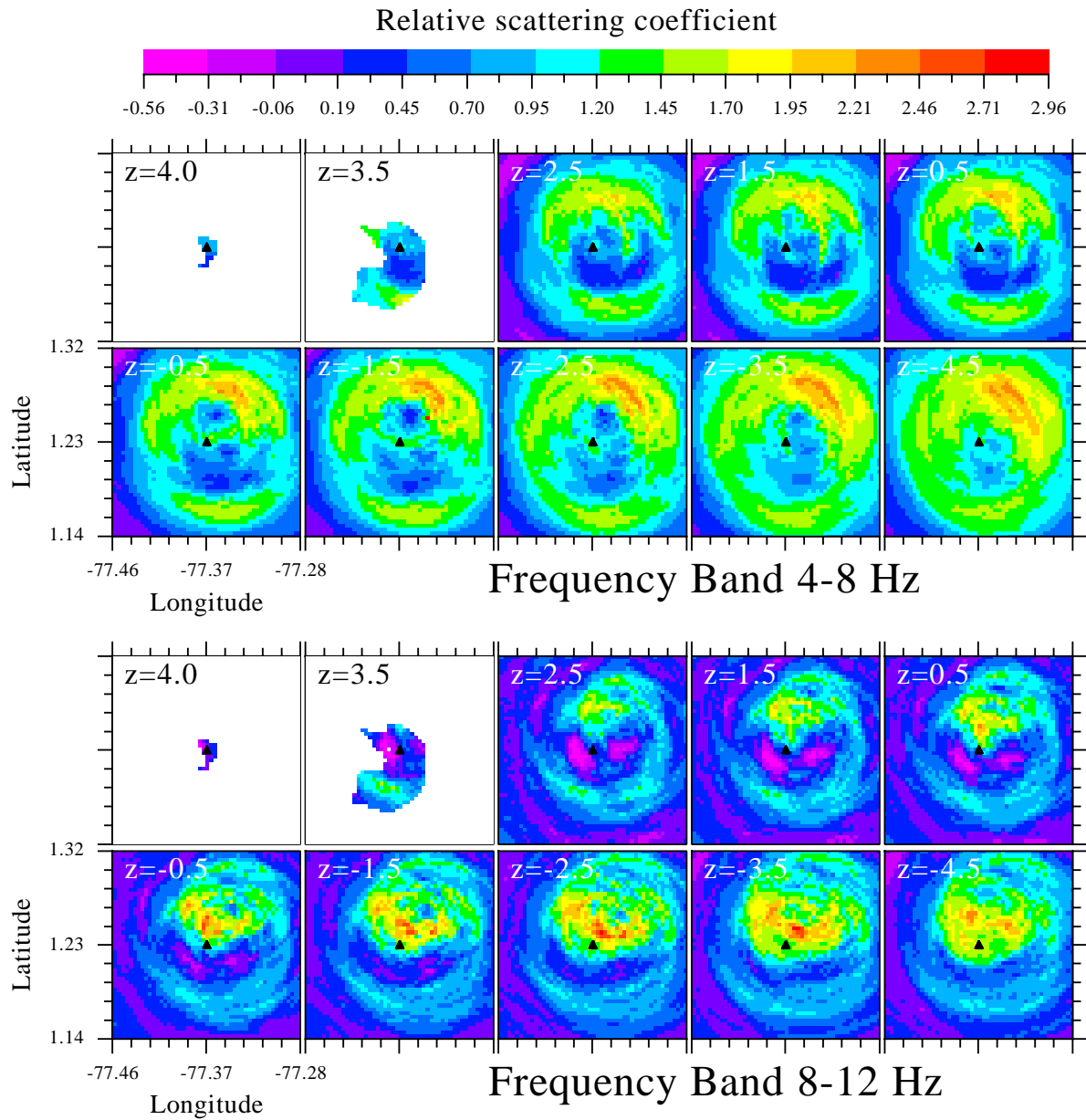
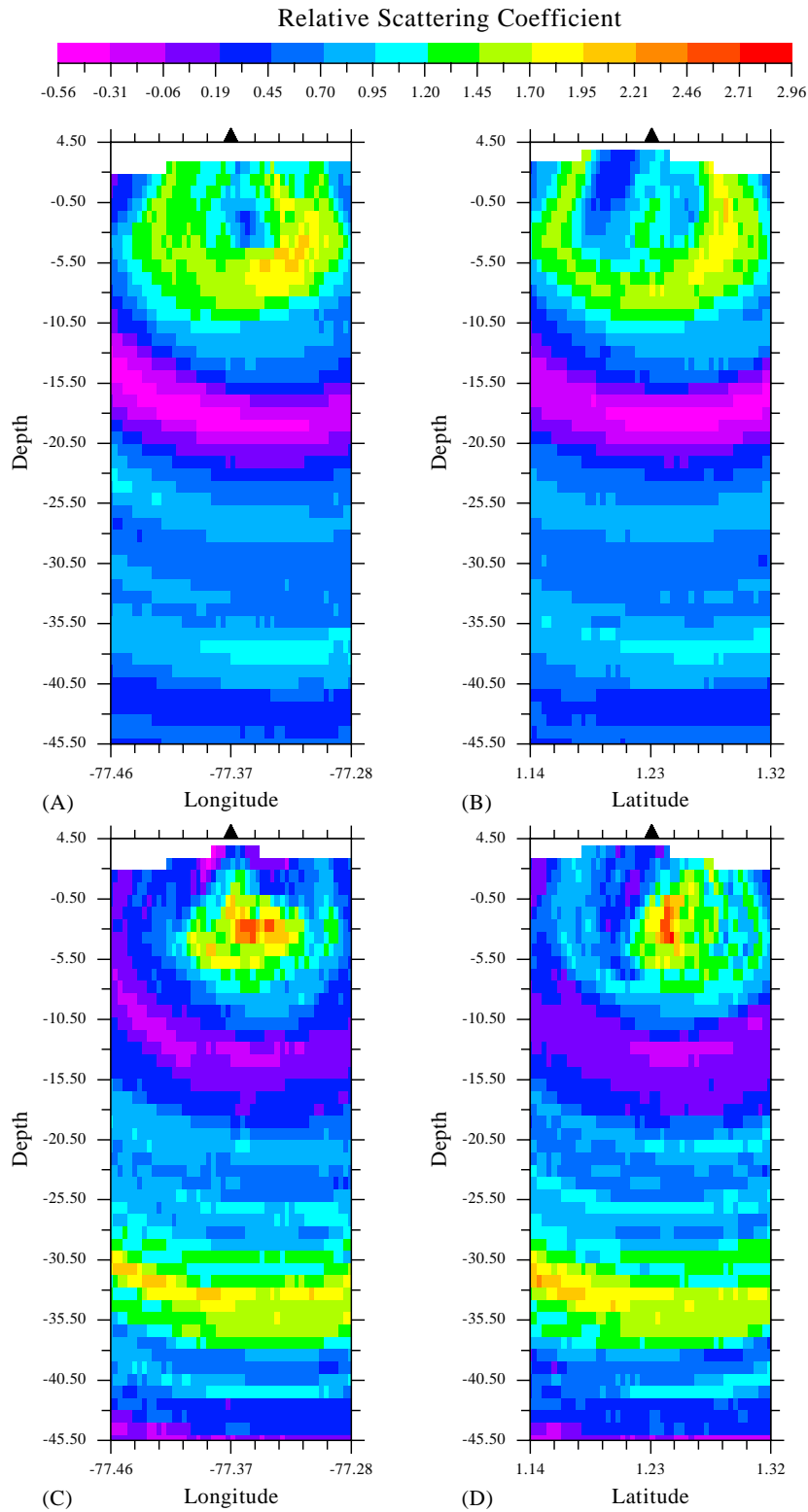


**Figure 6-8.** Horizontal sections of the study area showing the distribution of the relative scattering strength ( $\alpha-1$ ) at different depths from 4 km to -4.5 km. The solid triangle indicates the location of the Galeras volcano summit. The topographic contour lines at 4000 m and 3500 m levels are also plotted.

## 6.6 DISCUSSION

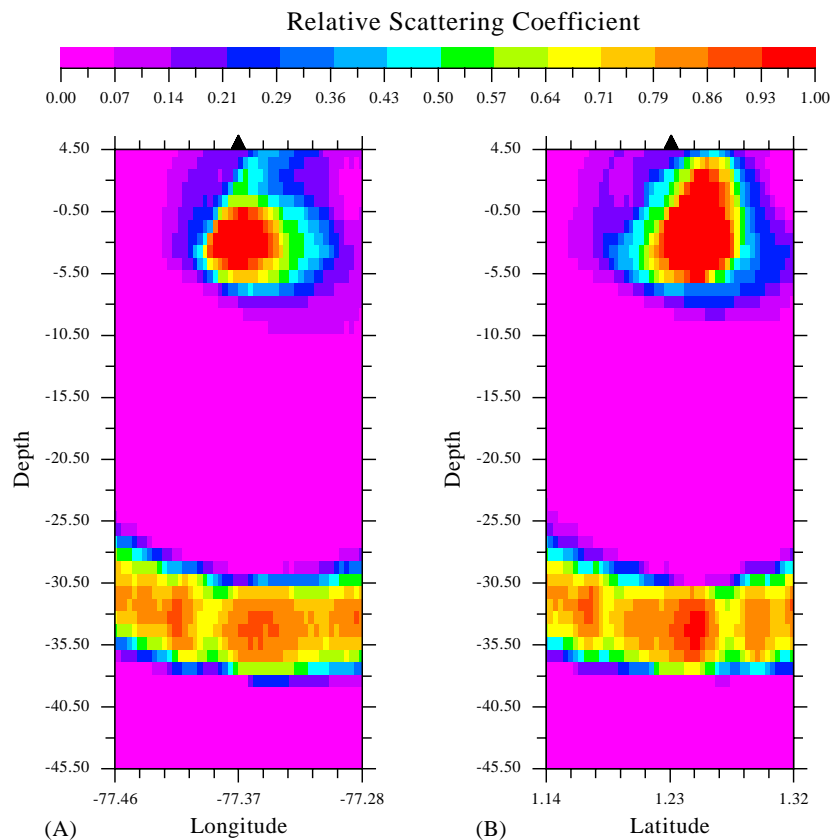
Figure 6-8 shows that the region of  $\pm 10$  km in horizontal and 10 km in depth centred at the Galeras volcano summit presents a remarkable inhomogeneous distribution of relative scattering coefficients. More than the 83% and the 50% of the analyzed region for low and high frequencies, respectively, reveal a spatial perturbation of the scattering coefficient greater than +50%. For low frequencies, a strong scattering donut-shaped area with relative scattering coefficients between 0.96 and 3.0 is found around the volcano at all depths. The volume showing the strongest relative scattering coefficients ( $\alpha$ -1~2.0-3.0) is located to the northeast of the volcano at depths between -0.5 km and -4.5 km. At high frequencies, the strong scattering zone occurs slightly to the north of the axis of the volcano at the same depths. Also we may notice that the scattering strength is similar but slightly lower for the lower frequency band. Then, we may conclude that, at shallow depths, there is a single complex structure located at the north of the volcano that shows a frequency dependent behaviour. The relative scattering coefficients at high frequencies are stronger than those of low frequencies in a volume near the axis of the volcano, which means that small-size heterogeneities as small fractures (comparable to a wavelength of  $\sim 300$  m to  $\sim 400$  m for a centre frequency of 10 Hz) contribute more scattered energy than those with larger sizes. On the contrary, heterogeneities with sizes comparable to a wavelength of  $\sim 400$  to  $\sim 800$  m for a centre frequency of 6 Hz contribute more to the scattering energy at the north-east of the summit.

Figure 6-9 shows a vertical cross section of the region along the east-west and north-south directions centred at the volcano which shows the scattering perturbation at higher depths. A second strong scattering volume at depths between -29 km and -36 km is clearly observed at high frequencies and can be noticed at low frequencies. Unfortunately, in this case it is more difficult to establish the geometry of the scattering region. The ellipsoidal pattern imaged results from both a poor sampling and the geometry of the ellipses at these deeper levels, which are almost parallel. This makes it possible to establish only the depth and height of the region. A frequency dependence of the strength of the scattering coefficient is again observed thus indicating that small-scale heterogeneities contribute more scattering energy at these deeper levels.



**Figure 6-9.** Vertical cross section of the study region along the two planes defined by the summit coordinates, which indicated by the solid triangle (latitude  $1.23^\circ$  and longitude  $-77.36^\circ$ ). The color scale indicates the perturbation of the scattering coefficient  $\alpha-1$  for the 4-8 Hz (A, B) and 8-12 Hz (C, D) frequency bands.

The existence of both structures is in close agreement with the current magmatic plumbing system model beneath Galeras volcano. This model is based on petrologic and seismic data and it proposes a shallow conduit system with a distinct reservoir at a depth of 4-5 km from the summit which is periodically fed from a deeper magma reservoir which is located from km's to tens of km's depth [Calvache, 1990 [70]; Zapata et al., 1997,[72]].



**Figure 6-10.** Vertical cross section showing the results of the inversion analysis for a synthetic test consisting of two spherical structures buried at depths of -2 km and -33 km.

In order to establish the validity of the results of this study and to help their geological interpretation, we tested the inversion method by means of a synthetic test. We simulated the presence of two magmatic chambers located at the north of the volcano at depths of -2 km and -33 km by two spherical structures with positive perturbations of the scattering coefficient embedded in a non perturbed medium. Then, we synthesized the coda energy residuals from the observational equation using the synthetic pattern of scattering coefficients and the same distribution of stations and

events used in the analysis. Figure 6-10 shows the inversion of the synthesized residuals. It can be observed that both the pattern and the perturbation value of the scattering coefficient were well resolved in the considered region for shallow depths. A comparison of Figure 6-9 and Figure 6-10 suggests a reasonable agreement between synthetic and experimental results, thus supporting the identification of the scattering structures imaged with the magmatic chambers of the geological model.

## **6.7 CONCLUSIONS**

The three-dimensional spatial distribution of relative scattering coefficients has been estimated for the Galeras volcano, Colombia, by means of inversion analysis of coda wave envelopes from 1564 high quality seismic recordings by 31 stations of the Galeras seismograph network. Results reveal a highly non-uniform distribution of relative scattering coefficients in the region for the two analyzed frequency bands (4-8 and 8-12 Hz). Strong scatterers showed frequency dependence, which was interpreted in terms of the scale of the heterogeneities producing scattering. Two zones of strong scattering are detected: the shallower one is located at a depth from 4 km to 8 km under the summit whereas the deeper one is imaged at a depth of ~37 km from the Earth's surface. Both zones may be correlated with the magmatic plumbing system beneath Galeras volcano. The second strong scattering zone may be probably related to the deeper magma reservoir that feeds the system.



## 7 CONCLUSIONS

The behaviour of coda waves in seismograms is one of the observations supporting the existence of small-scale random heterogeneities in the Earth. The direct S wave observed in a seismogram from a local earthquake is followed by complex wave trains with amplitudes smaller than the direct wave and that exponentially decay with time, which are called S-coda. It is widely accepted that coda waves are formed by superposition of incoherent scattered waves from randomly distributed heterogeneities in the lithosphere, such as cracks, faults, folds, and velocity or density anomalies with scale length about the seismic wavelength. S-coda waves have an envelope shape common to all epicentres and stations in a given region after twice the S wave travel time. Total scattering coefficient ( $g$ ) and coda attenuation ( $Q_c^{-1}$ ) are the parameters which characterize the coda excitation (which measures the capacity of the medium to originate scattering) and the decay rate of coda envelopes (which is a measure of the attenuation of the medium) within a given frequency band, respectively.

A number of models have been proposed to relate scattering and coda wave amplitudes. One approach to model the coda envelopes is to consider the heterogeneities as randomly and uniformly distributed point-like scatterers. Using this model and on the basis of the energy transport (or radiative transfer) theory, the S-wave coda has been synthesized under the assumption of single isotropic scattering, multiple isotropic scattering and multiple non-isotropic scattering. Most of these models were reviewed with a certain detail in Chapter 2.

Scattering from randomly and non-uniformly distributed heterogeneities has also been studied to explain the features of the observed envelopes of S coda waves. The subject of Chapter 3 was to describe an existing inversion method of coda waveforms from local earthquakes to estimate the inhomogeneous spatial distribution of relative scattering coefficients in the crust. The method is based on the assumption that the fluctuation of the decay curve of the observed coda envelope from a reference curve, which was estimated by assuming single isotropic scattering and spherical radiation from the source, is caused by a non-uniform distribution of scatterers in the crust. This method has proved to be an effective approach to investigate the real heterogeneous structure in the crust of several regions in the world.

Several inversion algorithms have been used to solve the problem in order to obtain the strength of the scattering coefficients: standard inversion methods, recursive stochastic inversion methods, and the Algebraic Reconstruction Technique (ART).

In this thesis the inversion analysis was performed for the first time in this kind of seismological research by means of the Simultaneous Iterative Reconstruction Technique (SIRT) and Filtered Back-Projection method (FBP). We demonstrated that, whereas the first one allows to obtain more exact solutions, the second one is a much faster non-iterative algorithm that has proved to provide very accurate reconstructions.

The inversion analysis required a previous original theoretical development (which is presented in Chapter 4) in order to adapt the Filtered Backprojection algorithm to the geometry defined by the problem to be solved. Then, firstly, the Filtered Backprojection algorithm was derived using a simple approach: the reconstruction of a two-dimensional object from its projections. Secondly, we generalized the result to the two-dimensional case and, finally, by taking into account the special geometry of our problem we devised an algorithm adapted to our case.

The resulting algorithm is about 100 times faster than ART, and we showed that the solutions obtained have similar accuracy. Moreover, the speed improvement of our Filtered Backprojection algorithm allows to carry out inversions with a higher resolution.

Then, we applied the method for the first time to real seismic data from two regions with different geotectonic characteristics: a stable region in southern India and an active volcano in south-western Colombia. Both regions have a high scientific interest, since the crustal structural characteristics of these regions were still poorly known. Results from the present work are also important from the social point of view, since they represent a contribution to seismic hazard assessment in the target regions.

Chapter 5 presents the estimation of three-dimensional spatial distribution of relative scattering coefficients for the Gauribidanur seismic array (GBA) site in southern India. Data used consisted of selected 636 vertical-component, short period recordings of microearthquake codas from shallow earthquakes with magnitudes ranging from 0.7 to 3.7 and epicentral distances up to 120 km from the array centre

point. Results were almost independent of the inversion method used (SIRT and Filtered Backprojection) and they were frequency dependent. They showed a remarkably uniform distribution of the scattering strength in the crust around GBA. However, a shallow (0-24 km) strong scattering structure, which is only visible at low frequencies, seems to coincide with the Closepet granitic batholith which is the boundary between the eastern and western parts of the Dharwar craton.

Finally, Chapter 6 presents the three-dimensional spatial distribution of relative scattering coefficients for the Galeras volcano, Colombia. Coda wave envelopes came from 1564 high quality seismic recordings by 31 stations of the Galeras seismograph network. Results revealed a highly non-uniform distribution of relative scattering coefficients in the region for the two analyzed frequency bands (4-8 and 8-12 Hz). Strong scatterers showed frequency dependence, which was interpreted in terms of the scale of the heterogeneities producing scattering. Two zones of strong scattering were detected: the shallower one is located at a depth from 4 km to 8 km under the summit whereas the deeper one is imaged at a depth of ~37 km from the Earth's surface. Both zones may be correlated with the magmatic plumbing system beneath Galeras volcano. The second strong scattering zone may be related to the deeper magma reservoir that feeds the system.

Although the analysis method used assumes simple models of scattering, seismic source radiation, attenuation and velocity structure, the scattering images obtained appear to be coherent with the available geological information. The synthetic tests performed corroborate this assertion.

Concluding, the coda analysis method presented in this thesis seems to be one of effective approaches to investigate the real heterogeneous structure in the crust deterministically. We believe it is a very useful method for this purpose and we encourage further applications to other seismically active regions in the world. The improvement of the underlying scattering model to a more realistic one would be also necessary.



## APPENDIX A. EVENTS AT GBA REGION

In this appendix the events at the Gauribidanur seismic array region corresponding to the period 1992-1995 are identified with the corresponding date, origin time, distance (in km) to the array centre point, location coordinates and local magnitude. Depth of hypocenter is about 10 km for all the events.

Date			Origin Time (GMT)			Coordinates Hypocenter			Magnitude
d	m	y	hr	min	sec	D(km)	Lat (°N)	Long (°E)	
18	1	1992	11	12	31.0	51	13.37	77.02	2.2
4	2	1992	6	17	34.0	18	13.51	77.30	1.6
5	2	1992	7	10	34.0	91	13.14	76.74	1.0
23	2	1992	13	11	39.0	73	13.08	77.03	1.0
27	2	1992	12	18	49.0	93	14.42	77.63	1.1
7	3	1992	11	16	54.0	23	13.50	77.25	1.1
23	7	1992	8	49	54.0	81	14.31	77.23	1.2
3	8	1992	7	48	13.0	25	13.47	77.25	0.9
9	8	1992	12	6	24.0	31	13.84	77.59	0.7
9	8	1992	9	18	23.0	91	12.85	77.10	1.1
9	8	1992	9	35	16.0	91	12.85	77.10	1.0
12	8	1992	7	45	35.0	40	13.91	77.63	1.8
14	8	1992	12	4	48.0	44	13.94	77.65	1.4
16	8	1992	7	48	9.0	46	13.92	77.72	1.5
18	8	1992	13	20	21.0	41	13.88	77.70	0.8
4	11	1992	7	41	21.0	84	12.98	77.88	1.1
24	11	1992	6	59	32.0	104	14.47	77.82	2.1
24	12	1992	8	48	13.0	111	14.46	76.90	1.4
28	1	1993	9	23	36.0	41	13.59	77.05	1.7
6	4	1993	18	40	11.4	70	14.15	77.45	3.0
24	7	1993	6	6	7.0	75	12.94	77.59	2.9
28	7	1993	13	2	39.0	84	13.06	76.90	1.3
30	8	1993	8	49	21.0	85	13.23	78.13	1.6
12	10	1993	3	1	58.0	82	13.08	77.97	2.9
9	11	1993	13	34	46.0	59	13.07	77.41	2.0
12	2	1994	9	1	56.0	111	12.83	78.09	1.6
7	4	1994	5	9	49.0	90	14.30	77.86	1.7
2	5	1994	12	40	14.0	80	14.19	77.87	1.4
9	5	1994	11	49	40.0	81	13.84	78.15	2.8
18	6	1994	13	0	28.0	97	14.41	77.78	2.0
21	6	1994	12	48	19.0	97	14.27	78.03	1.6
23	6	1994	12	20	35.0	91	12.78	77.44	2.1
25	6	1994	13	57	55.0	96	14.31	77.95	2.0
29	6	1994	8	56	37.0	100	13.88	78.32	1.4

Date			Origin Time (GMT)			Coordinates Hypocenter			Magnitude
d	m	y	hr	min	sec	D(km)	Lat (°N)	Long (°E)	
29	6	1994	12	27	56.0	101	14.34	77.99	1.9
30	6	1994	8	14	51.0	100	13.91	78.31	1.7
25	1	1995	23	24	39	116	12,62	77,79	1,5
12	2	1995	5	6	36	100	12,91	76,85	1,5
12	2	1995	23	0	7	105	12,87	76,82	2,3
20	2	1995	3	54	0	63	13,92	77,92	1
12	3	1995	23	8	16	115	12,62	77,78	1,2
26	4	1995	6	28	18	79	13,66	78,17	1,9
25	5	1995	2	2	22	98	14,31	77,98	1,3
21	8	1995	11	57	50	91	13,11	76,76	1,3
26	8	1995	8	22	46	91	13,14	76,74	1,3
7	9	1995	12	53	36	17	13,73	77,35	0,9
17	9	1995	4	49	33	84	12,85	77,47	1,4
19	9	1995	11	35	37	95	13,09	76,73	1,3
1	10	1995	4	59	33	65	13,02	77,54	2,4
8	11	1995	12	27	50	111	14,46	77,99	1,5
15	11	1995	7	16	36	119	13,04	76,5	1,3
22	11	1995	12	8	10	118	14,51	78,02	1,2
4	12	1995	9	31	5	83	12,89	77,69	2,4
13	12	1995	16	26	27	109	14,48	77,9	1,4
15	12	1995	22	45	15	92	12,8	77,21	1,8
29	12	1995	12	49	59	113	14,47	77,99	1,9

## APPENDIX B. EVENTS AT GALERAS VOLCANO

In this appendix the events at Galeras volcano corresponding to the period 1989-1992 and 1993-2002 are identified with a number, the corresponding date and origin time, location coordinates depth and local magnitude.

### Events from 1982 to 1992

N	Code	Origin Time			Latitude		Longitude		Depth	Mag.
	yymmddx	Hour	Min.	Sec.	Deg.	Min.	Deg.	Min.	km	
0	8908040i	15	16	14.99	1	14.85	77	21.85	5	0.96
1	8908130u	23	28	2.97	1	13.26	77	22.15	3.49	1.15
2	8908150b	11	27	44.09	1	13.24	77	22.34	2.61	0.46
3	89091701	1	8	59.01	1	13.39	77	23.68	0.94	-0.32
4	89092607	7	9	15.92	1	12.24	77	20.76	0.85	0.81
5	89100111	22	22	46.38	1	13.21	77	22.02	2.99	0.58
6	8910220v	23	21	11.74	1	13.36	77	22.93	3.71	0.61
7	8910250c	7	4	17.75	1	12.51	77	21.76	4.91	1.2
8	89110505	2	29	40.92	1	13.53	77	23.19	3.13	0.37
9	89110605	3	31	25.13	1	13.37	77	22.99	2.69	1.04
10	89111804	2	53	55.07	1	13.31	77	22.67	2.4	0.79
11	8911261q	15	43	9.71	1	12.93	77	21.71	3.12	0.35
12	8912062k	17	29	44.43	1	13.26	77	23.01	3.3	0.81
13	8912062m	17	32	58.61	1	13.18	77	23.06	3.2	0.94
14	8912100u	20	26	56.46	1	13.13	77	22.83	5	0.82
15	89121303	4	14	31.39	1	12.8	77	23.01	5	0.66
16	8912230c	3	50	4.21	1	13.26	77	22.98	2.82	0.81
17	9001131u	21	55	37.82	1	12.7	77	22.4	2.44	0.67
18	9001181o	8	19	13.69	1	13.23	77	22.98	3.74	0.5
19	9001250g	13	17	24.84	1	13.34	77	21.92	3.99	0.15
20	90012802	4	51	39.5	1	13.27	77	22.98	3.44	1.05
21	90012803	4	57	8.66	1	13.25	77	23.07	4.85	0.76
22	90020415	14	24	17.14	1	12.73	77	23.04	2.99	0.86

N	Code	Origin Time			Latitude		Longitude		Depth	Mag.
	yymmddx	Hour	Min.	Sec.	Deg.	Min.	Deg.	Min.	km	
23	90020504	2	51	17.75	1	12.67	77	22.11	4.95	0.71
24	90020602	1	8	47.58	1	13.53	77	23.66	3.14	1
25	90020809	6	30	30.11	1	12.6	77	21.83	4.1	0.62
26	90020901	2	21	12.17	1	13.63	77	23.32	5.29	1.05
27	90022109	10	15	40.65	1	13	77	25.29	5.45	0.8
28	90022308	14	25	13.74	1	13.24	77	23.46	3.53	0.46
29	90022309	14	26	9	1	13.24	77	23.47	3.66	1.19
30	90022408	11	13	41.55	1	13.25	77	23.5	2.96	0.88
31	90030403	3	39	11.88	1	13.27	77	23.59	3.29	0.75
32	90030406	7	44	59.89	1	13.3	77	23.59	3.56	0.74
33	90030408	7	49	50.63	1	13.37	77	23.6	3.09	0.76
34	9003040a	9	44	44.63	1	13.34	77	23.56	3.27	0.81
35	90030801	2	17	28.09	1	13.24	77	23.11	3.51	0.94
36	90031702	2	24	35.22	1	13.26	77	23.61	4.29	0.75
37	9003261m	19	38	51.3	1	14.91	77	21.83	6.81	0.71
38	90032920	19	56	30.77	1	12.81	77	21.61	3.73	0.07
39	9004011h	11	37	17.8	1	13.49	77	23.08	4.4	0.62
40	90040409	3	44	16.33	1	13.43	77	22.85	3.91	0.59
41	9004040g	5	52	11.33	1	13.75	77	22.78	4.52	0.37
42	90040401	7	31	2.38	1	13.27	77	22.57	6.3	0.89
43	90040417	11	5	5.87	1	13.46	77	22.74	3.22	0.47
44	9004041r	15	3	27.45	1	12.74	77	22.94	4.39	0.34
45	90042605	1	39	28.77	1	13.09	77	22.22	2.68	0.77
46	90050506	0	42	46.1	1	12.68	77	21.97	3.62	0.79
47	9005050a	1	53	39.07	1	13.67	77	23.1	3.08	1.16
48	9005050m	5	41	59.64	1	13.67	77	23.14	3.29	0.69
49	9005050r	7	9	0.98	1	12.74	77	21.82	3.55	0.9
50	9005060f	5	18	9.79	1	13.77	77	23.1	3.05	0.73
51	90051102	3	7	44.14	1	13.23	77	23.47	2.8	0.7
52	9005110h	9	58	51.6	1	13.4	77	22.47	2.49	0.46

N	Code	Origin Time			Latitude		Longitude		Depth	Mag.
	yymmddx	Hour	Min.	Sec.	Deg.	Min.	Deg.	Min.	km	
53	90051702	6	59	24.46	1	13.38	77	22.99	3.73	0.2
54	9005270n	14	59	10.51	1	13.79	77	23.43	4.52	0.71
55	90052712	15	51	12.99	1	13.26	77	23.2	3.48	0.89
56	90052800	4	3	39.14	1	13.38	77	22.69	3.85	0.69
57	90052801	8	30	27.83	1	13.36	77	22.85	3.59	0.65
58	90080801	4	56	50.62	1	12.99	77	23.19	3	0.8
59	9008181f	20	6	17.01	1	12.5	77	22.92	3.15	-0.01
60	90082614	14	42	27.5	1	12.74	77	22.81	3.55	0.8
61	90082700	9	13	35.12	1	12.74	77	23.14	4.3	0.7
62	90082705	12	35	5.38	1	12.95	77	22.93	4.84	0.44
63	9008281b	12	2	18.9	1	12.74	77	22.98	4.62	0.51
64	90083015	14	8	52.05	1	12.97	77	22.89	3.68	0.48
65	90090307	1	3	55.21	1	12.65	77	22.97	4.13	0.53
66	9009061u	18	19	24.61	1	12.88	77	22.73	4.59	1.53
67	90110709	15	17	33.28	1	12.05	77	20.82	4.35	1.17
68	9012071a	17	10	39.82	1	12.98	77	23.12	3.4	1.5
69	9104222v	17	32	5.81	1	12.68	77	23.56	2.43	1.03
70	91042233	17	58	14.09	1	12.5	77	23.6	4.24	1.48
71	91050111	18	20	55.27	1	12.41	77	23.72	2.97	1.27
72	91052906	2	13	12.59	1	13.21	77	22.79	4.27	0.99
73	91052907	2	17	44.05	1	13.1	77	22.97	4.03	0.68
74	9109191r	8	18	45.39	1	14.29	77	21.26	3.48	0.78
75	9206020u	21	34	5.28	1	13.28	77	21.46	3.17	0.7
76	92080404	5	49	5.26	1	13.44	77	21.91	0.8	0.92
77	92081616	15	24	5.21	1	13.44	77	22.01	0.79	1.01

## Events from 1993 to 2002

N	Code	Origin Time			Latitude	Longitude	Depth	Mag.
	yymmddx	H	M	S	Deg. Min.	Deg. Min.	km	
78	93040800	6	4	2.99	1 13.49	77 22.12	1.48	1
79	93041100	2	59	26.93	1 13.17	77 22.65	6	1.03
80	9304262u	17	0	55.18	1 14.75	77 22.11	3.51	1.29
81	9304270a	0	54	0.98	1 14.85	77 22.04	4.36	1.25
82	9304270d	1	2	50.22	1 14.81	77 22.14	4.24	1.37
83	9304270f	1	12	9.87	1 14.88	77 21.95	4.24	1.33
84	9304270p	2	2	24.36	1 13.51	77 21.96	3.82	0.87
85	9304270u	2	10	2.72	1 15.06	77 21.76	4.62	1.19
86	93042707	0	52	6.08	1 14.89	77 22.07	4.25	1.59
87	93042708	0	52	6.07	1 14.91	77 22.07	4.32	1.22
88	9304271b	5	12	9.68	1 15.35	77 21.97	4.92	1.11
89	9304271g	8	30	10.6	1 15.19	77 22.06	4.67	1.41
90	9304271x	16	56	56.41	1 14.63	77 22.27	3.59	1.68
91	93042712	3	6	57.38	1 15.24	77 21.97	4.69	1.12
92	9304272d	20	23	23.01	1 15.18	77 21.95	4.36	1.53
93	93042802	0	41	49.18	1 15.45	77 21.93	5.41	1.45
94	93042808	3	46	4.02	1 14.90	77 21.93	3.83	1.6
95	93042901	12	14	30.4	1 14.68	77 22.15	3.64	1.32
96	93050102	2	37	41.82	1 14.80	77 21.95	4.35	1.32
97	93050201	10	16	52.03	1 15.27	77 21.95	4.62	1.58
98	93050906	3	33	11.93	1 14.84	77 21.47	4.73	1.06
99	9305130x	14	19	11.51	1 14.77	77 21.58	4.79	1.16
100	93051903	6	27	7	1 14.93	77 22.17	3.44	1.55
101	93052015	10	42	16.11	1 14.91	77 21.53	7.03	1.93
102	930602gx	20	25	49.16	1 12.98	77 26.01	9.02	2.08
103	9308052q	3	25	15.23	1 12.54	77 21.13	8.3	1.19
104	93102006	11	9	9.05	1 13.11	77 21.53	0.54	1.08
105	93103007	5	32	59.04	1 13.71	77 23.15	2.1	0.27
106	9312010m	4	18	14.65	1 14.91	77 21.65	4.35	1.12

N	Code	Origin Time			Latitude	Longitude	Depth	Mag.
	yymmddx	H	M	S	Deg. Min.	Deg. Min.	km	
107	9312011p	11	9	49.01	1 14.59	77 21.52	4.09	1.08
108	9407271h	16	49	17.11	1 13.43	77 23.55	6.61	0.44
109	9408093i	8	22	20.93	1 13.13	77 21.80	3.58	0.49
110	94081206	1	52	37.45	1 14.66	77 21.43	3.3	1.1
111	9412142u	23	32	7.21	1 13.82	77 22.04	1.53	0.42
112	9412230c	7	13	12.47	1 14.59	77 21.62	6.75	0.99
113	95011102	0	31	0.17	1 12.22	77 23.30	5.55	0.96
114	95021202	1	19	26.44	1 15.05	77 22.04	3.91	0.95
115	95021418	12	9	38.87	1 13.86	77 24.09	1.09	1.37
116	9502234f	22	28	51.94	1 13.56	77 24.62	5.86	0.94
117	9503041i	18	39	25.03	1 14.64	77 21.63	4.17	1.42
118	9503041t	18	49	2.24	1 14.57	77 21.59	4.53	1.37
119	9503041x	18	52	25.56	1 14.59	77 21.40	4.61	1.39
120	9503042w	19	26	16.94	1 14.40	77 21.22	4.89	0.77
121	95030434	19	34	12.96	1 14.76	77 21.52	4.04	1.44
122	9503043g	19	44	54.63	1 15.11	77 21.67	5.39	0.76
123	9503043i	19	47	54.62	1 14.65	77 21.44	5.17	1.1
124	95030502	0	2	16.75	1 14.89	77 21.52	4.57	1.26
125	9503052p	4	2	35.03	1 14.72	77 21.45	4.14	1.46
126	9503056r	12	49	12.32	1 14.70	77 21.38	4.71	0.84
127	9503058s	16	41	55.42	1 14.28	77 21.65	4.36	0.72
128	9503059m	19	25	43.65	1 14.89	77 21.55	4.4	1.12
129	9503059y	20	17	54.88	1 14.33	77 21.50	5.17	0.98
130	9503060u	3	44	8.31	1 14.79	77 21.60	4.62	1.12
131	95030720	10	34	53.34	1 14.72	77 21.70	4.83	0.93
132	95030806	0	23	9.53	1 14.79	77 21.56	4.8	1.21
133	9503083o	16	44	39.98	1 14.93	77 21.79	3.92	1.03
134	95030915	9	33	15.26	1 15.06	77 21.77	4.68	1.34
135	9503094h	23	21	13.12	1 15.64	77 18.73	5.31	0.72
136	9503100t	0	49	11.72	1 15.02	77 21.65	4.48	0.95

N	Code	Origin Time			Latitude	Longitude	Depth	Mag.
	yymmddx	H	M	S	Deg. Min.	Deg. Min.	km	
137	9503100z	0	56	15.96	1 15.37	77 19.55	6.37	0.27
138	95031012	0	58	12.42	1 15.24	77 19.53	7.02	1.63
139	95031013	0	59	46.15	1 15.25	77 20.04	6.46	1.25
140	95031008	0	24	40.53	1 15.53	77 18.83	5.76	1.76
141	9503101e	1	24	47.88	1 14.91	77 21.60	4.54	0.93
142	9503109s	23	36	42.19	1 15.30	77 21.31	5.12	0.78
143	95031091	21	34	54.7	1 15.11	77 21.61	5.17	1.96
144	95031107	1	35	47.57	1 15.45	77 19.08	7.08	0.67
145	9503113r	20	58	54.86	1 15.14	77 19.29	5.81	1.12
146	95031141	22	7	31.95	1 15.86	77 20.35	7.21	1.48
147	95031207	2	55	5.61	1 15.19	77 19.14	4.77	1.12
148	9503121f	11	36	23.67	1 15.44	77 18.90	4.83	0.78
149	9503121i	12	28	9.07	1 15.53	77 20.62	5.92	1
150	9503122s	20	13	55.83	1 15.47	77 19.03	7.84	1.22
151	9503123a	23	15	46.29	1 15.80	77 20.01	6.13	0.91
152	9503130g	4	49	33.17	1 15.84	77 20.42	4.77	0.88
153	9503130j	5	27	42.48	1 15.64	77 18.43	5.73	1.24
154	9503130r	7	15	49.06	1 15.08	77 21.43	5.78	1.45
155	9503130t	7	44	37.08	1 15.43	77 21.50	4.97	1.54
156	9503131x	13	12	37.93	1 15.23	77 19.85	6.29	1.19
157	9503131y	13	13	32.76	1 15.56	77 18.20	5.41	0.99
158	9503140i	5	19	34.53	1 15.67	77 18.70	4.47	0.72
159	9503140r	7	1	42.35	1 15.16	77 19.86	6.09	1.01
160	95031402	1	7	45.72	1 15.57	77 20.97	6.39	1
161	9503142i	19	14	21.45	1 15.54	77 19.76	6.2	1.11
162	9503142k	19	18	21.44	1 15.23	77 20.03	6.7	0.92
163	9503150h	6	3	29.14	1 15.86	77 18.94	4.27	0.99
164	9503150v	8	10	1.31	1 15.59	77 19.19	7.98	1.11
165	95031605	1	35	35.47	1 15.70	77 20.07	6.27	1.05
166	9503162f	21	58	56.02	1 15.43	77 20.47	6.88	1.03

N	Code	Origin Time			Latitude	Longitude	Depth	Mag.
	yymmddx	H	M	S	Deg. Min.	Deg. Min.	km	
167	95031623	19	8	8.27	1 15.94	77 20.64	6.33	0.99
168	9503170x	12	25	52.6	1 15.59	77 18.58	5.53	0.99
169	9503170z	12	33	50.9	1 15.34	77 19.00	4.94	1.13
170	95031704	2	32	6.24	1 15.56	77 18.82	5.79	0.98
171	9503171m	18	10	30.86	1 15.63	77 18.64	4.86	0.82
172	9503172b	21	9	52.38	1 15.05	77 19.06	5.45	1.08
173	9503172q	23	55	10.81	1 15.18	77 19.02	5.73	0.91
174	9503180d	6	54	8.54	1 15.25	77 19.21	5.76	1.09
175	95031801	1	32	41.94	1 15.42	77 19.09	5.31	0.89
176	9503191a	16	58	35.7	1 15.32	77 19.14	4.82	0.85
177	9503191p	18	55	54.3	1 15.61	77 18.40	5.15	0.9
178	95032004	14	50	51.41	1 15.12	77 19.08	5.16	0.91
179	95032020	21	0	22.34	1 15.59	77 18.30	5.15	1.11
180	95032024	21	58	31.39	1 15.77	77 19.43	6.31	1.11
181	9503211b	16	52	23.01	1 15.63	77 19.32	5.03	1.22
182	9503220x	7	31	18.76	1 15.71	77 19.12	5.2	1.16
183	95032217	9	18	22.06	1 15.69	77 20.85	6.52	1.11
184	95040106	4	6	49.13	1 15.70	77 18.70	5.41	1.17
185	9504030t	15	5	34.49	1 15.74	77 21.27	5.91	0.69
186	95040410	5	57	8.4	1 15.35	77 19.09	7.35	0.98
187	95040501	0	41	39.16	1 15.70	77 18.92	6.34	0.8
188	9504057e	22	20	22.46	1 15.30	77 19.12	5.39	0.61
189	95040605	4	5	2.93	1 15.44	77 19.69	6.22	0.64
190	9504140b	3	20	26.82	1 13.43	77 22.01	2.62	1.23
191	95041406	3	16	25.33	1 13.43	77 22.01	2.74	0.95
192	9504140n	4	32	35.63	1 13.40	77 21.99	2.42	1.14
193	95041701	0	2	9.86	1 14.08	77 21.22	5.97	1.02
194	95041702	0	8	10.22	1 14.50	77 20.94	5.88	1.28
195	9504181r	16	12	31.09	1 15.56	77 18.69	5.08	1.04
196	9505030u	11	35	31.24	1 15.56	77 17.36	7.77	1.34

N	Code	Origin Time			Latitude	Longitude	Depth	Mag.
	yymmddx	H	M	S	Deg. Min.	Deg. Min.	km	
197	95050304	2	40	42.41	1 15.68	77 19.09	7.85	0.9
198	95050502	0	49	12.91	1 14.96	77 19.61	6.88	1.05
199	95050603	3	5	48.77	1 15.75	77 20.04	6.79	1.73
200	9505070e	15	19	0.03	1 15.34	77 19.83	6.64	0.88
201	9505150x	23	38	15.54	1 15.29	77 21.80	5.68	1.38
202	9505191i	17	15	35.94	1 15.78	77 19.58	6.29	0.77
203	95052111	16	59	51.38	1 14.61	77 21.58	6.58	0.79
204	95052613	23	33	6.87	1 14.52	77 20.50	7.64	1.24
205	9505280t	19	13	35.16	1 15.67	77 19.46	6.26	0.97
206	9506020k	11	22	50.62	1 15.01	77 18.81	5.48	0.92
207	95060207	10	2	16.48	1 14.76	77 18.76	6.36	0.84
208	95060210	15	47	42.83	1 15.08	77 18.55	5.29	0.99
209	9506040d	10	42	15.57	1 15.26	77 21.60	5.06	1.68
210	9506080b	9	22	49.04	1 14.93	77 19.58	6.07	1.27
211	95060807	5	36	57.6	1 15.52	77 19.56	6.72	1.27
212	9506100e	16	0	54.29	1 15.66	77 19.19	7.09	0.84
213	95061203	4	51	35.76	1 15.86	77 20.05	6.87	0.78
214	95061405	3	21	14.86	1 15.18	77 20.83	6.41	0.88
215	95061607	16	9	53.76	1 15.73	77 20.12	7.02	1.14
216	95061704	4	3	43.81	1 15.83	77 20.20	6.91	1.17
217	95062108	7	32	3.77	1 14.06	77 23.54	3.25	0.86
218	9506300k	23	0	21.06	1 15.59	77 18.71	4.52	0.78
219	9507051o	18	8	27.71	1 14.90	77 19.00	5.61	1
220	95070516	13	21	30.41	1 14.75	77 20.10	5.68	1.1
221	9507060n	14	10	5.14	1 14.81	77 19.14	5.93	0.71
222	9507070h	6	32	50.95	1 14.90	77 18.92	6.06	1.03
223	95070702	2	42	19.56	1 15.00	77 18.95	5.97	1.15
224	95071814	12	0	3.28	1 14.22	77 19.75	6.3	1.22
225	95072503	1	2	12.6	1 15.44	77 20.29	6.93	1.26
226	95072905	1	30	14.42	1 15.91	77 19.82	6.93	1.02

N	Code	Origin Time			Latitude	Longitude	Depth	Mag.
	yymmddx	H	M	S	Deg. Min.	Deg. Min.	km	
227	95073021	3	30	20.86	1 14.02	77 20.60	5.86	1.48
228	9507311h	21	44	38.36	1 15.71	77 18.30	7.94	0.98
229	9508080k	23	56	57.5	1 15.38	77 19.40	5.15	1.4
230	9508092p	20	7	45.58	1 16.15	77 19.22	7.01	1.37
231	95081104	2	5	54.25	1 15.79	77 20.16	5.98	1.09
232	9508162u	12	11	25.34	1 15.62	77 18.99	5.28	1.27
233	95081717	20	56	18.59	1 15.91	77 19.90	6.97	0.96
234	9508281t	21	7	55.86	1 15.65	77 20.25	5.74	1.41
235	9509032o	3	32	35.19	1 15.78	77 21.63	5.79	0.85
236	9510120y	10	48	42.22	1 15.24	77 21.98	6.03	1.22
237	9510167f	7	54	45.37	1 14.70	77 21.41	5.52	1.79
238	9510190s	8	36	5.18	1 15.06	77 21.79	4.38	1.61
239	9511171g	17	58	25.23	1 15.64	77 20.05	6.26	
240	9511240h	10	2	49.59	1 14.12	77 19.58	6.49	1.29
241	9512050y	14	15	22.27	1 15.82	77 19.82	6.71	1.56
242	95120511	14	35	2.29	1 15.78	77 19.48	6.73	1.08
243	95120615	14	8	1.54	1 15.85	77 19.94	6.7	1.37
244	9601120j	8	7	41.86	1 15.46	77 20.15	4.09	0.48
245	96011307	4	54	23.06	1 16.49	77 19.18	6.07	0.56
246	9601151h	17	28	33.68	1 16.02	77 19.52	6.23	1.22
247	96011515	14	57	23.42	1 15.96	77 18.98	4.88	0.89
248	9601310v	16	57	14.46	1 15.84	77 19.40	6.28	0.55
249	9602051v	11	49	50.85	1 15.41	77 19.32	4.68	0.56
250	9602160z	9	15	36.48	1 13.90	77 20.22	7.48	1.26
251	96041608	14	59	57.66	1 16.26	77 19.55	4.76	0.76
252	9605080t	16	4	20.04	1 15.88	77 19.66	5.95	0.96
253	9605130e	16	14	22.26	1 16.16	77 19.60	5.37	0.89
254	9605300b	9	29	26.89	1 13.98	77 20.01	6.49	1.32
255	96060205	4	48	36.26	1 13.45	77 24.41	3.74	0.59
256	96080307	1	38	33.01	1 15.48	77 18.72	6.03	0.2

N	Code	Origin Time			Latitude	Longitude	Depth	Mag.
	yymmddx	H	M	S	Deg. Min.	Deg. Min.	km	
257	96081908	8	18	13.95	1 16.03	77 19.86	7.36	0.72
258	9608260d	10	18	13.78	1 16.60	77 19.89	7.54	0.63
259	9609011q	9	53	25.29	1 15.90	77 18.93	5.73	1.11
260	9609100d	5	9	15.4	1 14.46	77 23.50	7.3	0.73
261	96100909	10	32	15.13	1 16.04	77 19.72	6.22	0.86
262	9610110f	9	23	52.18	1 14.98	77 20.58	5.49	0.53
263	9610110l	11	33	45.4	1 15.00	77 20.30	5.44	0.82
264	9610110o	12	58	37.01	1 14.99	77 20.73	5.05	1
265	9610110w	14	13	47.34	1 15.04	77 20.28	5.11	0.77
266	96101119	18	6	53.94	1 14.92	77 20.90	5.56	1.1
267	9610121q	14	19	20.04	1 16.08	77 20.10	6.23	0.6
268	96102412	16	8	51.23	1 15.46	77 19.18	4.52	0.54
269	9610280d	3	46	32.65	1 16.35	77 18.75	6.26	0.98
270	96102816	19	37	37.17	1 16.55	77 20.87	9.72	0.58
271	96103107	5	4	19.67	1 15.81	77 18.88	5.33	0.92
272	9611080s	14	1	5.38	1 16.49	77 21.50	4.47	1.39
273	9611081e	18	59	19.85	1 16.49	77 21.25	5.35	1.55
274	96111804	3	8	21.82	1 16.04	77 19.41	6.58	1.06
275	9701120k	4	14	36.24	1 15.86	77 20.45	6.32	0.56
276	9701120m	4	15	58.15	1 15.51	77 19.53	4.24	0.3
277	9701120o	4	16	54.2	1 16.01	77 20.05	5	0.59
278	9701120p	4	18	6.12	1 15.91	77 19.86	4.17	0.19
279	9701130c	7	19	12.8	1 15.56	77 19.45	3.51	0.47
280	97011814	23	41	11.16	1 13.57	77 21.77	3.31	0.44
281	97012315	9	10	29.88	1 15.69	77 19.52	4.53	0.62
282	97020201	1	18	52.36	1 14.94	77 20.84	5.8	0.33
283	97021401	0	23	38.43	1 15.50	77 19.77	5.74	0.72
284	97022214	17	1	38.43	1 16.44	77 21.49	4.32	0.96
285	9703020f	9	47	33.51	1 16.12	77 19.74	6.04	1.6
286	9703051s	18	36	17.66	1 16.50	77 21.49	4.53	0.71

N	Code	Origin Time			Latitude	Longitude	Depth	Mag.
	yymmddx	H	M	S	Deg. Min.	Deg. Min.	km	
287	9703051u	18	47	20.5	1 16.44	77 21.50	4.05	0.99
288	97030607	3	35	20.26	1 15.77	77 20.04	4.97	0.78
289	9703085k	17	16	33.56	1 16.39	77 21.50	4.41	1
290	97031910	20	52	52.68	1 15.74	77 20.53	4.85	0.12
291	9703220a	4	41	10.77	1 15.93	77 17.22	7.81	0.72
292	97032213	15	19	10.89	1 16.14	77 21.52	3.9	1.09
293	9704040m	14	0	15.32	1 15.64	77 21.11	4.01	0.6
294	9704041b	22	10	38.71	1 15.55	77 21.24	3.77	0.52
295	9704140r	11	58	35.85	1 15.90	77 19.00	4.94	0.76
296	97041500	0	27	56.06	1 16.19	77 20.35	6.56	0.98
297	9704171f	14	4	17.35	1 16.12	77 19.80	7.89	0.92
298	97041818	16	35	35.94	1 16.30	77 21.48	4.65	0.71
299	97042112	13	58	54.9	1 15.52	77 19.39	4.01	0.59
300	9704290n	16	21	46.33	1 16.39	77 21.35	4.78	1.28
301	9704300z	22	45	18.55	1 15.90	77 19.98	5.39	1.11
302	97051126	20	17	30.31	1 15.89	77 19.36	5.48	0.87
303	9705197t	18	29	47.13	1 14.90	77 21.05	5	0.66
304	9705215h	18	26	48.84	1 16.19	77 18.87	7.72	0.93
305	9705221s	12	24	21.83	1 16.45	77 21.34	5.13	0.83
306	9705221z	16	56	45.56	1 16.50	77 21.37	4.66	1.03
307	9705260c	10	42	3.64	1 16.42	77 21.49	4.37	0.85
308	97060300	0	3	43.92	1 14.58	77 20.97	5.67	0.91
309	9706170l	16	16	0.47	1 16.43	77 21.29	4.67	0.93
310	9706220t	13	51	58.77	1 16.46	77 21.48	4.83	0.76
311	9706260g	12	31	33.38	1 16.60	77 21.13	6.43	0.96
312	970718im	16	20	28.54	1 16.37	77 21.64	5.26	1.36
313	9708215i	16	27	31.44	1 16.10	77 21.41	3.84	1.1
314	97091214	15	46	44.68	1 16.28	77 20.98	5.83	1.3
315	9709130a	7	32	32.41	1 16.20	77 21.11	2.9	0.76
316	97092000	0	23	11.71	1 12.83	77 24.00	3.59	0.75

N	Code	Origin Time			Latitude	Longitude	Depth	Mag.
	yymmddx	H	M	S	Deg. Min.	Deg. Min.	km	
317	971226by	14	50	23.09	1 16.35	77 21.58	4.37	1.06
318	9712260f	0	40	59.47	1 15.64	77 19.84	5.04	0.85
319	9712261y	4	24	19.56	1 14.02	77 23.30	1.51	0.4
320	9801201o	15	18	52.38	1 16.41	77 21.65	4.74	0.97
321	9801271m	14	40	59.48	1 16.06	77 21.31	4.07	0.97
322	98012723	17	11	38.08	1 15.87	77 19.94	5.56	0.79
323	9802031a	10	19	5.13	1 16.30	77 21.63	4.11	0.92
324	98020406	2	13	15.67	1 15.53	77 20.36	5.7	0.91
325	9802181m	11	52	19.53	1 15.51	77 20.35	4.71	0.17
326	98021906	4	25	45.54	1 14.08	77 20.89	5.08	0.62
327	98021927	13	58	14.05	1 13.10	77 23.12	1.97	0.66
328	9802220d	11	8	34.47	1 13.76	77 21.80	2.46	0.18
329	9802230t	10	22	26.47	1 15.48	77 19.50	5.8	0.31
330	9802231m	18	18	16.56	1 13.05	77 21.78	0.95	1.08
331	9802231w	22	47	31.74	1 15.31	77 21.15	5.13	0.21
332	98030101	0	39	24.79	1 15.33	77 20.59	4.9	0.33
333	9803040u	7	22	2.56	1 14.99	77 20.26	5.08	0.41
334	98030610	9	31	8.92	1 15.43	77 17.82	8.06	0.83
335	98031810	8	16	7.16	1 13.23	77 20.67	5.12	0.46
336	9804090e	4	56	18.63	1 15.57	77 18.58	9.75	1.07
337	9804145q	22	4	57.32	1 14.10	77 21.15	3.45	0.43
338	98042908	8	34	5.08	1 15.90	77 19.85	6.63	0.59
339	98052509	6	5	1.15	1 15.77	77 19.55	8.35	1.45
340	98052555	17	19	14.44	1 14.86	77 21.30	5.6	0.28
341	98052708	4	12	55.77	1 14.58	77 21.25	6.01	0.6
342	98052968	15	39	6.52	1 16.38	77 21.49	4.39	0.86
343	9806020o	11	25	0.02	1 13.06	77 21.71	1.36	0.18
344	9806111j	16	51	3.57	1 14.60	77 20.32	6.8	0.41
345	9806267m	19	22	21.1	1 17.06	77 18.60	9.02	0.37
346	98071300	1	25	42.47	1 15.74	77 20.53	4.87	0.73

N	Code	Origin Time			Latitude	Longitude	Depth	Mag.
	yymmddx	H	M	S	Deg. Min.	Deg. Min.	km	
347	980716a6	22	51	39.17	1 13.34	77 21.60	4.02	0.87
348	980722dm	15	42	31.17	1 15.64	77 19.87	6.01	0.12
349	980722dn	15	42	56.99	1 15.63	77 19.26	5.01	0.53
350	98072332	14	22	14.91	1 15.79	77 19.97	5.47	0.75
351	9807254m	15	52	55.51	1 15.41	77 20.29	5.04	0.67
352	9808100e	5	20	34.22	1 13.92	77 21.24	4.39	0.18
353	9808155v	14	49	40.29	1 16.44	77 21.57	4.39	1.12
354	98081669	17	44	34	1 16.10	77 18.80	6.44	1.02
355	9808210e	1	57	10.92	1 11.94	77 21.16	4.1	0.51
356	98082350	11	5	59.96	1 14.89	77 20.48	3.57	0.55
357	9808270j	4	14	53.18	1 13.31	77 21.94	0.51	0.4
358	9903124s	19	38	36.76	1 15.45	77 19.61	5.67	0.39
359	9903220l	13	3	12.3	1 12.80	77 21.88	5.81	0.2
360	9903265q	15	18	43.27	1 14.25	77 23.46	4.41	0.26
361	9903295r	22	37	17.79	1 15.18	77 19.20	5.84	0.28
362	99042529	23	35	39.58	1 16.24	77 18.41	7.25	1.06
363	9905040e	9	19	30.05	1 13.14	77 24.91	6.09	0.55
364	9905089i	16	19	49.5	1 15.79	77 17.16	6.58	0.37
365	9905230s	11	17	30.49	1 15.82	77 19.25	4.75	0.79
366	99061400	2	7	19.43	1 16.61	77 19.62	6.54	1.21
367	99062600	0	4	53.19	1 15.76	77 19.96	5.73	0.27
368	99062664	16	53	16.77	1 15.35	77 19.59	5.18	0.96
369	9906290e	2	37	22.16	1 15.32	77 17.62	7.32	0.52
370	9907124z	15	39	44.7	1 16.57	77 19.59	9.14	1.01
371	99071608	6	30	19.68	1 16.49	77 19.95	7.65	1.24
372	9912026n	16	11	46.71	1 15.80	77 19.52	7.03	1.27
373	9912080m	8	43	6.03	1 17.51	77 19.88	7.26	0.75
374	99121002	2	8	31.09	1 15.43	77 19.55	6.02	1.28
375	9912292d	14	9	58.08	1 13.44	77 21.61	2.08	0.92
376	10636	21	16	46.25	1 15.87	77 19.87	7.91	1.54

N	Code	Origin Time			Latitude	Longitude	Depth	Mag.
	yymmddx	H	M	S	Deg. Min.	Deg. Min.	km	
377	0001200d	3	39	56.05	1 16.62	77 24.05	3.86	0.97
378	12064	23	17	40.39	1 15.98	77 19.48	7.99	0.77
379	22703	2	21	8.08	1 13.44	77 21.56	2.16	1.06
380	0002281l	8	28	58.14	1 13.27	77 21.74	0.8	0.92
381	30409	5	40	8.09	1 16.13	77 19.48	7.96	0.83
382	31312	7	45	23.85	1 13.44	77 21.92	1.17	0.29
383	000406ch	23	41	31.81	1 15.27	77 19.74	8.18	1.76
384	41010	4	44	58.79	1 16.47	77 19.95	6.56	0.75
385	0004105v	23	48	58.18	1 12.98	77 23.18	2.44	0.41
386	41910	5	38	16.2	1 15.85	77 18.36	6.08	0.97
387	0004205y	12	28	21.21	1 15.41	77 17.20	7.96	1.4
388	0004207l	21	12	32.92	1 12.13	77 20.38	4.94	0.44
389	0005011d	12	1	27.06	1 16.25	77 19.82	5.24	0.56
390	0006040g	0	51	12.26	1 15.87	77 17.20	8.41	0.94
391	0006177b	21	7	5.56	1 16.72	77 19.09	8.11	1.18
392	000630g4	19	38	43.31	1 16.21	77 20.60	6.01	0.68
393	72202	3	3	31.18	1 15.77	77 19.36	6.14	0.33
394	0007313o	15	59	5.85	1 15.25	77 17.73	7.49	0.81
395	0008023z	15	18	44.3	1 15.45	77 17.59	7.65	1.34
396	000804cd	21	14	14.18	1 16.60	77 18.24	8.16	0.73
397	0008055b	19	57	30.16	1 15.39	77 19.40	9.3	0.98
398	0008233j	22	32	16.1	1 15.92	77 19.97	5.35	1.21
399	010620a4	21	20	52.23	1 15.32	77 19.56	5.48	0.38
400	0105110u	5	8	35.44	1 16.41	77 20.98	6.71	0.96
401	0105144s	20	49	43.72	1 17.67	77 19.48	7.74	0.69
402	0106018k	18	20	56.83	1 16.34	77 20.09	6.48	0.85
403	010612es	22	54	11.25	1 16.33	77 20.19	5.1	0.48
404	1061660	19	4	5.17	1 16.26	77 19.92	7.7	0.76
405	0106194v	14	19	4.25	1 14.83	77 19.63	7.61	1.15
406	1062000	0	40	32.07	1 14.63	77 19.40	6.34	1.03

N	Code	Origin Time			Latitude	Longitude	Depth	Mag.
	yymmddx	H	M	S	Deg. Min.	Deg. Min.	km	
407	1062011	8	10	54.12	1 15.35	77 17.81	6.91	0.82
408	1050124	7	54	12.25	1 16.24	77 20.06	5.5	0.84
409	1093008	4	18	56.9	1 16.33	77 20.66	4.53	0.5
410	0107135l	22	23	58.53	1 16.38	77 18.63	5.46	1.1
411	010820ac	13	15	4.03	1 16.18	77 20.27	5.72	1.01
412	010820ae	13	16	5.07	1 15.97	77 20.19	6.74	1.01
413	0108220h	2	2	45.86	1 16.22	77 18.09	6.05	0.79
414	0108220n	2	44	33.22	1 16.34	77 18.42	5.86	0.6
415	0109031h	11	43	39.2	1 15.39	77 17.02	8.13	0.86
416	1091105	3	58	6.63	1 16.85	77 18.39	7.8	0.83
417	0109110b	4	59	52.41	1 16.75	77 18.25	7.82	0.78
418	0107135e	21	27	22.48	1 16.67	77 18.87	5.73	1.1
419	0110121k	16	11	44.06	1 16.29	77 20.73	4.56	0.78
420	1100915	9	23	10.31	1 16.26	77 20.95	4.97	1.06
421	1100121	16	11	43.89	1 16.44	77 20.67	5.28	0.72
422	1101404	2	54	33.92	1 12.90	77 22.98	4.98	0.17
423	011031ap	20	6	22.49	1 15.25	77 24.14	8.17	0.9
424	0111083p	11	6	49.79	1 12.71	77 23.34	4.24	0.11
425	1111605	2	49	40.08	1 16.68	77 19.83	6.05	1.77
426	0111173k	18	48	53.01	1 16.69	77 18.98	8.76	1.28
427	011202io	21	28	38.14	1 15.76	77 18.52	7.65	0.93
428	1121110	9	38	34.27	1 13.90	77 20.85	5.95	0.09
429	0112182h	20	48	9.43	1 14.83	77 19.34	6.04	0.95
430	0112201v	23	7	7.23	1 16.47	77 20.58	4.8	0.89
431	0203140r	19	11	54.23	1 13.13	77 20.75	5.92	0.1
432	0204080a	5	8	14.6	1 13.39	77 21.56	0.78	0.74
433	0204083g	15	41	50.2	1 15.11	77 19.57	5.36	0.67
434	2041705	5	32	14.59	1 13.69	77 21.67	2.38	0.74
435	2041900	2	54	54.01	1 13.72	77 21.38	3.27	0.16
436	0206101y	9	56	18.8	1 13.13	77 21.84	4.13	-0.03

N	Code	Origin Time			Latitude	Longitude	Depth	Mag.
	yymmddx	H	M	S	Deg. Min.	Deg. Min.	km	
437	2061026	10	14	23.02	1 13.41	77 22.08	1.41	0.22
438	2061031	11	59	25.86	1 13.28	77 22.15	2.65	0.1
439	0206103a	12	21	12.49	1 13.34	77 22.07	2.29	-0.13

## **APPENDIX C. PROGRAM CODE**

The C++ code written for solving the coda waves' envelopes inversion problem by means of the Back-Projection algorithm is attached. A free version of Borland C++ (BuilderX [3]) and a commercial compiler as Microsoft Visual C++ [4] was used to assure a high compatibility. The program reads data from text files. How data is organized is easily deduced by reading the program.

```

/*****\
*
*          BACKPROJECTION ALGORITHM          *
*
\*****/

#define PIMITJ 1.570796326794896619231322
#define PI 3.141592654

#include <stdlib.h>
#include <string.h>
#include <stdio.h>
#include <math.h>
#include <malloc.h>
#include <time.h>
#include <dos.h>
#include "nrutil2.h"
#include "fresnel.h"

void main(void)
{

FILE *fp, *fp2;
FILE *fp1,*fp3;
char buffer[10];
int i, j, k, ns, nt, t, n, m, s,count=0, ii, jj, kk, radi, int_ssx, int_ssy, ch;
int int_x, int_y, *nr,nrr;
int ndat,num, num1,num2,rec,cuenta_elipses;
unsigned char **IMA;
float **res,*b;
long int nx,ny,nz;
double cx1,cy1,cx2,cy2,dt,cz,vmax=0.0,vmin=0.0, vmed=0.0,alea;
double *sx,*sy,*sz,*ex,*ey,*ez,*time,dato, *vec, *a, *af;
double x, y, z, ssx, ssy,ssz,correccio_alsada;
double lx, ly, unitat_x, unitat_y, unitat_z, escala_y, escala_y2, escala_z, escala_z2;
double velocitat1, velocitat2,temps,distancial,distancia2,distancia,tempo;
double tini;
double semi_a,semi_b,exc, r, L, area, valor_mig, factor_elipse, cont;

/***** DEFINITION OF IMPORTANT VARIABLES *****/
*****

(cx1,cy1)          origin coordinates
(cx2,cy2)          end coordinates
cz                maximum depth
nx                number of blocks direction x
ny                number of blocks direction y
nz                number of blocks direction z
ns                number of seismografs
nt                number of events
t                maximum number of time intervals
dt                time interval

(sx[],sy[],sz[])  coordinates of seismograms

(ex[],ey[],ez[])  coordinates of events

nr[]              number of residues for each event
vec[]             residues of one event
a[]              result of inversion

vmax              maximum of a[]
vmin              minimum of a[]
vmed              average of a[]

unitat_x          longititude of a block in x direction
unitat_y          longititude of a block in y direction
unitat_z          longititude of a block in z direction

```

```

cuenta_elipses          number of residues of a certain block

*****/

printf("/*****/\n");
printf("/*                                     */\n");
printf("/*          BACKPROJECTION IN ACTION          */\n");
printf("/*                                     */\n");
printf("/*          Version 2.0                          */\n");
printf("/*                                     */\n");
printf("/*          Observatori de l'Ebre                  */\n");
printf("/*                                     */\n");
printf("/*          By: Eduard Carcol%c                    */\n",130);
printf("/*                                     */\n");

printf("\n\n\t Press any key to continue...\n\n");
getchar();

printf("\n\n\tVELOCITY MODEL:\n\n");

printf("\n\t z = 4.2    v = %.2f ",velocity1(4.2));
printf("\n\t z = 3.2    v = %.2f ",velocity1(3.2));
printf("\n\t z = 2.2    v = %.2f ",velocity1(2.2));
printf("\n\t z = 1.0    v = %.2f ",velocity1(1.0));
printf("\n\t z = 0.2    v = %.2f ",velocity1(0.2));
printf("\n\t z = -2.0   v = %.2f ",velocity1(-2.0));
printf("\n\t z = -3.8   v = %.2f ",velocity1(-3.8));
printf("\n\t z = -10   v = %.2f ",velocity1(-10.0));
printf("\n\t z = -21.8  v = %.2f ",velocity1(-21.8));
printf("\n\t z = -30    v = %.2f ",velocity1(-30));
printf("\n\t z = -39.8  v = %.2f ",velocity1(-39.8));
printf("\n\t z = -50.0  v = %.2f ",velocity1(-50.0));

printf("\n\n\n\n\t Press any key to continue...\n\n");
getchar();

/**** open and read data ****/

fp=fopen("datos.dat","r");

fscanf(fp,"%lf",&cx1);fscanf(fp,"%lf",&cy1);
fscanf(fp,"%lf",&cx2);fscanf(fp,"%lf",&cy2);
fscanf(fp,"%lf",&cz);

fscanf(fp,"%li",&nx); fscanf(fp,"%li",&ny); fscanf(fp,"%li",&nz);

fscanf(fp,"%i",&ns);

fscanf(fp,"%i",&nt);

fscanf(fp,"%i",&t);

fscanf(fp,"%lf",&dt);

/**** memory allocation ****/

sx =(double *) dvector (ns);
sy =(double *) dvector (ns);
sz =(double *) dvector (ns);
ex =(double *) dvector (nt);
ey =(double *) dvector (nt);
ez =(double *) dvector (nt);
a = (double *)dvector(nx*ny*nz);
b = (float *)dvector(nx);
af = (double *)dvector(nx*ny*nz);
res = (float **) hfmatrix(0, nt*ns ,0,t);
vec = (double *) dvector(t);
time =(double *) dvector (ns*nt);
IMA = (unsigned char **)hcmatrix(0,ny,0,nx);
nr = (int *) ivector(0,ns*nt);

```

```

if(sx == NULL || sy == NULL || sz == NULL
   || ex == NULL || ey == NULL || ez == NULL
   || time == NULL || a == NULL || vec == NULL || res == NULL || IMA == NULL
   || af == NULL || nr == NULL)
{printf("oooooh!!!!");exit(0);}

/**** reading coordinates of stations ****/

for(i=0;i<ns;i++){
  fscanf(fp,"%lf",&dato);sy[i]=dato;
  fscanf(fp,"%lf",&dato);sx[i]=dato;
  fscanf(fp,"%lf",&dato);sz[i]=dato;
}

/**** reading coordinates of events ****/

for(i=0;i<nt;i++){
  fscanf(fp,"%lf",&dato);ex[i]=dato;
  fscanf(fp,"%lf",&dato);ey[i]=dato;
  fscanf(fp,"%lf",&dato);ez[i]=dato;
}

fclose(fp);

/**** screen output of data ****/

printf("\ncx1 = %lf;",cx1);
printf("  cy1 = %lf",  cy1);
printf("\ncx2 = %lf;",cx2);
printf("  cy2 = %lf",  cy2);
printf("\ncz = %lf; ",cz);
printf("\nnx = %li;",nx);
printf("  ny = %li ; ",ny);
printf("nz = %li; ",nz);
printf("\nns = %i;",ns);
printf("  nt = %i",nt);
printf("\nt = %i;",t);
printf("  dt = %lf",dt);

printf("\n\n") ;

for(i=0;i<ns;i++){
  printf("\rsx = %lf; sy = %lf; sz = %lf",sx[i],sy[i],sz[i]);
}

printf("\n\n");

for(i=0;i<nt;i++){
  printf("\rex = %lf; ey = %lf; ez = %lf",ex[i],ey[i],ez[i]);
}

printf("\n");

/**** opening file of residues ****/

fp=fopen("residual.dat","r");

/**** reading number of events ****/

fscanf(fp,"%i",&ndat);
printf("\n ndat = %i",ndat);

/**** reading residues ****/

rec = 4;
for(i=0;i<nt;i++){
  for(j=1;j<(ns+1);j++){

    fscanf(fp,"%i",&num);

```

```

fscanf(fp, "%i", &num2);
fscanf(fp, "%i", &nrr);
fscanf(fp, "%lf", &tini);

for(k=0;k<nrr;k++) {fscanf(fp, "%lf", &dato); vec[k]=dato; }

count=count+1;

if(count>ndat) break;

if(num > rec && j!=1) i++;

if(num2 != j ) {
    j=num2;

    time[(j-1)+i*ns]=tini;
    nr[(j-1)+i*ns] = nrr;
    for(k=0;k<nrr;k++) res[(j-1)+i*ns][k]=vec[k];
}
else {
    time[(j-1)+i*ns]=tini;
    nr[(j-1)+i*ns] = nrr;
    for(k=0;k<nrr;k++) res[(j-1)+i*ns][k]=vec[k]; }
    printf("\rSisme = %d; Sismog. = %d; T_Ini = %.11f; N_Sismes = %d; N_Sismog. =
        %d"
        ,num,num2,tini, i,j);
    rec = num;
}
}

fclose(fp);

/**** computation starts *****/

printf("\n\nCalculating...\n\n");

/**** definitions and conversions *****/

cx1 = cx1*111.0;  cx2 = cx2*111.0;   cy1 = cy1*111.0;   cy2 = cy2*111.0;
lx = cx2-cx1;  ly = cy2-cy1;

/**** adimensional lengths *****/

unitat_x = lx/nx;
unitat_y = ly/ny;
unitat_z = cz/nz;

escala_y = unitat_y/unitat_x;
escala_z = unitat_z/unitat_x;

escala_y2= escala_y*escala_y;
escala_z2= escala_z*escala_z;

/**** screen output of units of length *****/

printf("\nunitat_x = %lf; ",unitat_x); printf("unitat_y = %lf; ",unitat_y);
printf("unitat_z = %lf\n",unitat_z);
printf("\nescala_y = %lf; ",escala_y); printf("escala_z = %lf; ",escala_z);
printf("\n\n");

/***** INVERSION *****/
/***** n number of events *****/
/***** m number of time intervals *****/
/***** i corresponds to x *****/
/***** j corresponds to y *****/
/***** k corresponds to z *****/

/**** output to file resultat.txt in text format *****/

fp = fopen("resultat.txt", "w");
fprintf(fp, "%li\n", nx*ny*nz );

```

```

printf("\n");
fprintf(fp, "\n");

/* definition of a parameter that indicates the minimum depth of the computation */
correccio_alsada = 4.5/unitat_z;
//correccio_alsada = 0.0;

for(k=0;k<nz;k++){ printf("seccio %i\r",k);

if(k==0){
  correccio_alsada = 4.5/unitat_z;
} else {
  correccio_alsada = 5.0/unitat_z;
}

for(j=0;j<ny;j++){
  for(i=0;i<nx;i++){

a[i+j*nx+k*ny*nx]=0.0;
  cont =0;
  cuenta_elipses = 0;

  for (n=0;n<nt;n++){

    x = ex[n]*111.0; y = ey[n]*111.0; z = ez[n];

    velocitat2 =
      velocity2((-1.0)*(k-correccio_alsada+0.5)*unitat_z,z)/unitat_x;

    x = (x-cx1)/unitat_x;
    y = (y-cy1)/unitat_y;
    z = z /unitat_z;

    for(s=0;s<ns;s++){

if(time[n*ns+s]<0.1) continue;

      ssx = sx[s]*111.0; ssy = sy[s]*111.0; ssz = sz[s];

      velocitat1 = velocity2((-1.0)
        *(k-correccio_alsada+0.5)*unitat_z,ssz)/unitat_x;

      ssx = (ssx-cx1)/unitat_x;
      ssy = (ssy-cy1)/unitat_y;
      ssz = (ssz)/unitat_z;

      /**** distance HYPOCENTER-STATION *****/

      r = sqrt( pow(x-ssx,2)
        +escala_y2*pow(y-ssy,2)
        +escala_z2*pow(z-ssz,2));

      /**** distance HIPOCENTER-BLOCK (i,j) *****/

      distancia2 = sqrt( pow(x-(i+0.5),2)
        + escala_y2*pow(y-(j+0.5),2)
        + escala_z2*pow(z-(-1.0)*(k-correccio_alsada+0.5),2));

      /**** distance STATION-BLOCK (i,j) *****/

      distancial = sqrt( pow(ssx-(i+0.5),2)
        + escala_y2*pow(ssy-(j+0.5),2)
        + escala_z2*pow(ssz-(-1.0)*(k-correccio_alsada+0.5),2));

      /**** parameters *****/

      L = distancial + distancia2;
      exc = r/L;semi_b = L/2.0;
      semi_a = sqrt(pow(semi_b,2)-pow((r/2.0),2));

```

```

area = 2.0*PI*semi_a*semi_a + 2.0*PI*(semi_a*semi_b/exc)*asin(exc);
valor_mig = (4.0*PI/(L*r))*log((L+r)/(L-r));
valor_mig = valor_mig/area;
factor_elipse = (pow(1.0/(distancia1*distancia2),2)/valor_mig);

/**** time corresponding to event n of station s ****/

tempo = distancia1 / velocitat1 + distancia2/velocitat2;

/**** number of the residue to needed for average ****/

m = ceil( (tempo-(time[n*ns+s]+dt/2.0))/dt );
t = nr[n*ns+s];

/**** average ****/

if(m>=1 && m<t){
    temps = time[n*ns+s]+dt/2.0+m*dt;
    a[i+j*nx+k*ny*nx] = a[i+j*nx+k*ny*nx]
        +(factor_elipse)*( res[n*ns+s][m]*(temps-tempo)
            + res[n*ns+s][m-1]* (tempo-(temps-dt) ))/dt;
    cont = cont + factor_elipse;
    cuenta_elipses++;
}
}
}

if (cont != 0) a[i+j*nx+k*ny*nx] = a[i+j*nx+k*ny*nx]/(cont*1.0);
else a[i+j*nx+k*ny*nx]=1.0;

/**** Counting residues instead of inversion ****/

// if(cont < 10) a[i+j*nx+k*ny*nx] = 0.0;
// a[i+j*nx+k*ny*nx]=cuenta_elipses;
}
}
}

/**** statistics of inversion ****/

for(k=0;k<nz;k++){
    for(j=0;j<ny;j++){
        for(i=0;i<nx;i++){
            vmed = vmed + a[i+j*nx+k*ny*nx]/(nx*ny*nz*1.0);
            if(vmax<a[i+j*nx+k*ny*nx]) vmax=a[i+j*nx+k*ny*nx];
            if(vmin>a[i+j*nx+k*ny*nx]) vmin=a[i+j*nx+k*ny*nx];
        }
    }
}

/**** output to text file ****/

for(k=0;k<nz;k++){
    for(j=0;j<ny;j++){
        for(i=0;i<nx;i++){
            fprintf(fp, "%lf\n ", a[i+j*nx+k*ny*nx]);
        }
    }
}
fprintf(fp, "\n");
fclose(fp);

/**** Output to binary file ****/

fp3 = fopen("resultat.raw", "wb");

for(k=0;k<nz;k++){
    for(j=0;j<ny;j++){
        for(i=0;i<nx;i++){

```

```

        b[i] = a[i+j*nx+k*ny*nx];
    }
    fwrite(b, sizeof(float), nx, fp3);
}
}
fclose(fp3);

/**** Files for Surfer ****/
/**** horitzontal sections ****/

printf("\n");
for(n=0;n<nz;n++){

    sprintf(buffer, "secc%i.dat", n);
    printf("%s\r", buffer);
    fp=fopen(buffer, "w");

    for(i=0;i<nx;i++){
        for(j=0;j<ny;j++){
            fprintf(fp, "%lf %lf %f\n",
                (cx1 + ((cx2-cx1)/nx)*i + ((cx2-cx1)/nx)/2.0)/111.0,
                (cy1+((cy2-cy1)/ny)*j+((cy2-cy1)/ny)/2.0)/111.0,
                a[i+j*nx+n*ny*nx]-1.0);
        }
    }

    fclose(fp);
}

/**** Vertical sections ****/

printf("\n");
for(j=0;j<ny;j++){

    sprintf(buffer, "tall%i.dat", j);
    printf("%s\r", buffer);
    fp=fopen(buffer, "w");

    for(i=0;i<nx;i++){
        for(n=0;n<nz;n++){
            fprintf(fp, "%lf %lf %f\n",
                (cx1+((cx2-cx1)/nx)*i+((cx2-cx1)/nx)/2.0)/111.0,
                (n*cز/nz + 0.5*cز/nz),
                a[i+j*nx+n*ny*nx]-1.0);
        }
    }

    fclose(fp);
}

printf("\n vmax = %lf, vmin = %lf, vmed = %lf", vmax, vmin, vmed);

fp=fopen("resultat.txt", "a");
fprintf(fp, "\n vmax = %lf, vmin = %lf, vmed = %lf", vmax, vmin, vmed);
fclose (fp);

/**** conversion inversion to .RAW image (for Photoshop) ****/

for(k=0;k<nz;k++){
    for(j=0;j<ny;j++){
        for(i=0;i<nx;i++){
            af[i+j*nx+k*ny*nx] = a[(nx-1-i)+(ny-1-j)*nx+k*ny*nx];
        }
    }
}

for(k=0;k<nz;k++){
    for(j=0;j<ny;j++){
        for(i=0;i<nx;i++){
            a[i+j*nx+k*ny*nx] = af[i+j*nx+k*ny*nx];
        }
    }
}

```

```

    }
  }
}

/**** Horizontal seccions ****/

printf("\n");
for(n=0;n<nz;n++){

  sprintf(buffer, "secc%i.raw", n);
  printf("%s\r",buffer);
  fp=fopen(buffer, "wb+");

  for(i=0;i<nx;i++){
    for(j=0;j<ny;j++){
      IMA[j][i]=255.0*(a[i+j*nx+n*nx*ny]-vmin)/(vmax-vmin);
    }
  }

  for ( i=0; i<ny; i++ ) fwrite((void*)IMA[i], 1, nx, fp);
  fclose(fp);
}

/**** vertical sections ****/

printf("\n");
for(j=0;j<ny;j++){

  sprintf(buffer, "tall%i.raw", j);
  printf("%s\r",buffer);
  fp=fopen(buffer, "wb+");

  for(i=0;i<nx;i++){
    for(n=0;n<nz;n++){
      IMA[n][i]=255.0*(a[i+j*nx+n*nx*ny]-vmin)/(vmax-vmin);
    }
  }
  for ( i=0; i<nz; i++ ) fwrite((void*)IMA[i], 1, nx, fp);

  fclose(fp);
}
/*****/

}

/**** computes average of two velocities ****/

double velocity2 (double z1,double z2){

  return((velocity1(z1)+velocity1(z2))/2.0);

}

/**** velocity at a certain depth (by interpolating) ****/

double velocity1 (double z){

  if( z>=4.2 )
    return (1.966);

  else if( z<4.2 && z>= 2.2 )
    return ( ((1.966-2.079)/2.0)*z + 1.966 - ((1.966-2.079)/2.0)*4.2 );

  else if( z<2.2 && z>=0.2 )
    return( ((2.079-2.247)/2.0)*z + 2.079 - ((2.079-2.247)/2.0)*2.2 );

  else if( z<0.2 && z>=(-3.8))
    return( ((2.247-3.371)/4.0)*z + 2.247 - ((2.247-3.371)/4.0)*0.2 );
}

```

---

```
else if( z<(-3.8) && z>=(-21.8))
return( ((3.371-3.820)/18.0)*z+ 3.371 - ((3.371-3.820)/18.0)*(-3.8) );

else if(z<(-21.8) && z>=(-39.8))
return( ((3.820-4.494)/18.0)*z+ 3.820 - ((3.820-4.494)/18.0)*(-21.8) );

else if(z<(-39.8))
return(4.494);
}
```

## 8 REFERENCES

---

- [1] Stein, S. and Wysession M. (2003) “An Introduction to seismology, earthquakes and earth structure”, Blackwell Publishing.
- [2] Aki, K. Richards, P.G. (1980), “Quantitative seismology, theory and methods”, W.H. Freeman and Company.
- [3] Borland, C++ BuilderX downloads,  
[http://www.borland.com/downloads/download\\_cbuilderx.html](http://www.borland.com/downloads/download_cbuilderx.html).
- [4] Microsoft Visual C+, <http://msdn.microsoft.com/visualc/>.
- [5] Michels H., Max Planck Institute for Solar Research,  
<http://www.mps.mpg.de/dislin/overview.html>.
- [6] Picture under GNU license from Wikipedia.
- [7] Wallace, R.E.,  
[http://en.wikipedia.org/wiki/Image:San\\_Andreas\\_Fault\\_-\\_Carrizo\\_Plains.jpg](http://en.wikipedia.org/wiki/Image:San_Andreas_Fault_-_Carrizo_Plains.jpg)
- [8] Aki, K. (1969), “Analysis of seismic coda of local earthquakes as scattered waves”, *J. Geophys. Res.*, **74**, 615-631.
- [9] Aki, K. and B. Chouet, (1975), “Origin of Coda Waves; source, attenuation and scattering effects”, *J. Geophys. Res.*, **80**, 3322-3342.
- [10] Sato, H. and M. C. Fehler (1998), “Seismic wave propagation and scattering in the heterogeneous earth”, *AIP Series in Modern Acoustics and Signal Processing*, Springer-Verlag, New York, 308 p.
- [11] Wu, R. S. and K. Aki (1988), “Multiple scattering and energy transfer of seismic waves – Separation of scattering effect from intrinsic attenuation. II. Application of the theory to Hindu-Kush region”, *Pure Appl. Geophys.*, **128**, 49-80.
- [12] Frankel, A. and L. Wennerberg (1987), “Energy-flux model of seismic coda: separation of scattering and intrinsic attenuation”, *Bull. Seism. Soc. Am.*, **77**, 1223-1251.
- [13] Hoshiaba, M., M. Fehler and H. Sato (1991), “Numerical basis of the separation of scattering and intrinsic absorption from full seismogram envelope. A Monte-Carlo simulation of multiple isotropic scattering”, *Pa. Meteorol. Geophys., Meteorol. Res. Inst.*, **42**, 65-91,.
- [14] Matsunami, K. (1991), “Laboratory tests of excitation and attenuation of coda waves using 2-D models of scattering media”, *Phys. Earth Planet. Inter.*, **67**, 36-47.
- [15] Dainty, A. M. and M. N. Toksöz (1990), “Array analysis of seismic scattering”, *Bull. Seism. Soc. Am.*, **80**, 2242-2260.

- 
- [16] Margerin, L. (2005), "Introduction to radiative transfer of seismic waves, in Seismic Earth: Array Analysis of Broadband Seismograms", A. Levander and G. Nolet (Ed.), *Geophysical Monograph Series*, Vol. 157, Ch 14, pp. 229-252, AGU, Washington,.
- [17] Rautian, T. G. and V. I. Khalturin (1978), "The use of the coda for determination of the earthquake source spectrum", *Bull. Seism. Soc. Am.*, **68**, 923-948.
- [18] Sato H. (1977), "Energy propagation including scattering effects, single isotropic scattering approximation", *J. Phys. Earth*, **25**, 27-41.
- [19] Wesley, J. P. (1965), "Difussion of seismic energy in the near range", *J. Geophys. Res.*, **70**, 5099-5106.
- [20] Dainty, A. M., P. J. Pines, and M. N. Toksöz (1974), "Strong scattering of seismic waves: Examples from model experiments and the moon" (abstract), *Eos Trans. AGU*, **55**, 362.
- [21] Weisstein, E. W., "Prolate Spheroidal Coordinates." *MathWorld*--A Wolfram Web Resource. <http://mathworld.wolfram.com/ProlateSpheroidalCoordinates.html>
- [22] Nakamura, Y. (1977). "Seismic energy transmission in an intensively scattering environment", *J. Geophys.*, **43**, 389-399.
- [23] Dainty, A. M. and M. N. Toksöz (1981), "Seismic codas on the earth and the moon: a comparison", *Phys. Earth. Planet. Inter.*, **26**, 250-260.
- [24] Bullock, R., Shearer, P., and C. Johnson (2003), "Comprehensive Processing of the Apollo Lunar Seismic Data", AGU Meeting, S. Francisco.
- [25] Chandrasekhar S. (1960), "Radiative Transfer" Chapter 1, Dover, London.
- [26] Turner, J. (1994), "Radiative transfer of ultrasound", Chapter 3, *Ph.D. thesis*, University of Illinois.
- [27] Ishimaru A. (1999), "Wave Propagation and Scattering in Random Media", Chapter 4, *IEEE Press Series on Electromagnetic Wave Theory.*, Oxford University Press Classic Reissue.
- [28] Wu, R.S. (1985), "Multiple scattering and energy transfer of seismic waves-separation of scattering effect from intrinsic attenuation – I. Theoretical modelling", *Geophys. J.R. astr. Soc.*, **82**, 57-80.
- [29] Shang T. and L. Gao (1988), "Transportation theory of multiple scattering and its application to seismic coda waves of impulsive source", *Scientia Sinica (series B, China)*, **31**, 1503-1514.
- [30] Zeng Y., F. Su and K. Aki (1991), "Scattering Wave energy Propagation in a Random Isotropic Scattering Medium, 1. Theory.", *J. Geophys. Res.*, **96** , 507-519.
- [31] Sato, H., H. Nakahara, and M. Ohtake (1997), "Synthesis of scattered energy density for non-spherical radiation from a point shear dislocation source based on radiative transfer theory", *Phys. Earth Planet. Inter.*, **104**, 1-13.

- 
- [32] Sato, H. (1994), "Formulation of the multiple non-isotropic scattering process in 2-D space on the basis of the energy transport theory", *Geophys. J. Int.*, **117**, 727-732.
- [33] Sato, H. (1995), "Formulation of the multiple non-isotropic scattering process in 3-D space on the basis of the energy transport theory", *Geophys. J. Int.*, **121**, 523-531.
- [34] Paaschens J. C. J. (1997), "Solution of the time dependent Boltzmann equation", *Phys. Rev. E*, **56**, 1135-1141.
- [35] Brigham, O. E. (1974), "The Fast Fourier Transform", Prentice Hall, Inc., Englewood Cliffs, New Jersey, 252 p.
- [36] Bouchon, M. (1979), "Discrete Wave Number Representation of Elastic Wave Fields in Three-Space Dimensions", *J. Geophys Res.*, **84**, 3609-3614.
- [37] R. Cools, D. Laurie and L. Pluym (1997), "Cubpack++: A C++ package for automatic two-dimensional cubature". *ACM Trans. Math. Software*, **23**, 1-15.
- [38] Robinson, I. and M. Hill (2002), "Algorithm 816: r2d2lri: An algorithm for automatic two-dimensional cubature", *ACM Trans. on Math. Software*, **28**, 73-89.
- [39] Hill, M. and I. Robinson (2002), "A Comparison of Strategies for the Automatic Computation of Two-Dimensional Integrals over Infinite Domains", *Numerical Algorithms*, **34**, 325-338.
- [40] Nishigami, K. (1991), "A new inversion method of coda waveforms to determine spatial distribution of coda scatterers in the crust and uppermost mantle", *Geophys. Res. Lett.*, **18**, 2225-2228.
- [41] Nishigami, K. (1997), "Spatial distribution of coda scatterers in the crust around two active volcanoes and one active fault system in central Japan: Inversion analysis of coda envelope", *Phys. Earth Planet. Int.*, **104**, 75-89.
- [42] Nishigami, K. (2000), "Deep crustal heterogeneity along and around the San Andreas fault system in central California and its relation to the segmentation", *J. Geophys. Res.*, **105**, 7983-7998.
- [43] Chen, X. and L. T. Long (2000), "Spatial Distribution of Relative Scattering Coefficients Determined from Microearthquake Coda", *Bull. Seism. Soc. Am.*, **90**, 512-524.
- [44] Asano Y. and A. Hasegawa (2004), "Imaging the fault zones of the 200 western Tottori earthquake by a new inversion method to estimate three-dimensional distribution of the scattering coefficient", *J. Geophys. Res.*, **109**, B06306.
- [45] Fisher, T., "Tony Fisher's Home page". <http://www-users.cs.york.ac.uk/~fisher/> and <http://www-users.cs.york.ac.uk/~fisher/mkfilter/trad.html>.
- [46] Press, W. H., B. P. Flannery, S. A. Teukolsky, and W. T. Vetterling (1992), "Numerical Recipes in C : The Art of Scientific Computing", Chapter 2, Cambridge University Press.
- [47] Kaczmarz, S. (1937), "Angenaherte auflosung von systemen linearer gleichungen", *Bull. Acad. Pol. Sci. Lett. A*, **6-8A**, pp. 335-357,

- 
- [48] Kak, A. C. and M. Slaney (1988), "Principles of Computerized Tomographic Imaging", Chapters 3 and 7, *IEEE Press*, New York.
- [49] Gilbert, H. (1972), "Iterative methods for the three-dimensional reconstruction of an object from projections", *J. Theor. Biol.* **36**, 105-117.
- [50] Penczek, P. A., J. Zhu, R. Schröder, and J. Frank (1997), "Three-dimensional reconstruction with contrast transfer function compensation from defocus series", *Scanning Microscopy Supplement*, **11**, 1-10.
- [51] Zhu, J., P. A. Penczek, R. Schröder, and J. Frank (1997), "Three-dimensional reconstruction with contrast transfer function correction from energy-filtered cryoelectronmicrographs: procedure and application to the 70S *Escherichia coli* ribosome", *J. Struct. Biol.*, **118**, 197-219.
- [52] Chen X. and L. T. Long (2000), "Spatial Distribution of Relative Scattering Coefficients Determined from Microearthquake Coda", *Bull. Seism. Soc. Am.*, **90**, 512-524,.
- [53] Webb, S. (1992), "The Physics of Medical Imaging", Chapter 4, IOP Publishing, Bristol.
- [54] Liebling M., "Computerized Tomography", <http://bigwww.epfl.ch/demo/jtomography/demo.html>
- [55] Biomedical Imaging Group: CT reconstruction, École Polytechnique Fédéral de Laussane. <http://bigwww.epfl.ch/demo/ctreconstruction/index.html>.
- [56] Eleri P, "Laser Tomography", <http://users.aber.ac.uk/ruw/teach/340/tomo.html>.
- [57] Ali, A. M., Z. Melegy, M. Morsy, R.M. Megahid, T. Bucherl, and E.H. Lehmann (2004), "Image reconstruction techniques using projection data from transmission method", *Annals of Nuclear Energy*, **31**, 1415–1428.
- [58] Mohan G. and S. S. Rai (1992), "Imaging of seismic scatterers beneath the Gauribidanur (GBA) array", *Phys. Earth Planet Int.*, **71**, 36-45.
- [59] Moyen, J. F., A. Nédélec, H. Martin, and M. Jayananda M. (2003), "Syntectonic granite emplacement at different structural levels: the Closepet granite, South India.", *J. Struc. Geol.*, **25**, 611-631.
- [60] Tripathi J.N. and A. Ugalde (2004), "Regional estimation of  $Q$  from seismic coda observations by the Gauribidanur seismic array", *Phys. Earth Planet Int.*, **145**, 115-126.
- [61] Moyen, J.F., <http://jfmoyen.free.fr/recherche/planches.html>
- [62] Arora, S. K. (1971), "A study of the earth's crust near Gauribidanur, South India.", *Bull. Seism. Soc. Am.*, **61**, 671-683.
- [63] Krishna, V. G. and D. S. Ramesh (2000), "Propagation of crustal-waveguide-trapped Pg and seismic velocity structure in South Indian shield", *Bull. Seism. Soc. Am.*, **90**, 1281-1294.

- 
- [64] Berteussen K.A.(1977), "Quantitative assessment of the crust-upper mantle heterogeneities beneath the gauribidanur seismic array in southern india", *Earth Planet. Sci. Lett.*, **37**, 326-332.
- [65] Banks, N. G., M. L. Calvache, and S. N. Williams (1997), "14C ages and activity for the past 50 ka at Volcano Galeras, Colombia", *J. Volcanol. Geotherm. Res.*, **77**, 39-55.
- [66] Calvache, M. L., G. P. Cortés, and S. N. Williams (1997), "Stratigraphy and chronology of the Galeras volcanic complex, Colombia", *J. Volcanol. Geotherm. Res.*, **77**, 5-19.
- [67] This image is a work of a United States Geological Survey employee, taken or made during the course of the person's official duties. As a work of the United States Government, the image is in the public domain.
- [68] Gómez, D. M. and R. A. Torres (1997), "Unusual low-frequency volcanic seismic events with slowly decaying coda waves observed at Galeras and other volcanoes", *J. Volcanol. Geotherm. Res.*, **77**, 173-193.
- [69] Moncayo, E., C. A. Vargas, and J. Durán (2004), "Temporal variation of coda- $Q$  at Galeras volcano, Colombia", *Earth Sci. Res. J.*, **8**, 19-24.
- [70] Calvache, M. L. (1990), "Geology and volcanology of the recent evolution of Galeras volcano, Colombia", *M. S. Thesis*, Louisiana State Univ., Baton Rouge, LA, 171 p.
- [71] Ugalde, A., E. Carcolé, and J. N. Tripathi, (2006), "Spatial distribution of scatterers in the crust by inversion analysis of coda envelopes: a case study of Gauribidanur seismic array (southern India)", *Geophys. J. Int.*, (*in press*).
- [72] Zapata, J. A., M. L. Calvache, G. P. Cortés, T. P. Fisher, G. Garzón, D. Gómez, L. Narváez, M. Ordóñez, A. Ortega, J. Stix, R. Torres, and S. N. Williams (1997), "SO<sub>2</sub> fluxes from Galeras volcano, Colombia, 1989-1995: progressive degassing and conduit obstruction of a Decade volcano", *J. Volcanol. Geotherm. Res.*, **77**, 195-208.
- [73] Phillips, W. and K. Aki (1986), "Site amplification of coda waves from local earthquakes in central California", *Bull. Seism. Soc. Am.*, **76**, 627-648.

---

**PUBLICACIONES DIRECTAMENTE RELACIONADAS CON  
EL CONTENIDO DE LA TESIS**



# Spatial distribution of scatterers in the crust by inversion analysis of coda envelopes: a case study of Gauribidanur seismic array (Southern India)

A. Ugalde,<sup>1</sup> E. Carcolé<sup>1</sup> and J. N. Tripathi<sup>2</sup>

<sup>1</sup>Ebro Observatory, CSIC – URL, Observatori de l'Ebre, Horta Alta 38, 43520 Roquetes, Tarragona, Spain. E-mail: augalde@obsebre.es

<sup>2</sup>Department of Earth and Planetary Sciences, University of Allahabad, Allahabad—211002, India

Accepted 2006 April 21. Received 2006 February 15; in original form 2005 August 4

## SUMMARY

The 3-D spatial distribution of relative scattering coefficients in southern India was estimated by means of an inversion technique applied to coda wave envelopes. The inversion analysis was performed for the first time in this kind of seismological research by means of the simultaneous iterative reconstruction technique and filtered backprojection method. Whereas the first one allows to obtain more exact solutions, the second one is a much faster non-iterative algorithm that has proved to provide very accurate reconstructions. Data used consisted of selected 636 vertical-component, short-period recordings of microearthquake codas from shallow earthquakes with magnitudes ranging from 0.7 to 3.7 and epicentral distances up to 120 km recorded by the Gauribidanur seismic array (GBA). Results are almost independent of the inversion method used and they are frequency dependent. They show a remarkably uniform distribution of the scattering strength in the crust around GBA. However, a shallow (0–24 km) strong scattering structure, which is only visible at low frequencies, seems to coincide with the Closepet granitic batholith which is the boundary between the eastern and western parts of the Dharwar craton.

**Key words:** crustal heterogeneity, inversion analysis, scattering coefficient, seismic coda, southern India.

## 1 INTRODUCTION

The behaviour of coda waves in seismograms is one of the observations supporting the existence of small-scale random heterogeneities in the Earth (Aki 1969; Aki & Chouet 1975; Sato *et al.* 2002). The direct *S* wave observed in a seismogram from a local earthquake is followed by complex wave trains with amplitudes smaller than the direct wave and that exponentially decay with time, which are called *S*-coda. It is widely accepted that coda waves are formed by superposition of incoherent scattered waves from randomly distributed heterogeneities in the lithosphere, such as cracks, faults, folds, and velocity or density anomalies with scale length about the seismic wavelength. *S*-coda waves have an envelope shape common to all epicentres and stations in a given region after twice the *S* wave traveltime (Rautian & Khalturin 1978). Total scattering coefficient ( $g$ ) and coda attenuation ( $Q_c^{-1}$ ) are the parameters, which characterize the coda excitation (which measures the capacity of the medium to originate scattering) and the decay rate of coda envelopes (which is a measure of the attenuation of the medium) within a given frequency band, respectively.

A number of models have been proposed to relate scattering and coda wave amplitudes. One approach to model the coda envelopes is to consider the heterogeneities as randomly and uniformly dis-

tributed point-like scatterers. Using this model and on the basis of the energy transport (or radiative transfer) theory (Wu 1985), the *S*-wave coda has been synthesized under the assumption of single isotropic scattering (SIS) (Sato 1977), multiple isotropic scattering (Hoshiya 1991; Zeng *et al.* 1991) and multiple non-isotropic scattering (Hoshiya 1995; Sato 1995).

On the other hand, scattering from randomly and non-uniformly distributed heterogeneities has also been studied to explain the features of the observed envelopes of *S* coda waves. Nishigami (1991) developed an inversion method of coda waveforms from local earthquakes to estimate the inhomogeneous spatial distribution of relative scattering coefficients in the crust. The method is based on the assumption that the fluctuation of the decay curve of the observed coda envelope from a reference curve, which was estimated by assuming SIS and spherical radiation from the source, is caused by a non-uniform distribution of scatterers in the crust. This method has proved to be an effective approach to investigate the real heterogeneous structure in the crust of several regions in the world: Nishigami (1991) detected zones of strong scattering related to major active faults in central Japan; Nishigami (1997) revealed significant heterogeneous structures in the crust around one active fault system and two active volcanoes in central Japan; and Nishigami (2000) showed the segmentation structure along the San Andreas fault system in

central California. Chen & Long (2000), in the Piedmont Province of central Georgia, found a correlation at shallow depths between zones of strong scattering and the location of hypocentres and areas with greater topographic relief, and were able to identify a strong reflecting layer which was consistent with a thrust plain previously reported using other geophysical methods. More recently, Asano & Hasegawa (2004) suggested the correlation between large scattering zones with the existence of fault-damaged zones in southwestern Japan, as well as other scattering properties of the region at different depths.

Several inversion methods have been used in order to obtain the strength of the scattering coefficients. Whereas Nishigami (1991) solved the problem using a standard inversion method, Nishigami (1997, 2000) used a recursive stochastic inversion method, and Chen & Long (2000) solved the inversion problem using the algebraic reconstruction technique (ART). On the other hand, Asano & Hasegawa (2004) revised the inversion analysis and obtained absolute values of the scattering coefficients by considering a depth dependent velocity structure and double-couple sources, and assuming an intrinsic absorption parameter.

The aim of this paper is to perform a coda envelope inversion analysis to microearthquake recordings by the Gauribidanur seismic array (GBA) to estimate a 3-D distribution of relative scattering coefficients in southern India. We will follow the method presented by Nishigami (1991). This method implies a previous knowledge of the depth dependent velocity model and it assumes a synthetic SIS model for the absolute reference scattering coefficients (Sato 1977). The observed data will be inverted using two different algorithms that are commonly used in biomedical applications but that have not been used previously in this kind of seismological applications: the simultaneous iterative reconstruction technique (SIRT) and the filtered backprojection (FBP) method. The first one allows to obtain better reconstructions than other inversion algorithms, however, it is slower. On the other hand, the FBP is a non-iterative method that has proved to provide fast and accurate solutions.

## 2 METHODS

### 2.1 The observation equation

Sometimes, the observed envelopes of  $S$  coda waves differ from those synthesized by models based on the hypothesis of uniform distribution of scatterers (e.g. Aki & Chouet 1975; Sato 1977). Small amplitude fluctuations or ripples overlying on a smoothly decaying coda envelope which is predicted by the scattering theory, are often observed. This observed behaviour can be explained by a non-uniform 3-D distribution of scatterers in the crust. Following Nishigami (1991), the structures causing strong scattering can be identified by analysing the observed coda envelope fluctuations from a synthesized (or reference) model.

In the present study we will consider the SIS approximation as the theoretical model for the absolute reference scattering coefficients. It models the shape of the coda of local earthquakes (Sato 1977) by assuming SIS, random and homogeneous distribution of scatterers in a constant velocity medium, and spherical radiation of elastic energy. According to the SIS model, and considering the anelastic attenuation effect, the coda energy density at a frequency  $f$ , hypocentral distance  $r$  and lapse time  $t$  in a 3-D space can be expressed as an integral all over the space in the form (Sato 1977):

$$E_s(f|r, t) = \int_V \frac{W_0(f)g(f)}{(4\pi)^2 \beta r_1^2 r_2^2} e^{-2Q_c^{-1}\pi f t} \delta \left[ t - \frac{r_1 + r_2}{\beta} \right] dV, \quad (1)$$

where  $dV = d^3 \mathbf{x}$ ;  $\mathbf{x}$  is the coordinate vector of the scattering point;  $r_1 = |\mathbf{x}|$  is the distance between the hypocentre and the scatterer;  $r_2 = |\mathbf{x} - \mathbf{r}|$  is the distance between the scatterer and the station;  $r = |\mathbf{r}|$ ;  $t$  is the lapse time measured from the origin time of the earthquake;  $\beta$  is the average  $S$ -wave velocity;  $W_0(f)$  represents the total energy radiated from the source within a unit frequency band around  $f$ ; and  $g(f)$  is the total scattering coefficient for the frequency  $f$ . In a constant velocity medium, the scatterers responsible for the generation of coda waves at a distance  $r$  and time  $t$  are contained in a spheroidal shell whose foci are located at the source and receiver, which is expressed by the term  $(1/\beta)\delta [t - (r_1 + r_2)/\beta]$  in eq. (1). Following Sato (1977) the integration of eq. (1) gives

$$E_s(f|r, t) = \frac{W_0(f)g_0(f)}{4\pi r^2} K(a) e^{-2Q_c^{-1}\pi f t}, \quad (2)$$

for a homogeneous spatial distribution of the scattering coefficient  $g_0(f)$ , being  $K(a) = (1/a) \ln [(a+1)/(a-1)]$  for  $a > 1$ ;  $a = t/t_S$ ; and  $t_S$  the  $S$ -wave traveltime. For  $a \gg 1$   $K(a) \approx 2/a^2$ , and therefore, eq. (2) becomes

$$E_s(f|r, t) \approx \frac{W_0(f)g_0(f)}{2\pi\beta^2 t^2} e^{-2Q_c^{-1}\pi f t}, \quad (t > 2t_S), \quad (3)$$

which corresponds to the single scattering model of Aki & Chouet (1975).

We divide the volume under consideration into a number  $N$  of small blocks of volume  $\delta V$ , as it will be detailed later. Therefore, by multiplying the right side of eq. (1) by the factor  $1/2$  for including the effect of a half-space, then by integrating eq. (1) in the radial direction over the spheroidal shell (which radius is approximated by  $\beta t/2$ ), which corresponds to the lapse time window  $t_j \pm \delta t/2$ , we obtain:

$$E_{sa}(f|t_j)\delta t \approx \frac{W_0(f)g_0(f)}{4\pi^2\beta t} e^{-2Q_c^{-1}\pi f t_j} \sum_{i=1}^{N_j} \frac{\delta_{ij}}{(r_{1,i}r_{2,i})^2} \delta V, \quad (4)$$

where the integral has been approximated by a summation of the blocks, where each term corresponds to a certain block  $i$ . The sub index  $a$  in the energy density indicates the consideration of an average scattering coefficient  $g_0$  over the half-space.  $\delta_{ij}$  equals 1 when the  $i$ th block lays inside the spheroidal shell which corresponds to the  $j$  time window.  $N_j$  is the total number of scatterers in each spheroidal shell.

The observed coda envelope fluctuations from the theoretical model due to the non-uniform distribution of scatterers can be expressed mathematically as spatial perturbations of the average scattering coefficient of the medium due to an individual scatterer in the form:  $g = g_0 \alpha_i$  ( $\alpha_i \geq 0$ ). Thus, the integration of eq. (1) gives

$$E_s(f|t_j)\delta t = \frac{W_0(f)g_0(f)}{4\pi^2\beta t} e^{-2Q_c^{-1}\pi f t_j} \sum_{i=1}^{N_j} \frac{\alpha_i \delta_{ij}}{(r_{1,i}r_{2,i})^2} \delta V. \quad (5)$$

For obtaining eqs (4) and (5) we have assumed a constant value of  $Q_c$  in the region (see Tripathi & Ugalde 2004 for an estimation of coda attenuation in the GBA region), thus neglecting the effect of an spatial variation of  $Q_c$  on the fluctuations of the coda envelope and considering that they are caused mainly by the spatial variations of the scattering coefficient. In order to get a system of equations that will allow us to estimate the spatial perturbations of the scattering coefficient we divide eq. (5) by eq. (4),

$$\frac{E_s(t_j)}{E_{sa}(t_j)} = \frac{1}{\sum_i \frac{\delta_{ij}}{(r_{1,i}r_{2,i})^2}} \sum_i \frac{\alpha_i \delta_{ij}}{(r_{1,i}r_{2,i})^2}, \quad (6)$$

where the left side of eq. (6) is called coda wave energy residual ( $e_j$ ) and it measures the ratio of the observed energy density in this part of the coda to the average energy density of the medium.

If we divide the coda of one seismogram into several small time windows, we will have one equation based on eq. (6) for each time window. Also for each time window, the scatterers contributing to the energy density are contained in a spheroidal shell. Thus, eq. (6) can be rewritten in the following form

$$\begin{aligned} w_{11}\alpha_1 + \dots + w_{i1}\alpha_i + \dots + w_{N1}\alpha_N &= e_1 \\ &\vdots \\ w_{1j}\alpha_1 + \dots + w_{ij}\alpha_i + \dots + w_{Nj}\alpha_N &= e_j, \\ &\vdots \\ w_{1M}\alpha_1 + \dots + w_{iM}\alpha_i + \dots + w_{NM}\alpha_N &= e_M \end{aligned} \quad (7)$$

where  $M$  is the total number of equations (number of seismograms multiplied by the number of coda time windows considered),  $N$  is the total number of scatterers (number of small blocks into which the study region is divided) and

$$w_{ij} = \frac{1}{\sum_i \frac{\delta_{ij}}{(r_{1,i}r_{2,i})^2}} \frac{\delta_{ij}}{(r_{1,i}r_{2,i})^2}. \quad (8)$$

## 2.2 The inversion methods (SIRT and FBP)

To solve systems of equations as large as eq. (7) there exist some powerful iterative methods (e.g. Kak & Slaney 1988). These methods were first successfully used in tomographic imaging for medical applications and have been extended to other scientific fields. The simplest iterative method is the so-called ART algorithm. For the use of this method it is necessary to make an arbitrary initial guess of the solution  $\vec{\alpha}^0 = (\alpha_1^0, \alpha_2^0, \dots, \alpha_N^0)$ . In our case we simply assign a unity value to all the  $\alpha_j^0$ . Then the ART iteration process can be mathematically described by the following equation:

$$\Delta\alpha_j^{(i)} = \alpha_j^{(i)} - \alpha_j^{(i-1)} = \frac{\vec{\alpha}^{(i-1)} \cdot \vec{w}_i - e_i}{\vec{w}_i \cdot \vec{w}_i}, \quad (9)$$

where  $\vec{w}_i = (w_{i1}, w_{i2}, \dots, w_{iN})$ , and the next solution  $\alpha_j^{(i)}$  is changed from the preceding one  $\alpha_j^{(i-1)}$  by the addition of the quantity  $\Delta\alpha_j^{(i)}$ . This method was applied by Chen & Long (2000) to solve a similar problem.

However, ART reconstructions usually suffer from ‘salt and pepper’ noise which is caused by the inconsistencies introduced in the set of equations by the approximations commonly used in the calculation of the matrix parameters. The SIRT (Kak & Slaney 1988) is another algorithm which eliminates the continual and competing block update as each equation is considered. Then, by using the SIRT algorithm, smoother and better-looking reconstructions are usually obtained at the expense of slower convergence. It is also known that SIRT algorithms perform better in extreme situations such as uneven distribution of data, incompleteness, etc., and it is also possible to easily incorporate constraints as positivity and limited spatial support. The SIRT algorithm computes the correction for each block at each iteration by the use of the same equations as in the ART algorithm, but before making any changes, all the equations are considered and only at the end of each iteration the block values are updated. The correction applied to each block is then the average value of all the computed changes for that block.

In many ART and SIRT implementations the  $w_{ij}$ ’s are simply replaced by 1’s and 0’s depending on whether the centre of the  $i$ th block is within the  $j$ th spheroidal shell. However, the width of the

shell is usually smaller than the width of the block. Thus, in our case, in order to perform a more accurate inversion, we approximately evaluate the fraction of volume  $V_{ij}$  of each block lying inside the  $j$ th spheroidal shell. In this way we prevent the overestimation or underestimation that occurs when only 1’s and 0’s are considered. Thus, we rewrite the coefficients  $w_{ij}$  as:

$$w_{ij} = \frac{1}{\sum_i \frac{V_{ij}}{(r_{1,i}r_{2,i})^2}} \cdot \frac{V_{ij}}{(r_{1,i}r_{2,i})^2}. \quad (10)$$

It is also important to use a relaxation (or smoothing) parameter  $\lambda$  (a factor smaller than unity multiplying the correction factor). If incorrectly selected, it will either cause premature termination and incorrect result or, if the number of iterations or  $\lambda$  is too small, it will result in a reconstruction lacking high-frequency details. By trial and error we chose  $\lambda \sim 0.01$  for about 120 iterations.

There are other faster non-iterative methods which provide solutions to this type of systems of equations. A very convenient and widely used method is the FBP algorithm (Kak & Slaney 1988). In this algorithm the scattering coefficients become simply a weighted average value of the residuals that correspond to a certain block. This makes FBP much faster than any other iterative method. Computation times are about 100 times smaller than the ones for ART or SIRT and no relaxation parameter has to be chosen. The correspondence between the scattering coefficients and the residuals are established following several steps:

(i) For each earthquake  $k$ , the traveltime of the signal from the source to the  $i$ th block plus the traveltime from the  $i$ th block to each seismograph  $l$  is computed. This time is named  $T_{ikl}$ . With this data we define the corresponding spheroidal surface  $S_{ikl}$ . The centre of the  $i$ th block lies on  $S_{ikl}$  and the foci correspond to the location of the hypocentre and the station. Note that each block defines a different spheroidal surface.

(ii) The corresponding magnitude of the residuals for each earthquake  $k$  and each station  $l$  at the time  $T_{ikl}$  is then computed by simple linear interpolation between two consecutive  $e_j$ , because the available discrete data is spaced  $\delta t$ . We call this magnitude  $R(T_{ikl})$ .

(iii) The contribution of each block is proportional to  $1/(r_{1,i}r_{2,i})^2$ . This factor indicates whether the contribution of a certain block is more or less important than the contribution of other blocks on the spheroidal surface  $S_{ikl}$ . Then the spatial perturbation of the scattering coefficient may be written as:

$$\alpha_i = \frac{\sum_k \sum_l w_{ikl} R(T_{ikl})}{\sum_k \sum_l w_{ikl}}. \quad (11)$$

Note that each weight in eq. (11) corresponds to a different spheroidal surface. In order to normalize the contribution of the weights for each spheroidal surface we consider that a good definition for the weights would be:

$$w_{ikl} = \frac{(1/r_{1,i})^2(1/r_{2,i})^2}{\left\langle (1/r_{1,i})^2(1/r_{2,i})^2 \right\rangle_{S_{ikl}}}. \quad (12)$$

We think this definition is very convenient because an analytical expression can be written for the average value. In this way the weights only depend on the location of the  $i$ th block, the hypocentre and the station. This is an important point in order to perform a faster calculation. The average value can be written as:

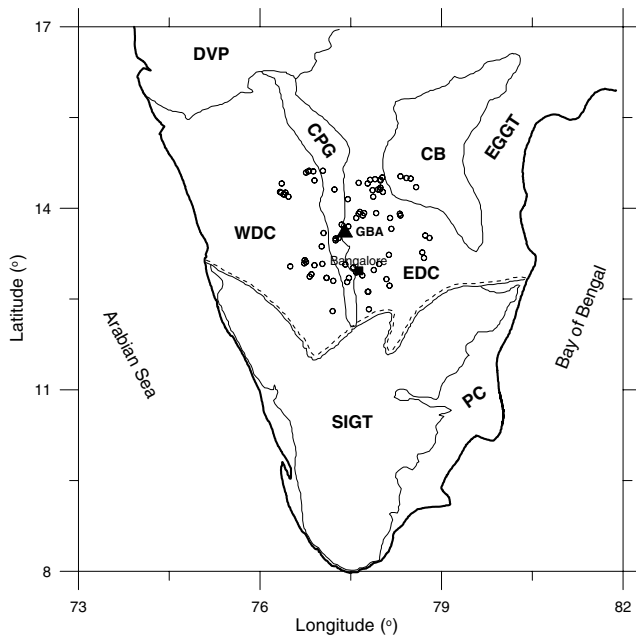


**Figure 1.** General geological sketch map of southern India. DVP, Deccan volcanic province; WDC, western Dharwar craton; EDC, eastern Dharwar craton; SIGT, south Indian granulite terrain; EGGT, eastern Ghat granulite terrain; CPG, closepet granite; CB, Cuddapah basin and PC, Phanerozoic sedimentary cover. Dotted line indicates Fermor's line (boundary between Dharwar craton and south India granulite terrain). The location of the epicentres used for the analysis is also shown (from Tripathi & Ugalde 2004).

$$\langle (1/r_{1,i})^2 (1/r_{2,i})^2 \rangle_{S_{ikl}} = \frac{1}{A_{ikl}} \int_{S_{ikl}} (1/r_{1,i})^2 (1/r_{2,i})^2 dS, \quad (13)$$

where  $A_{ikl}$  is the area of  $S_{ikl}$ . This integral is analogous to the one solved by Sato (1977). Thus, we may write:

$$\int_{S_{ikl}} (1/r_{1,i})^2 (1/r_{2,i})^2 dS = \frac{4\pi}{r\beta T_{ikl}} \cdot \ln \left( \frac{\beta T_{ikl} + r}{\beta T_{ikl} - r} \right). \quad (14)$$

By considering the expression for the area of a spheroid we may then write:

$$A_{ikl} = \frac{\pi}{2} \left( \beta^2 T_{ikl}^2 - r^2 + \beta^2 T_{ikl}^2 \frac{\sqrt{1 - (r/\beta T_{ikl})^2}}{r/\beta T_{ikl}} \arcsin(r/\beta T_{ikl}) \right). \quad (15)$$

And finally we obtain:

$$w_{ikl} = \frac{r\beta T_{ikl}}{8(r_{1,i}r_{2,i})^2} \frac{\left( \beta^2 T_{ikl}^2 - r^2 + \beta^2 T_{ikl}^2 \frac{\sqrt{1 - (r/\beta T_{ikl})^2}}{r/\beta T_{ikl}} \arcsin(r/\beta T_{ikl}) \right)}{\ln \left( \frac{\beta T_{ikl} + r}{\beta T_{ikl} - r} \right)}. \quad (16)$$

In this work, we compare the results of the application of the two inversion algorithms described. Additionally, some conclusions about the practical implementations of the methods are reached.

### 3 GEOLOGICAL SETTING AND DATA

The GBA is located in the Indian peninsula, about 90 km north of Bangalore, on the western flank of the eastern Dharwar craton which is one of the oldest geological provinces in southern India

(Fig. 1). The region is divided into the western (which is composed of old gneisses and greenstones with very few granites) and eastern (which is made of younger rocks with widespread N–S elongate plutons of late Archaean granites) parts by the 400 km long and 20–30 km wide, north–south trending granitic intrusion named Closepet batholith (Moyen *et al.* 2003). The area around the array is relatively flat, with a few hill ranges towards the east and the south. Thus, the topographic influence on scattering would be very small. A crustal model consisting of a 16 km thick top granitic layer over a second layer 19 km thick above the mantle (i.e. with the Moho at 35 km depth) was proposed by Arora (1971) and observed *S*-wave velocities were 3.46, 3.96 and 4.61 km s<sup>-1</sup>, respectively.

Waveform data used were selected from 80 earthquakes with epicentral distances up to 120 km which were recorded by the GBA in the period 1992 January to 1995 December. GBA is an *L*-shaped seismic array and each arm contains 10 short-period ( $T_0 = 1$  s) vertical-component seismometers spaced at intervals of about 2.5 km. The recorded signals are digitized at a sampling interval of 0.05 s. All the events are shallow (depths less than 10 km) and local magnitudes range between 0.3 and 3.7. Attending to the quality of data and after a careful visual inspection, only 636 vertical-component, high-quality waveforms were finally processed.

### 4 DATA ANALYSIS AND RESULTS

One example of the analysis procedure (Nishigami 1991) is shown in Fig. 2. First, each seismogram was bandpass filtered over the

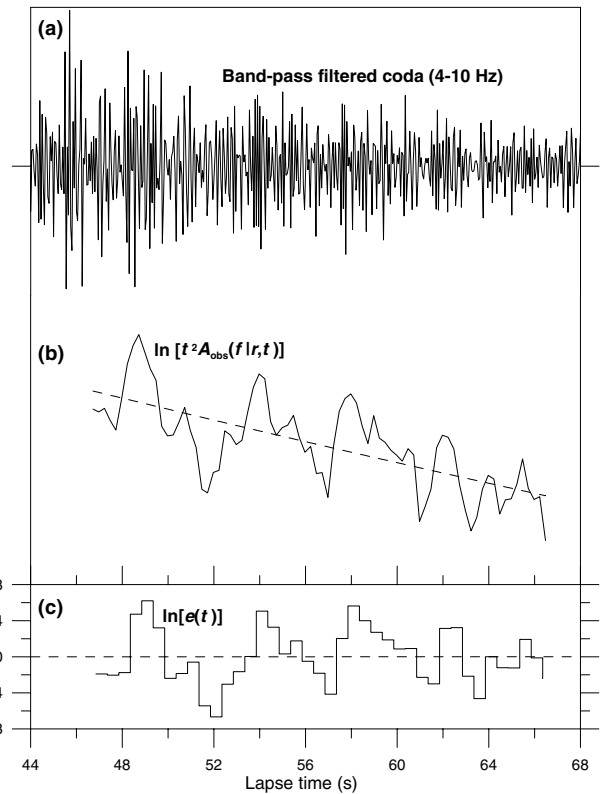


**Figure 2.** Example of the processing steps for obtaining the coda energy residuals: (a) bandpass filtered coda waveform of an earthquake at an epicentral distance of 90.6 km; (b) logarithm of the running mean-squared amplitudes corrected for geometrical spreading effect. The discontinuous line is the best linear fitting function to the logarithmic trace and (c) logarithm of the coda energy residuals averaged in a time window of 0.5 s.

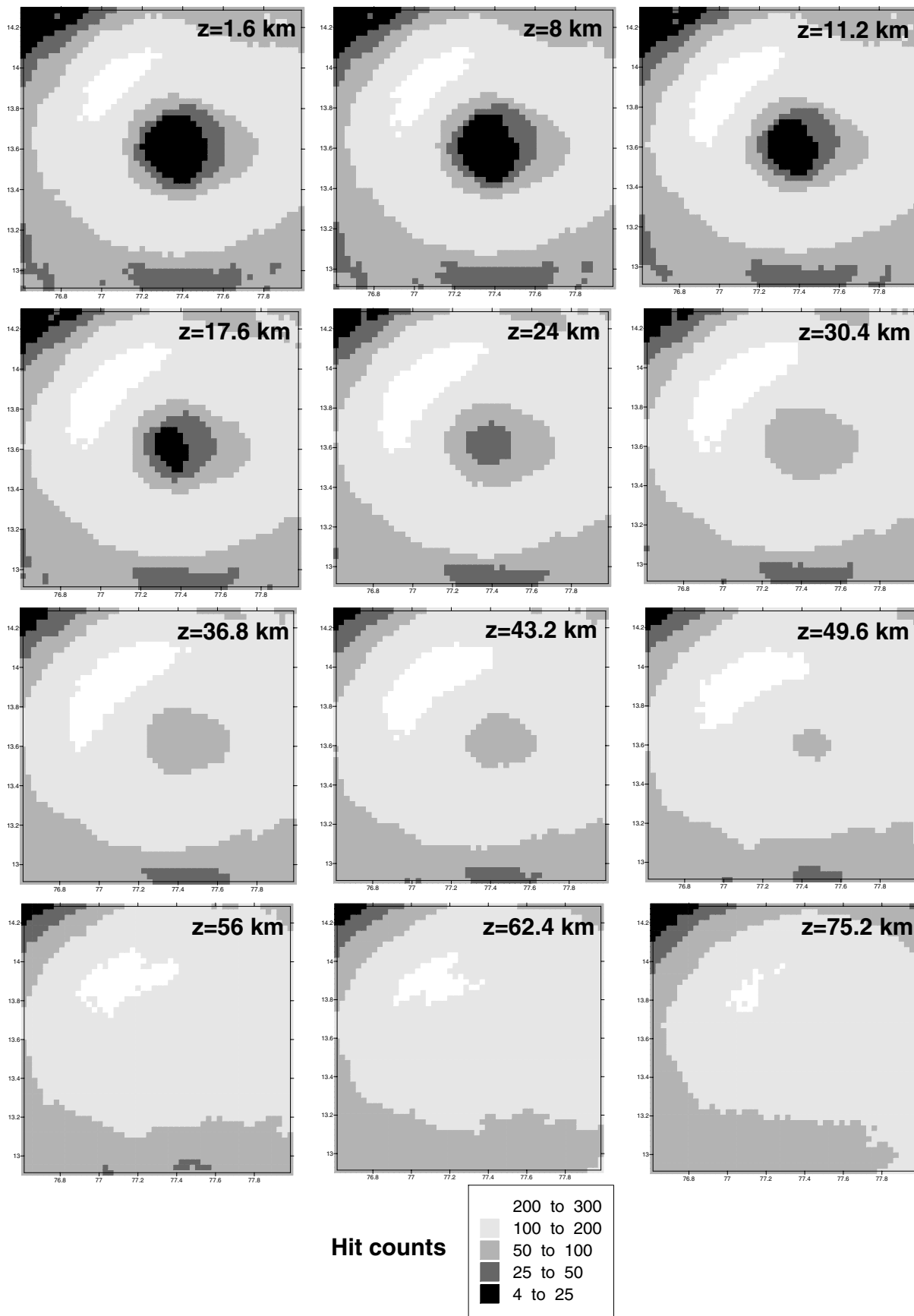


**Figure 3.** Hit counts or number of coda residuals contributed by each block. It measures the number of times each block is sampled by the scattering shells of observed coda data. The darker areas are the zones lesser sampled by the spherical shells.

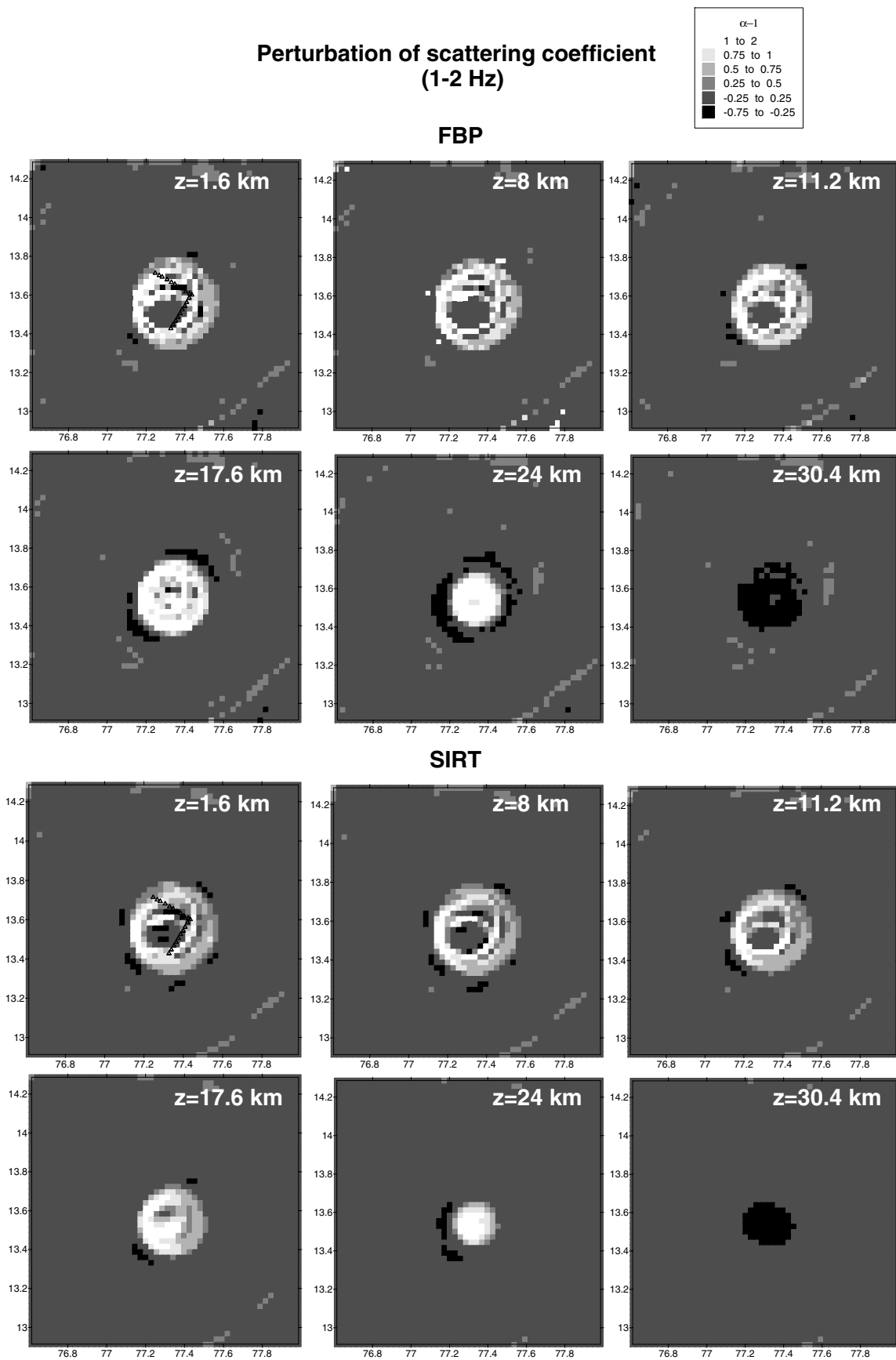


**Figure 4.** Spatial distribution of relative scattering coefficients for different depths and for the two inversion methods used: (a) results for the frequency band 1–2 Hz; (b) 2–4 Hz and (c) 4–10 Hz. The lightest zones indicate the strongest perturbations from an average scattering coefficient.

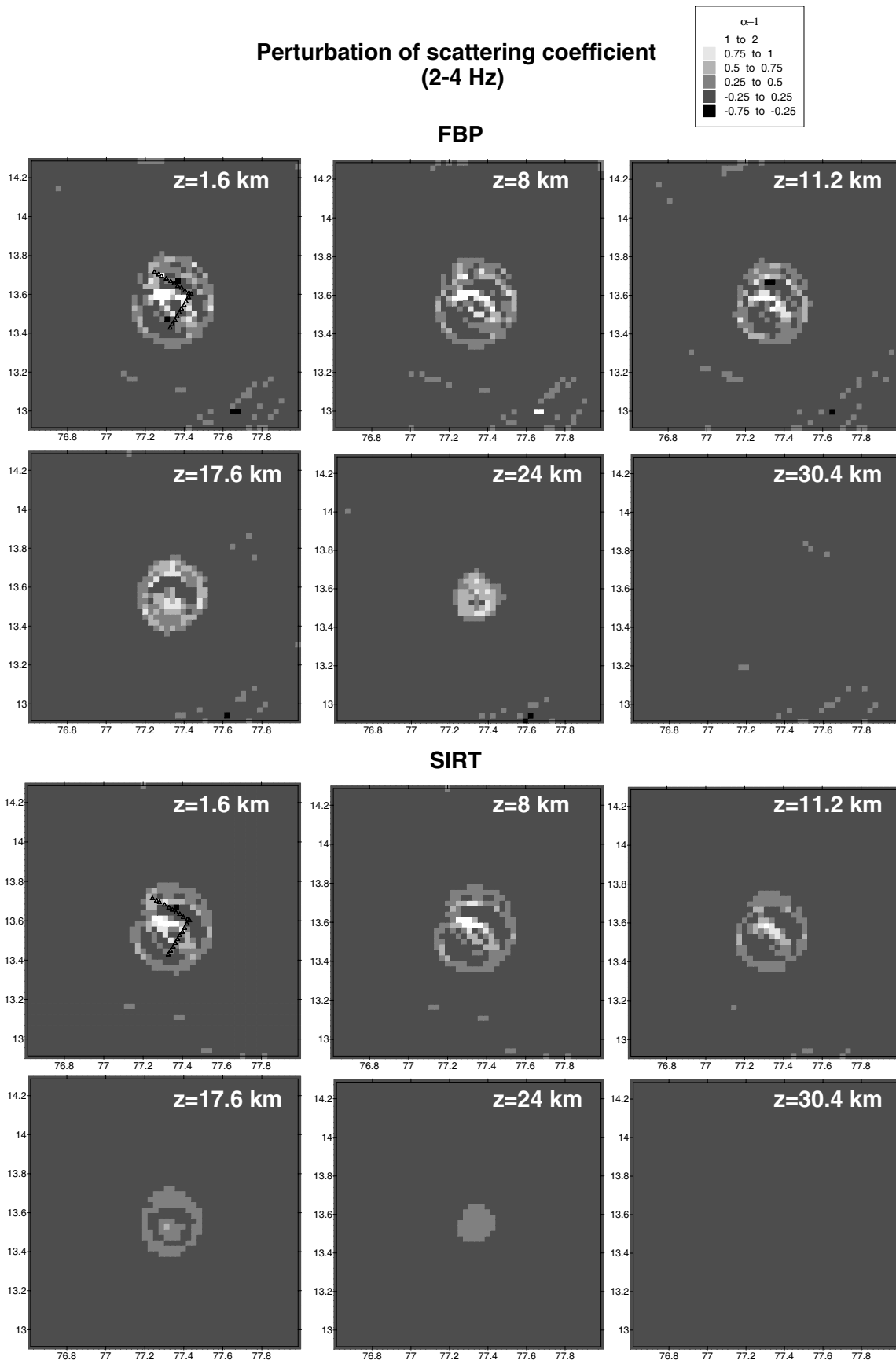


Figure 4. (Continued.)

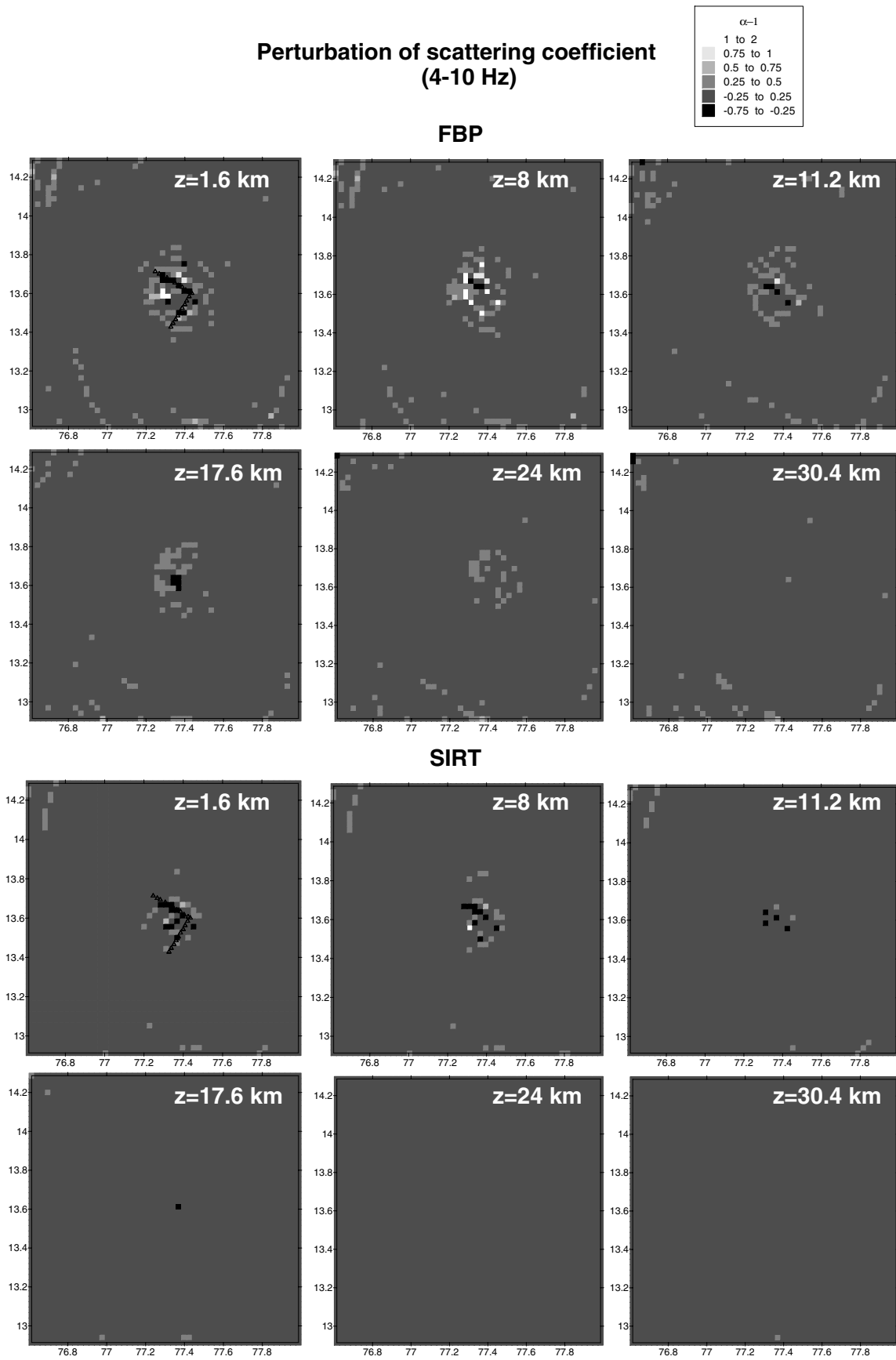
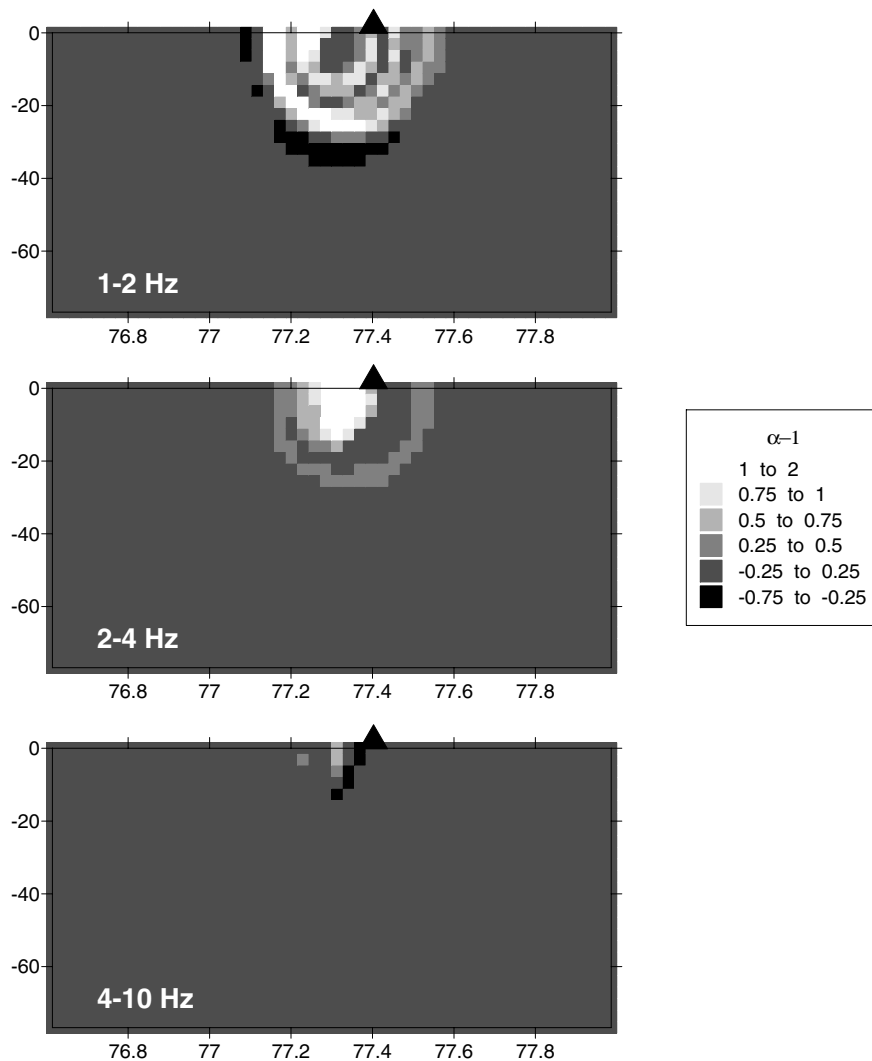


Figure 4. (Continued.)



**Figure 5.** Vertical cross-section of relative scattering coefficients at the parallel  $13.6^\circ$ , which corresponds to the latitude of the array crosspoint.

frequency bands 1–2 ( $1.5 \pm 0.5$ ) Hz, 2–4 ( $3 \pm 1$ ) Hz and 4–10 ( $7 \pm 3$ ) Hz. Then, the rms amplitudes  $A_{\text{obs}}(f|r, t)$  were calculated by using a 0.25 s spaced moving time window of length  $t \pm 2$  s,  $t \pm 1$  s, and  $t \pm 0.5$  s for the first, second and third frequency band, respectively. The time interval for the analysis started at 1.5 times the  $S$ -wave traveltimes (in order to increase the resolution near the source region) and had a maximum length of 20 s (to minimize the effects of multiple scattering). The rms amplitudes for a noise window of 10 s before the  $P$ -wave arrival were also computed and only the amplitudes greater than two times the signal to noise ratio were kept. The amplitudes were then corrected for geometrical spreading by multiplying by  $t^2$  which is valid for body waves in a uniform medium. Then, the average decay curve was estimated for each seismogram by means of a least-squares regression of  $\ln[t^2 A_{\text{obs}}(f|r, t)]$  versus  $t$  and only the estimates with a correlation coefficient greater than 0.60 were kept. The observed coda residuals  $e(t)$  were then calculated by taking the ratio of the corrected observed amplitudes to the estimated exponential decay curve. Finally the residuals were averaged in time windows of  $\delta t = 0.5$  s to get  $e_j$  at discrete lapse times  $t_j$ . The decrease of  $\delta t$  increases the spatial resolution, but also the size of the inversion problem. In this case, the system (7) has a number of equations of  $\sim 2700$  for the frequency bands centred at

1.5 and 7 Hz, and  $\sim 5200$  equations for the 3 Hz centre frequency. The time window for the averaging must also satisfy the condition  $\delta t \leq 2(\delta V)^{1/3}/\beta$ , where  $\delta V$  is the volume of one small block into which the study area is divided and  $\beta = 3.65 \text{ km s}^{-1}$  in this region (Arora 1971; Krishna & Ramesh 2000). This condition assures that the width of each spheroidal shell is smaller than the size of a block.

We selected a  $155 \times 155$  km in horizontal and 80 km in depth study region attending to the stations and hypocentres distribution and it was divided into  $N = 50 \times 50 \times 25$  blocks. Then, the observational system of eq. (7) was created by assuming the layered velocity structure by Arora (1971) and it was solved using the SIRT and FBP algorithms.

Before discussing the results, we examine the reliability of the solution. Fig. 3 shows the hit counts, or number of coda residuals contributed by each block, that shows which grid zones may be affected by sampling insufficiency for the grid defined. It can be observed that the entire region is sampled by the ellipses, however, the hit counts are much less in an area close around the array and they increase both in horizontal and depth directions up to the considered depth of 80 km. This happens because the stations are concentrated in a small area, which makes all the blocks which are close to the

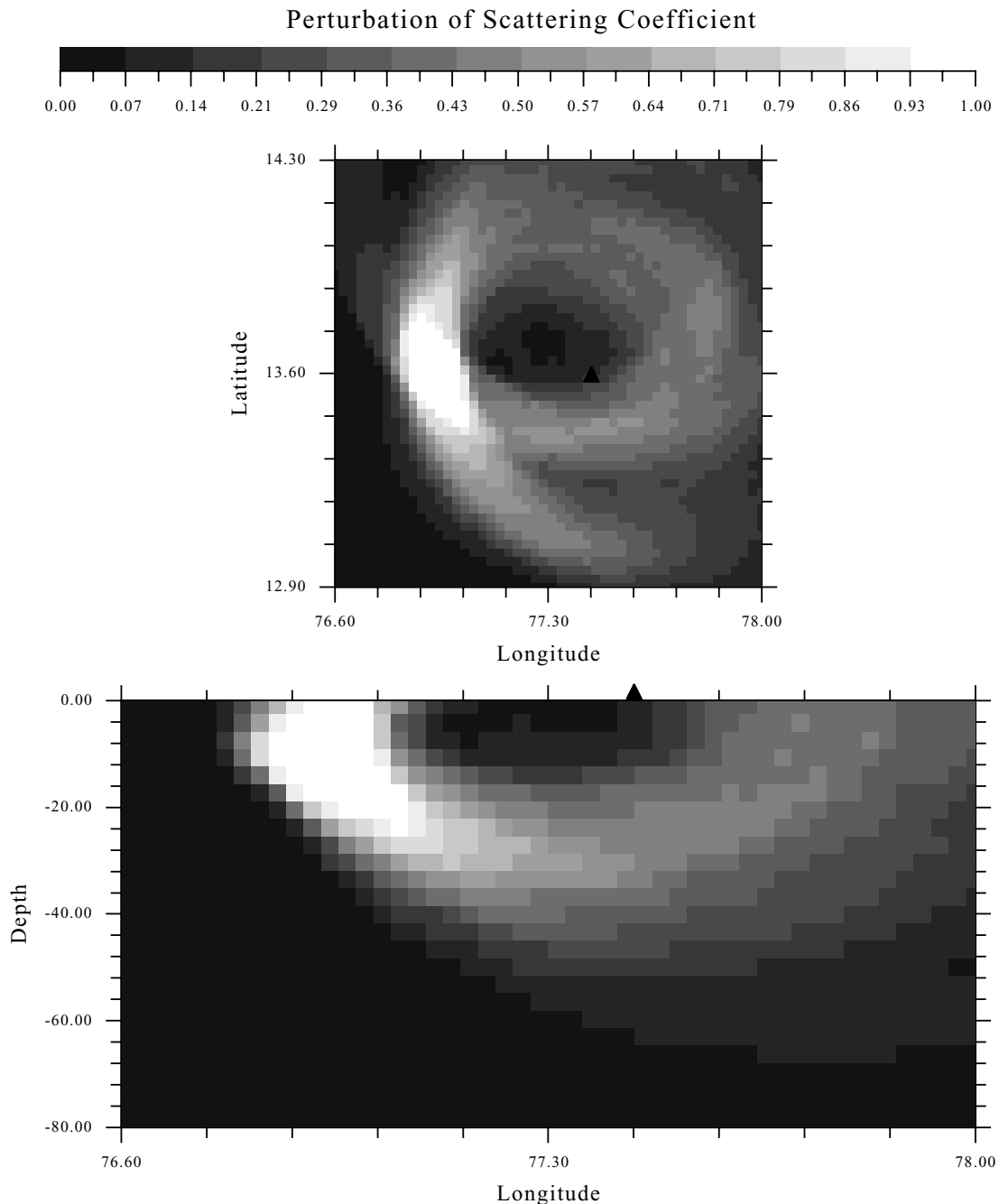


**Figure 6.** Spatial distribution of relative scattering coefficients for a synthetic test consisting of one spheroidal structure with two horizontal semi-axes of 13 km and the vertical semi-axis of 9.3 km. It was located at different distances from the array centre point, which is shown by a solid triangle: (a) to the west; (b) below and (c) to the east. The pattern recovered at a depth of 0 km is plotted at the top of the figure. The vertical cross-section along the plane defined by the latitude of the array centre point is also shown.

array to correspond to short lapse times, and they are few because we omitted the earliest portion of the  $S$ -wave coda by adopting  $1.5t_S$  as start time for the analysis.

On the other hand, we tested the resolution of the inversion methods by synthesizing the coda energy residuals from the observational equation using a given test distribution of scattering coefficients and the same distribution of stations and events used in the analysis. We generated vertical structures with positive perturbations of the scattering coefficient with horizontal dimensions equal to one block and depths up to 80 km embedded in a non-perturbed medium. Then the

synthesized residuals were inverted. Results show that although the vertical structures are seen almost up to the maximum depth considered of 80 km, they are well reproduced (more than 50 per cent of the perturbation value is returned) only up to the seventh block (22.4 km).

The resulting distribution of relative scattering coefficients  $\alpha - 1 = (g - g_0)/g_0$  in the study region for the three analysed frequency bands and for different depths is plotted in Fig. 4. The lightest tones indicate scattering coefficients larger than the average in this region.

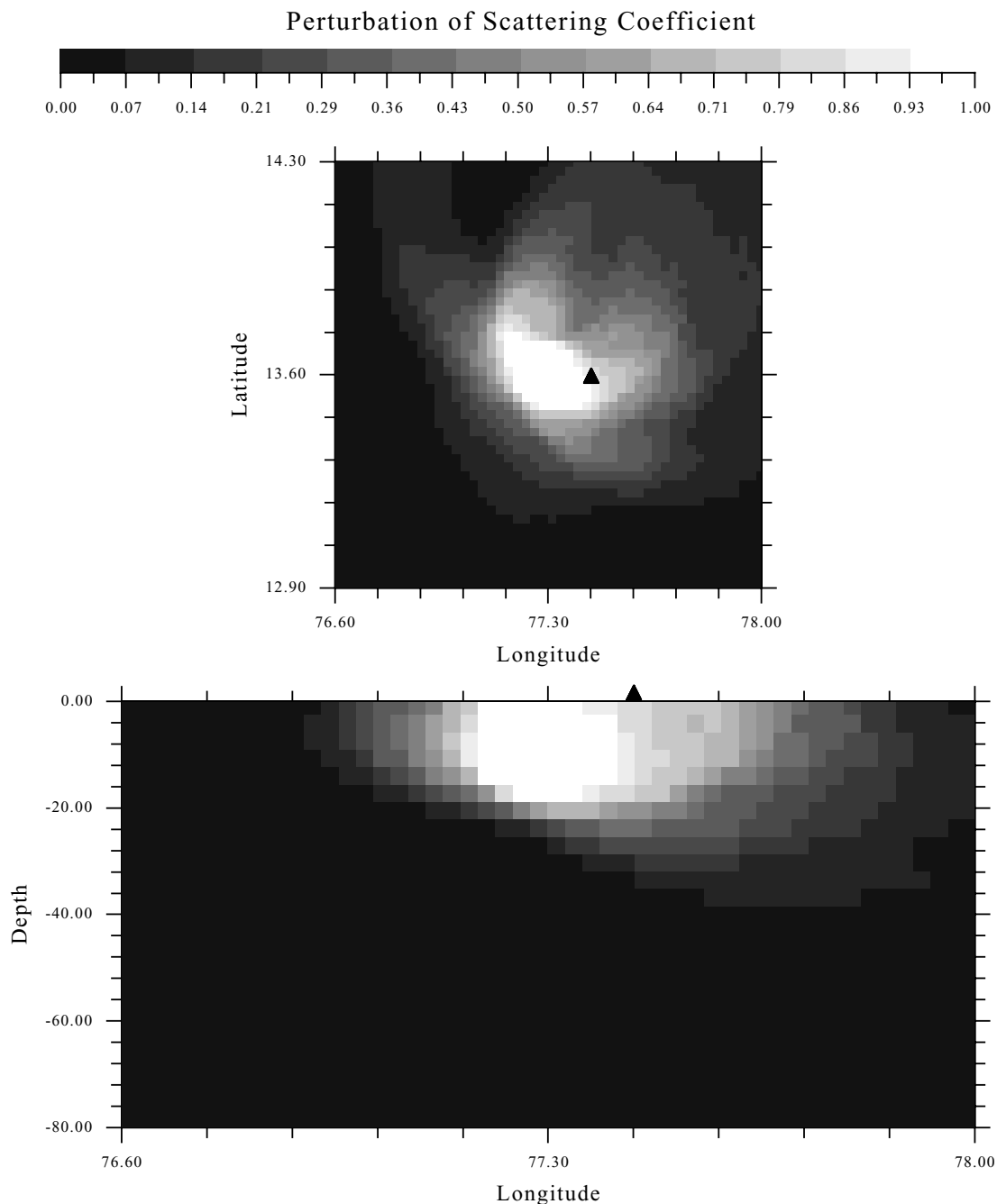


**Figure 6.** (Continued.)

## 5 DISCUSSION

It can be observed that we obtain practically the same distribution of relative scattering coefficients regardless of applying the SIRT or FBP inversion algorithms. Whereas the SIRT algorithm provides slightly lower values of the relative scattering coefficients, the FBP method provides more contrast. Thus, we would recommend the use of the FBP method, which requires much lesser (about 100 times) computation time.

On the other hand, Fig. 4 shows that more than the 90 per cent of the analysed region reveals a spatial perturbation of the scattering coefficient between  $\pm 25$  per cent. This means that the crust around GBA presents a remarkably uniform distribution of scattering

coefficients. For low frequencies, this uniformity is broken by the presence of a strong scattering area which is recognized from the surface up to a depth of 24 km just below the array. This structure is not observed at high frequencies. In fact, each analysed frequency band is giving us information about inhomogeneous structures with sizes comparable to the seismic wavelengths ( $\sim 1.8$  to  $\sim 3.6$  km for 1–2 Hz,  $\sim 900$  m to  $\sim 1.8$  km for 2–4 Hz, and  $\sim 360$  m to  $\sim 900$  m for 4–10 Hz in this case). Fig. 5 shows a cross-section of relative scattering coefficients shown in Fig. 4 projected onto the vertical plane defined by the parallel of the array centre point. It can be observed that the strongest scatterers are located on the western part of GBA. However, Figs 4 and 5 show that the heterogeneity follows an ellipsoidal pattern. This may happen because this area is poorly sampled

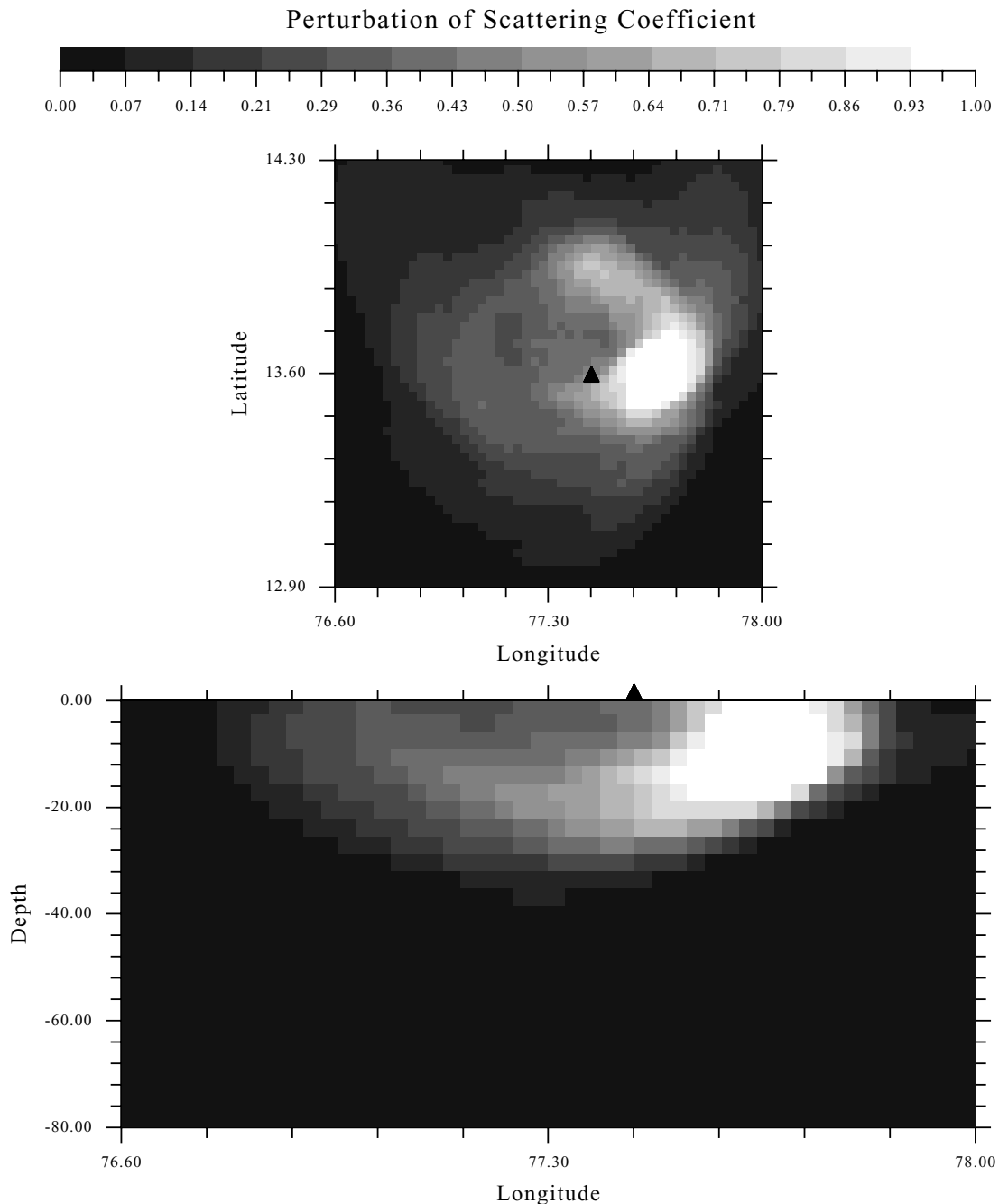


**Figure 6.** (Continued.)

by the ellipses as previously discussed in Fig. 3, however, the behaviour is only observed for the lowest frequency band analysed. In fact, we detected high values of the residuals at low frequencies and short lapse times. In order to establish the validity of the results of this study we tested the inversion method by means of a synthetic test. Because the most notable geological feature in the considered region is the 400 km long and 20–30 km wide, north–south trending Closepet granitic intrusion, we simulated the existence of a single spheroidal structure with positive perturbations of the scattering coefficient at different locations in a non-perturbed medium. Results of the inversion of the synthesized residuals are shown in Fig. 6. It can be observed that the patterns of the test are well reproduced. We may then conclude that the scattering region observed near the

array centre point (Fig. 4) is neither a ghost image nor a mathematical artefact. Thus we may consider that the inversion method may reproduce up to a certain extent the observed data.

With respect to the uniform distribution of scattering coefficients, our results are in accordance with previous studies performed in the region. In an early work in this region using statistical analysis of observed teleseismic traveltime residuals, Berteussen *et al.* (1977) remarked that the area on which GBA is sited presents exceptionally homogeneous structures, apart from the general existing velocity perturbations of the order of a few percent. This conclusion was partly supported by Mohan & Rai (1992), who also detected the presence of a prominent scatterer in the deep crustal and uppermost mantle level (30–55 km) in this region from a

semblance technique analysis. The scattering region coincided with the Closepet granitic intrusion in the region. Krishna & Ramesh (2000) performed a frequency–wavenumber ( $f$ – $k$ ) spectral analysis of  $P$ -coda waveforms to mine tremors and explosions recorded at GBA array. They found a near-on azimuth dominant energy peak with apparent velocity appropriate to the upper crustal depths and they interpreted the result by the presence of a scattering waveguide at upper crustal depths (5–15 km) which might be also related to the granitic batholith. In our case, the zone of strong relative scattering coefficients at low frequency to the west of the GBA array cross-point also coincides with the so-called Closepet batholith, which is a granitic intrusion that acts as the major geological boundary in the region and it is believed to be a Precambrian suture zone between the eastern and western Dharwar craton.

## 6 CONCLUSIONS

We estimated the 3-D distribution of relative scattering coefficients in the crust in southern India by means of an  $S$ -wave coda envelope inversion technique applied to local recordings by the GBA. Two different inversion algorithms were used for the first time in this type of seismological research: the SIRT and the FBP method. The results allowed us to reach the following conclusions:

- (1) The spatial distribution of the relative scattering coefficients obtained was almost independent of the inversion method used.
- (2) The FBP method is very convenient and appropriate for solving these kinds of problems because it requires about 100 times less computation time than the SIRT algorithm to invert the data.
- (3) The crust of the analysed region around GBA showed a remarkably uniform distribution of scatterers at more than the 90 per cent of the area, which is in accordance with the conclusions of previous studies in the region using statistical analysis of observed teleseismic traveltime residuals.
- (4) An inhomogeneous structure with size comparable to a wavelength of  $\sim 1.8$  to  $\sim 3.6$  km for 1.5 Hz was detected to the west of GBA from the surface up to a depth of about 24 km just below the array and it coincides with the Closepet granitic intrusion which is the major geological boundary between the eastern and western Dharwar craton.

## ACKNOWLEDGMENTS

The authors are very grateful to the GBA authorities and staff for providing the data used in this study. We also acknowledge useful comments and suggestions by H. Sato, L. T. Long and Y. Asano. The editor A. Curtis, J. Spetzler and an anonymous reviewer provided helpful comments which improved the manuscript.

## REFERENCES

- Aki, K., 1969. Analysis of the seismic coda of local earthquakes as scattered waves, *J. geophys. Res.*, **74**, 615–631.
- Aki, K. & Chouet, B., 1975. Origin of coda waves: source, attenuation and scattering effects, *J. geophys. Res.*, **80**, 3322–3342.
- Arora, S.K., 1971. A study of the earth's crust near Gauribidanur, South India, *Bull. seism. Soc. Am.*, **61**, 671–683.
- Asano, Y. & Hasegawa, A., 2004. Imaging the fault zones of the 2000 western Tottori earthquake by a new inversion method to estimate three-dimensional distribution of the scattering coefficient, *J. geophys. Res.*, **109**, B06306, doi:10.1029/2003JB002761.
- Berteussen, K.A., Husebye, E.S., Mereu, R.F. & Ram, A., 1977. Quantitative assessment of the crust-upper mantle heterogeneities beneath the Gauribidanur seismic array in southern India, *Earth Planet. Sci. Lett.*, **37**, 326–332.
- Chen, X. & Long, L.T., 2000. Spatial distribution of relative scattering coefficients determined from microearthquake coda, *Bull. seism. Soc. Am.*, **90**, 512–524.
- Hoshiya, M., 1991. Simulation of multiple scattered coda wave excitation based on the energy conservation law, *Phys. Earth planet. Int.*, **67**, 123–136.
- Hoshiya, M., 1995. Estimation of nonisotropic scattering in western Japan using coda wave envelopes: application to a multiple nonisotropic scattering model, *J. geophys. Res.*, **100**, 645–657.
- Kak, A.C. & Slaney, M., 1988. *Principles of Computerized Tomographic Imaging*, IEEE Press, New York.
- Krishna, V.G. & Ramesh, D.S., 2000. Propagation of crustal-waveguide-trapped Pg and seismic velocity structure in South Indian shield, *Bull. seism. Soc. Am.*, **90**, 1281–1294.
- Mohan, G. & Rai, S.S., 1992. Imaging of seismic scatterers beneath the Gauribidanur (GBA) array, *Phys. Earth Planet. Int.*, **71**, 36–45.
- Moyen, J.F., Nédélec, A., Martin, H. & Jayananda, M., 2003. Syntectonic granite emplacement at different structural levels: the Closepet granite, South India, *J. Struct. Geol.*, **25**, 611–631.
- Nishigami, K., 1991. A new inversion method of coda waveforms to determine spatial distribution of coda scatterers in the crust and uppermost mantle, *Geophys. Res. Lett.*, **18**, 2225–2228.
- Nishigami, K., 1997. Spatial distribution of coda scatterers in the crust around two active volcanoes and one active fault system in central Japan: Inversion analysis of coda envelope, *Phys. Earth planet. Int.*, **104**, 75–89.
- Nishigami, K., 2000. Deep crustal heterogeneity along and around the San Andreas fault system in central California and its relation to segmentation, *J. geophys. Res.*, **105**, 7983–7998.
- Pullii, J.J., 1984. Attenuation of coda waves in New England, *Bull. seism. Soc. Am.*, **74**, 1149–1166.
- Rautian, T.G. & Khalaturin, V.I., 1978. The use of coda for determination of the earthquake source spectrum, *Bull. seism. Soc. Am.*, **68**, 923–948.
- Sato, H., 1977. Energy propagation including scattering effects; single isotropic scattering, *J. Phys. Earth*, **25**, 27–41.
- Sato, H., 1995. Formulation of the multiple non-isotropic scattering process in 3-D space on the basis of the energy transport theory, *Geophys. J. Int.*, **121**, 523–531.
- Sato, H., Fehler, M. & Wu, R.-S., 2002. Scattering and attenuation of seismic waves in the lithosphere, Chapter 13 in *International Handbook of Earthquake and Engineering Seismology*, pp. 195–208, eds Jennings, P., Kanamori, H. & Lee, W.
- Tripathi, J.N. & Ugalde, A., 2004. Regional estimation of  $Q$  from seismic coda observations by the Gauribidanur seismic array (southern India), *Phys. Earth planet. Int.*, **145**, 115–126.
- Wu, R.-S., 1985. Multiple scattering and energy transfer of seismic waves—separation of scattering effect from intrinsic attenuation—I. Theoretical modelling, *Geophys. J. R. astr. Soc.*, **82**, 57–80.
- Zeng, Y., Su, F. & Aki, K., 1991. Scattered wave energy propagation in a random isotropic scattering medium, I, Theory, *J. geophys. Res.*, **96**, 607–619.



## Three-dimensional spatial distribution of scatterers in Galeras volcano, Colombia

E. Carcolé,<sup>1</sup> A. Ugalde,<sup>1</sup> and C. A. Vargas<sup>2</sup>

Received 12 January 2006; revised 16 March 2006; accepted 29 March 2006; published 27 April 2006.

[1] A three-dimensional spatial distribution of relative scattering coefficients is estimated for the Galeras volcano, Colombia, by an inversion of the coda wave envelopes from 1564 high quality seismic recordings at 31 stations of the Galeras seismograph network. The inversion reveals a highly non-uniform distribution of relative scattering coefficients in the region for the two analyzed frequency bands (4-8 and 8-12 Hz). Strong scatterers show frequency dependence, which is interpreted in terms of the scale of the heterogeneities producing scattering. Two zones of strong scattering are detected: the shallower one is located at a depth from 4 km to 8 km under the summit whereas the deeper one is imaged at a depth of  $\sim 37$  km from the Earth's surface. Both zones may be associated with the magmatic plumbing system beneath Galeras volcano. The second strong scattering zone may be related to a deeper magma reservoir that feeds the system. **Citation:** Carcolé, E., A. Ugalde, and C. A. Vargas (2006), Three-dimensional spatial distribution of scatterers in Galeras volcano, Colombia, *Geophys. Res. Lett.*, 33, L08307, doi:10.1029/2006GL025751.

### 1. Introduction

[2] Galeras volcano (1.23°N, 77.36°W; summit elevation 4,276 m) is a 4,500 years old active cone of a more than 1 Ma old volcanic complex which is located in the Central Cordillera of the southwestern Colombian Andes (Figure 1). It is historically the most active volcano in Colombia and it has been re-activated frequently in historic times [*Banks et al.*, 1997]. It is located only 9 km west of the city of San Juan de Pasto which has a population of more than 300,000 and another 100,000 people live around the volcano. Although it has a short-term history of relatively small-to-moderate scale eruptions, the volcanic complex has produced major and hazardous eruptions [*Calvache et al.*, 1997] thus constituting a potential risk to the human settlements in this region. Galeras was designated a Decade Volcano in 1991, which identified it as a target for intensive and interdisciplinary study during the United Nations' International Decade for Natural Disaster Reduction.

[3] The re-activation of Galeras volcano was recognized in 1988 after forty years of repose [*Williams et al.*, 1990] and the eruptive period lasted until 1995. Since then, the volcano has been in a relatively calm stage with some ash and gas emission episodes and low-level eruptive activity. A

crater located to the east of the main one was re-activated in 2002 after more than 10 years of inactivity. A new eruptive episode consisting of three explosive events began in 2004 and it continues active at the time of this writing.

[4] Seismicity in the region since 1988 has been characterized by long period events, volcano-tectonic earthquakes and tremor episodes. A type of unusual shallow-source, low frequency seismic signals called "tornillos" which are related to magmatic activity have also been recorded during different stages of volcanic activity at Galeras [*Gómez and Torres*, 1997]. The level of seismic activity has fluctuated, alternating periods of low-level seismicity with episodes of increased seismic activity in terms of the number and/or magnitude of the events. Some shallow (up to 8 km) volcano-tectonic earthquakes have reached local magnitudes up to 4.7.

[5] With the aim of enlarging the knowledge of the internal structure of the volcano as well as to serve for its seismic hazard assessment, the present study is a different complementary contribution to the interdisciplinary research (geological, geophysical and geochemical) being conducted in the region since the re-activation of Galeras volcano. We will focus on the imaging of small-scale heterogeneities by estimating the three-dimensional spatial distribution of relative scattering coefficients from shallow earthquakes that occurred under the volcano region.

### 2. Data and Method

[6] Data used in this study is a selection of 1564 high quality records of the S-wave coda from shallow earthquakes (depths less than 10 km from the Earth's surface) with local magnitudes less than 2.0 which occurred in the region from 1989 to 2002. The 31 short-period ( $T_0 = 1$  s), vertical component recording stations used were deployed at different stages of the Galeras seismic network operation and they were located at distances less than 10 km from the active crater (Figure 1).

[7] In order to estimate the inhomogeneous spatial distribution of relative scattering coefficients in the crust we followed the method proposed by *Nishigami* [1991] by using an inversion method of coda waveforms from local earthquakes. This method assumes that the fluctuation of the decay curve of the observed coda envelope is caused by a non-uniform distribution of scatterers. The decay curve is then compared with a reference curve, which is estimated by assuming single isotropic scattering and spherical radiation from the source. This method with some adaptations has proved to be an effective approach to investigate the real heterogeneous structure in the crust of several regions in the world [*Nishigami*, 1991, 1997, 2000; *Chen and Long*, 2000; *Asano and Hasegawa*, 2004; *Ugalde et al.*, 2006].

<sup>1</sup>Observatori de l'Ebre, CSIC—Universitat Ramon Llull, Roquetes, Spain.

<sup>2</sup>Departamento de Geociencias, Universidad Nacional de Colombia, Bogotá, Colombia.

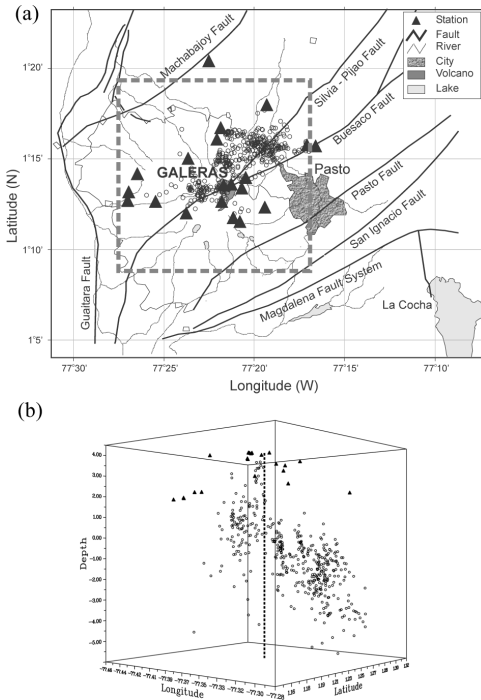


**Figure 1.** Map of the Galeras volcanic complex region showing the location of the epicenters and seismic stations used: (a) horizontal projection at the surface where the study area is indicated by a dotted square; and (b) a 3-D representation of the stations and hypocenters location.

[8] According to *Nishigami* [1991] the observational system of equations relating the spatial distribution of relative scattering strength to the observed coda energy residuals under the assumption of single isotropic scattering and spherical radiation of a seismic source can be written as:

$$\begin{aligned}
 w_{11}\alpha_1 + \dots + w_{i1}\alpha_i + \dots + w_{N1}\alpha_N &= e_1 \\
 &\vdots \\
 w_{1j}\alpha_1 + \dots + w_{ij}\alpha_i + \dots + w_{Nj}\alpha_N &= e_j \\
 &\vdots \\
 w_{1M}\alpha_1 + \dots + w_{iM}\alpha_i + \dots + w_{NM}\alpha_N &= e_M
 \end{aligned} \quad (1)$$

[9] This system of equations is obtained by dividing the coda of each seismogram into several small time windows, thus having one equation based on (1) for each time window. Also for each time window, the scatterers contributing to the energy density are contained in a spheroidal shell. Therefore,  $M$  is the total number of equations (number of seismograms multiplied by the number of coda time windows considered), and  $N$  is the total number of scatterers (number of small blocks into which the study region is divided). The right side of equation (1) is called coda wave energy residual ( $e_j$ ) which measures the ratio of the observed energy density in this part of the coda to the average energy density of the medium [*Sato*, 1977], and the unknowns  $\alpha_i \geq 0$  are the spatial perturbations of the average scattering coefficient of the medium due to an individual scatterer. The weights  $w_{ij}$  are defined as:

$$w_{ij} = \frac{1}{\sum_i \frac{1}{(r_{1,i}r_{2,i})^2}} \frac{1}{(r_{1,i}r_{2,i})^2} \quad (2)$$

where  $r_{1,i}$  and  $r_{2,i}$  are the distances between the hypocenter and the scatterer  $i$  and the scatterer  $i$  and the station, respectively.

[10] To solve systems of equations as large as (1) there are some powerful iterative and non-iterative methods [e.g., *Kak and Slaney*, 1988] that were first successfully used in tomographic imaging for medical applications and that have been extended to other scientific fields. A very convenient non-iterative method is the Filtered Back-Projection (FBP) algorithm which has proved to be about 100 times faster than the Algebraic Reconstruction Technique (ART) or Simultaneous Iterative Reconstruction Technique (SIRT) iterative methods [*Ugalde et al.*, 2006].

### 3. Analysis and Results

[11] Because each analyzed frequency band is giving us information about inhomogeneous structures with sizes comparable to the seismic wavelengths, and given that the signal energy contents of the available data decays abruptly for frequencies  $f$  above 12 Hz, we decided to calculate the coda wave energy residuals [*Nishigami*, 1991; *Ugalde et al.*, 2006] for the frequency bands 4–8 ( $6 \pm 2$ ) Hz and 8–12 ( $10 \pm 2$ ) Hz, thus allowing us to image structures of sizes comparable to wavelengths of  $\sim 400$  to  $\sim 800$  m for 4–8 Hz, and  $\sim 300$  m to  $\sim 400$  m for 8–12 Hz. These sizes are derived by considering an average S-wave velocity of  $\beta = 3.3$  km/s in the study region. From the bandpass-filtered seismograms, we calculated the rms amplitudes  $A_{obs}(f|r, t)$  for each hypocentral distance  $r$  by using a 0.25 s spaced moving time window of length  $t \pm 1$  s, and  $t \pm 0.5$  s for the 6 Hz and 10 Hz center frequencies, respectively. The time interval for the analysis started at 1.5 times the S-wave travel times (in order to increase the resolution near the source region) and had a maximum length of 20 s (to minimize the effects of multiple scattering). We also computed the rms amplitudes for a noise window of 10 s before the P-wave arrival and only the amplitudes greater than two times the signal to noise ratio were kept. Then, the average decay curve was estimated for each seismogram by means of a linear regression of  $\ln[r^2 A_{obs}(f|r, t)]$  vs.  $t$ , where the term  $r^2$  is a geometrical spreading correction which is valid for body waves in a uniform medium. We only kept the estimates with a correlation coefficient (of the linear regression) greater than 0.60. The observed coda energy residuals  $e(t)$  were then calculated by taking the ratio of the corrected observed amplitudes to the estimated exponential decay curve. Finally the residuals were averaged in time windows of  $\delta t = 0.25$  s to get  $e_j$  at discrete lapse times  $t_j$ . The decrease of  $\delta t$  increases the spatial resolution, but also the size of the inversion problem.

[12] A 20 km  $\times$  20 km in horizontal and 50 km in depth study region was selected taking into account the distribution of stations and hypocenters. The study region was divided into  $N = 50 \times 50 \times 50$  blocks, the volume of which satisfies the condition  $\delta t \leq 2(\delta V)^{1/3}/\beta$ . Then, the observational system of equations (1) was created by assuming the layered velocity structure shown in Table 1 and it was solved using the FBP algorithm [*Ugalde et al.*, 2006].

[13] To check for sampling insufficiencies, we computed the hit counts, or number of coda residuals contributed by each block. We found that the entire region is sampled by

**Table 1.** Layered Velocity Structure Model Considered<sup>a</sup>

Depth (km)	S-Wave Velocity (km/s)
4	2.0
2	2.1
0	2.2
-4	3.4
-22	3.8
-40	4.5

<sup>a</sup>D. Gómez (Vulcanological and Seismological Pasto Observatory, personal communication, 2005).

the ellipses although the number of hit counts is smaller at the deepest levels and also inside a shallow area to the north-east of the volcano summit.

[14] The resulting distribution of relative scattering coefficients  $\alpha - 1$  in the study region for the analyzed frequency bands and for different depths up to 10 km from the summit is plotted in Figure 2. The colour scale indicates the perturbation of scattering coefficients from the average in this region, being the largest values  $\sim 3.0$  and the minimum  $\sim 0.5$ . The stability of the solution was checked by decreasing  $\delta t$  and increasing the number of blocks. The resulting image showed the same distribution of strong and low scattering areas with slightly different values of the relative scattering coefficients.

**4. Discussion and Conclusions**

[15] Figure 2 shows that the region of  $\pm 10$  km in horizontal and 10 km in depth centred at the Galeras

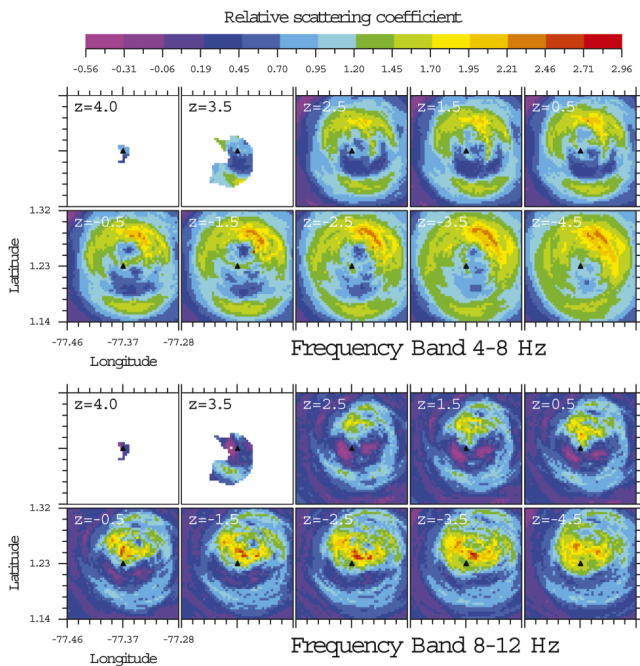


**Figure 2.** Horizontal sections of the study area showing the distribution of the relative scattering strength ( $\alpha-1$ ) at different depths from 4 km to  $-4.5$  km. The solid triangle indicates the location of the Galeras volcano summit. The topographic contour lines at 4000 m and 3500 m levels are also plotted.

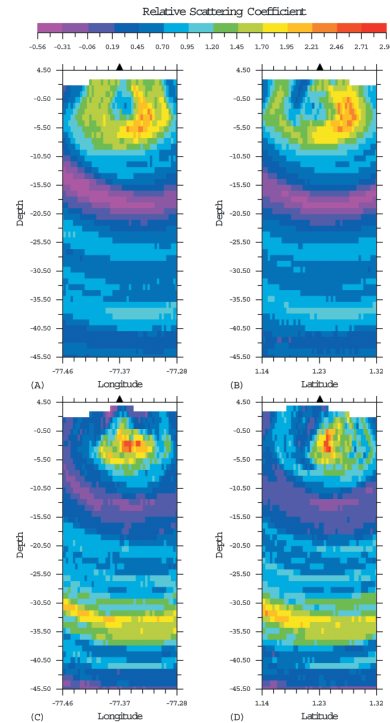


**Figure 3.** Vertical cross section of the study region along the two planes defined by the summit coordinates, which is indicated by the solid triangle (latitude  $1.23^\circ$  and longitude  $-77.36^\circ$ ). The color scale indicates the perturbation of the scattering coefficient  $\alpha-1$  for the (a and b) 4–8 Hz and (c and d) 8–12 Hz frequency bands.

volcano summit presents a remarkable inhomogeneous distribution of relative scattering coefficients. More than the 83% and 50% of the analyzed region for low and high frequencies, respectively, reveal a spatial perturbation of the scattering coefficient greater than +50%. For low frequencies, a strong scattering donut-shaped area with relative scattering coefficients between 0.96 and 3.0 is found around the volcano at all depths. The volume showing the strongest relative scattering coefficients ( $\alpha - 1 \sim 2.0-3.0$ ) is located to the northeast of the volcano at depths between  $-0.5$  km and  $-4.5$  Km. At high frequencies, the strong scattering zone occurs slightly to the north of the axis of the volcano at the same depths. Also we may notice that the scattering strength is similar but slightly lower for the lower frequency band. Then, we may conclude that, at shallow depths, there is a single complex structure located at the north of the volcano that shows a frequency dependent behaviour. The relative scattering coefficients at high frequencies are stronger than those at low frequencies in a volume near the axis of the volcano, which means that the area contains small-size heterogeneities such as small fractures (comparable to a wavelength of  $\sim 300$  m to  $\sim 400$  m for a centre frequency of 10 Hz) which contribute more scattered energy than those with larger sizes. On the contrary, heterogeneities with sizes comparable to a wavelength of  $\sim 400$  to  $\sim 800$  m for a centre frequency of 6 Hz contribute more to the scattering energy at the north-east of the summit.

[16] Figure 3 shows a vertical cross section of the region along the east-west and north-south directions centred at the

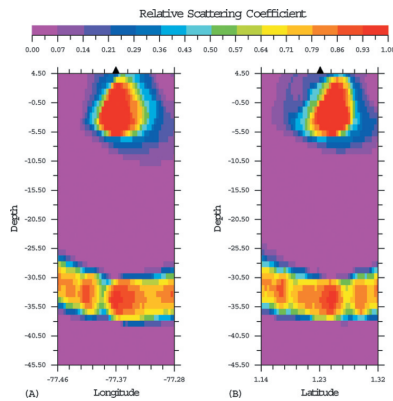


**Figure 4.** Vertical cross section showing the results of the inversion analysis for a synthetic test consisting of two spherical structures buried at depths of  $-2$  km and  $-33$  km.

volcano which shows the scattering perturbation at higher depths. A second strong scattering volume at depths between  $-29$  km and  $-36$  km is clearly observed at high frequencies and can be noticed at low frequencies. Unfortunately, in this case it is more difficult to establish the geometry of the scattering region. The ellipsoidal pattern imaged results from both a poor sampling and the geometry of the ellipses at these deeper levels, which are almost parallel. This makes it possible to establish only the depth and height of the region. A frequency dependence of the strength of the scattering coefficient is again observed thus indicating that small-scale heterogeneities contribute more scattering energy at these deeper levels.

[17] The existence of both structures is in close agreement with the current magmatic plumbing system model beneath Galeras volcano. This model is based on petrologic and seismic data and it proposes a shallow conduit system with a distinct reservoir at a depth of  $4$ – $5$  km from the summit which is periodically fed from a deeper magma reservoir which is located from km's to tens of km's depth [Calvache, 1990; Zapata et al., 1997]. In order to establish the validity of the results of this study and to help their geological interpretation, we tested the inversion method by means of a synthetic test. We simulated the presence of two magmatic chambers located at the north of the volcano at depths of  $-2$  km and  $-33$  km by two spherical structures with positive perturbations of the scattering coefficient embedded in a non perturbed medium. Thus, we assigned  $\alpha_t - 1 = 1$  to the blocks located inside the spherical structures and  $\alpha_t - 1 = 0$  to the blocks located outside. Then, we computed the corresponding coda energy residuals from the observational equation (1) using the same distribution of stations and events used in the analysis. Figure 4 shows the inversion of the synthesized residuals.

It can be observed that both the pattern and the perturbation value of the scattering coefficient were well resolved in the considered region for shallow depths. A comparison of Figures 3 and 4 suggests a reasonable agreement between synthetic and experimental results, thus supporting the identification of the scattering structures imaged with the magmatic chambers of the geological model.

[18] **Acknowledgments.** We are very grateful to Diego Gómez and the people of the *Observatorio Vulcanológico y Sismológico de Pasto*, Colombia, for providing us with information about the recent activity history of the volcano and the seismic data used in this study.

## References

- Asano, Y., and A. Hasegawa (2004), Imaging the fault zones of the 2000 western Tottori earthquake by a new inversion method to estimate three-dimensional distribution of the scattering coefficient, *J. Geophys. Res.*, *109*, B06306, doi:10.1029/2003JB002761.
- Banks, N. G., M. L. Calvache, and S. N. Williams (1997),  $^{14}\text{C}$  ages and activity for the past 50 ka at Volcán Galeras, Colombia, *J. Volcanol. Geotherm. Res.*, *77*, 39–55.
- Calvache, M. L. (1990), Geology and volcanology of the recent evolution of Galeras volcano, Colombia, M.S. thesis, 171 pp., La. State Univ., Baton Rouge.
- Calvache, M. L., G. P. Cortés, and S. N. Williams (1997), Stratigraphy and chronology of the Galeras volcanic complex, Colombia, *J. Volcanol. Geotherm. Res.*, *77*, 5–19.
- Chen, X., and L. T. Long (2000), Spatial distribution of relative scattering coefficients determined from microearthquake coda, *Bull. Seismol. Soc. Am.*, *90*, 512–524.
- Gómez, D. M., and R. A. Torres (1997), Unusual low-frequency volcanic seismic events with slowly decaying coda waves observed at Galeras and other volcanoes, *J. Volcanol. Geotherm. Res.*, *77*, 173–193.
- Kak, A. C., and M. Slaney (1988), *Principles of Computerized Tomographic Imaging*, IEEE Press, New York.
- Nishigami, K. (1991), A new inversion method of coda waveforms to determine spatial distribution of coda scatterers in the crust and uppermost mantle, *Geophys. Res. Lett.*, *18*, 2225–2228.
- Nishigami, K. (1997), Spatial distribution of coda scatterers in the crust around two active volcanoes and one active fault system in central Japan: Inversion analysis of coda envelope, *Phys. Earth Planet. Inter.*, *104*, 75–89.
- Nishigami, K. (2000), Deep crustal heterogeneity along and around the San Andreas fault system in central California and its relation to segmentation, *J. Geophys. Res.*, *105*, 7983–7998.
- Sato, H. (1977), Energy propagation including scattering effects; single isotropic scattering, *J. Phys. Earth*, *25*, 27–41.
- Ugalde, A., E. Carcolé, and J. N. Tripathi (2006), Spatial distribution of scatterers in the crust by inversion analysis of coda envelopes: A case study of Gauribidanur seismic array (southern India), *Geophys. J. Int.*, in press.
- Williams, S. N., M. L. Calvache, N. C. Sturchio, J. A. Zapata, R. A. Méndez, B. Calvache, A. Londoño, F. Gil, and Y. Sano (1990), Premonitory geochemical evidence of magmatic reactivation of Galeras volcano, Colombia, *Eos Trans. AGU*, *71*(17), 647.
- Zapata, J. A., et al. (1997),  $\text{SO}_2$  fluxes from Galeras volcano, Colombia, 1989–1995: Progressive degassing and conduit obstruction of a Decade volcano, *J. Volcanol. Geotherm. Res.*, *77*, 195–208.

E. Carcolé and A. Ugalde, Observatori de l' Ebre, CSIC—Universitat Ramon Llull, E-43520 Roquetes, Spain. (augalde@obsebre.es)

C. A. Vargas, Departamento de Geociencias, Universidad Nacional de Colombia, Ciudad Universitaria, Bogotá D.C., Colombia.